THE ASSESSMENT OF SEISMIC SITE EFFECTS DURING THE 24 JANUARY 2020 ELAZIG-SIVRICE M_W: 6.8 EARTHQUAKE

A THESIS SUBMITTED TO
THE GRADUATE SCHOOL OF NATURAL AND APPLIED SCIENCES
OF
MIDDLE EAST TECHNICAL UNIVERSITY

BY

ALAA ELSAID

IN PARTIAL FULFILLMENT OF THE REQUIREMENTS
FOR
THE DEGREE OF MASTER OF SCIENCE
IN
EARTHQUAKE STUDIES

FEBRUARY 2022

Approval of the thesis:

THE ASSESSMENT OF SEISMIC SITE EFFECTS DURING
THE 24 JANUARY 2020 ELAZIG-SIVRICE M_W: 6.8 EARTHQUAKE

submitted by **Alaa Elsaid** in partial fulfillment of the requirements for the degree of **Master of Science** i**n Earthquake Studies, Middle East Technical University** by,

Prof. Dr. Halil Kalıpçılar

Dean, Graduate School of **Natural and Applied Sciences**

Prof. Dr. Ayşegül Askan Gündoğan

Head of the Department, **Earthquake Studies**

Prof. Dr. Kemal Önder Çetin

Supervisor, **Civil Engineering, METU**

Examining Committee Members:

Prof. Dr. Erdal Çokca
Civil Engineering, METU

Prof. Dr. Kemal Önder Çetin

Civil Engineering, METU

Prof. Dr. Zeynep Gülerce

Civil Engineering, METU

Assoc. Prof. Dr. Onur Pekcan

Civil Engineering, METU

Dr. Lecturer Mesut GÖR

Civil Engineering, Fırat University

Date: 11.02.2022

I hereby declare that all information in this document has been obtained and presented in accordance with academic rules and ethical conduct. I also declare that, as required by these rules and conduct, I have fully cited and referenced all material and results that are not original to this work.

Name Last name : Alaa Elsaid

Signature :

ABSTRACT

THE ASSESSMENT OF SEISMIC SITE EFFECTS DURING THE 24 JANUARY 2020 ELAZIG-SIVRICE M_W: 6.8 EARTHQUAKE

Elsaid, Alaa
Master of Science, Earthquake Studies
Supervisor : Prof. Dr. Kemal Önder Çetin

February 2022, 269

At 8:55 p.m. local time (17:55 GMT) on January 24, the Sivrice district of Elazig, located on Turkey's second-largest fault system, was struck by a severe earthquake with a magnitude of 6.8 (AFAD) or 6.7 according to USGS. Tragically, the earthquake resulted in severe devastation, including structural damage and fatalities. In order to aid in the mitigation of potential earthquake damage that may occur in the region and to serve as a guide for site-specific seismic design for future earthquakes, the seismic site effects of the earthquake were assessed.

Within the scope of this study, the assessments of seismic site effects during the 2020 Sivrice-Elazig earthquake were undertaken following mainly three stages; (i) the performance of seismic site response analyses, (ii) the investigation of soil liquefaction hazard, and (iii) the construction of seismic zonation maps. Geotechnical and geophysical data were acquired prior to initiating the study. A total number of 210 boreholes were included in the study and were used to create the

idealized soil profile. The strong ground motion shaking of Elazig-Sivrice event, recorded by a total of seven strong ground motion stations (SGMS), was then calibrated and scaled locally in order to generate the rock motion needed in the site-specific seismic response analysis. Additionally, Deepsoil software was used to conduct the seismic site response analysis, whereas the Cetin et al. (2000, 2004, 2018) approach was adapted for the soil liquefaction study. Finally, the seismic parameters collected from the aforementioned analyses were used in the construction of the seismic zonation of Elazig-Center. This was accomplished by developing peak ground acceleration (PGA), spectral acceleration (S_a), and soil liquefaction hazard maps. Finally, recommendations for assessing seismic hazard for the Elazig-Center district were developed as part of this study's conclusion. As a word of caution, geotechnical data culled from the literature was assumed to be valid and representative throughout the analysis; therefore, any inaccuracies in the adopted geotechnical data can alter the results.

Keywords: site effects, Elazig-Sivrice earthquake, site response analyses, soil liquefaction, seismic zonation.

ÖZ

24 OCAK 2020 ELAZIĞ-SIVRICE 6.8 BÜYÜKLÜĞÜNDEKİ DEPREM ZEMİN SAHA ETKİLERİNİN DEĞERLENDİRİLMESİ

Elsaid, Alaa
Yüksek Lisans, Deprem Çalışmaları
Tez Yöneticisi: Prof. Dr. Kemal Önder Çetin

Şubat 2022, 269

24 Ocak 2020 tarihinde yerel saat ile 20:55'te (17:55 GMT), Türkiye'nin en büyük ikinci fay hattı üzerinde yer alan Elazığ'ın Sivrice ilçesinde, USGS'ye göre 6.7 veya AFAD'a göre 6.8 büyüklüğünde şiddetli bir deprem meydana gelmiştir. Ne yazık ki deprem, can kaybı ve hasarla birlikte bölgede şiddetli bir yıkıma neden olmuştur. Bölgede meydana gelebilecek olası deprem hasarlarının en aza indirgenmesine yardımcı olmak ve gelecekteki depremler için sahaya özel sismik tasarım rehberi olması amacıyla, depremin sismik alan etkileri değerlendirilmiştir.

Bu çalışma kapsamında, 2020 Sivrice-Elazığ Depremi sismik alan etkilerinin değerlendirilmesi başlıca üç aşamada gerçekleştirilmiştir; (i) sismik zemin tepki analizleri, (ii) zemin sıvılaşması riskinin araştırılması ve (iii) sismik mikrobölgelendirme haritalarının oluşturulması. Çalışmaya başlamadan önce, ilk olarak jeoteknik ve jeofizik veriler edinilmiştir. İdeal zemin profilini oluşturabilmek için 210 adet sondaj kuyusunun verileri çalışmaya dahil edilmiştir. Daha sonra, toplam yedi deprem kayıt istasyonu (SGMS) tarafından kaydedilen Sivrice-Elazığ

Depremi'nin kuvvetli yer hareketi sarsıntısı, sahaya özel sismik tepki analizi için gerekli olan kaya hareketini oluşturmak için yerel olarak ölçeklendirilmiş ve kalibre edilmiştir. Ek olarak, sismik zemin tepki analizlerini yapmak için Deepsoil programı kullanılırken, zemin sıvılaşması çalışmalarını yapmak için Cetin vd. (2000, 2004 ve 2018) methodu uygulanmıştır. Yukarıda bahsedilen analizlerden elde edilen sismik parametreler Elazığ-Merkez'in sismik mikrobölgelendirilmesinin oluşturulmasında kullanılmıştır. En büyük yer ivmesi (PGA), spektral ivme (Sa) ve zemin sıvılaşma riski haritaları geliştirilmiştir. Son olarak, bu çalışmanın bir sonucu olarak Elazığ-Merkez'in sismik tehlikesinin değerlendirilmesi için öneriler geliştirilmiştir. Bir uyarı: Literatürden toplanan jeoteknik verilerin analiz boyunca geçerli ve temsili olduğu varsayıldığı için, bu verilerdeki herhangi bir yanlışlık sonuçları değiştirebilir.

.

Anahtar Kelimeler: saha etkileri, Elazığ-Sivrice depremi, saha tepki analizleri, zemin sıvılaşması, sismik mikrobölgeleme.

To my country

To my grandparents

To my mother

To my father

To my sisters and brothers

ACKNOWLEDGMENTS

First and foremost, I would like to express my gratitude to my illustrious supervisor, Prof. Dr. Kemal Önder Çetin, without whom I would have been unable to complete my dissertation. His unflinching support and wisdom have served as an inspiration throughout this course of study. He gave unwavering assistance, advise, criticism, inspiration, and tolerance throughout the length of the research.

I would like to show my gratitude to Dr. Mesut Gör for providing me with an incredible chance to perform this research by providing the necessary resources and geotechnical data for Elazig. I would want to show my appreciation to him for his aid, since it would have been hard for me as a foreign student to access local data in a foreign language without his assistance.

My deepest gratitude goes out to my treasured family for their unflinching support and boundless devotion. They were always eager to assist me anytime I required assistance. My beloved mother, Amall Daredi, and my dear father, Mohammed Elsaid, deserve a great deal of thanks for their unwavering support and efforts in assisting me in accomplishing my goals. I'd want to express my gratitude to my sisters Samar, Aya, Malak, and Hajer Elsaid, as well as to my brother Anwar Elsaid, for their valuable contributions, constructive views, and opinions. I would like to express my gratitude to my nephew Adam Gurgi for inspiring me. I'd want to express my gratitude to my aunt, Asma Daredi, for inspiring and motivating me.

For their companionship, suggestions, and comments throughout the study, my friends Emre Gürlük, Hilal Uğurlu, Ahmed Al-Suhaily, Salih Gedük, Elife Çakır, Linda Dalipi, Anastasia Çeka, and Efekan Çevik have my warmest appreciation and thanks for being an incredible source of support and encouragement with their never-ending patience and encouragement.

I'd want to convey my heartfelt gratitude to my Libyan friends who have never forgotten me despite the distance; Raneem Bin Khayal, Raja Franka, Amna Al-Emsillati, and Salwa Zlitni have all been a constant source of encouragement and support for me.

Last but not least, I would like to express my gratitude and appreciation to the members of the community who attended my thesis defense, Prof. Dr. Zeynep Gülerce, Prof. Dr. Erdal Çokça, Assoc. Prof. Dr. Onur Pekcan, and Dr. Mesut Gör, I would like to express my gratitude and appreciation for their support and patience during the process.

TABLE OF CONTENTS

APPENDIX

LIST OF TABLES

LIST OF FIGURES

LIST OF ABBREVIATIONS

$[C]$	: Soil Viscous Damping Matrix
$[K]$	: Soil Stiffness Matrix
1-D	: One Dimensional
AFAD	: The Ministry of Interior Disaster and Emergency Management Presidency
a_{max}	: Maximum Acceleration
ASK14	: Abrahamson, Silva, And Kaman Attenuation Relationships
C_B	: Borehole Diameter Correction Factor
CB14	: Campbell And Bozorgnia Attenuation Relationships
C_E	: Energy Ratio Correction Factor
C_N	: Overburden Pressure Correction Factor
C_n	: Correction Factor to Convert The SPT-N Values to Reference Energy Value SPT-N60 Values
C_R	: Rod Length Correction Factor
CRR	: Cyclic Resistance Ratio
C_S	: Sampling Method Correction Factor
CSR	: Cyclic Strain Ratio
CY14	: Chiou And Young Attenuation Relationships
DES	: Vertical Electric Drilling
D_R	: Relative Density
EAFS	: East Anatolian Fault System
EAFZ	: East Anatolian Fault Zone
Ec8	: Euro-Code-8
FFT	: Fast Fourier Transformation

FS : Factor of Safety

GIS : Geographic Information System

GMPE : Ground Motion Prediction Equations

GMPEs : Ground Motion Prediction Equations

GMPs : Ground Motion Parameters

h : Soil Height

I14 : Idriss Attenuation Relationships

Is : Point Loading Index

Ke : Upper Cretaceous

Kh : Upper Maastrichtian

Kσ : Correction Factor of Overburden Pressure

LL : Liquid Limit

LSS : Limited Strain Softening

M_w : The Magnitude of Earthquake

MASW : Spectrum Analysis and Multichannel Analysis

METU : Middle East Technical University

MTA : General Directorate of Mineral Research and Exploration

N_{45} : Raw SPT Blow Counts For 45% Energy

NAFZ : North Anatolian Fault Zone

NE-SW : Northeast – Southwest

NGA : New Generation Attenuation

NGAW2 : Next Generation Attenuation Relationships for Western US

PEER : Pacific Earthquake Engineering Research Center

PGA : Peak Ground Acceleration

PGV : Peak Ground Velocity

Prt : Pressuremeter Tests

PzMzk : Permo-Triassic

Qal	: Quaternary
RQD	: Rock Quality Designation
S	: Period
Sa	: Spectrum Acceleration
SGM	: Strong Ground Motion
SGMS	: Strong Ground Motion Stations
SH	: Strain Hardening
SIS	: Seismic Refraction Velocities
SK	: Bore Hole
SPT-N	: SPT Blow Count Index
SS	: Strain Softening
T	Period
Ta	: Alibonca Formation
Tk	: Kirkgecit Formation
Tkb	: Upper Miocene-Lower Pliocene Karabakir Formation
Ts	: Seske Formation
USCS	: Unified Soil Classification System
V_s	: Shear Wave Velocity
$V_{s, rock}$	: Shear Wave Velocity at The Bedrock
w_c	: Water Content
Yd	: Artificial Filling
CPT	: Cone Penetration Test
C_u	: Uniformity Coefficient
D_{50}	: Median Grain Size
D_{min}	: Minimum Damping Ratio
ER	: Efficiency Ratio
E_m	: Elastic Modulus
FC	: Fine Contents

G	: Shear Modulus
GWT	: Ground Water Table
G_{max}	: Maximum Shear Modulus
M	: Event's Moment Magnitude
$N_{1,60}$	: Overburden Corrected SPT Value For 60% Energy
N_m	: Raw SPT-N Value Measured
PI	: The Plasticity Index
PI	: Plasticity Index
P_a	: Atmospheric Pressure.
R_{JB}	: Joyner-Boore Distance
R_{RUP}	: Rupture Distance
SPT	: Standard Penetration Test
SSR	: Effective Shear Strain Ratio
V_p	: Primary Compressional Wave Velocity
V_s	: Shear Wave Velocity
$V_{s,12}$	: Average Shear Wave Velocity at the Upper 12 Meters
$V_{s,30}$	: Average Shear Wave Velocity at the Upper 30 Meters
$V_{s,7}$	: Average Shear Wave Velocity at The Upper 7 Meters
Z_{TOR}	: Depth to the Top of The Rupture
a	: Curvature Coefficient,
$a(t)$	: Ground Surface Acceleration at Time t
e	: Void Ratio
e_0	: Initial Void Ratio
g	: Gravity Acceleration
r_d	: Stress Reduction Factor

LIST OF SYMBOLS

ξ	: Damping Ratio
γ'	: Effective Confining Pressure
γ_r	: Reference Strain
σ_0'	: Mean Effective Confining Stress
γ	: Unit Weight
σ_{vo}'	: Vertical Effective
σ_{vo}	: Total Stress
τ_{max}	: Maximum Shear Stress
$\delta_{\boldsymbol{x}}$	: Distance Between Two Bore Holes
$\delta_{\boldsymbol{elv}}$	: Elevation Difference Between Two Bore Holes
ρ	: Density Of the Soil

CHAPTER 1

INTRODUCTION

On January 24, at 8.55 p.m. local time (17:55 GMT), a severe earthquake hit the Sivrice district of Elazig province of Turkey, which is located in the southwest of the Eastern Anatolia region. The earthquake was reported to have a magnitude of $M_w = 6.8$ by AFAD (The Ministry of Interior Disaster and Emergency Management Presidency; www.afad.gov.tr), or a magnitude of $M_w = 6.7$ according to the USGS (United States Geological Survey; www.usgs.gov). The main shock of this earthquake had a reported peak ground acceleration (PGA) of 0.292 g.

According to AFAD's official statements, the earthquake was felt in around 20 Turkish cities, as well as in Iraq, Palestine, Lebanon, and Syria. AFAD also indicated that 41 people were killed, 37 in Elazig and 4 in Malatya, while 1466 were injured. Additionally, 50 structures were demolished in Elazig, 308 were severely damaged, and 150 were declared to be moderately damaged. Malatya city suffered from the destruction of 155 structures, and additionally 1278 structures sustained significant damage. In Diyarbakir, eight structures were destroyed, and another 16 structures sustained significant damage.

To aid in the mitigation of possible earthquake damage in the region and serve as a reference for site-specific seismic design for future earthquakes, the seismic site impacts of the eventwere examined.

The investigation was performed in three stages, the first in which seismic site response analyses were done utilizing Deepsoil software. Following that, soil liquefaction hazard evaluation was conducted and finally, the collected seismic parameters were used for the construction of the seismic site zonation maps.

Within the scope of the investigation, 210 borehole data from the Elazig (Central) Municipality Geological-Geotechnical Survey Report Based on Zoning Plan (Akare Planlama, 2015) were included. One should mention that the geotechnical results from Akare Planlama were presumed to represent soil and site conditions; any deviation from this assumption might affect the findings.

1.1 Research Goals and Objectives

This thesis aims to present the results and findings of seismic site-effect evaluation of the earthquake that occurred in Elazig's Sivrice district on the 24th of January 2020 with the intent to reduce future possible earthquake damages and provide recommendations referencing seismic parameters to be utilized in future seismic designs. This will be accomplished by providing seismic zonation maps of PGA, Sa, and liquefaction hazard.

1.2 Thesis Organization

After Chapter 1, where the research topic was introduced, Chapter 2 will conduct a literature review covering the critical concepts used in this study. The first part of Chapter 2 offers an overview of earthquakes and the factors that impact them. The chapter will next examine the ideas underlying one-dimensional site response studies and provide an overview of the software tools used to conduct these analyses that are available in the literature. Following that, a review of the literature will be conducted to provide dynamic soil characteristics, and finally, a summary of the most fundamental liquefaction concepts will be offered.

Next, in Chapter 3, the geological and seismological setting of the study area will be introduced; This chapter summarizes the location of the research region, Elazig-Center, including its geographical location, geological characteristics, and seismic settings, before delving deeper in later chapters. It is essential to emphasize that, at this point, none of the information offered in this chapter is the author's original work; rather, this part contains information gathered following a thorough assessment of the literature.

Continuing to Chapter 4, where the subsurface investigation of the Elazig-center district was conducted, Akare Planlama's (2015) geological-geotechnical survey report served as a valuable source for this chapter based on the zoning plan of the municipality of Elazig Center. The investigation includes 210 boreholes (with a total depth of 3050 m). Each borehole produces a typical sample with profiles ranging in depth from 5.00 to 30.0 m. Additionally, 170 seismic cracks with an aperture of 95 meters, 100 microtremors, and 173 vertical electric soundings were detected. Moreover, 50 pressuremeter tests in ten boreholes were undertaken, totaling 100 pressuremeter tests. After calibrating the geotechnical and geophysical data and establishing essential assumptions, 210 idealized soil profiles were developed, along with the dynamic soil parameters required to evaluate the site effects.

In Chapter 5, the observed strong ground motion will be investigated using the region's existing acceleration time histories and the NGA-WEST2 ground motion prediction equations (GMPE's). Global GMPE's were calibrated for this event with event specific SGM records. These calibrated GMPE's were used for the purpose.Prior to the site response analyses, an idealized shear wave velocity profile is constructed. Furthermore finally, the equivalent linear seismic site response analyses will be performed after locally scaling the bedrock motion for each borehole (210 total boreholes).

Next, in Chapter 6, soil liquefaction assessments will be performed; the Cetin et al. (2000, 2004, 2018) approach will be adapted for the liquefaction study.

In Chapter 7, in the light of the findings, a siesmic zonation map is constructed with counters for Peak Ground Acceleration (PGA), a spectrum acceleration map (Sa), and a liquefaction assessment map. The purpose of zonation mapping is to provide maps to the public in order to increase public awareness and minimize the possible damage that the risks might cause to the community.

Finally, chapter 8 discusses and summarizes the site effects assessment results obtained in the previous chapters and finalizes the work by providing a conclusion including some seismic recommendations to serve as mitigation for potential earthquakes as well as being a reference for dynamic parameters for future seismic designs within Elazig-center.

CHAPTER 2

LITERATURE REVIEW

The first section of this chapter will provide a quick overview of earthquakes and the characteristics that influence them. The chapter will then proceed to a review of the concepts related to one-dimensional site response analyses, as well as an introduction to the software tools available in the literature that are used to perform these analyses. Following that, a study of the literature will be undertaken in order to present dynamic soil characteristics. Lastly, a summary of the most essential ideas related to liquefaction will be provided.

2.1 Earthquakes

Evidence of earthquakes as far back as 3000 years ago has been found, and some of these earthquakes were described as very severe (Kramer, 1996). At this point, one may ask how earthquakes are generated. An answer could be that rocks that are subjected to enormous pressures break down and release a significant amount of energy from deep under the earth's crust. This energy release manifests itself in the form of waves traveling from the source to the surface. These waves have the potential to cause structural collapse, induced life losses, and soil liquefaction.

Moreover, the elastic rebound theory was developed to explain the energy released when a fault ruptures. That is, rocks along a fault maintain elastic stress until they are no longer capable of supporting it, at which point the stored energy is released in the form of an earthquake, according to Wood (1912). Earthquakes can be major or minor, and can last for a few seconds or a few minutes. The intensity, or magnitude, of an earthquake can be used to measure the size of its energy (Kramer, 1996).

2.1.1 Ground Motion Parameters (GMPs)

Seismographs and accelerographs can record ground vibrations during earthquakes. A "time history" is a visual depiction of the data acquired during an earthquake occurrence. These time histories often comprise data on acceleration, velocity, or displacement during an earthquake. This information is incredibly valuable since it may be used to predict ground motions for future occurrences that are comparable to this one. There are several ways ground motion parameters may be used to classify an event. A single metric will never be able to capture all the nuances of ground motion (Jennings, 1985; Joyner & Boore, 1988). The ground motion parameters are generated using time history records. Of the ground motion parameters, there are three main categories, namely, amplitude parameters, frequency content, and duration.

To begin, amplitude typically measures the maximum value of a time series. Amplitude parameters may be obtained from acceleration, velocity, and displacement time histories. The peak ground acceleration (PGA) is the most used parameter among the metrics mentioned above, followed by the peak ground velocity (PGV). On the other hand, peak ground displacements are theoretical but seldom used due to processing and filtering concerns (G. S. Campbell, 1985; Joyner and Boore, 1988). Although amplitude ground motion characteristics are essential, they cannot offer a complete picture of an earthquake since different earthquakes release different amounts of energy-dependent on other parameters. To illustrate, Figure 2.1 is supplied, at which two time-history records are provided. While both time histories have the same PGA value, A person may perceive that Figure 2.1 (b) is more hazardous because of its greater release of energy and longer duration. As a result, more ground motion parameters are needed to comprehend the earthquake's ground vibrations in a thorough manner.

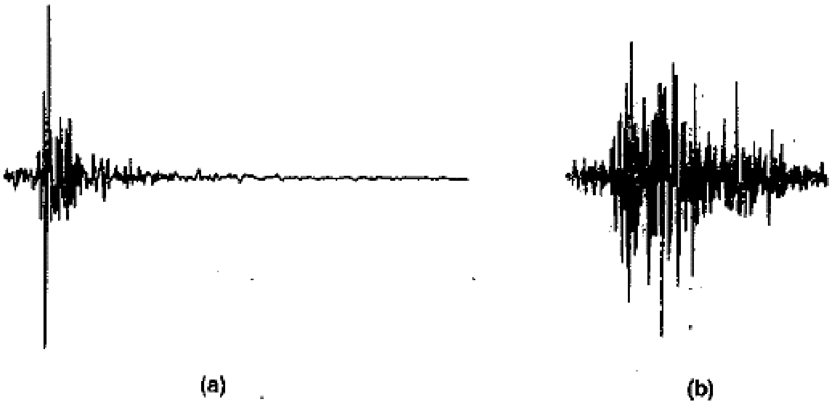

Figure 2.1. Time history records with the same PGA value (after Kramer,1996)

The following ground motion parameter is the frequency content. The frequency content of a ground motion indicates how its energy is divided throughout various frequencies or periods. A Fourier spectrum is a typical approach to understanding these frequencies.

Finally, the last ground motion parameter to be covered is the earthquake's duration. Prolonged exposure to intense ground vibrations increases induced damage because damage accumulates over time. The most used duration parameter is bracketed duration, which measures the time between two successive threshold accelerations.

2.1.2 Ground Motion Prediction Equations (GMPEs)

A comprehensive database of earthquake time histories has been built due to the number of ground motions documented recently. Using these datasets, researchers created empirical ground motion parameter correlations called attenuation equations or ground motion prediction equations (GMPEs). Engineers use ground motion prediction equations to anticipate potential ground motion characteristics in an earthquake.

Most empirical relationships contain high data dispersion, and GMPEs are no exception. Since more ground motion data is available in seismically active areas, the equations are most useful in those areas. The usage of GMPEs in areas with a limited number of historical ground motions has considerable constraints. These correlations may be utilized in places where fewer earthquakes have been recorded because of the ergodic assumption, which states that if other factors (e.g., magnitude, source-to-site distance) are maintained constant, two ground motions in two distinct geographic locations should be comparable (Arndt, 2017).

The first attenuation relationships were based only on magnitude and distance factors, as shown in Figure 2.2. These attenuation relationships have gotten more intricate over time as more data on the ground motion has been accessible. Late in the decade of the 2000s, the Pacific Earthquake Engineering Research Center (PEER) embarked on a mission to create a comprehensive, validated ground motion database containing all currently accessible crustal earthquake data. Following the database's completion, PEER selected five research teams to construct new GMPEs called the New Generation Attenuation (NGA) (Abrahamson & Silva, 2008; Boore & Atkinson, 2008; Chiou & Youngs, 2008; K. W. Campbell & Bozorgnia, 2008; and Idriss, 2008).

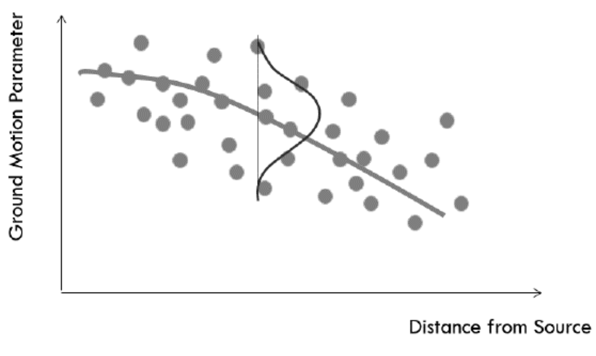

Figure 2.2. Early graph used for the attenuation relationships (after Arndt, 2017).

The goal of NGA East is to bring the GMPEs for continental tectonic zones up to date. PEER is also doing a second investigation to examine the earthquake "fingerprint" of ground movements near subduction zone sources, which were not included in the original NGA correlations (Arndt, 2017).

2.2 One Dimensional Site Response Analysis

When a fault ruptures, body waves move in all directions away from the source. Reflection and refraction occur at the borders between various geological materials. When inclined rays hit horizontal layer borders, they are often reflected in a more vertical orientation because the propagating velocities of shallower materials are typically lower than those of the materials below them. Multiple refractions bend the rays nearly vertically when they reach the earth's surface, as shown in Figure 2.3.

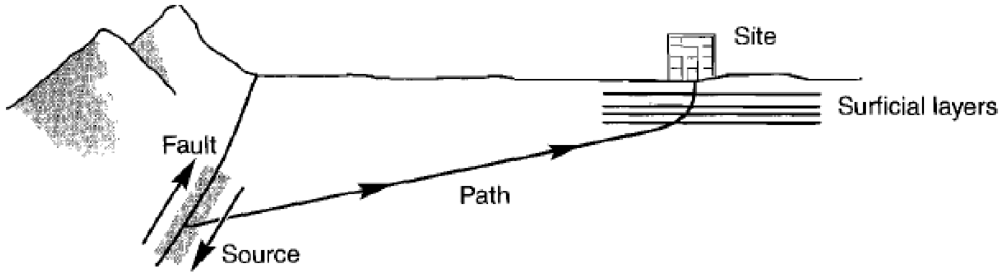

Figure 2.3. Refraction causes near-vertical wave propagation (Kramer, 1996)

Before explaining any of the ground response models, it is essential to define a few concepts. One of these concepts is the within and the outcrop motions. A bedrock motion is a motion at the base of the soil deposit (or bedrock). A rock outcropping motion occurs when bedrock exposes to the earth's surface. The motion at the top of the bedrock would be the bedrock outcropping motion Figure 2.4 (b).

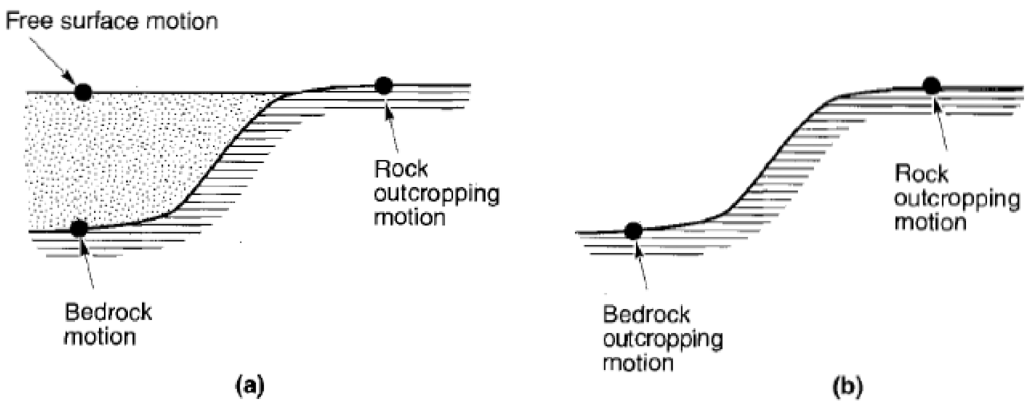

Figure 2.4. (a) soil free surface overlying bedrock; (b) outcropping bedrock. The vertical scale is distorted (retrieved from Kramer, 1996).

In a one-dimensional site response analysis, seismic waves move vertically from the bedrock underneath to the ground surface. Layer boundaries are assumed to be indefinitely stretched and perpendicular to the wave propagation direction. One-dimensional site response analysis is often performed using equivalent linear and nonlinear methodologies. A question that can be raised at this point is which approach a person should follow while performing site response analysis? The produced cyclic shear strain during an earthquake is a significant factor in determining whether a linear or nonlinear approach is preferable.

The input motions for 1D studies are based on the acceleration time histories of prior earthquakes. To better explain, when an earthquake occurs at a particular location, the motion that is recorded on the free surface (considered as the most common case) is carried downward (after being scaled appropriately) to the bedrock of other locations of interest. All of this is being done in order to forecast surface motions of the new location of interest. A 1D site-specific seismic site response analysis is depicted in Figure 2.5.

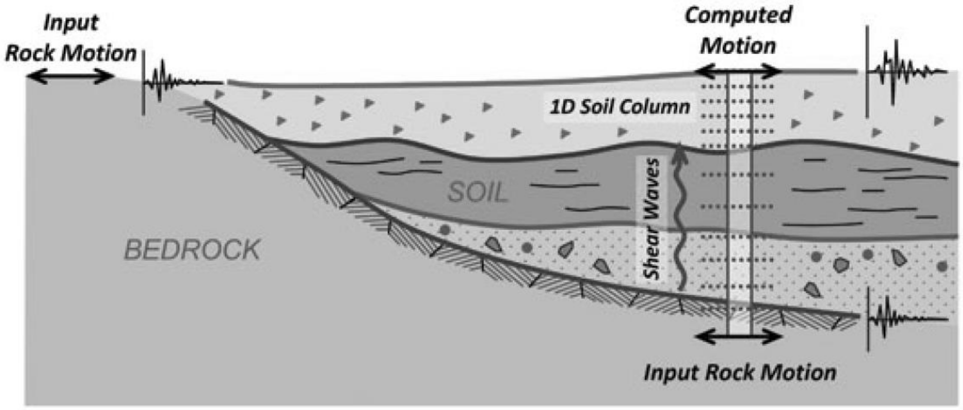

Figure 2.5. Site Response Analysis (after Nikolaou, 2009).

As mentioned previously, there is a wide range of model types and analytic methods to choose from when conducting site response analyses (linear, equivalent linear, and fully nonlinear). Indeed, depending on the dimensions considered, one, two, and three-dimensional site response analyses exist.

A seismic site response analysis involves either equivalent linear or nonlinear analyses. 1-D equivalent linear is the most commonly used approach in seismic engineering today, and it will be adapted in this study.

2.2.1 Equivalent Linear Analysis

Schnabel et al. (1972) pioneered the equivalent linear analysis technique, a variant of the linear approach that enables more precise site response prediction. The linear approach is generally used to determine the amplification factor and phase shift for each frequency encountered during shaking. The soil column impedance ratios and layer thicknesses play a significant role in determining how much the soil column amplifies or de-amplifies each frequency of the input motion (Hutabarat, 2016).

Fast Fourier Transformation (FFT) will transform the input acceleration time histories from the time domain into the frequency domain. This transformed function is usually the bedrock input motion. The fast Fourier transformation calculates the original time history from the input motion for each frequency in the Fourier amplitude spectrum. The output motion's Fourier series is created by multiplying this series by the transfer function and then dividing the resulting series by the frequency range, that is, the outcrop surface motion. The output Fourier series is then converted back into the time domain using the inverse fast Fourier transformation in order to acquire the output motion's time history. Kramer (1996) provides a thorough description of the 1-D site response analysis.

The linear approach assumes that the soil is a Kelvin-Voight material with a constant G_{max} and D_{min} damping ratio. Because of the tremendous strains involved, this assumption cannot anticipate the results accurately. On the other hand, the equivalent linear approach accounts for the nonlinearity in an indirect way. That is, G/G_{max} and damping curves are used at the relevant strain level with repeated, iterative computations until the strain level matches the effective shear strain with an acceptable error (Figure 2.6).

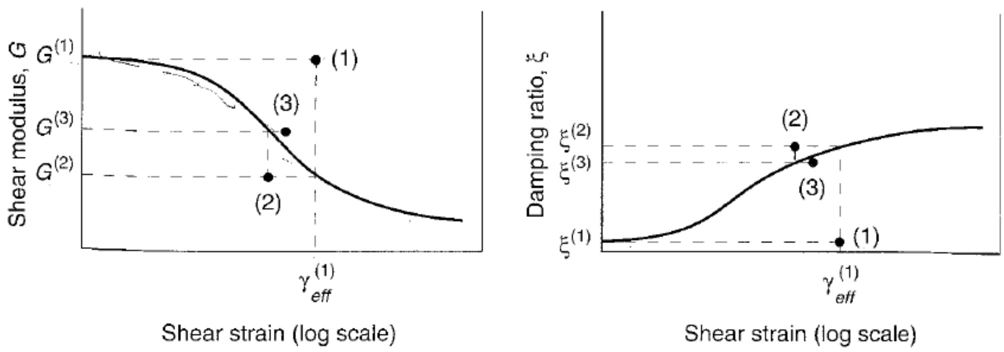

Figure 2.6. The iterative solution used in the equivalent linear site response analysis approach (retrieved from Kramer, 1996)

When doing an equivalent linear analysis, it is usual practice to employ superficial, readily available soil characteristics and low processing needs, as the computation is conducted in the frequency domain (Hashash et al., 2010).

2.2.2 Nonlinear Site Response Analysis

In the nonlinear site response analysis approach, the dynamic wave equation (provided in Equation 2-1) is adapted (this is the case for the time domain). Equation 2-1 and the one-dimensional wave propagation Equation 2-2 are the two most widely used equations in the Newtonian method (Nonlinear Analysis). Analysis of structure reaction to input ground motions is often carried out by employing nonlinear analysis in a time-step approach (Chopra, 2012).

$$[M]\{\ddot{u}\} + [C]\{\dot{u}\} + [M]\{u\} = -[M]\{I\}\ddot{u}_g \tag{2-1}$$

$$\frac{\partial \tau}{\partial z} = \rho \frac{\partial^2 u}{\partial^2 t^2} = \rho \frac{\partial}{\partial} \dot{u} \tag{2-2}$$

Furthermore, the soil viscous damping matrix $[C]$, which is often generated using Rayleigh damping or a frequency-independent approach, is commonly produced as a lumped mass system (Phillips & Hashash, 2009). The key to the nonlinear analytic approach is the continuous update of the soil stiffness matrix $[K]$ (Matasovic & Vucetic, 1993; Itasca, 2011; and Groholski et al., 2016b) or an advanced constitutive soil model (Iwan W, 1967; Mroz, 1967; Yang, 2000; and Iai et al., 2011). In order to get the response (i.e., displacement, velocity, and acceleration) of each node of interest, the equation is numerically solved for each time step using a time integration methodology such as Newmark's method (Newmark, 1959).

To solve the equation of seismic wave propagation given in Equation 2-2, a forward finite difference approach (Kramer, 1996; Bardet & Tobita, 2001) or a finite element analysis can be used. Using this technique, the soil column is divided into several sublayers, each with a different thickness. The finite difference method is used to get the answer at each node (depth) and time step in the partial differential equation.

Introducing viscous damping in Equation 2-1 is necessary to reduce oscillations and adapt the nonlinear models to the system that the nonlinear models do not describe (Stewart et al., 2008). However, when it comes to Equation 2-2, $[C]$ is not needed since it assumes that all material damping is included in the stiffness. Excluding Rayleigh damping may help mitigate the problem of overdamping at high strain levels (Kaklamanos et al., 2015).

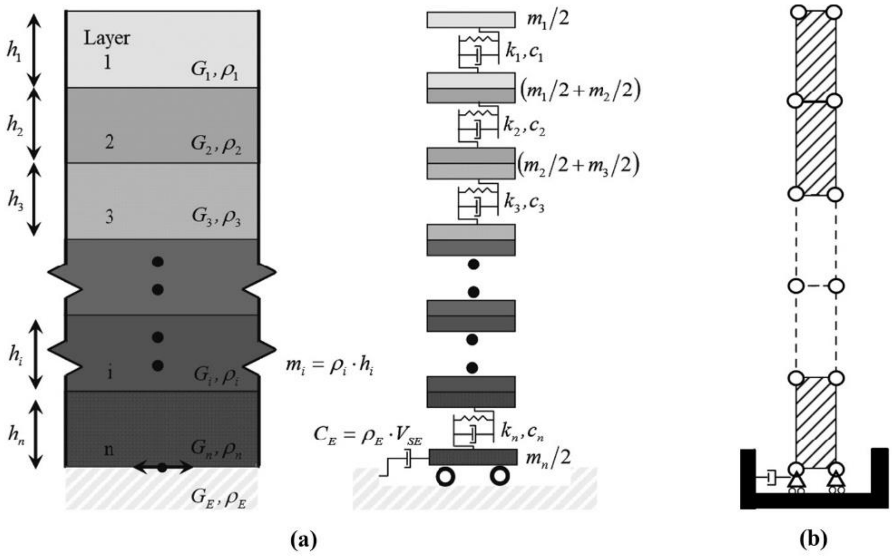

Figure 2.7. A multi-degree-of-freedom and lumped mass system (Hashash, 2010, after Stewart, 2008).

Soil dynamic properties are considered when solving the displacement, velocity, and acceleration equations at each time step (G_{max} and D_{min}). In order to determine the shear strain inside each layer, the value obtained is then utilized.

In order to update the soil's shear modulus, which is subsequently used to compute the response in the following time step, the amount of generated shear strain is compared to the nonlinear or advanced constitutive soil model. This approach is repeated until the response at each node is determined for the length of the input motion (i.e., time histories of acceleration, velocity, displacement, shear stresses, shear strains, and pore water pressure if the analysis is conducted using the effective stress technique).

Despite the fact that these two methodologies are used to solve separate equations in site response analysis, the procedure remains the same. Both of their governing equations are solved at the start of each time step to produce particle displacement, velocity, and acceleration using starting soil dynamic characteristics (G_{max} and D_{min}). The outcome is then utilized to calculate the shear strain inside each layer. The induced shear strain is then matched to the nonlinear soil model or advanced constitutive soil model to update the soil's shear modulus, which is utilized to compute the response in the following time step. This procedure is continued for the duration of the input motion until the response at each node is computed (i.e., time histories of acceleration, velocity, displacement, shear stresses, shear strains, and pore water pressure if the effective stress technique is used).

The nonlinear technique uses a stress-strain relationship to mimic the actual nonlinearity under cyclic loading by updating the soil stiffness parameters after each time step. The nonlinear soil model utilized will significantly impact the accuracy of the estimate.

(Matasovic & Vucetic, 1993; Phillips & Hashash, 2009; and Itasca, 2011) Use target G_{max} and damping curves and try to fit their model by altering the model's core equation with fitting curve parameters. Modulus reduction and damping can be fitted to a higher degree of precision when damping is fitted to a lesser degree of precision, and vice versa.

As for the third aspect, the technique provided by Yee et al. (2013) is to alter the target curve such that it does not exceed the soil's peak shear strength (strength correction procedure). By enabling soil peak shear strength to be determined while also offering flexibility to match minor strain soil behavior, Groholski et al. (2016) propose a new equation for performing the curve-fitting technique with significantly more accuracy.

2.2.3 Available Equivalent Linear Site Response Analysis Software

The equivalent-linear method has become one of the most extensively utilized site response analysis methodologies since it was first developed by Schnabel et al. (1972). Because the analyses would have taken a long time and the technique is based on trial and error, numerous software applications implementing the equivalent-linear method have been developed over the years since the method was first published. This section will introduce the most widely used and well-known tools for equivalent linear analysis.

The first well-known equivalent-linear code is SHAKE, created by B. Schnabel et al. in 1972. In years, this program was undergone several upgrades, and different versions were developed. Its first upgrade was called SHAKE91; this version is considered a source code for most of the other software. The next update is SHAKEVT moving to the next upgrade, SHAKE2000. Finally, the last version available today is the EduSHAKE and ProSHAKE programs which are also based on the SHAKE original code (Lasley et al., 2014).

DeepSoil may be considered the second most popular equivalent linear site response analysis program. At the University of Illinois at Urbana–Champaign, Youssef M.A. Hashash directed the development of DEEPSOIL, a one-dimensional site response analysis program (Hashash, 2018). Its popularity stems from the fact that it is free and available to everybody. It also includes a user-friendly graphical user interface. This program can perform linear analyses in the time and frequency domains, as well as equivalent-linear analyses in the frequency domain and, lastly, nonlinear site response analyses in the time domain. Furthermore, this program includes a variety of damping and normalized shear modulus degradation curves and the user's opportunity to input his own degradation curves. It is also worth noting that exporting the output data to Microsoft Excel is an option in DeepSoil. Throughout this study, DeepSoil software will be used to perform the equivalent linear site response analyses.

Strata, developed at the University of Texas at Austin by Albert Kottke and Ellen M. Rathje (Kottke & Rathje, 2009), is another popular equivalent linear site response analysis tool.

Lasley et al., (2014) conducted a study in which they have compared the available site response analyses software; they examined five implementations of the equivalent-linear method for a single profile and ground motion using (ShakeVT2, SHAKE91, SHAKEVT, Strata, and DEEPSOIL). In their investigation, identical inputs were implemented, and as a result, they obtained similar solutions. However, they have reported that complex shear modulus and effective strain ratio can impact the findings, especially for high-frequency records with much energy. It has also been demonstrated that discretizing the profile when plotting the maximum shear strain against depth with DEEPSOIL, SHAKEVT, or SHAKE91 may hide peaks. When the input motion file includes an odd number of columns, SHAKE91 and SHAKEVT suffer from an implementation error that generates inaccurate results.

2.3 Dynamic Soil Properties

Soil dynamic properties such as shear modulus (G) and damping ratio (D) are used in the 1D analysis. These dynamic soil properties have been simulated over a wide range of soil types through several relationships (Kondner & Zelasko, 1963; Hardin & Drnevich, 1972; and, Hasash & Park, 2001). There are several variations on older scholars' modulus and damping equations, but each is based on Massing's (1926) cyclic shear stress and shear strain behavior. The G and D curves supplied for each layer are essential to the validity of both the corresponding linear and nonlinear solutions. Modifications were made to the Darendeli & Stokoe (2001) G and D curves to accommodate coarse-grained material data, such as gravel, for use in this investigation. Both relationships will be addressed in this section.

The Hardin & Drnevich (1972) model was modified by Stokoe and Darendeli (2001). In order to calibrate and update their model for sand, silt, and clay soils, they acquired an enormous quantity of experimental data. The shear stress curve was also given a curvature coefficient and a damping component to be more in line with experimental findings (Stokoe & Darendeli, 2001).

The dependency of the shape of the modulus reduction curve (G/G_{max}) on the value of the uniformity coefficient, C_u, was a significant result from Menq (2003). Menq (2003) established the reference strain, γ_r, as a relationship determined by the median grain size, D_{50}, the void ratio e, and the effective confining pressure, γ'. The model indicates that C_u has the most significant impact on $\gamma_r$which decreases as C_u rises.

The primary difference between the models developed by Menq (2003) and Stokoe and Darendelli (2001) is that Menq (2003) employed a database of gravelly soil samples rather than sand and clay samples. Menq (2003) established a changing curvature coefficient to more correctly predict the shear strain correlation of gravels.

This coefficient was significantly adjusted from the relationship produced by Stokoe and Darendeli (2001) and is provided in Equation 2-3, where $\sigma_0{}'$ is the mean effective confining stress in the model at the mid-depth of a soil layer and P_a is atmospheric pressure.

$$a = 0.86 + 0.1 * \log(\frac{\sigma_0{}'}{P_a}) \quad (2\text{-}3)$$

Menq (2003) discovered that Equation 2-4, based on the relationship between γ_r and C_u, better-approximated gravel's reference shear strain calculations.

$$\gamma_r(\%) = 0.12 * C_u^{-0.6} * \left(\frac{\sigma_0{}'}{P_a}\right)^{0.5*C_u\text{^}-0.15} \quad (2\text{-}4)$$

It is now possible to describe G and D characteristics by considering a change in the curvature coefficient, a, which typically rises with increasing effective confining pressure, as opposed to the constant curvature coefficient recommended by Stokoe and Darendeli in Menq (2003). Stokoe and Darendeli (2001) continued to utilize the damping ratio, scaling coefficient, and fitting parameters $c1, c2, and\ c3$ that they had previously used for soils composed of sand, silt, and clay for coarse material.

2.4 Liquefaction

Earthquake liquefaction is a relatively new phenomenon in the geotechnical earthquake engineering community. Generally speaking, Scientists in the 1960s first recognized it, but evidence of the phenomena may be found in numerous historical earthquakes. Liquefaction was observed in action during two significant earthquakes of that decade, one in USA-Alaska and the other in Japan-Niigata. This early evidence helped define earthquake liquefaction as the process by which pore-water pressure rises and effective stress falls, resulting in the transition of solid materials into liquids. (Marcuson, 1978).

Mogami and Kubo used the word "liquefaction" (1953). While the specific definition of liquefaction has been contested, it is invariably the result of excess pore pressure buildup under undrained loads (Kramer, 1996). Excess pore pressures are often formed when cohesionless, saturated, and loose soil contracts due to some disturbance. Excess pore pressures reduce the soil's effective stresses, weakening it. Error (2017) reported in his thesis that the excess pore pressures could be caused by monotonic, transient, or recurrent disturbances or loadings from a range of sources, including anthropogenic (e.g., artificial fills, mine tailings piles, pile driving, blasting, and building vibrations) or seismic occurrences. However, Within this thesis, the term "liquefaction" refers to seismically generated soil liquefaction.

2.4.1 Definition of Liquefaction

In general, and as the name implies, solids are transformed into "viscous liquefied" states as part of the "liquefaction" Phenomenon. Several factors contribute to earthquake-induced soil liquefaction: Rapid loading (e.g., an earthquake) causes an undrained condition to be met; this leads to increased interparticle pore pressure, resulting in a reduction in effective stress, hence a reduction in shear strength occurs.

Rapidly decreasing shear strength causes solid particles to undertake a transition and convert into a viscous-liquid condition. Many researchers have defined the liquefaction phenomena in various ways in the literature. According to NCEER (1997), liquefaction is characterized by the propagation of enormous pore-water pressures, resulting in fine-grained soils' deformation. The liquefaction of granular materials is the process by which they go from a solid to a liquid state due to a decrease in effective stresses caused by an increase in pore pressure, as defined by Marcuson (1978). During liquefaction, an undrained loading situation is met. While liquefaction phenomena occur in loose saturated sand, on the loose to relatively dense granular soils with strong drainage capability, like silty sand or sand and gravel with an impermeable deposit junction (NCEER, 1997), liquefaction is observed.

2.4.2 Liquefaction Types

NCEER (1997) elucidated the distinct behaviors of loose and thick soils when subjected to undrained triaxial compression testing. NCEER (1997) reported results from undrained triaxial compression tests performed by (Ishihara, 1993) on Toyoura sand. The Ishihara (1993) investigation results are depicted in Figure 2.9. Ilgaç (2015) explained the study of Ishihara (1993); she reported that Ishihara utilized a very loose sand specimen with an initial void ($e_0 = 0.916$) and relative density (D_R=16%). She stated that it is discovered that the behavior varies under various confining stress levels. For instance, at 0.1 MPa confining stress, deviatoric stress achieves a peak value more significant than the ultimate stress value referred to as the "ultimate state." This is referred to as strain-softening behavior. However, the material exhibits strain hardening behavior at smaller confining stresses (e.g., 0.01 MPa).

2.4.2.1 Flow Liquefaction

NCEER (1997) elucidated the distinct behaviors of loose and thick soils when subjected to undrained triaxial compression testing. NCEER (1997) reported results from undrained triaxial compression tests performed by (Ishihara, 1993) on Toyoura sand. The Ishihara (1993) investigation results are depicted in Figure 2.9. Ilgaç (2015) explained the study of Ishihara (1993); she reported that Ishihara utilized a very loose sand specimen with an initial void ($e_0 = 0.916$) and relative density (D_R=16%). She stated that it is discovered that the behavior varies under various constraining stress levels. For instance, at 0.1 MPa confining stress, deviatoric stress achieves a peak value more significant than the ultimate stress value referred to as the "ultimate state." This is referred to as strain-softening behavior. However, the material exhibits strain hardening behavior at smaller confining stresses (e.g., 0.01 MPa).

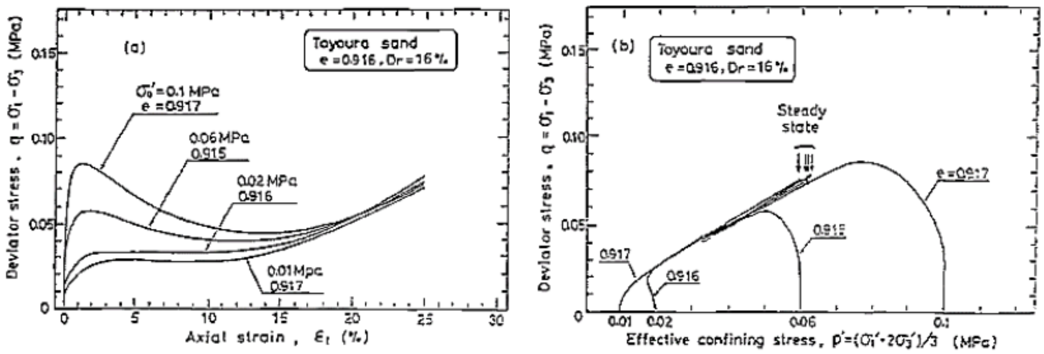

Figure 2.8. Undrained behavior of Toyoura sands (after Ishihara, 1993)

In triaxial compression testing, NCEER (1997) shows that sand behaves in an undrained monotonic way (after Robertson, 1994). Three different behaviors were observed by NCEER (1997). They were referred to as follows: strain softening (SS), strain hardening (SH), and limited strain softening (LSS) In which depending on whether the particles' void ratio is greater, less, or very close to the ultimate state line, respectively. "Flow liquefaction" is the name given to this form of liquefaction involving two strains, and the behavior explained by NCEER (1997) is shown in Figure 2.9.

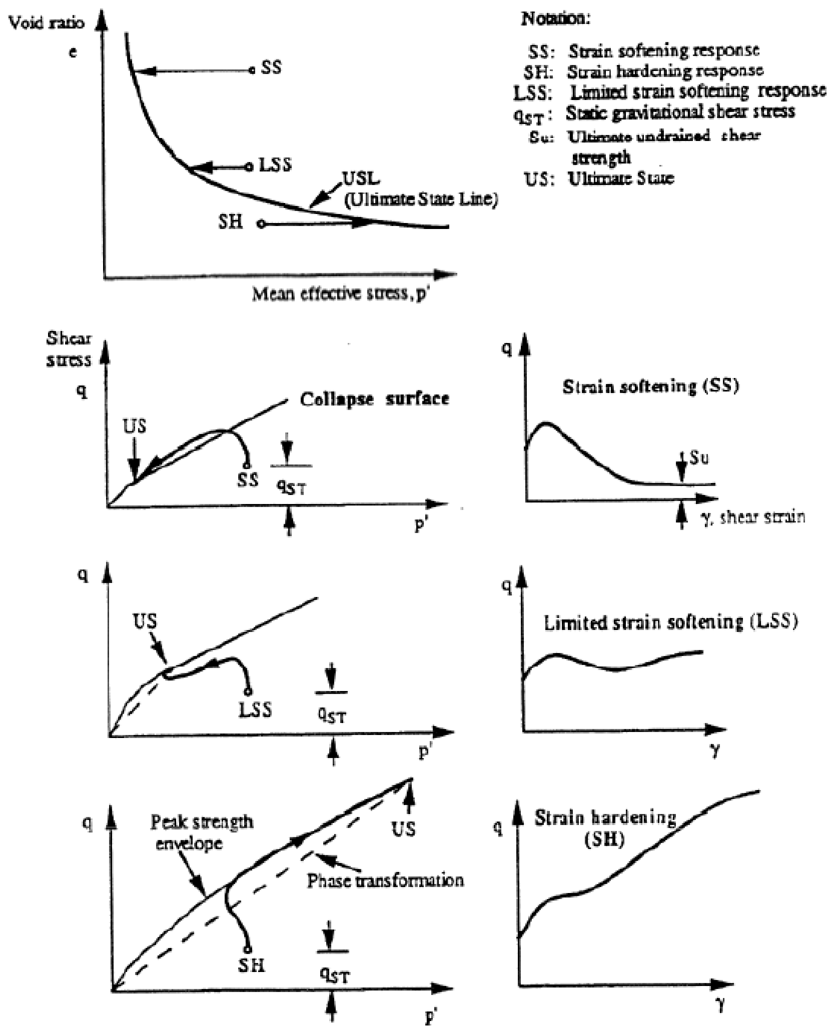

Figure 2.9. A triaxial compression test results illustrating the monotonic underained behaviour of sands (after Robertson, 1994)

When the initial shear stresses in a liquefied soil exceed the steady-state strength of the liquefied soil, flow liquefaction occurs. Soil that has been liquefied will deform until the driving shear forces reach or exceed the steady-state strength. Only soils that plot inside the shaded zone of Figure 2.10 may undergo flow liquefaction. If the initial stress level of the soil is smaller than the liquefied steady-state strength, flow liquefaction cannot occur. The more away from a soil's initial stress state plot is from the FLS, the more resistant it is to liquefaction (Kramer 1996).

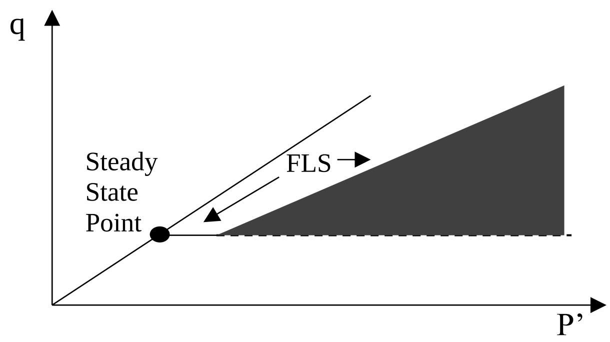

Figure 2.10. Flow liquefaction (modified after Kramer, 1996)

2.4.2.2 Cyclic Mobility

When the shear stresses necessary for static equilibrium are less than the steady-state strength, cyclic mobility results. Thus, cyclic mobility may be present in the shaded area in Figure 2.11. This phenomenon occurs in both loose and dense soils. (Error, 2017).

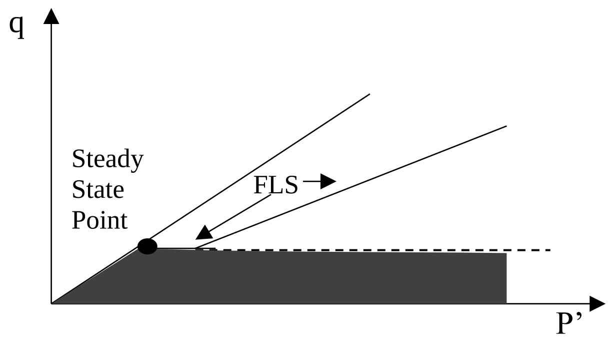

Figure 2.11. Cyclic mobility (modified after Kramer, 1996)

Sand's cyclic undrained behavior was confirmed by NCEER (1997), which demonstrated cyclic liquefaction (After Robertson, 1994). According to NCEER (1997), Saturated cohesionless soils yield positive pore pressures when subjected to cyclic undrained stress. During cyclic loading, the effective stress is zero if shear reversals occur. This behavior is described as cyclic liquefaction. If soil approaches this zero effective stress value, particle stiffness will be pretty low. To explain the enormous distortions, this is what is happening: In the case of steeply sloped sites subjected to moderate cyclic loading, there are no shear reversals during cyclic loading, but certain deformations may still take place despite the absence of the zero effective stress condition. Cyclic mobility is the term for this type of deformation.

2.4.3 Approaches to Evaluating Liquefaction Initiation

Initially, laboratory tests were utilized to measure liquefaction potential. These procedures were beneficial, but challenging to get undisturbed specimens (Seed & Idriss, 1971), thus engineers developed methods to forecast liquefaction using in-situ soil strength. These approaches are called "empirical" or "observation-based" methods.

In today's liquefaction evaluation, cycle strain-based and cyclic stress-based methods are used. In Çetin (2000), he explains that every empirical approach requires two variables, a demand term (cyclic strain ratio (CSR), earthquake intensity, accelerogram energy, etc.)and a capacity term. Soil strength parameters are represented by (SPT, CPT, V_s , etc.). Additionally, Çetin (2000) stated that the most utilized combination of these demand and capacity variables was CSR and SPT-N values.

2.4.3.1 Cyclic Stress Ratio

Seed and Idriss proposed a more straightforward approach for evaluating liquefaction potential in 1971. This process was the first to employ empirical methods for liquefaction analysis. The initial equations provided by Seed and Idriss (1971) remain the foundation for most of the models today. Following the occurrence of major earthquakes in Alaska and Japan in 1964, these approaches were accessible. At that time, massive amounts of subsurface data were acquired, which aided in the construction of a liquefaction triggering model based on soils that were confirmed to have liquefied or not liquefied during the same seismic event.

The streamlined technique used two main parameters: seismic demand on a soil layer and soil liquefaction resistance (Youd & Idriss, 2001). The computation of a liquefaction safety factor became a ratio of the soil's demand and capacity to withstand liquefaction.

The most common way for determining liquefaction triggering is to compare earthquake loads against a soil's ability to withstand liquefaction. Earthquake loading is evaluated using cyclic shear stresses normalized by the effective vertical stress and expressed as a cyclic stress ratio (CSR).

NCEER (1997) defined CSR as the seismic demand on a soil layer, whereas CRR is the soil layer's capacity to resist seismic soil liquefaction. For a stiff soil block, shear forces at the base can be written in Equation 2-5.

$$\tau(\mathrm{t})_{\mathrm{rigid}} = \gamma \mathrm{h} \frac{\mathrm{a(t)}}{g} \tag{2-5}$$

where;

$a(t)$ is the ground surface acceleration at time t, g is the gravity acceleration, h is the soil height, and γ is the unit weight

Seed and Idriss (1971) demonstrated that soil acts as a deformable body, resulting in lower generated shear stresses than Equation 2-6. According to Seed and Idriss (1971), a stress reduction factor (r_d) is required.

$$\tau(t)_{deformable} = \gamma h \frac{a(t)}{g} \; r_d \tag{2-6}$$

An average shear stress value should be used to depict seismological shear stress time histories, according to Cetin (2000), because the time histories of these stresses are irregular. Using Equation 2-7, Seed and Idriss (1971) determined that 65 percent of the maximum shear stress is a reasonable starting point for calculating the average shear stress.

$$\tau(t)_{average} = 0.65 \, \gamma h \frac{a(t)}{g} \; r_d \tag{2-7}$$

It was argued by Seed and Idriss (1971) that the cyclic stress ratio (CSR) could adequately reflect generated shear stresses once the effective vertical stress had been normalized. For calculating CSR, Seed and Idriss (1971) provided an expression that includes the vertical effective and total stress ($\sigma'_{vo}, \sigma_{vo}$) as shown in equation Equation 2-8, as well as depicting the loads operating on a soil block in Figure 2.12.

$$CSR = \left(\frac{\tau_{av}}{\sigma'_{vo}}\right) = 0.65 \left(\frac{a_{max}}{g}\right)\left(\frac{\sigma_{vo}}{\sigma'_{vo}}\right) r_d \qquad (2\text{-}8)$$

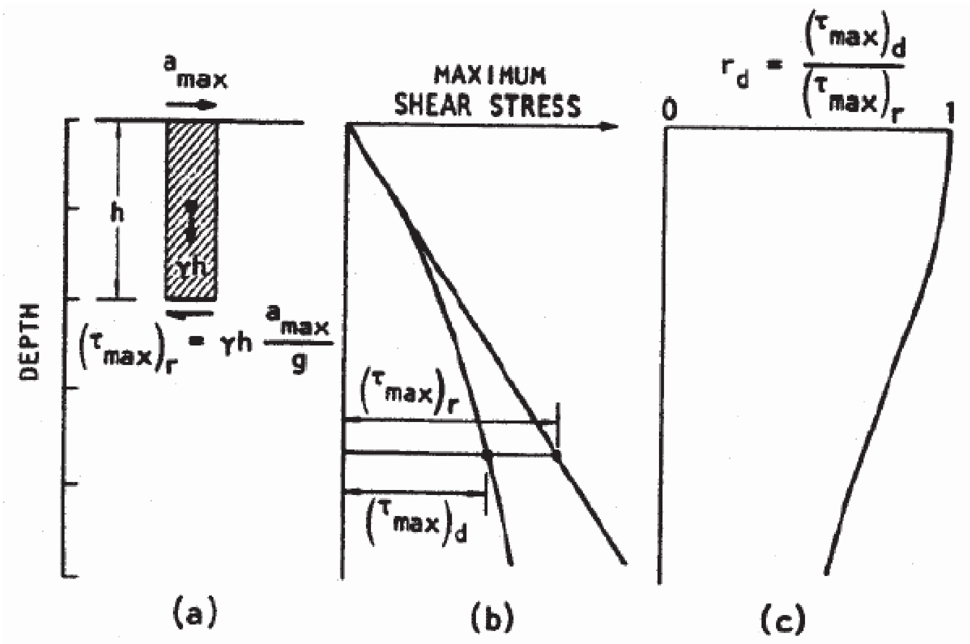

Figure 2.12. Maximum shear stress determination (Seed & Idriss, 1971)

Furthermore, the stress reduction factor, or in other terms, mass participation factor r_d is introduced in different ways by many researchers. To begin with, Cetin (2000) claimed that stratigraphy, soil properties, and input ground motion characteristics were necessary. Cetin (2000) states that site response analysis may not be possible for some locations; hence r_d correlations were suggested as a substitute.

Seed and Idriss (1971) offered a chart method to figure out r_d. Afterward, NCEER (1997) digitalized Seed and Idriss' (1971) curves and supplied a mathematical formula with a bit of adjustment. In Addition, In the case of a horizontal deposit being moved horizontally, Ishihara (1977) applied wave propagation theory. The appendix of Ishihara (1977) has a mathematical estimate of the $r_d$value. After this, based on six site response analysis findings from two alluvial sites, Iwasaki et al. (1978) proposed another correlation to determine r_d. Next, based on 143 ground response evaluations, Imai et al. (1981) advocated another r_d correlation. After that, in 1989, site response assessments were conducted for three soil sites by Golesorkhi. He computed the r_d values using 35 distinct ground motions with variable peak ground accelerations and moment magnitudes. Afterward, Idriss and Golesorkhi (1997) provided an empirical form of r_d correlation after Golesorkhi (1989). Finally, using 42 different types of ground motion as input, Cetin et al. (2004) carried out site response analysis on 50 different types of liquefiable soils. Analysis of 2153 site responses is carried out.

In this particular study, the Cetin et al. (2004) approach will be adapted, for this reason, the equations used in this approach are demonstrated, Cetin et al. (2004) suggest a link between r_d and several variables, this is shown in Equation 2-9, Equation 2-10 and, Equation 2-11. On the other hand, Figure 2.14 shows the average V_s, M_w, and a_{max} values for each site, as well as the r_d values derived from those data.

For $d < 20$ m:

$$r_d\left(d, M_w, a_{max}, V^*_{s,12m}\right) = \frac{1+\frac{-23.012-2.949\ a_{max}+0.999\ M_w+0.0525\ V^*_{s,12m}}{16.258+0.201.e^{0.341\ \left(-d+0.0785.v^*_{s,12\ m}+7.586\right)}}}{1+\frac{-23.012-2.949\ a_{max}+0.999\ M_w+0.0525\ V^*_{s,12m}}{16.258+0.201.e^{0.241\ \left(0.0785.v^*_{s,12\ m}+7.586\right)}\mp\sigma_{\varepsilon_{r_d}}}} - 0.0046(\mathrm{d}-20) \mp \sigma_{\varepsilon_{r_d}} \tag{2-9}$$

For $d \geq 20$ m:

$$r_d\left(d, M_w, a_{max}, V^*_{s,12m}\right) = \frac{1+\frac{-23.012-2.949\ a_{max}+0.999\ M_w+0.0525\ V^*_{s,12m}}{16.258+0.201.e^{0.341\ \left(-d+0.0785.v^*_{s,12\ m}+7.586\right)}}}{1+\frac{-23.012-2.949\ a_{max}+0.999\ M_w+0.0525\ V^*_{s,12m}}{16.258+0.201.e^{0.241\ \left(0.0785.v^*_{s,12\ m}+7.586\right)}-0.0046(\mathrm{d}-20)\mp\sigma_{\varepsilon_{r_d}}}} \tag{2-10}$$

$$d < 12m\ (\approx 40ft) \rightarrow \sigma_{\varepsilon_{r_d}}(d) = \mathrm{d}^{0.8500}.\, 0.0198 \quad (2\text{-}11)$$

$$d < 12m\ (\approx 40ft) \rightarrow \sigma_{\varepsilon_{r_d}}(d) = 12^{0.8500}.\, 0.0198 \quad (2\text{-}12)$$

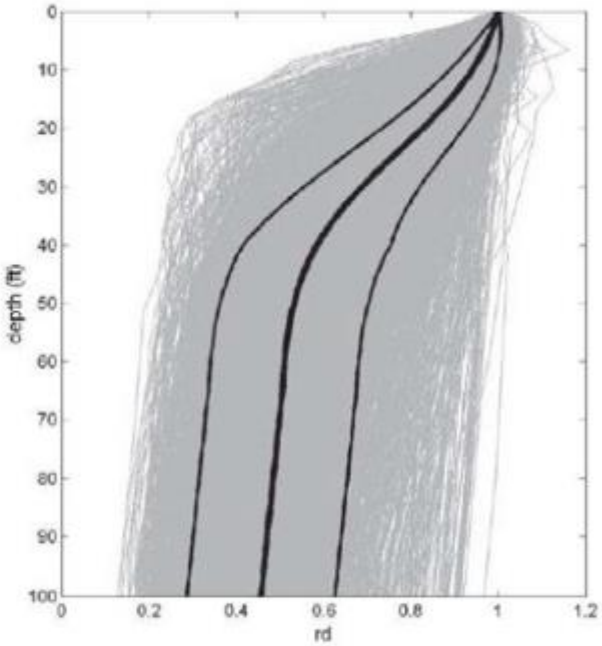

Figure 2.13. The average Vs, Mw, and a_{max} values for each site, as well as the r_d values (retrieved from Ilgaç, 2015 after Cetin et al. (2004))

CHAPTER 3

GEOLOGICAL AND SEISMOLOGICAL SETTING OF THE STUDY AREA

On the 24th of January, 2020, The Elazig-Sivrice Earthquake struck Turkey's second-biggest fault system, the Sivrice-Puturge portion of the East Anatolian Fault Zone, denoted by (EAFZ), which was struck by a left-lateral strike-slip fault. This zone is defined by fault segments that connect the eastern end of the North Anatolian Fault Zone (NAFZ) to the Mediterranean Sea in the Gulf of Iskenderun. The EAFZ is located in northern Turkey (Taymaz et al. 1991). The Karlıova intersection is where the NAFZ and EAFZ meet.

This work will focus mainly on Elazığ, a city located in eastern Turkey (N38.3593°, E39.0630°); **Error! Reference source not found.** shows the location of Elazığ city o n the map (Google Maps). During the event, Elazig city was roughly located 37 kilometers south-southwest of the epicenter; this event had a focal depth of 8.06 kilometers (AFAD). The Sivrice-Puturge section is located within the East Anatolian Fault system, which forms the tectonic border between the Eurasian, Arabian, and African plates and the Anatolian Plate. It accommodates roughly 5-10 mm yearly slip (Gülerce et al., 2017). The Elazig-Sivrice earthquake's impacts have been felt throughout the Elazig and Malatya areas, from Hazar Lake in the east to downtown Malatya in the west. The cities of Kahramanmaras, Diyarbakir, Adiyaman, Sanliurfa, and Batman were also shaken by the earthquake (METU, 2020).

This chapter provides a summary of the research area, Elazig, including its geographical location, geological features, and seismic settings before moving on to more in-depth investigation in subsequent chapters.

It is important to note that none of the information presented in this chapter is the author's original work; rather, this section comprises information compiled after a comprehensive review of the literature.

Figure 3.1. The location of Elazig on Turkey’s map (Google Maps).

3.1 The Geographical Location of the City of Elazig

Elazig is a province located in the Upper Euphrates section of the Eastern Anatolia region, having a total area of 9,281 kilometers, of which 8,455 kilometers are land, and 826 kilometers are the dam and natural lake regions. Elazig, 1,067 meters above sea level, has a landform composition, including steep hills, plateaus, and plains. The province has an area of 0.12 percent of Turkey's landmass and is located between 40^{o} 21' and 38^{o} 30' east longitudes and 38^{o}17' to 39^{o}11' north latitudes.

Within this context, Elazig's roughly rectangular area measures around 150 kilometers in the east-west direction and around 65 kilometers in the north-south. It is positioned at the crossroads of the highways linking Eastern Anatolia and Western

Anatolia. The province is bounded on the east by the lands of Bingol, on the north by the lands of Tunceli via the Keban Dam Lake, on the west and southwest by the lands of Malatya via the Karakaya Dam Lake, and on the south by Diyarbakir. The Euphrates and its tributaries are the most significant rivers within the province. Moreover, Hazar Lake, covering an area of 86 square kilometers, is located 30 kilometers from the city center. Additionally, it is bordered by significant dam lakes, including Keban, Karakaya, Kralkiz, and Ozluce (Elazig Municipality geological-geotechnical report, 2015).

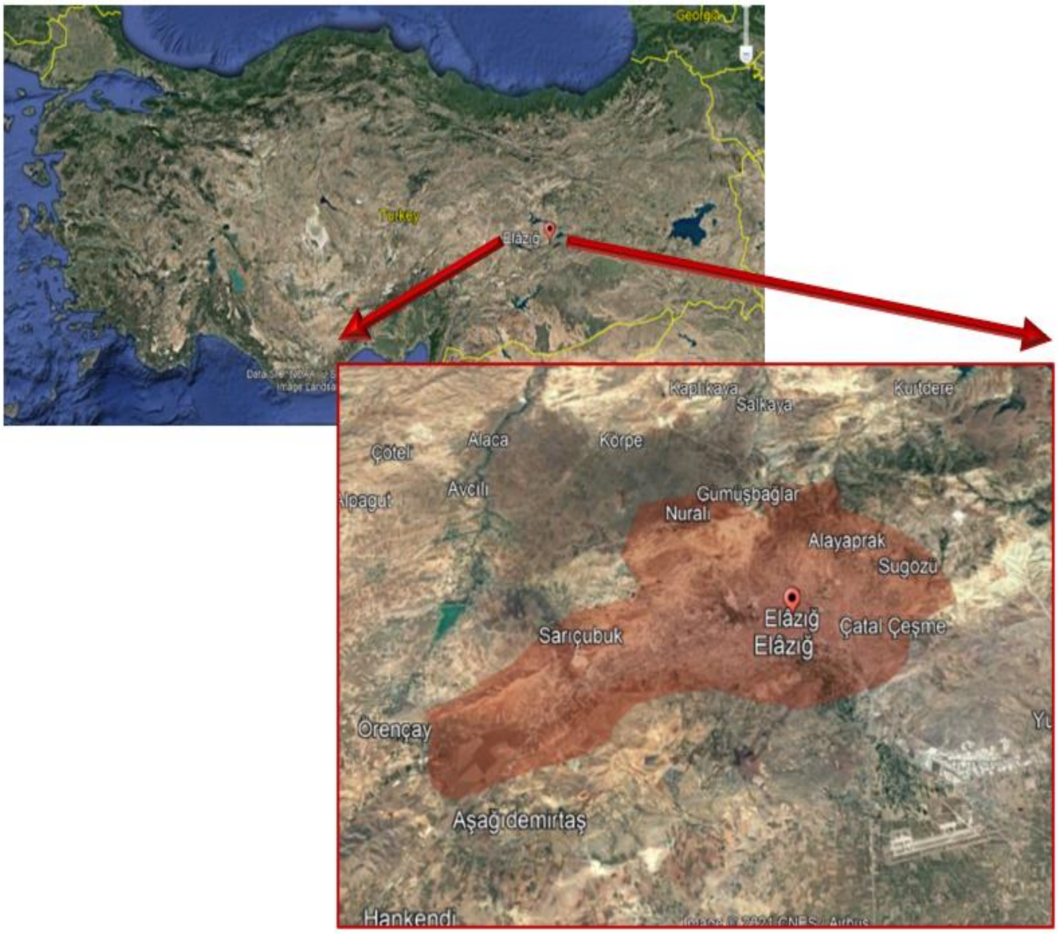

Figure 3.2. Geographical location of the study area (Google Earth)

3.2 The Geological Setting of Elazig

In this subsection, a summary of the geological settings of Elazig will be provided, beginning with a brief introduction to the overall geological structure of the city, followed by extensive explanations of each geological unit existing in Elazig, and finalizing the section by providing a generalized stratigraphic section of the study region.

Azak et al. (2020) listed the geological units of Elazig province according to their chronological order from the oldest to the youngest as follows:

- Among the most notable are the **Keban metamorphics**, which are composed of Permo Triassic-aged crystallized limestones (Permo-Triassic; PzMzk).
- **Elazig Magmatites**, which are composed of Senonian-aged granite, granodiorite, basalt, basaltic pillow lava, andesite and dacite dykes, and volcanosedimanter rocks (Upper Cretaceous; Ke).
- **Harami Formation**, which is composed of Upper Maastrichtian-aged massive limestones (Upper Maastrichtian; Kh).
- The **Kirkgecit Formation**, which consists of Middle Eocene-Upper Oligocene-aged conglomerate, sandstone, marl, and limestones, as well as other sedimentary rocks.
- **Mine Complex** consisting of sedimentary rocks such as mudstone, sandstone, and claystone, as well as magmatic rocks such as basalt, andesite, and diabase, and a variety of other rocks.
- The **Karabakir Formation** is composed of tuff, agglomerate, basaltic lava, and lacustrine limestones that date from the upper Miocene to the Lower Pliocene.

In addition to the mentioned formations, “Elazığ (Merkez) Belediyesi İmar Planına Esas Jeolojik-Jeoteknik Etüt Raporu” (2015) highlighted approximately three more formations that are present in the studied region:

- Upper Paleocene-Lower Eocene **Seske Formation** (Ts),
- Lower Miocene aged **Alibonca Formation** (Ta),
- **Artificial Filling** (Yd).

Figure 3.3 depicts the formations mentioned above on a geological map of the study area (the map is not scaled).

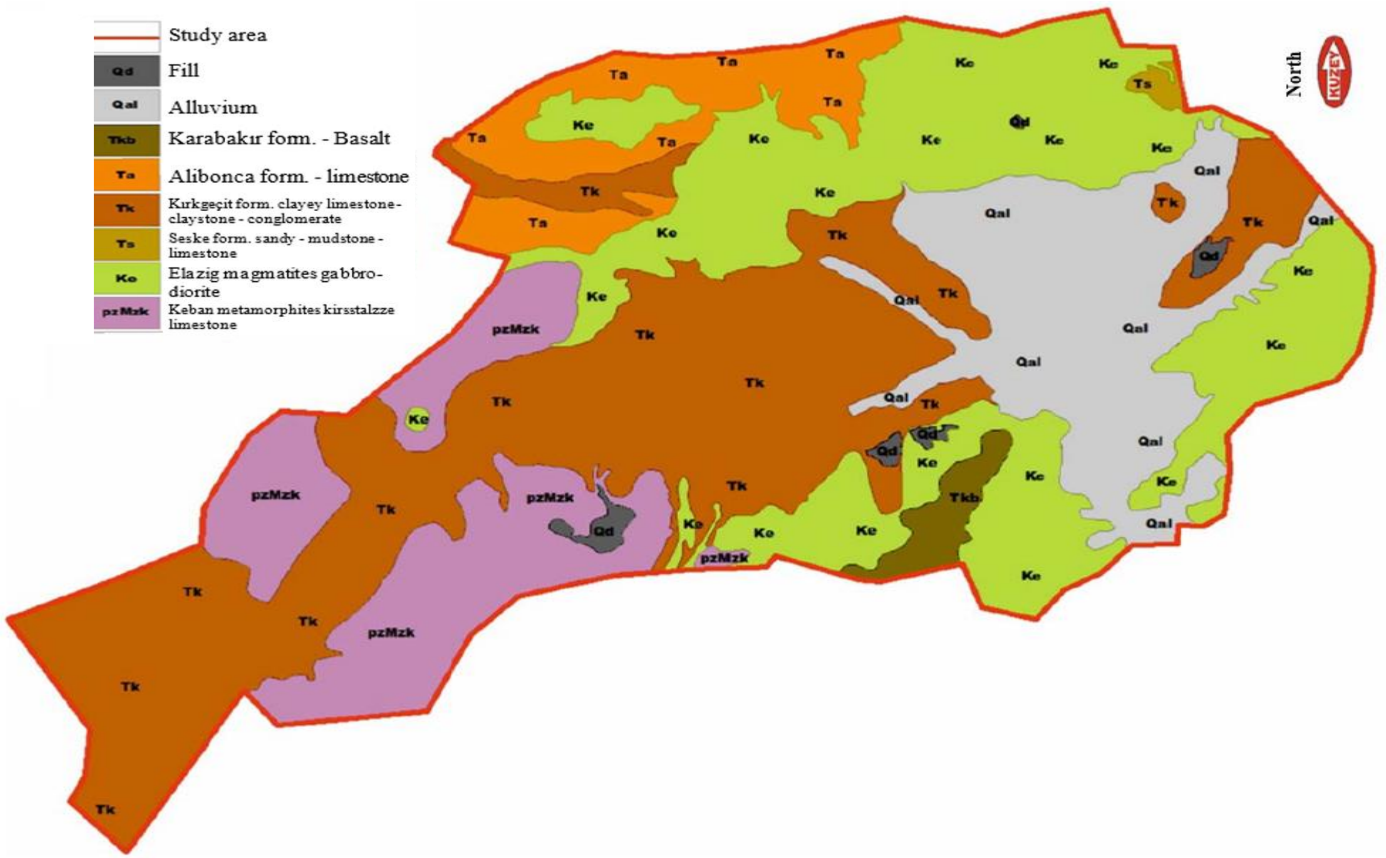

Figure 3.3. Unscaled geological map of the study area. (after Akare Planlama, 2015)

3.2.1 Keban metamorphics (Permo-Triassic; PzMzk)

Özgül (1976) was the first to designate the formation and defined it as Keban Metamorphics. Those metamorphics are outcropping near Bitlis Massif and Keban, and they display typical characteristics of Alanya Unit features (Palutoglu, 2014).

Akgül (1987) conducted a top-to-bottom analysis of the Keban metamorphics. He indicated that there are mainly three formations: recrystallized limestones (calcschist), marble, and metaconglomerate (calcphyllite). In their investigation in the Tunceli-Ovacik district, Palutoglu (2014) stated that Özgül and Turşucu (1984) established the same sequence. The marbles are conformably overlain by the recrystallized limestone-calcschist formation, and subsequently, the marbles are tectonically forced over the recrystallized limestone-calcschist formation (Akgül, 1987).

The Keban metamorphics were examined by Kaya (2001), who subdivided them into four formation units. These formations are stratigraphically consistent with one another; they include the Early Permian Arapgir recrystallized limestones, the Late Permian Nimri formation, the Permo-Triassic Keban marble, and the Late Triassic Delimehmet formation (Palutoglu, 2014).

3.2.2 Elazig Magmatites (Upper Cretaceous; Ke)

Perinçek, in 1977, initially characterized and called the Elazig Magmatites formation (Perinçek, 1979; Palutoglu, 2014). According to Palutoglu (2014), this formation is composed of serpentinite, gabbro, diabase, basalt, granite, granodiorite, tuff, agglomeration, limestone, shale, and volcanic sandstone (Tuna, 1979; İ. Türkmen, 1988; and Palutoglu, 2014).

Elazig Magamatites are intersected by diorite, tonalite, granodiorite, and basaltic pillow lavas, andesitic lava flows, and granite dykes and intrusions that cut through all depth and surface rocks, including pyroclastics, volcanoclastic, and gabbros from the Kömürhan ophiolites below, according to (Bingöl & Beyarslan, 1996). Specifically, they claim that it comprises dacite dykes and dacite domes that cross andesitic lava pyroclastics and volcanoclastic, as well as andesitic lava. Locally intrusive within the gabbros that compose the top half of Kömürhan Ophiolite, the granitic depth rocks of the unit offer a source of information about the unit's origin. The Elazig Magmatites are tectonically overlain by the Kömürhan Ophiolite and the Maden Complex; the volcanic rocks are known as Elazig Magmatites (Palutoglu, 2014).

Elazig migmatites, gabbro, diorite, monzonite, monzodiorite depth rocks at the bottom of the study area, basalt and basaltic lava flows, andesite, agglomerate, lapillistone, tuff, and interbedded volcano-sedimentaries, and all of them intersecting, volcano-sedimanteres, granodiorites, and gran Granite and dacites are the leading composites (Palutoglu, 2014).

3.2.3 Harami Formation (Upper Maastrichtian; Kh)

Palutoglu (2014) has stated that this formation was first described by Erdoğan in 1975; he stated that this formation is composed of conglomerate, sandstone, sandy limestone, and massive limestones. The unit was discovered near Harami village in the north of the Gölbaşi district of Adiyaman. Harami formations can be found in small areas of a few hundred square meters in the north, south, and east of Harput. According to Azak et al. (2020), the Kirkgecit Formation, which is composed primarily of large limestones, covers the unit that contains the Elazig Magmatites. This formation is characterized by a succession that begins with red-colored conglomerate and sandstones at the base of the study area and continues upward with yellowish beige sandy limestone and crystallized limestones at the top of the formation. The transition is gradual and smooth when moving between units in the lateral and vertical directions.

3.2.4 Kirkgecit Formation

As Palutoglu (2014) declared, TPAO geologists 1978 were the first to characterize and identify the Kirkgecit Formation in the vicinity of Kirkgecit Village in the southeast of Van (Naz, 1979; Türkmen, 1988; and Palutoglu, 2014).

The formation, which is widely distributed across the Elazig Region, commonly overlies the pre-tertiary units irregularly, although it overlies the Seske formation in particular outcrops. The Alibonca, Karabakir, and Palu formations exist around it.The formation in the neighborhood of Elazig exhibits regional lithological variances; it is mainly composed of conglomerate, sandstone, limestone, and marls. While limestones dominate the region's northern surface, the southern surface is dominated by conglomerate, sandstone, and marls. (Türkmen et al., 2001).

3.2.5 Karabakir Formation

The Karabakir formation is divided into three geological units: volcanics, limestone, and conglomerate-sandstone. Volcanics are the most abundant geological unit in Karabakir. Volcanic rocks may be found around one kilometer east of Yenikoy and one kilometer west of Yadigar districts. Limestone members may be found in the neighborhood of Rizvan and Baz Hills and in the western districts of Dogukent, Saibaba, and Atalcesme. The conglomerate-sandstone formation may be found in the northern and northeastern parts of Yenikoy District and in the vicinity of Yadigar District. The Karabakir Formation encompasses the Keban Metamorphics, Elazig Magmatites, and the Kirkgecit Formation unconformity, among other things. Some alluviums are unconformity Pleistocene in age. According to paleontological evidence, the Karabakir formation is believed to have formed during the Upper Miocene period. (Azak et al., 2020).

3.2.6 Alluvium (Quaternary; Qal)

The study area's youngest formations are alluviums of the Quaternary period. In the studied region, alluviums produce extremely massive outcrops. It includes terraces and current alluviums in river beds and alluvial fans that emerge in front of seasonal rivers (Palutoglu, 2014).

The alluvium is composed of large and small pebbles, sand, and silt, and its thickness varies between 6-7 meters. This material is entirely distinct because it is derived from the rocks in the research region. The size of the material rises as one moves from the southern to the northern regions of the study area (Palutoglu, 2014).

3.2.7 Seske Formation (Ts)

The municipality survey report of geological and geotechnical settings of the region (2015) mentioned that Seske formation is detected in the research region around the Harput castle, mostly comprised of limestones. It is commonly seen in medium-thick bedded, light gray, and yellowish-grey tones. Moreover, this unit is rich in microfossils. It appears to be a biomicrite with fossil and shell pieces in micritic mud under the microscope. In addition, Outcrops of clayey limestones may be found in the research region, and they typically display stratifications.

3.2.8 Alibonca Formation (Ta)

According to Elazig's geological-geotechnical survey report (2015), the unit is found in the northwest regions of the research area; it begins with red-colored conglomerates, progresses through sandy limestones, and finally concludes with sandstone-marl alternation. Moreover, sandstone has been found throughout the study region, in locations where the Alibonca formation is visible, and sandstone layers with limestone intercalations have been discovered in outcrops.

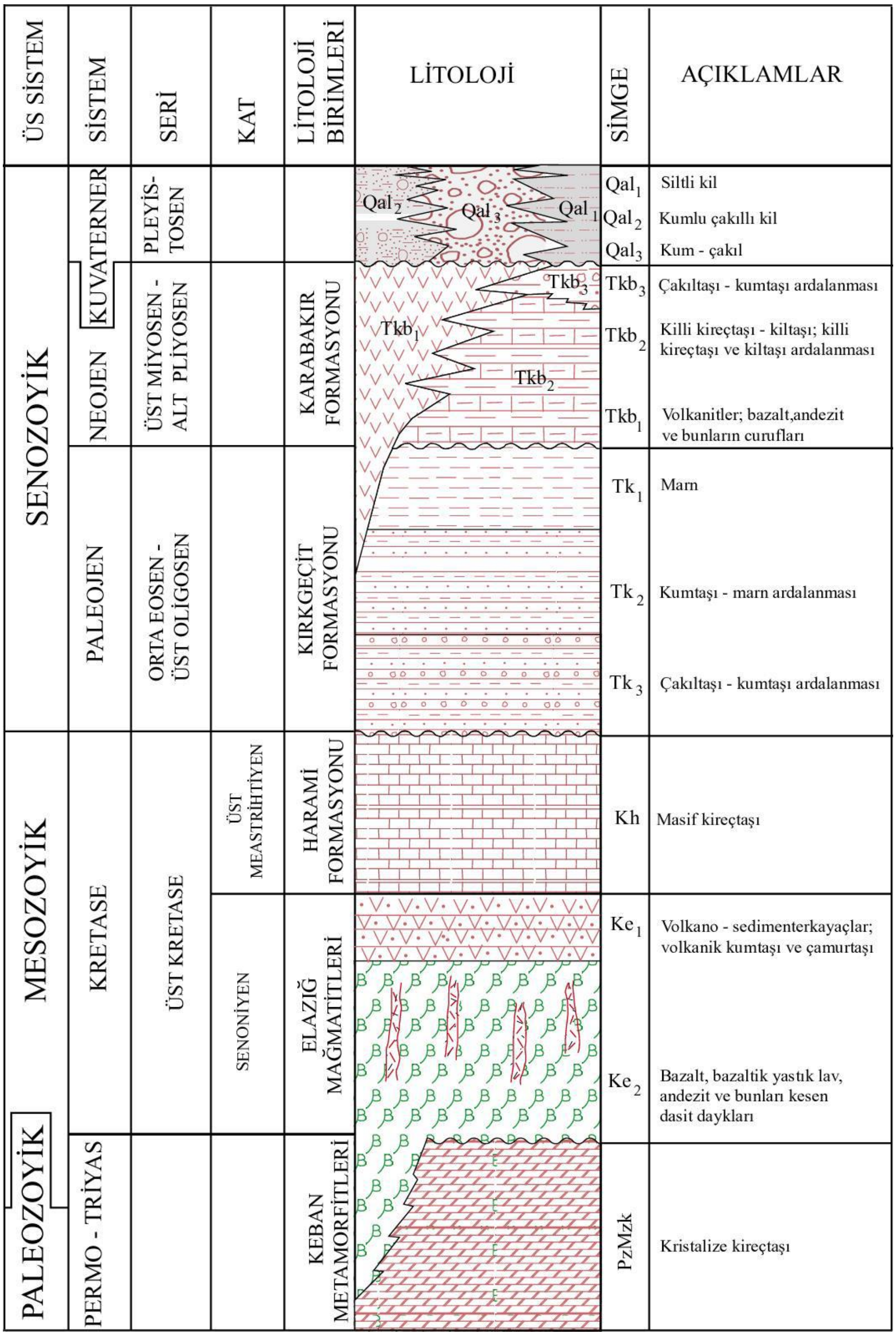

Figure 3.4. Generalized stratigraphic section of the study area (Palutoğlu & Tanyolu, 2006).

3.3 Historical Earthquakes

A number of major earthquakes ($M_w > 6$) and surface rupturing with complicated movement patterns occurred in the EAFZ over the twentieth century. (Barka, 1996; Utkucu et al., 2003; and METU, 2020). According to AFAD 2020, 299 earthquakes with magnitudes greater than 4.0 occurred in the EAFZ in the 20th century, the greatest of which was a 6.9 magnitude earthquake. Additionally, the area had 40 previous earthquakes before 1900. The following table (summarized from METU's 2020 Elazig–Sivrice Earthquake report) lists a few of the most devastating earthquakes as compiled by the USGS:

Table 3.1 Significant historical earthquake that happened close to the study region.

Name	Date	Mw	Epicenter *	Effect
Bingol earthquake	May 1971	6.9	150 kilometers northeast of the epicenter	It killed 65 people and caused considerable damage
Lice earthquake	September 1975	6.7	140 kilometers east	More than 2,000 people were killed, and thousands of homes were damaged
Surgu earthquake	May 1986	6.1	120 kilometers to the west	15 people were killed & nearly 4,000 homes were destroyed
Bingol earthquake	May 2003	6.4	40 kilometers northeast	More than 700 structures were damaged
Elazig-Kovanclar earthquake	March 2010	6.1	100 kilometers to the northeast	42 people were killed, 100 were wounded, and close to 300 houses were demolished

* The location of the epicenter given concerning the 2020 Elazig-Sivrice Earthquake's epicenter

3.4 Seismological Settings of Elazig

Extending from the Karlova junction to Antakya, the EAFZ is an intracontinental strike-slip fault with NE-SW striking and left-lateral intracontinental. The EAFZ fault is illustrated in Figure 3.5. For the EAFZ fault strand, Duman & Emre (2013) recommended seven segments with segment lengths ranging from 31 to 113 km. MTA accepted these segments in their Updated Active Fault Maps (Emre et al., 2013). Duman and Emre (2013) distinguish between the Palu and Lake Hazar segments and the Puturge and Lake Hazar/Sincik segments separated by the Lake Hazar releasing bend (METU, 2020). The 2010 Kovanclar earthquake is thought to have boosted stress levels on the fault that would be responsible for the 2020 occurrence (Akkar et al., 2011; and METU, 2020).

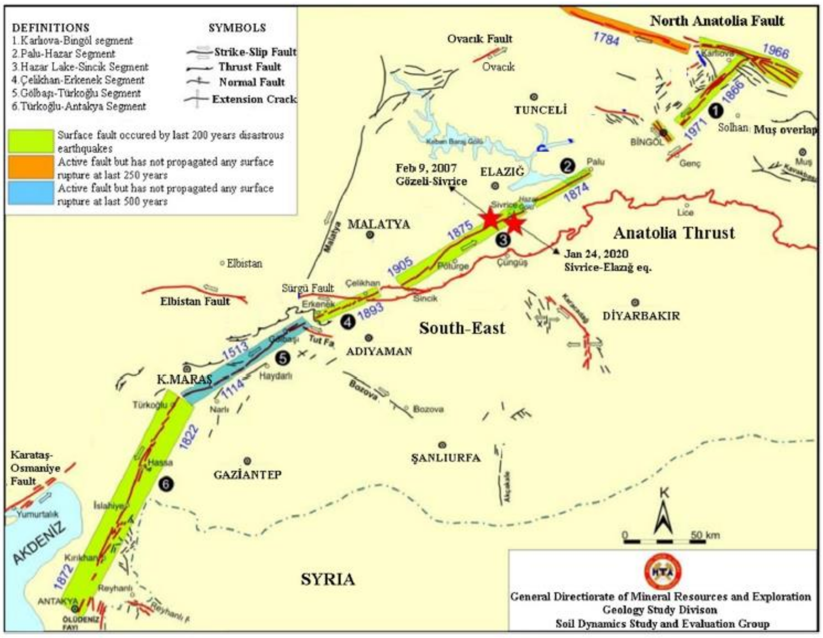

Figure 3.5. A map of the East Anatolian Fault Zone and the most destructive earthquakes in the region's history, borrowed from MTA (Kürçer et al. 2020)

3.4.1 Active Faults

On the 24th of January Sivrice – Elazig Earthquake took place in Turkey’s East Anatolian Fault Zone (EAFZ), which is reported to be an intra-continental left-lateral strike-slip fault striking Northeast – Southwest (Cetin et al., 2021). The EAFZ shows translational features due to the Arabian-African and Eurasian plates colliding. The region's strong seismicity is caused by the collision of four major tectonic plates: Arabian, Eurasian, Indian, and African, plus a comparatively minor tectonic block called Anatolia (Azak et al., 2020). As stated by Palutoğlu & Tanyolu (2006), there are mainly two active faults lying in the study area: Elazig Fault and Palu – Sincik Fault. The active faults of the study area are listed in the following sub-sections in more detail.

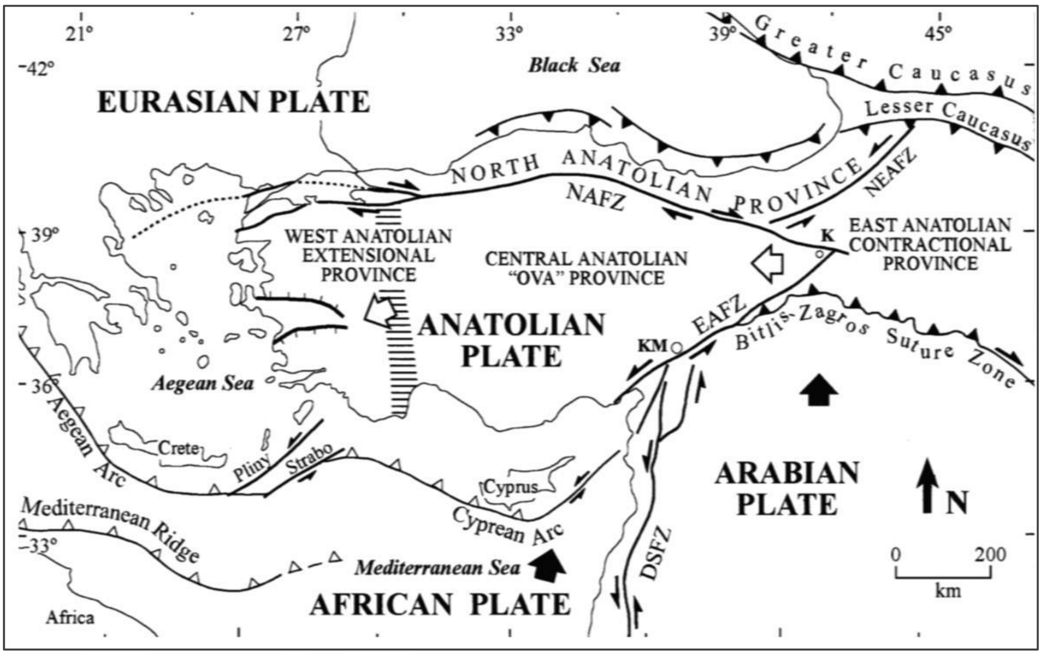

Figure 3.6. Tectonic mechanisim of the study area (Bozkurt, 2001)

3.4.1.1 Elazig Fault

According to Palutoğlu & Tanyolu (2006), the fault extends east-west through the Elazig City Center Settlement Area and north-south beyond the study area. The Elazig fault was called from the route it takes through the residential areas of Elazig city center, including the Abdullahpasa district, Cumhuriyet district, Firat University campus, Izzetpasa Ulukent district, and Dogukent district. The western extension of the fault lies near Harput College. It runs almost parallel to the road on the north end of the Elazig-Malatya Highway, crossing via Hilalkent from the north end of Bilgem College.

Palutoğlu & Tanyolu (2006) reported that the Elazig fault is an E-W trending reversal fault in the area. However, the fault may exhibit normal fault characteristics from location to location. Because a portion of this fault, known as the Elazig Fault, cuts the conglomerate–sandstone section of the Karabakir Formation, it must be Upper Miocene-Lower Pliocene in age or younger.

3.4.1.2 Palu–Sincik Fault

The DAF is approximately 145 kilometers long. It is located south of Palu, extending along the iro Stream from the Hazar Lake–Sivrice–Doanyol route to the north of Sincik. It is located outside the EAF-Caspian Lake area in a small zone. The fault divides the Maden Complex from the Oligocene-aged Krkgeçit Formation in the Palu region. It passes through the Hazar Complex, which dates from the Upper Cretaceous to the Lower Eocene to the northeast of Hazar Lake. It passes through the Maden Complex to the south of the lake and continues southwestward. It is in charge of the Plio-Quaternary fan deposits in the vicinity of Sivrice (Palutoğlu & Tanyolu, 2006).

3.4.2 Focal Solutions

As a general rule, the Sivrice earthquake is likely to have a left-lateral strike-slip fault mechanism, consistent with the typical features of EAFS. The earthquake's primary shock and any aftershocks with a magnitude higher than 4.0 were studied by AFAD (2020) for their focal mechanism solutions and information on the fault system in which they occurred. Figure 3.7 illustrates a map prepared by AFAD showing the focal mechanisms; from the figure, one can conclude that the left-sided strike-slip fault mechanism is the primary cause of the earthquakes.

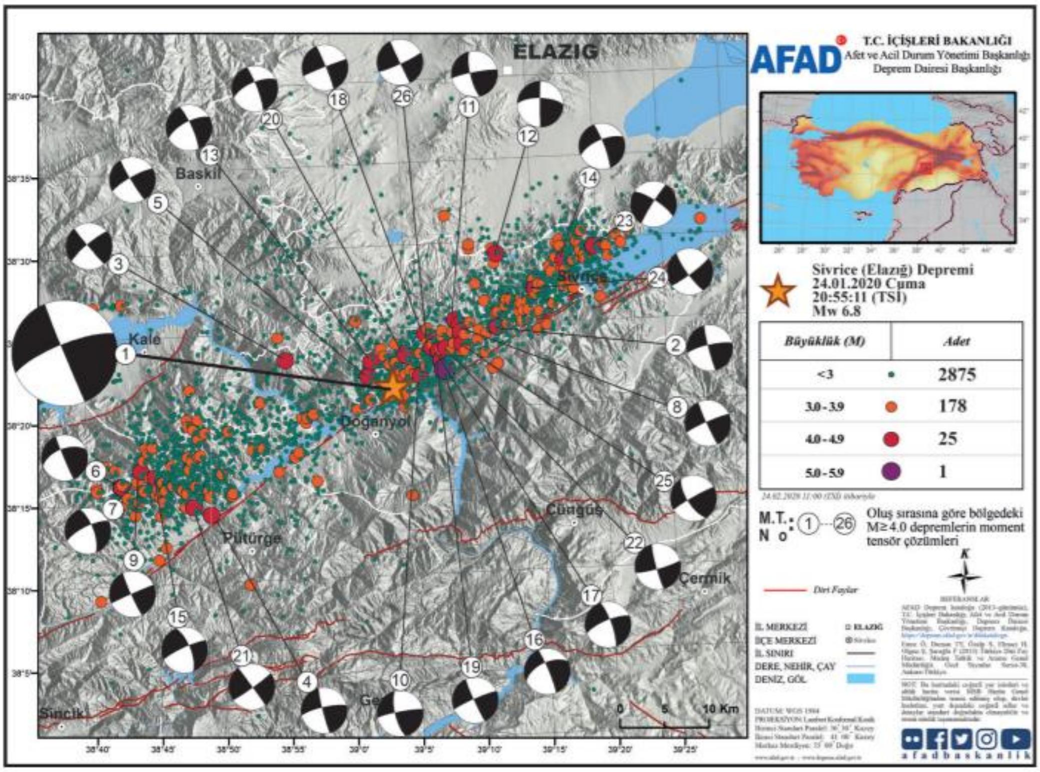

Figure 3.7. The focal solution of EFAS (AFAD, 2020)

CHAPTER 4

SUB-SURFACE INVESTIGATION OF THE STUDY AREA

The geotechnical aspects and features of the subsurface soil are discussed in detail in this chapter. It was required to conduct a literature study in order to obtain the necessary geotechnical data for the study area, Elazig, to begin a geotechnical investigation and generate regionally idealized soil profiles. Just a few researchers presented borehole data and soil lithology at the Elazig Center. Nevertheless, the geological-geotechnical survey report provided by Akare Planlama (2015) was jam-packed with helpful information, and it was the primary source used in this thesis. The aforementioned survey report is based on the Elazig Center municipality zoning plan. Within the report's content, 210 boreholes (with a total depth of 3050 m) were presented. The geographical coordinates of all the boreholes are summarized in table 4.1. Each borehole provides a representative sample with relatively deep profiles and depths ranging between 5.00 and 30.0 m. Aside from the borehole data, the survey reported results from 170 seismic fractures with a 95-meter opening, 100 microtremors, and 173 vertical electric soundings. It should also be mentioned that 50 pressuremeter tests were reported in ten boreholes for 100 pressuremeter tests.

The region covered by this study is approximately 13 365 h, located in Elazig center. This region is shown in Figure 4.1. This chapter will provide an overview of the acquired geotechnical data. At the same time, the following sections analyze these data and generate presentative soil profiles to allow for the subsequent performance of a site-specific seismic site response analysis and liquefaction investigations later on in this research.

Table 4.1 The geographical coordinates of the boreholes

Bh No	Y	X	Bh No	Y	X	Bh No	Y	X
SK-1	513800	4282711	**SK-36**	510527	4279847	**SK-71**	515672	4279484
SK-2	513185	4283595	**SK-37**	509298	4277005	**SK-72**	513440	4278995
SK-3	512665	4284140	**SK-38**	508916	4276172	**SK-73**	517414	4279282
SK-4	513472	4284161	**SK-39**	509246	4275391	**SK-74**	517372	4278337
SK-5	514082	4284124	**SK-40**	508471	4275442	**SK-75**	512533	4278507
SK-6	515304	4283250	**SK-41**	508201	4274955	**SK-76**	513502	4278523
SK-7	515065	4285039	**SK-42**	508539	4276986	**SK-77**	513391	4277775
SK-8	512703	4285065	**SK-43**	511111	4280313	**SK-78**	517288	4277872
SK-9	514331	4284985	**SK-44**	506477	4276242	**SK-79**	516699	4277923
SK-10	514354	4285398	**SK-45**	511051	4278790	**SK-80**	516061	4277833
SK-11	515810	4285013	**SK-46**	510399	4279590	**SK-81**	515824	4278293
SK-12	515215	4284303	**SK-47**	511061	4279538	**SK-82**	516424	4278414
SK-13	513539	4285087	**SK-48**	511266	4277492	**SK-83**	516655	4279310
SK-14	514379	4283775	**SK-49**	510359	4277660	**SK-84**	516130	4279809
SK-15	514385	4282453	**SK-50**	509199	4276425	**SK-85**	514304	4280145
SK-16	512469	4283217	**SK-51**	510098	4276972	**SK-86**	516796	4280337
SK-17	515057	4282351	**SK-52**	507578	4276121	**SK-87**	514766	4280370
SK-18	512977	4282505	**SK-53**	507181	4276789	**SK-88**	517605	4280241
SK-19	515707	4282757	**SK-54**	510206	4276150	**SK-89**	517551	4281047
SK-20	516009	4283194	**SK-55**	511236	4276707	**SK-90**	516937	4280628
SK-21	518192	4282952	**SK-56**	510817	4275920	**SK-91**	516158	4280837
SK-22	518130	4284235	**SK-57**	510265	4275330	**SK-92**	514509	4280732
SK-23	507263	4273869	**SK-58**	511088	4275626	**SK-93**	515087	4280865
SK-24	507756	4273743	**SK-59**	514421	4279623	**SK-94**	513528	4280263
SK-25	507876	4274411	**SK-60**	511602	4276382	**SK-95**	512932	4279916
SK-26	506944	4274423	**SK-61**	511576	4277163	**SK-96**	511938	4279365
SK-27	507123	4275124	**SK-62**	514218	4278481	**SK-97**	511770	4280246
SK-28	507688	4277213	**SK-63**	512635	4279185	**SK-98**	512930	4280769
SK-29	507632	4277427	**SK-64**	514467	4277680	**SK-99**	513245	4280978
SK-30	508824	4277939	**SK-65**	511555	4278019	**SK-100**	513481	4281652
SK-31	508987	4278705	**SK-66**	512367	4277783	**SK-101**	514373	4281599
SK-32	509314	4277819	**SK-67**	515003	4279559	**SK-102**	512175	4280714
SK-33	509466	4278783	**SK-68**	512097	4278612	**SK-103**	516091	4281957
SK-34	510338	4278561	**SK-69**	514917	4278694	**SK-104**	516656	4281563
SK-35	509410	4279100	**SK-70**	514859	4277953	**SK-105**	517458	4281746

Table 4.1 Continued

Bh No	Y	X
SK-106	518561	4281376
SK-107	516045	4285597
SK-108	516426	4285564
SK-109	517213	4284791
SK-110	516599	4285181
SK-111	515079	4285647
SK-112	517441	4284422
SK-113	519146	4282829
SK-114	516414	4283251
SK-115	517397	4283426
SK-116	517556	4284017
SK-117	516753	4282590
SK-118	518747	4283631
SK-119	519988	4283569
SK-120	520173	4283901
SK-121	520367	4283571
SK-122	521584	4284274
SK-123	522289	4284128
SK-124	522809	4284389
SK-125	523084	4283517
SK-126	523629	4282708
SK-127	523882	4283199
SK-128	523301	4282232
SK-129	522437	4283082
SK-130	522187	4282624
SK-131	522195	4281864
SK-132	522122	4281167
SK-133	522881	4281894
SK-134	523757	4281938
SK-135	524814	4282514
SK-136	522281	4279286
SK-137	524353	4281984
SK-138	521461	4279321
SK-139	521468	4279842
SK-140	521410	4280654

Bh No	Y	X
SK-141	520751	4281017
SK-142	520384	4280946
SK-143	519863	4279964
SK-144	520082	4279580
SK-145	519845	4278801
SK-146	520780	4279363
SK-147	521617	4278395
SK-148	522225	4278425
SK-149	520151	4280987
SK-150	519633	4281166
SK-151	519244	4280964
SK-152	518762	4280574
SK-153	518412	4281098
SK-154	517955	4280829
SK-155	518205	4280423
SK-156	518521	4279809
SK-157	519570	4281400
SK-158	522096	4280408
SK-159	520772	4278487
SK-160	518858	4279211
SK-161	519344	4280267
SK-162	518322	4279031
SK-163	518756	4278759
SK-164	518279	4278453
SK-165	518388	4277679
SK-166	518794	4277934
SK-167	521205	4277867
SK-168	520690	4277842
SK-169	519993	4277918
SK-170	520462	4277142
SK-171	520074	4277170
SK-172	522853	4278660
SK-173	522937	4279375
SK-174	522853	4280683
SK-175	522778	4280412

Bh No	Y	X
SK-176	523633	4280664
SK-177	524382	4280870
SK-178	517333	4282180
SK-179	516363	4283785
SK-180	515682	4284354
SK-181	521739	4281385
SK-182	520686	4282568
SK-183	520858	4281800
SK-184	521707	4282532
SK-185	521576	4282971
SK-186	520959	4280393
SK-187	524652	4282974
SK-188	518840	4286243
SK-189	518504	4286250
SK-190	520294	4286209
SK-191	519909	4286186
SK-192	521144	4286383
SK-193	518847	4285431
SK-194	518436	4285008
SK-195	519264	4284833
SK-196	520842	4284015
SK-197	517170	4285378
SK-198	519338	4283921
SK-199	518496	4285778
SK-200	520107	4284993
SK-201	520915	4284989
SK-202	517150	4281371
SK-203	520365	4285380
SK-204	520072	4285392
SK-205	521714	4284851
SK-206	517209	4281196
SK-207	517220	4281008
SK-208	517553	4281229
SK-209	517764	4281188
SK-210	517556	4280757

4.1 Borehole Data

The first stage in conducting a geotechnical subsurface investigation is to undertake a borehole exploration of the area of interest. With the borehole data in hand, one can expose the lithological properties. As previously stated, 210 borehole data sets were used in this research, sourced from the Akare Planlama (2015) survey report and used with permission. Those boreholes can be classified into the following groups based on the formation in which they were drilled:

- Boreholes drilled in places where the Permo-Triassic **Keban Metamorphics (PzMzk)** formation exists. The total number of boreholes within this unit is 31, with depths ranging between 7.5 and 15 m.
- Boreholes drilled in places where the Senonian-dated **Elazig Magmatites (Ke)** formation exists. The total number of boreholes existing within this unit is 63, with depths ranging between 7.5 and 18 meters. It was noted that, in some wells, weathered layers were recorded at a 15-meter depth.
- Boreholes drilled in places where the Lower Eocene-Upper Oligocene dated **Kirkgecit Formation (Tk)** formation exists. The total number of boreholes existing within this unit is 67, with depths ranging between 7.5 and 20 meters. It was noted that, within those boreholes, there existed layers of limestone and claystone.
- Boreholes drilled in places where the Lower Miocene dated **Alibonca Formation (Ta)** formation exists. The total number of boreholes existing within this unit is 64. 11 have a depth ranging between 7.5 and 18 meters within those boreholes. It was reported that the unit decomposes in the first 1-6 m of thickness.
- Two boreholes with a depth of 12.0 m were drilled in places where the **Upper Miocene-Lower Pliocene Karabakir Formation (Tkb)** exists.

- Thirty-six boreholes with depths ranging from 15.0-30.0 m were drilled in places where **Quaternary-aged Alluvium (Qal)** unit was detected.
- One borehole was drilled in the area where the **Artificial Fill (Yd)** unit is seen, and the bedrock continued beneath the filling unit.
- The **Upper Paleocene-Lower Eocene Seske Formation (Ts)** observation locations are protected, and some of them are highly inclined; a borehole could not be drilled. Samples of rock were taken from two places where this unit is seen.

The lithology information for some typical boreholes is included in Table 4.1, while the full list is tabulated in appendix 1. Moreover, all boreholes are visualized on Google Earth and are depicted in Figure 4.1.

Table 4.2 The formation of the boreholes used in the study.

Bh No	Depth	Lithology	
SK-1	0.00-1.00	Fill	Ta
	1.00-7.50	Sandstone - claystone	
SK-2	0.00-7.50	Pebble	Tk
SK-3	0.00-1.00	Organic Soil	Ta
	1.00-6.00	Weathered Sandstone	
	6.00-12.00	Sandstone	
SK-4	000-9.00	Claystone Sandstone	Ta
SK-5	0.00-1.00	Fill	Ta
	1.00-4.00	Weathered Sandstone	
	4.00-12.00	Sandstone	
SK-6	0.00-9.00	Diorite-Gabro	Ke
SK-7	0.00-9.00	Diorite-Gabro	Ke
SK-8	0.00-1.00	Organic Soil	Ta
	1.00-7.50	Sandstone	
SK-9	0.00-1.00	Fill	Ke
	1.00-10.50	Diorite-Gabro	
SK-10	10.00-9.00	Sandstone	Ta
SK-11	0.00-10.50	Diorite-Gabro	Ke
SK-12	0.00-0.50	Fill	Tk
	0.50-7.50	Pebble	
SK-13	0.00-7.50	Diorite-Gabro	Ke
SK-14	0.00-1.00	Fill	Tk
	1.00-3.00	Residual Zone	
	3.00-9.00	Pebble	
SK-15	0.00-3.00	Fill	Ke
	3.00-9.00	Diorite-Gabro	
SK-16	0.00-18.00	Sandstone	Ta
SK-17	0.00-9.00	Diorite-Gabro	Ke
SK-18	0.00-9.00	Diorite-Gabro	Ke
SK-19	0.00-9.00	Diorite-Gabro	zKe
SK-20	0.00-9.00	andesite	Ke
SK-21	0.00-1.00	Fill	Tk
	1.00-15.45	Brown Graveled Sandy Silty Clay	
SK-22	0.00-7.50	Diorite-Gabro	Ke

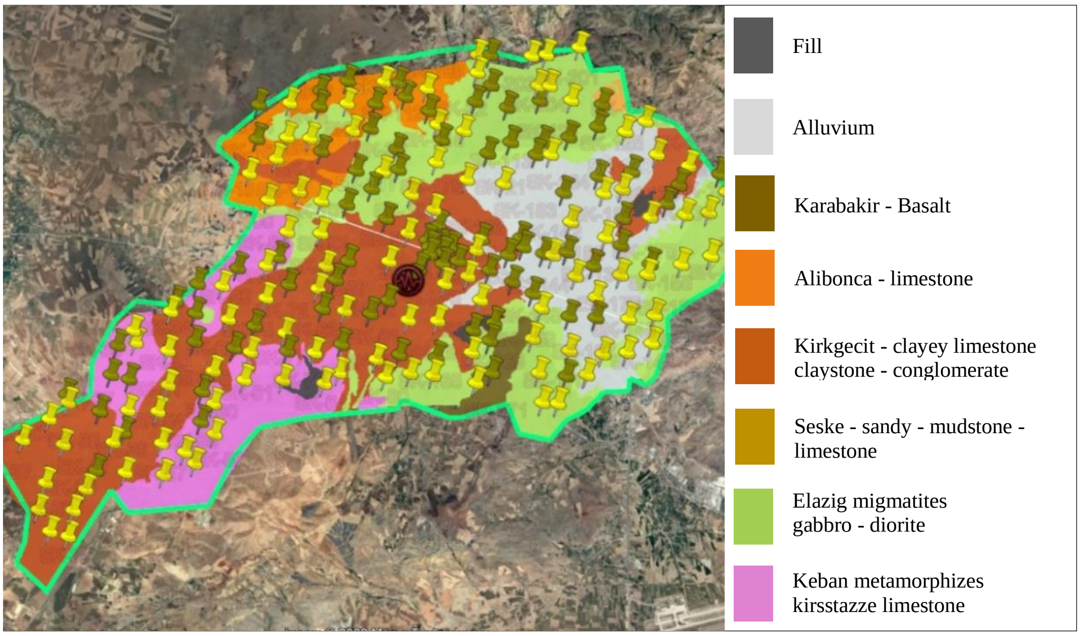

Figure 4.1. The location of the boreholes used for Elazig-Center on the geological map (Plotted in Google Earth)

4.2 In-Situ Test

When it comes to the geotechnical engineering field, the standard penetrations test (SPT) is one of the most significant and the most well-known in-situ tests. Among the in-situ tests performed within the conducted study by Akare Planlama (2015) is the SPT tests. This thesis's data sets were primarily coming from the reported SPT data. Moreover, pressuremeter measurements were also reported; those measurements were obtained at 50 different levels in ten different boreholes.

It is worth mentioning that in addition to the performed geotechnical laboratory tests, geophysical in-situ tests were also performed and presented in the same report. As mentioned previously, vertical electrical drilling investigations, microtremor, and seismic fracture were conducted as part of the project conducted by Akare Palanlama (2015). Within the scope of geophysical studies, seismic refraction in 170 profiles, microtremor at 100 points, and vertical electrical drilling measurements at 173 points were made. Bedrock, underground velocity structure, dynamic-elastic engineering characteristics of soils, soil classes, dominant soil vibration periods, soil amplification, and lateral and vertical discontinuities in the soil were all found using these measurements in the same report. Geophysical data were gathered in locations that most accurately depict the area. The conducted in-situ tests that are used for performing the analysis for the purpose of this thesis are listed below:

- Standard Penetration Test (SPT).
- Pressuremeter Tests (Prt).
- Vertical Electric Drilling (DES).
- Seismic Refraction.
- Microtremor Studies.

4.2.1 Laboratory tests

In-situ testing can be extremely valuable, but they are also deemed insufficient if used on their own; instead, they should be paired with laboratory studies to provide a complete description of the whole data set.

To provide a good source for assessing geotechnical characteristics, several laboratory test results were included in the content of the survey report accomplished by Akare Planlama (2015), including Triaxial Compression Test, Water Content, Sieve Analysis, and Atterberg Limits tests on disturbed (SPT), undisturbed (UD), and core (CR) samples, as well as giving a description of the rock types.

Furthermore, the consolidation test, point loading, and uniaxial compression tests on the rocks were performed, and the findings were included in the survey report by Akare Planlama (2015). It was also stated that the TS-1900 standard was implemented in all experiments and that the samples were classified using the combined soil classification (USCS).

To determine the index and physical properties of the units identified in the research region, 248 Atterberg Limits were done as well as 244 sieve analyses, 248 water content tests, 248 soil class classifications, and 248 Atterberg Limits were performed in the survey report by Akare Planlama (2015).

4.3 Calibration of Geotechnical and Geophysical Parameters Collected

Before starting the generation of the idealized soil profile, one should mention the geotechnical and geophysical soil parameters needed for the analyses that will be conducted later on in this research. Those parameters are;

- The unit weight, γ
- The Plasticity Index, PI
- Fine Contents, FC
- Ground Water Table GWT
- The shear wave velocity, $V_{s,30}, V_{s,12}$

4.3.1 Soil Unit Weight γ

The unit weight is represented by the symbol γ. There were a total of 124 unit weight laboratory tests undertaken, according to the report published by Akare Planlama (2015). However, this did not include all of the boreholes. Therefore, to determine the missing unit weight for the other boreholes, the author assumed that the boreholes with no calculated unit weight value had the same unit weight as their equivalent formations that had been tested and whose unit weight had been reported. To illustrate, borehole No. 36 (SK-36) in the reference report does not have a unit weight assigned to it. However, because borehole No:133 (SK-133) reported a unit weight of 18.2 kN/m^3 and is located in the same formation as SK-36, "Gravelly Sandy Silty Clay," the unit weight of SK-133 is ascribed to SK-36.

4.3.2 Soil Index Properties and Fine Contents

Akare Planlama (2015) provided laboratory test results for 248 Atterberg Limits, 248 sieve analyses, 248 water content experiments, and 248 soil class definitions in order to determine the index and physical properties of the units found in the study region. The fine contents (FC) and the index properties, including the plasticity index (PI), are taken from the report. Similar to the unit weight, a needed property is not reported for any borehole. The missing property is assigned from another equivalent borehole, i.e., a borehole that shares the same formation.

According to Akare Planlama (2015) survey report, sieve analyses were conducted on disturbed and undisturbed soil samples. The grain size distributions of the soils were identified, categorized according to their geological units, and described in Table 4.2. Additionally, they computed the index properties of all units, grouped them according to their geological units, and presented them in Table 4.3.

Table 4.3 Average particle size distribution intervals of the soils in the study area according to the geological units (After Akare Planlama, 2015).

Unit	Average Gravel	Average Sand	Average Clay-silt	Soil Classification
Alluvium (Qal)	8.78 %	22.09 %	69.13 %	CL-MH-SM-ML-GM-CH
Alibonca (Ta)	15.43 %	46.89 %	37.68 %	SM-SC-CL
Kirkgeçit* (Tk) limestone-claystone	10.26 %	20.08 %	69.66 %	SM-CH-CL-ML
Elazığ Mağmatitleri (Ke)	9.69 %	28.96 %	61.35 %	SM-CH-CL-ML
Keban Metamorphics (PzMzk)	37.36 %	19.58 %	43.06 %	GM-CL-ML

Table 4.4 Plasticity Index of soils in the study area according to geological units After Akare Planlama, 2015).

	Plasticity Index (PI) %	
Unit	Min	Max
Alluvium (Qal)	7.80	38.90
Alibonca (Ta)	25.20	32.60
Kirkgeçit* (Tk) limestone-claystone	6.50	40.60
Elazığ Mağmatitleri (Ke)	18.70	41.10
Keban Metamorphics (PzMzk)	17.40	17.50

4.3.3 Ground Water Table Level (GWT)

Only five boreholes were reported to have direct Ground Water Table (GWT) (SK-138, SK-139, SK-140, SK-141, SK-142). This data is tabulated in the following table:

Table 4.5 GWT levels in Elazig-Center

Borehole	GWT (m)	Altitude (m)
SK-138	10.00	1119.0
SK-139	12.00	1013.1
SK-140	14.00	1023.0
SK-141	13.00	1049.2
SK-142	12.00	1065.0

Nevertheless, Google Earth is utilized to estimate the groundwater table level in the remaining boreholes for completeness, as shown in figure 4.2. This is accomplished by comparing the elevation difference between the boreholes with and without reported GWT levels. Table 4.5 contains an example of the first ten boreholes. It should be stated that the groundwater table level found on Google Earth is too deep, and it does not affect the calculations. However, it is still used. A detailed information related to the water table is presented in Chapter 7.

Table 4.6 Determination of the groundwater table level using google earth

Borehole	altitude (m)	Closest borehole	δ_x (m)	δ_{elv} (m)	GWT (m)
SK-1	1192.0	SK-142	6816	127.0	139.0
SK-2	1189.6	SK-142	7671	124.6	136.6
SK-3	1162.3	SK-142	8354	97.3	109.3
SK-4	1259.0	SK-142	7623	194.0	206.0
SK-5	1277.8	SK-142	7058	212.8	224.8
SK-6	1294.5	SK-142	5578	229.5	241.5
SK-7	1365.0	SK-142	6712	300.0	312.0
SK-8	1202.8	SK-142	8716	137.8	149.8
SK-9	1290.3	SK-142	7277	225.3	237.3
SK-10	1329.3	SK-142	7495	264.3	276.3

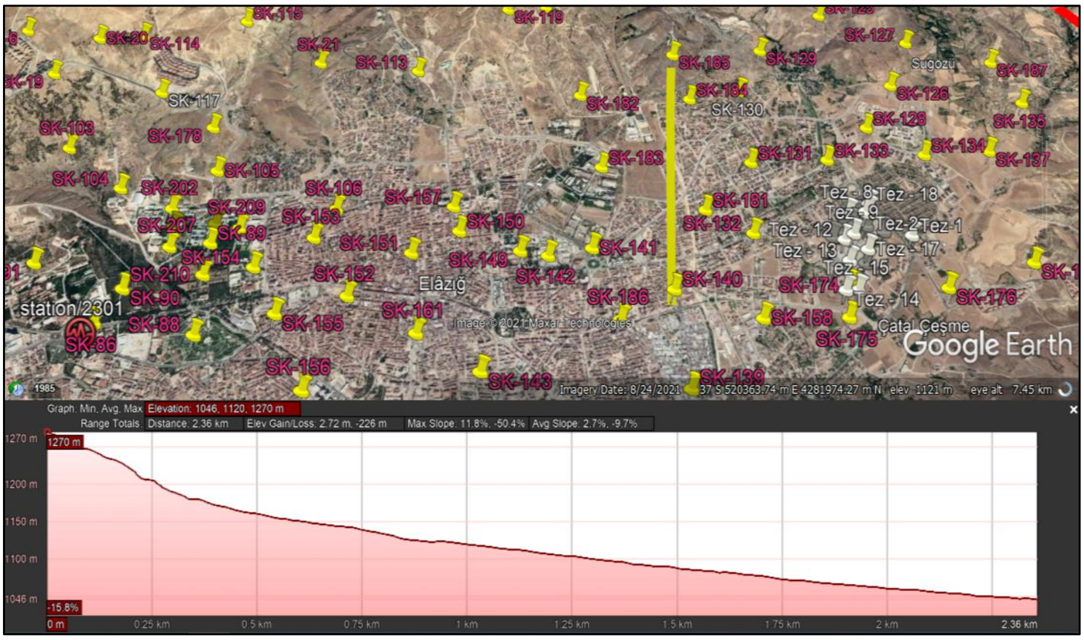

Figure 4.2. The Elevation difference between SK-140 and SK-185

4.3.4 Shear Wave Velocity Vs

In the study area, P and S wave velocity measurements were made in Akare Planlama (2015) report, and 170 profiles were reported in order to determine the underground velocity structure, dynamic-elastic engineering properties of the soil, soil classes based on earthquake regulations, dominant vibration periods, soil amplification, and lateral and vertical discontinuities in the soil.

In accordance with Akare Planlama (2015), the geophone intervals were 4 m, and the laying lengths were 95 m, depending on the field conditions. The geophone intervals were reported to be taken by making two shots against each other The distance between the two points was 3 meters. A signal-accumulating seismograph of the "Geometrics" brand, model "GEOD," with 24 channels, was employed in the seismic refraction studies. Using the results of seismic fracture experiments that were conducted in the study area, it was possible to classify the results according to the formation of the existing soil. The following table summarizes the results of the seismic cracking tests on the first and second layers, including the geological formation of the layers and the shear wave velocities of the first and second layers:

Table 4.7 Summary for the shear wave velocity (V_s and V_p) of Elazig-Center

Formation	$V_{p,layer1}$ m/s	$V_{S,layer1}$ m/s	$V_{p,layer2}$ m/s	$V_{S,layer2}$ m/s
Keban Metamorphics (PzMzk) (Limestone-Shale)	536-1885	422-1126	2427-4021	1573-2627
Elazig Magmatics (Ke) (Gabro-Diorite)	467-1204	306-721	1770-5502	1254-2471
Seske formation (Sandstone-Mudstone-Limestone)	571	419	1985	1327
Kırkgecit formation (Tk) (Clayston-Limestone)	448-882	264-552	1460-3323	935-2100
Kırkgecit formation (Tk) (Pebble Stone)	440-604	316-475	1790-2067	901-151
Alibonca formation (Ta) (Sandstone)	503-1070	367-629	1641-3230	1121-2331
Karabakir formation (Tbk) (Basalt)	500-686	374-394	1820-2650	1348-1646
Alluvium (Qal) (Silty Sandy Pebble Clay)	417-1015	296-635	1499-536	734-1475
Fill (Qd)	472-728	503-563	1540-1645	716-718

The X and Y coordinates of the measured shear wave velocity locations are taken from the Akare Planlama report (2015) and plotted on Google Earth alongside the plotted borehole data, as shown in Figure 4.3.

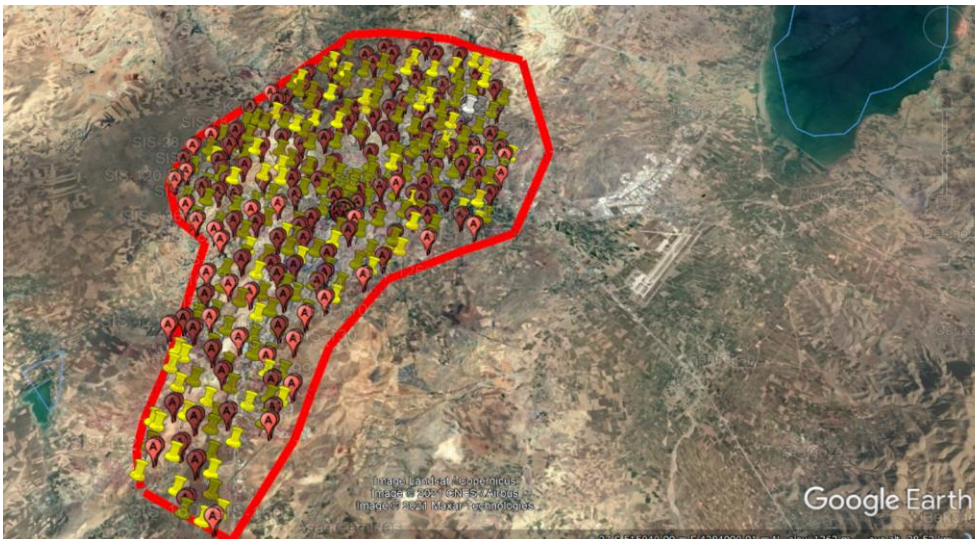

Figure 4.3. The recorded seismic refraction velocities plotted on Google Earth

The $V_{s,30}$ values obtained as a result of the seismic studies carried out in the study area can also be summarized according to their geological formations in the following table;

Table 4.8 The range values of $V_{s,30}$ according to their geological formation

Geological formation	$V_{s,30}$ **range**
In the fill (Qd)	660 - 681
Alluvium (Qal)	605 - 734
Karabakır formation (Tbk/Basalt)	874 - 884
Alibonca formation (Ta)	888 - 929
Kırkgecit formation (Tk/Gravel)	742 - 748
Kırkgecit formation (Tk/Clay Limestone-Claystone)	754 - 872
Seske formation (Ts)	926
Elazig Magmatics (Ke)	869 - 1129
Keban Metamorphites (PzMzk)	1019 - 1938

Table 4.8 provides only a range of shear wave velocity values for each geological formation. However, data for each of the reported seismic refraction velocities (SIS) is also included. The following table summarizes some of these data.

Table 4.9 Summary of $V_{s,30}$, V_p and V_s values for the the first 15 seismic fractions

SIS No	$V_{s,30}$ (m/s)	Layer No	V_p (m/s)	V_s (m/s)	h (m)	Formation
SIS 1	605	1	608	318	10	Qal
		2	3536	1105	-	
SIS 2	681	1	728	563	6	Qal
		2	1540	718	-	
SIS 3	888	1	627	468	6	Ta
		2	1641	1145	-	
SIS 4	660	1	742	503	6	Qal
		2	1645	716	-	
SIS 5	840	1	634	506	6	Tk
		2	1800	1006	-	
SIS 6	684	1	713	507	7	Qal
		2	1681	766	-	
SIS 7	1009	1	795	370	6	Ke
		2	2569	1777	-	
SIS 8	708	1	769	580	6	Qal
		2	1734	750	-	
SIS 9	676	1	657	488	7	Qal
		2	1499	765	-	
SIS 10	865	1	683	509	6	Tk
		2	1680	1048	-	
SIS 11	713	1	955	635	7	Qal
		2	2623	741	-	
SIS 12	1232	1	780	570	7	Pzmzk
		2	2626	1904	-	
SIS 13	867	1	547	423	5	Tk
		2	1722	1098	-	
SIS 14	1087	1	902	672	7	Ke
		2	2555	1339	-	
SIS 15	1707	1	1885	817	6	Pzmzk
		2	3217	2347	-	

The observed seismic refraction velocities do not coincide exactly with the boreholes used for the analyses in the subsequent chapters' studies. To account for that, the distance between each borehole and the nearest shear wave velocity measurement was computed, and the borehole was allocated the values of the closest velocities' values. There is a short distance between the seismic refraction velocities and the boreholes. The majority of the distance is between 100 and 400 meters, although there are few outliers. Figure 4.4 illustrates how shear wave velocity data is assigned to boreholes. The data for the shear wave velocity are tabulated and included in table 4.9 (where sis stands for the seismic crack measurement and dist for the distance range between the borehole and the shear wave velocity measurement). In addition, the obtained velocities from the seismic refraction tests from the first layer (Average 6m - 8m), second layer, and for the average 30 meter are presented in Figures 4.5, 4.6, and 4.7 respectively.

Figure 4.4. Measuring the distance between the borhole SK-1 and the closest seismic refraction shear wave velocity (Google Earth)

Table 4.10 The assigned Vs values of each of the boreholes

SK NO	sis	dist (m)	Vs_{rock}	VS_7	VS_{30}
SK-1	SIS-164	300 - 400	1424	398	889
SK-2	SIS-170	300 - 400	1560	407	889
SK-3	SIS-70	400 -500	1136	316	748
SK-4	SIS-170	200 -300	1560	407	889
SK-5	SIS-25	200 -300	1379	545	913
SK-6	SIS-102	400 -500	2405	364	1001
SK-7	SIS-17	100 - 200	1314	721	1090
SK-8	SIS-120	200 -300	1327	469	911
SK-9	SIS-7	400 -500	1777	370	1009
SK-10	SIS-28	300 - 400	1121	626	916
SK-11	SIS-124	200 -300	1549	401	929
SK-12	SIS-154	500 - 600	1151	327	745
SK-13	SIS-168	200 -300	1339	672	923
SK-14	SIS-82	100 - 200	983	374	742
SK-15	SIS-106	400 -500	1778	414	1005
SK-16	SIS-136	300 - 400	2331	431	917
SK-17	SIS-102	500 - 600	2405	364	1001
SK-18	SIS-22	300 - 400	2627	1126	1938
SK-19	SIS-5	400 -500	2405	364	840
SK-20	SIS-101	500 - 600	2471	330	983
SK-21	SIS-89	200 -300	1163	408	676
SK-22	SIS-93	200 -300	1572	363	944
SK-23	SIS-160	400 -500	1382	369	852
SK-24	SIS-160	200 -300	1382	369	852
SK-25	SIS-155	500 - 600	1219	413	802
SK-26	SIS-155	200 -300	1219	413	802
SK-27	SIS-155	600 - 700	1219	413	802
SK-28	SIS-140	700 - 800	1487	373	828
SK-29	SIS-140	800 -900	1487	373	828
SK-30	SIS-140	700 - 800	1487	373	828
SK-31	SIS-12	1350	1904	570	1232
SK-32	SIS-139	900 -1000	1487	373	843
SK-33	SIS-117	900 -1000	11603	311	760
SK-34	SIS-122	300 - 400	952	412	754

SK NO	sis	dist (m)	Vs_{rock}	VS_7	VS_{30}
SK-35	SIS-12	800 -900	11603	311	1232
SK-36	SIS-118	200 -300	1128	428	785
SK-37	SIS-145	600 - 700	1281	414	861
SK-38	SIS-145	300 - 400	1281	414	861
SK-39	SIS-146	700 - 800	1473	360	764
SK-40	SIS-152	300 - 400	1928	379	866
SK-41	SIS-152	300 - 400	1928	379	866
SK-42	SIS-140	200 -300	1487	373	828
SK-43	SIS-15	200 -300	2347	817	1707
SK-44	SIS-142	800 -900	1192	374	829
SK-45	SIS-114	400 -500	1264	413	854
SK-46	SIS-118	200 -300	1991	610	785
SK-47	SIS-114	200 -300	1264	413	854
SK-48	SIS-138	500 - 600	1279	423	869
SK-49	SIS-139	300 - 400	1488	348	843
SK-50	SIS-146	400 -500	1281	414	764
SK-51	SIS-139	300 - 400	1488	348	843
SK-52	SIS-151	300 - 400	1537	304	790
SK-53	SIS-142	300 - 400	1192	374	829
SK-54	SIS-146	500 - 600	1473	360	764
SK-55	SIS-34	400 -500	1588	643	1141
SK-56	SIS-165	400 -500	1945	554	1165
SK-57	SIS-133	300 - 400	1860	454	1019
SK-58	SIS-159	300 - 400	1713	615	1160
SK-59	SIS-103	400 -500	2100	264	801
SK-60	SIS-165	300 - 400	1945	554	1165
SK-61	SIS-34	100 - 200	1588	643	1141
SK-62	SIS-4	200 -300	716	503	660
SK-63	SIS-113	100 - 200	1232	483	872
SK-64	SIS-94	100 - 200	2053	628	1279
SK-65	SIS-138	200 -300	1279	423	869
SK-66	SIS-92	100 - 200	2399	514	1489
SK-67	SIS-84	400 -500	923	441	757
SK-68	SIS-113	600 - 700	1232	483	872

Table 4.9. Continued

SK NO	sis	dist (m)	Vs_{rock}	VS_7	VS_{30}
SK-69	SIS-90	200 -300	1896	527	1180
SK-70	SIS-90	400 -500	1896	527	1180
SK-71	SIS-109	700 - 800	1815	376	868
SK-72	SIS-111	300 - 400	1162	396	838
SK-73	SIS-100	200 -300	1456	366	812
SK-74	SIS-129	100 - 200	1265	411	894
SK-75	SIS-74	600 - 700	1829	647	1205
SK-76	SIS-74	200 -300	801	470	1205
SK-77	SIS-110	200 -300	2338	422	1225
SK-78	SIS-129	400 -500	1265	411	894
SK-79	SIS-153	100 - 200	2217	407	1129
SK-80	SIS-126	300 - 400	2109	450	1214
SK-81	SIS-126	700 - 800	2109	450	1214
SK-82	SIS-153	600 - 700	2217	407	1129
SK-83	SIS-105	100 - 200	1815	376	871
SK-84	SIS-105	500 - 600	1815	376	871
SK-85	SIS-69	300 - 400	1166	361	767
SK-86	SIS-50	400 -500	1215	412	767
SK-87	SIS-68	300 - 400	1121	428	814
SK-88	SIS-48	200 -300	1112	411	823
SK-89	SIS-48	500 - 600	1358	429	823
SK-90	SIS-50	200 -300	1215	412	767
SK-91	SIS-66	400 -500	1125	454	807
SK-92	SIS-69	200 -300	1166	361	767
SK-93	SIS-68	300 - 400	1121	428	814
SK-94	SIS-73	400 -500	1135	402	796
SK-95	SIS-75	500 - 600	1157	450	847
SK-96	SIS-113	400 -500	1232	483	872
SK-97	SIS-167	300 - 400	1246	377	831
SK-98	SIS-75	300 - 400	1157	450	847
SK-99	SIS-75	600 - 700	1157	450	847
SK-100	SIS-67	400 -500	1573	691	1174
SK-101	SIS-108	200 -300	1639	425	983
SK-102	SIS-16	400 -500	1787	977	1609
SK-103	SIS-5	300 - 400	1006	506	840

SK NO	sis	dist (m)	Vs_{rock}	VS_7	VS_{30}
SK-104	SIS-21	200 -300	1278	388	812
SK-105	SIS-20	100 - 200	1815	376	819
SK-106	SIS-163	400 -500	1283	400	808
SK-107	SIS-144	400 -500	1402	457	888
SK-108	SIS-144	100 - 200	1475	385	888
SK-109	SIS-128	200 -300	1491	412	925
SK-110	SIS-137	200 -300	1346	434	903
SK-111	SIS-78	200 -300	1330	430	894
SK-112	SIS-128	400 -500	1491	412	925
SK-113	SIS-44	300 - 400	1232	483	699
SK-114	SIS-101	300 - 400	2471	330	983
SK-115	SIS-97	100 - 200	1282	465	992
SK-116	SIS-162	100 - 200	1717	577	1078
SK-117	SIS-10	200 -300	1048	509	865
SK-118	SIS-29	300 - 400	1254	595	941
SK-119	SIS-11	100 - 200	741	635	713
SK-120	SIS-11	400 -500	741	635	713
SK-121	SIS-9	200 -300	765	488	676
SK-122	SIS-8	500 - 600	2070	489	708
SK-123	SIS-6	300 - 400	766	507	684
SK-124	SIS-1	100 - 200	1105	318	605
SK-125	SIS-88	300 - 400	961	364	695
SK-126	SIS-35	100 - 200	955	399	721
SK-127	SIS-35	400 -500	955	399	721
SK-128	SIS-39	200 -300	814	333	609
SK-129	SIS-87	100 - 200	757	380	623
SK-130	SIS-83	100 - 200	1014	370	721
SK-131	SIS-58	200 -300	972	442	760
SK-132	SIS-52	200 -300	1099	296	621
SK-133	SIS-39	200 -300	814	333	609
SK-134	SIS-157	400 -500	1610	464	995
SK-135	SIS-119	400 -500	1993	306	991
SK-136	SIS-61	100 - 200	947	345	702
SK-137	SIS-119	300 - 400	1993	306	991
SK-138	SIS-62	100 - 200	954	364	666

Table 4.9. Continued

SK NO	sis	dist (m)	Vs_{rock}	VS_7	VS_{30}
SK-139	SIS-57	200 -300	1026	457	725
SK-140	SIS-72	200 -300	1061	309	677
SK-141	SIS-46	200 -300	772	562	679
SK-142	SIS-56	300 - 400	826	417	663
SK-143	SIS-148	500 - 600	1348	394	1057
SK-144	SIS-148	300 - 400	1780	428	1057
SK-145	SIS-143	300 - 400	1262	473	946
SK-146	SIS-62	400 -500	1780	428	666
SK-147	SIS-63	200 -300	923	377	703
SK-148	SIS-65	300 - 400	813	408	643
SK-149	SIS-56	200 -300	826	417	663
SK-150	SIS-45	500 - 600	924	398	683
SK-151	SIS-43	500 - 600	935	522	821
SK-152	SIS-47	300 - 400	1338	392	856
SK-153	SIS-47	300 - 400	1338	392	856
SK-154	SIS-47	500 - 600	1338	392	856
SK-155	SIS-79	200 -300	881	330	660
SK-156	SIS-98	300 - 400	1280	429	837
SK-157	SIS-45	400 -500	924	398	683
SK-158	SIS-76	100 - 200	801	470	668
SK-159	SIS-63	500 - 600	923	377	703
SK-160	SIS-149	200 -300	2292	395	1081
SK-161	SIS-43	100 - 200	935	522	821
SK-162	SIS-150	500 - 600	2028	428	1120
SK-163	SIS-150	200 -300	2028	428	1120
SK-164	SIS-150	100 - 200	2028	428	1120
SK-165	SIS-141	200 -300	1646	382	874
SK-166	SIS-134	300 - 400	1545	386	883
SK-167	SIS-166	200 -300	1463	398	926
SK-168	SIS-166	500 - 600	1463	398	926
SK-169	SIS-158	400 -500	1672	423	1020
SK-170	SIS-135	500 - 600	1651	433	943
SK-171	SIS-135	200 -300	1651	433	943
SK-172	SIS-147	0 -100	1475	305	729
SK-173	SIS-132	200 -300	2068	447	1051
SK-174	SIS-127	300 - 400	1822	455	1071

SK NO	sis	dist (m)	Vs_{rock}	VS_7	VS_{30}
SK-175	SIS-76	400 -500	801	470	668
SK-176	SIS-131	200 -300	1812	436	1044
SK-177	SIS-125	400 -500	2142	389	1007
SK-178	SIS-13	300 - 400	1098	423	867
SK-179	SIS-27	400 -500	1273	464	1122
SK-180	SIS-169	300 - 400	1273	464	869
SK-181	SIS-49	200 -300	883	391	631
SK-182	SIS-77	100 - 200	1234	319	699
SK-183	SIS-46	400 -500	772	562	679
SK-184	SIS-83	300 - 400	916	417	721
SK-185	SIS-33	200 -300	916	417	684
SK-186	SIS-72	200 -300	969	353	677
SK-187	SIS-37	300 - 400	788	411	666
SK-188	SIS-26	400 -500	2109	450	962
SK-189	SIS-156	500 - 600	1443	483	1033
SK-190	SIS-30	200 -300	1389	458	988
SK-191	SIS-30	400 -500	1642	434	988
SK-192	SIS-30	700 - 800	1389	458	988
SK-193	SIS-156	200 -300	1443	483	1033
SK-194	SIS-80	300 - 400	1498	444	964
SK-195	SIS-80	300 - 400	1498	444	964
SK-196	SIS-9	300 - 400	765	488	676
SK-197	SIS-116	400 -500	1768	367	905
SK-198	SIS-29	200 -300	1254	595	941
SK-199	SIS-156	300 - 400	826	417	1033
SK-200	SIS-85	200 -300	1357	455	972
SK-201	SIS-86	500 - 600	2070	489	1112
SK-202	SIS-20	300 - 400	996	517	819
SK-203	SIS-59	300 - 400	1642	434	942
SK-204	SIS-59	200 -300	1642	434	942
SK-205	SIS-86	100 - 200	2070	489	1112
SK-206	SIS-20	400 -500	996	517	819
SK-207	SIS-50	300 - 400	1215	412	767
SK-208	SIS-20	500 - 600	996	517	819
SK-209	SIS-48	500 - 600	996	517	823
SK-210	SIS-48	200 -300	1358	429	823

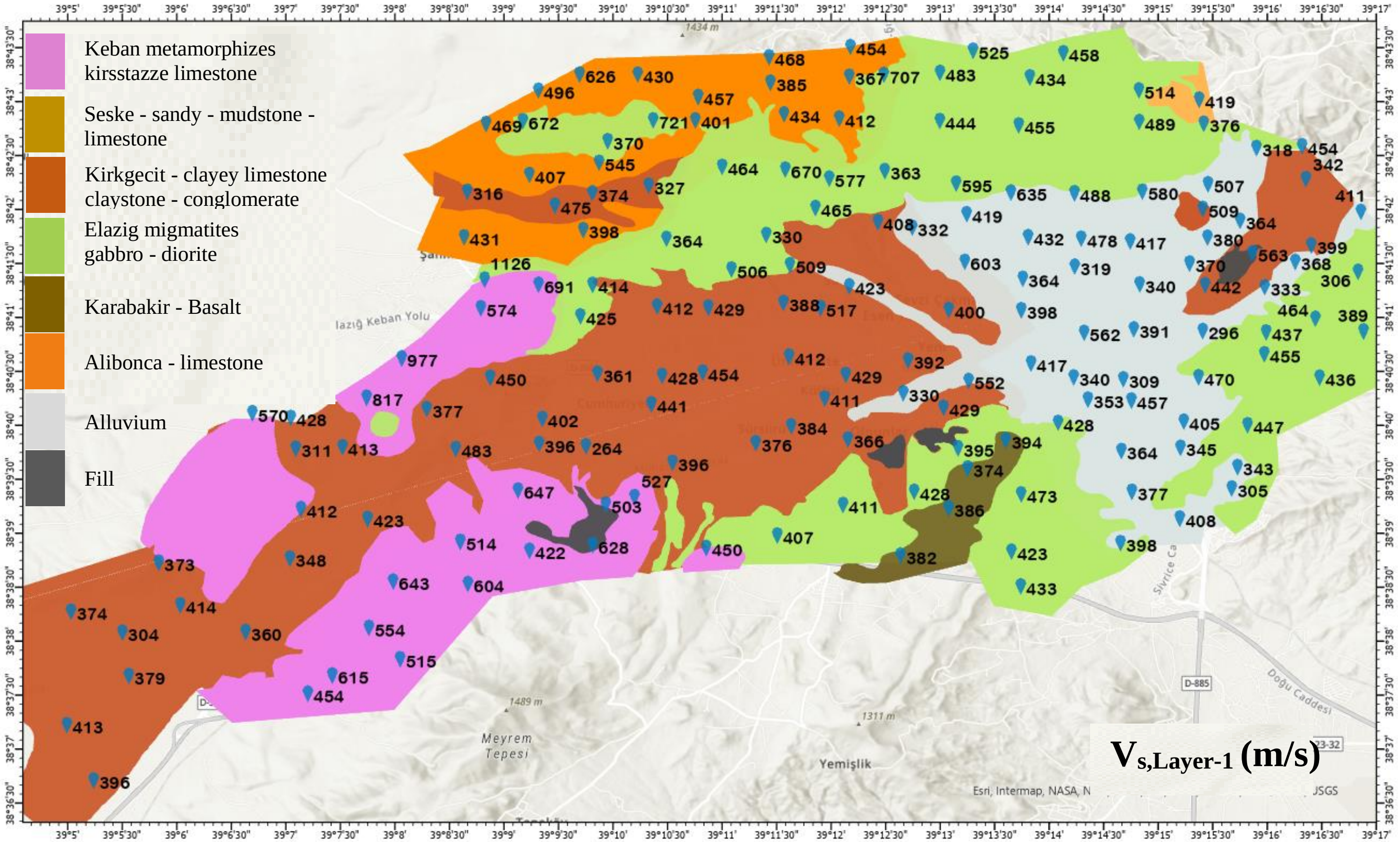

Figure 4.5. Vs measured for the first layer using seismic refraction tests and plotted on the geological map of Elazig-center

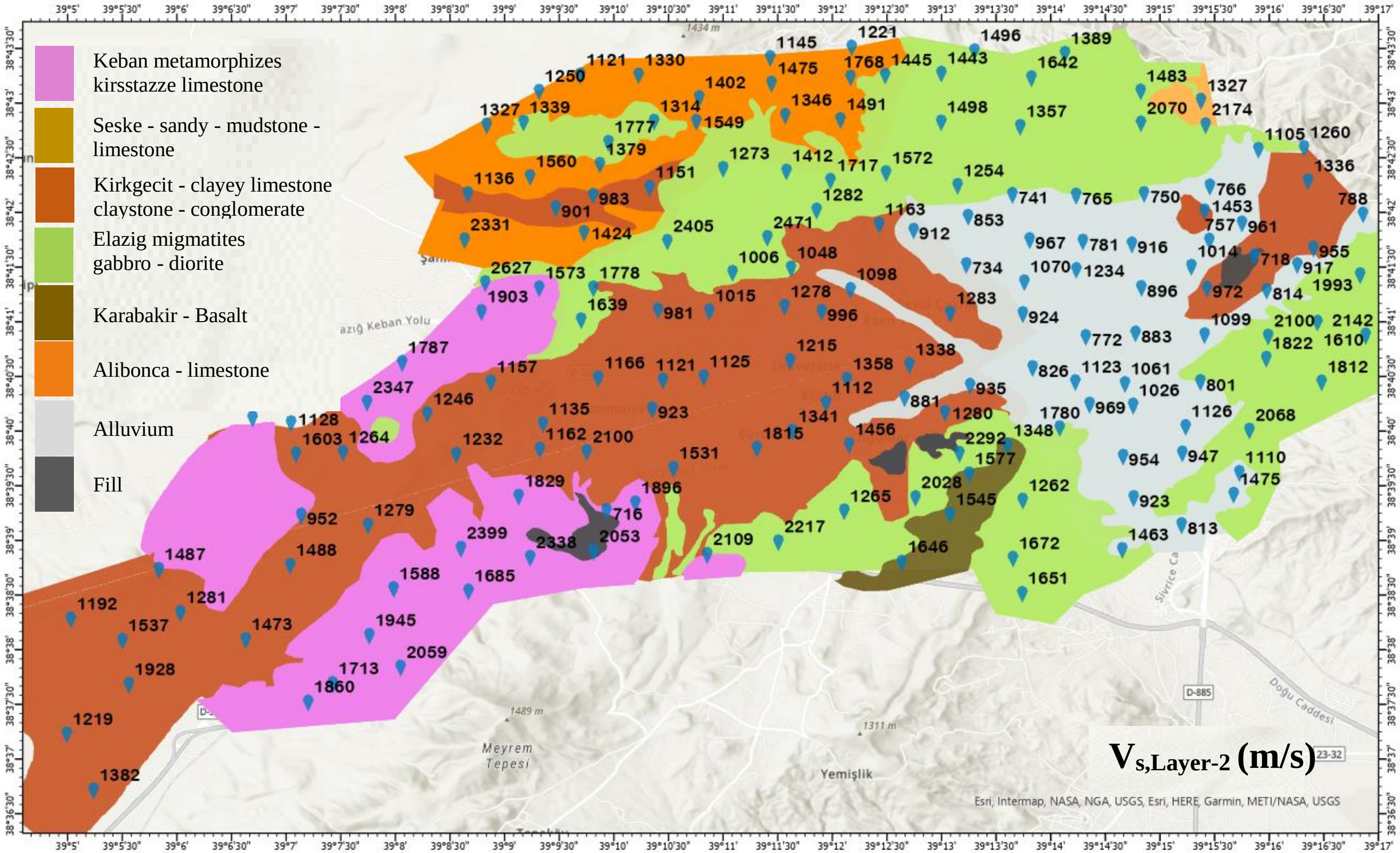

Figure 4.6. Vs measured for the second layer using seismic refraction tests and plotted on the geological map of Elazig-center

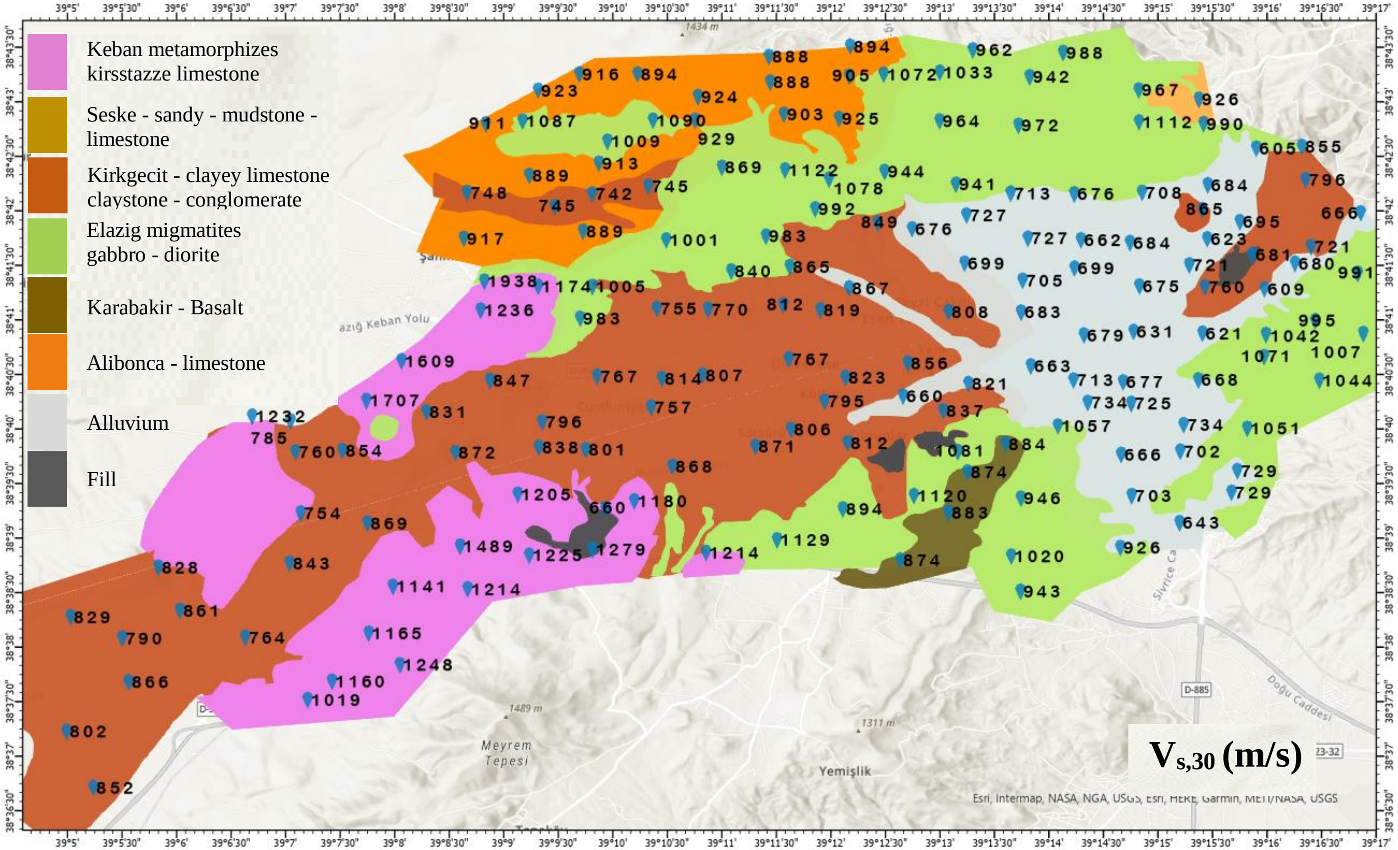

Figure 4.7. Vs_{30} plotted on the geological map of Elazig-center

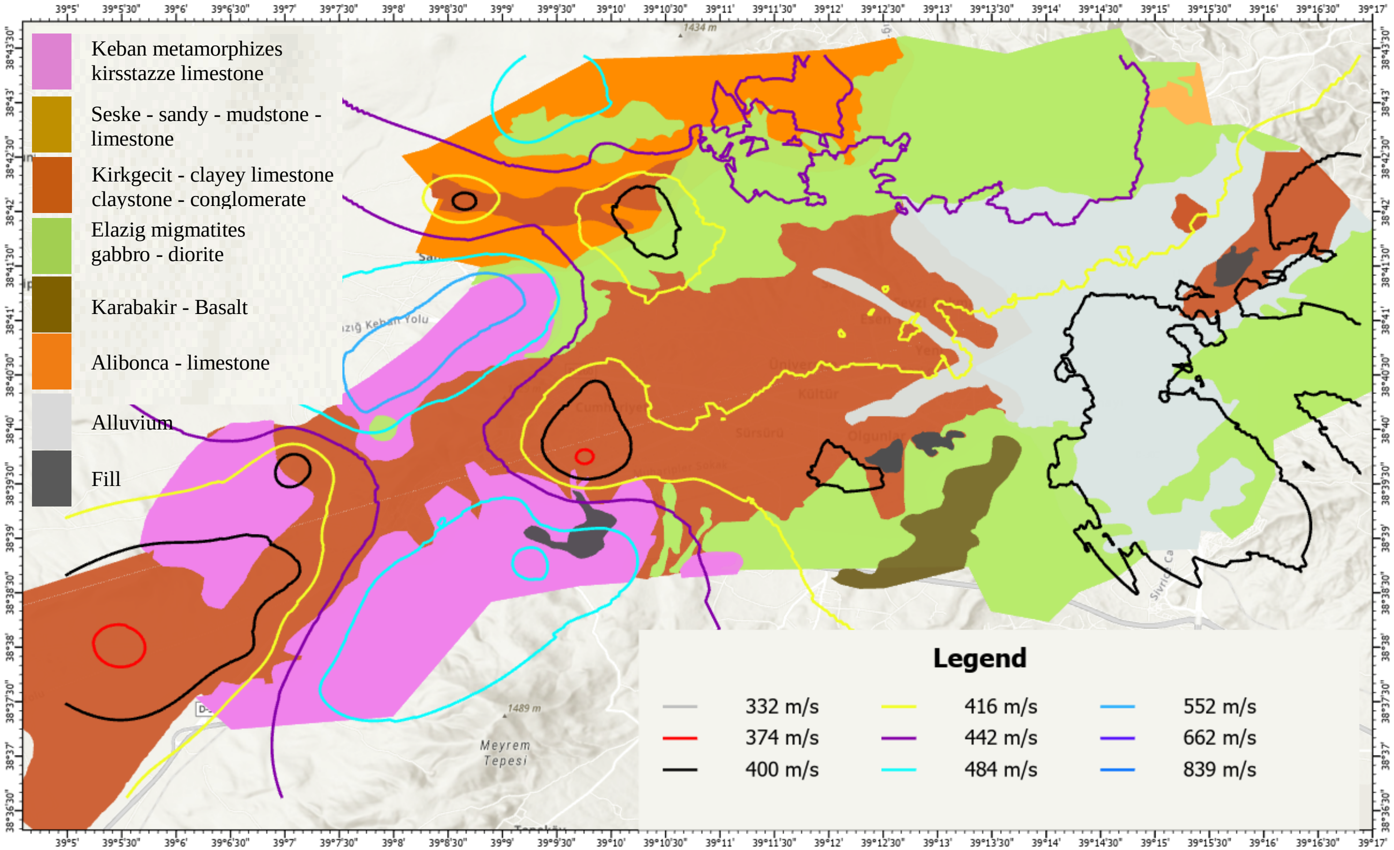

Figure 4.8. Contours for Vs measured for the first layer using seismic refraction tests and plotted on the geological map of Elazig-center

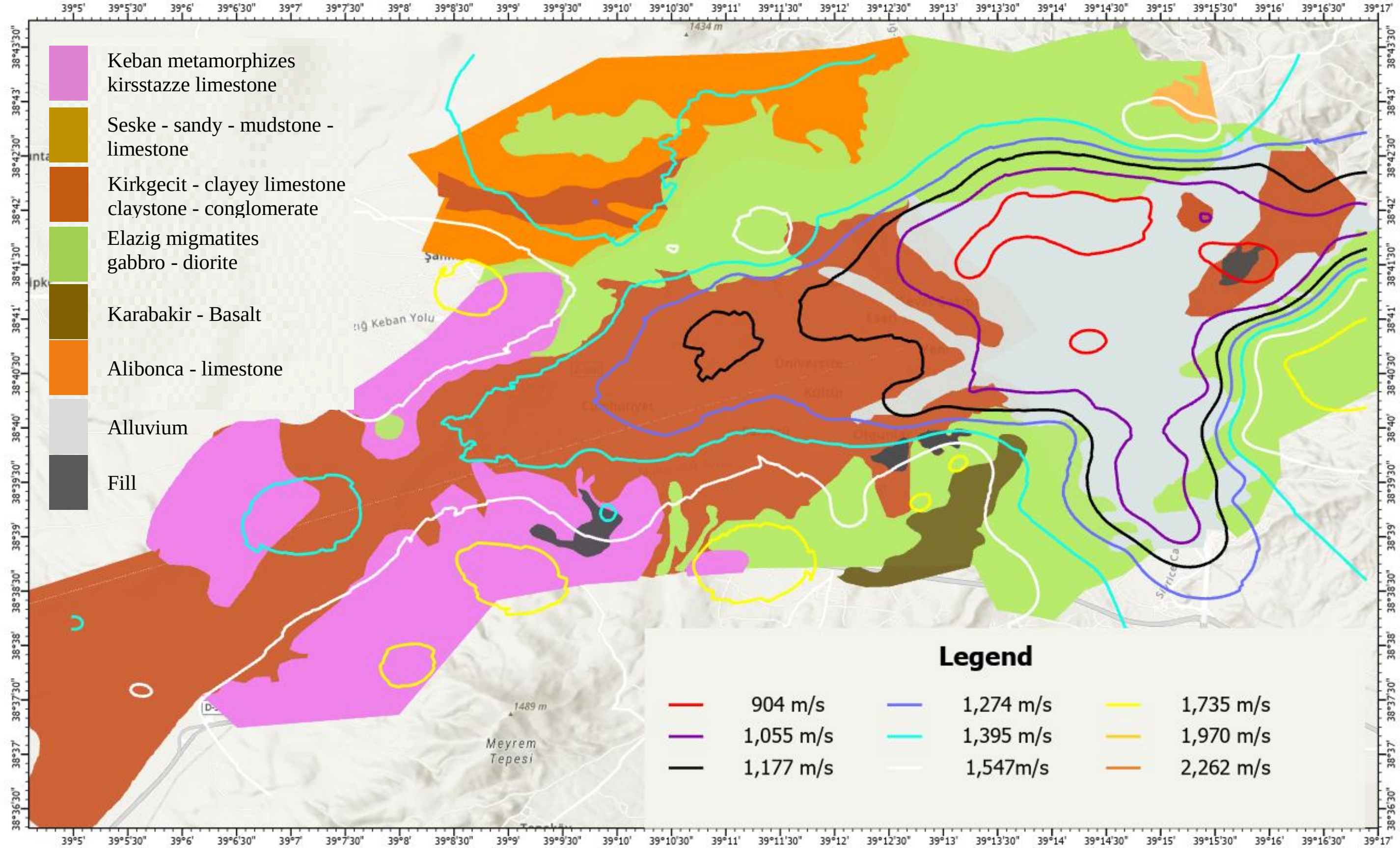

Figure 4.9. Contours for Vs measured for the 2nd layer using seismic refraction tests and plotted on the geological map of Elazig-center

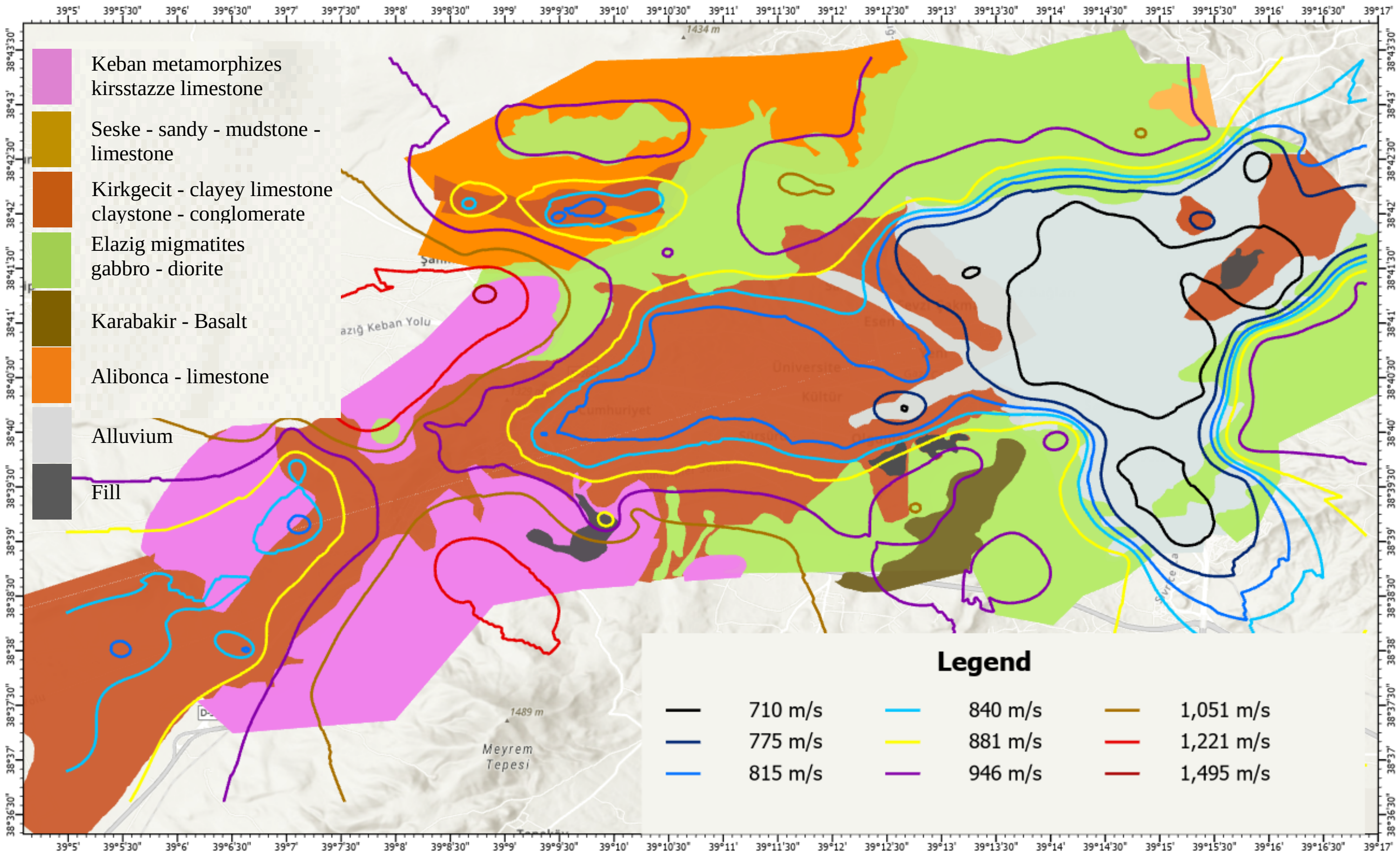

S

Figure 4.10. Contours for Vs_{30} plotted on the geological map of Elazig-center

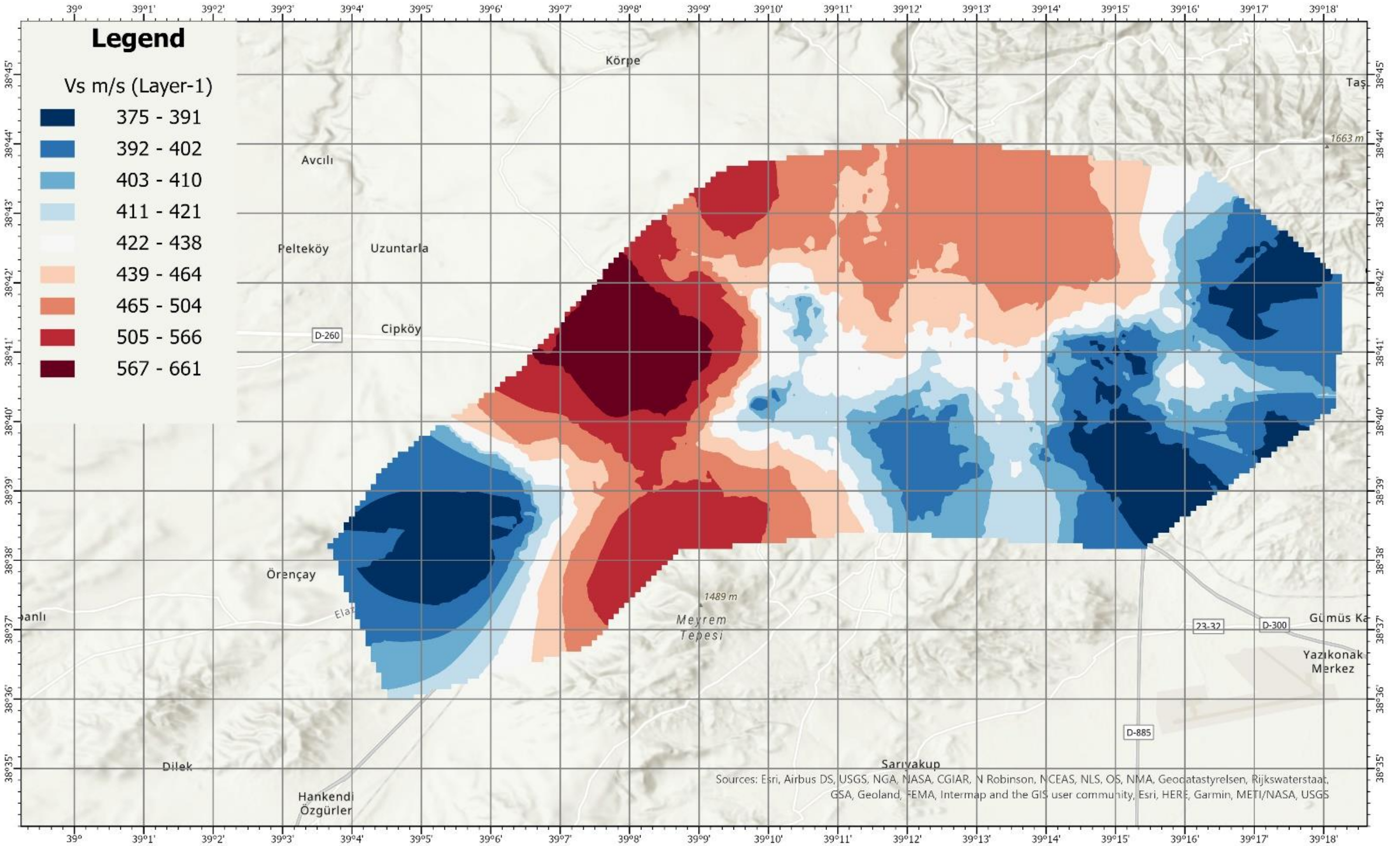

Figure 4.11. Shear wave velocity zonation for the 1st layer measured using seismic refraction tests on Elazig - center

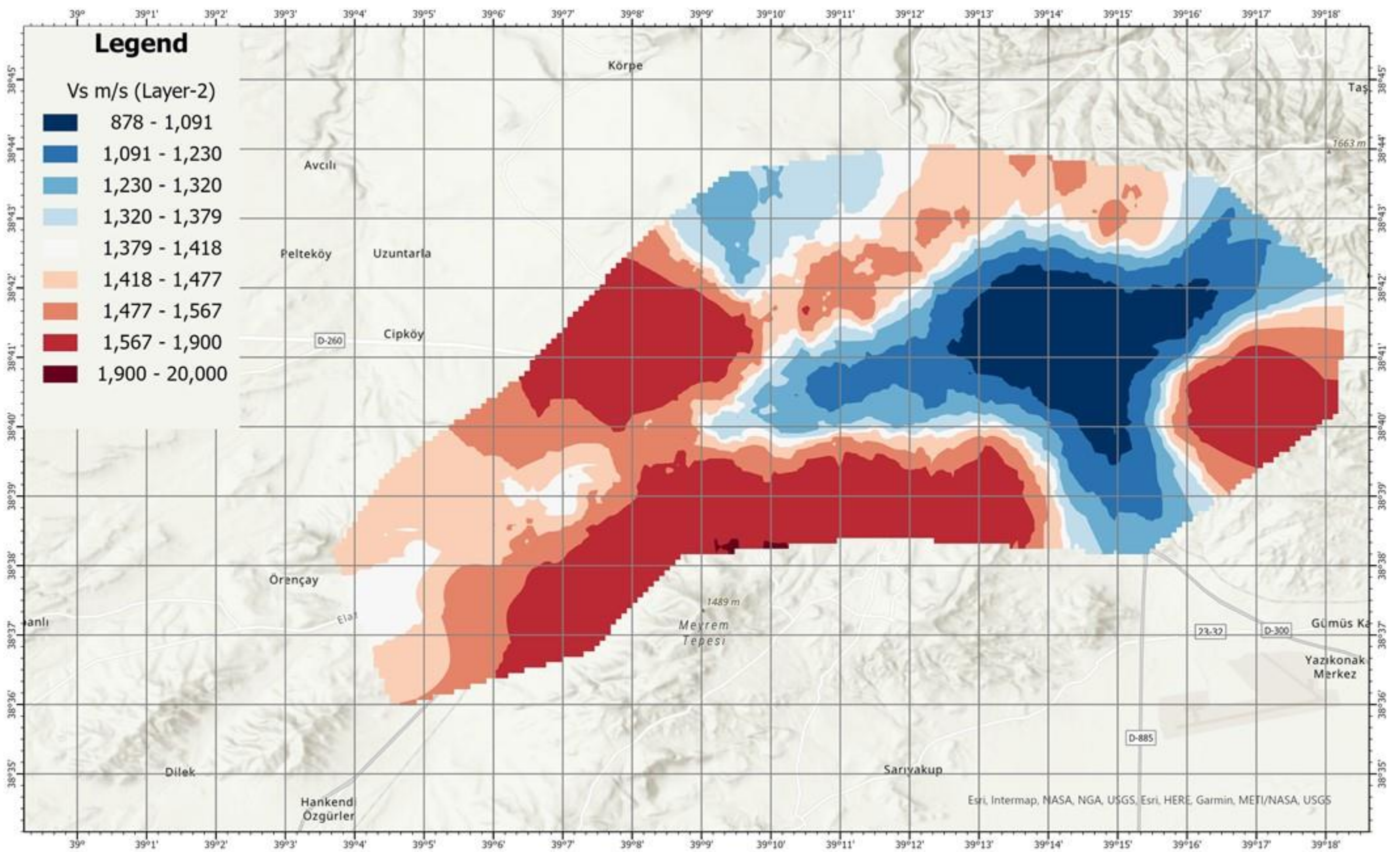

Figure 4.12. Shear wave velocity zonation for the 2nd layer measured using seismic refraction tests on Elazig - center

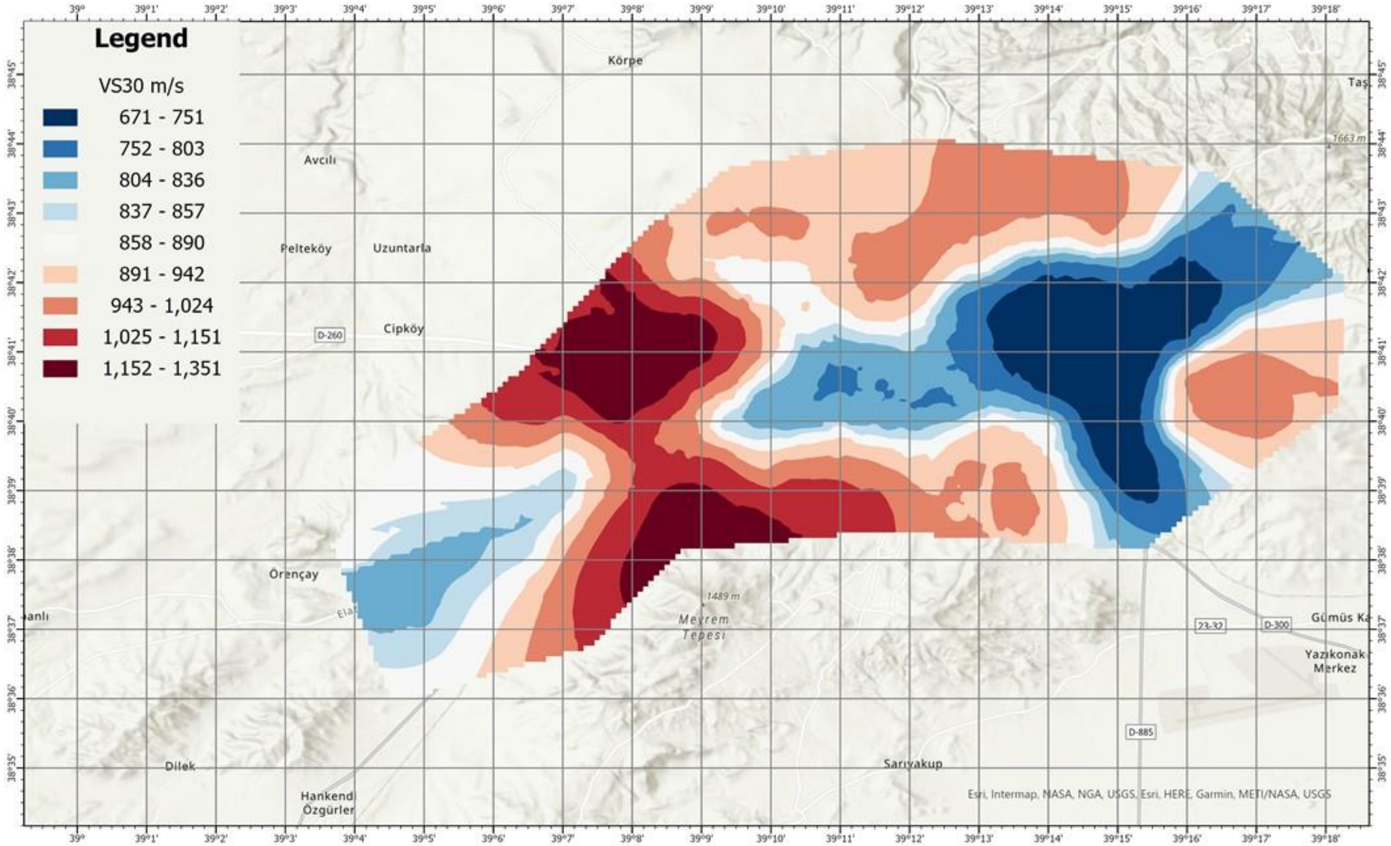

Figure 4.13. Vs_{30} zonation on Elazig - center

4.4 Rock Units

According to field investigations and observations obtained in the study region, rock units are formed by seven distinct formations. Volcanic and sedimentary rocks dominate the research region:

- Limestones belonging to the Keban Metamorphics (PzMzk)
- Gabbro-diorites belonging to Elazig Migmatites (Ke)
- Clay limestones of Seske Formation (Ts)
- Conglomerate-sandstone levels of Kirkgecit Formation (Tk)
- Limestone-claystone levels to Kirkgecit Formation (Tk)
- Sandstones of the Alibonca Formation (Ta)
- Basalt levels of the Karabakir Formation (Tkb)

Akare Planlama report (2015) reported that rock samples were sent to the laboratory, and point loading and unconfined pressure tests were performed on the samples. 74 point loading (Is) tests and 75 unconfined pressure tests were performed on the core (CR) samples taken. According to these values;

- In the limestones of the Keban Metamorphics (PzMzk), the free pressure value was found to be 385.15 - 523.20 kgf/cm^2, and the point loading index (Is) value was found to be in the range of 17.20 - 23.40 kgf/cm^2 (low-medium strength rock units).
- The free pressure value of the gabbro-diorites belonging to the Elazig Migmatites (Ke) was found in the range of 232.0 - 530.0 kgf/cm^2, and the point loading index (Is) value was found in the range of 10.87 - 21.50 kgf/cm^2 (very low-low-medium strength rock units).

- The point loading index (Is) value in the clayey limestones of the Seske Formation (Ts) was found in the range of 21.35 - 23.50 kgf/cm^2 (medium strength rock units).
- Point loading index (Is) value of 13.40 - 18.40 kgf/cm^2 was found in the conglomerate-sandstone belonging to Kirkgecit Formation (Tk) (low strength rock units).
- In the limestone-claystone levels of the Kirkgecit Formation (Tk), the free pressure value was found to be 148.95 - 287.50 kgf/cm^2, and the point loading index (Is) value was found to be between 7.85 - 16.12 kgf/cm^2 (very low-low strength rock units).
- In the sandstones of the Alibonca Formation (Ta), the free pressure value was found in the range of 165.50-184.50 kgf/cm^2, and the point loading index (Is) value was found in the range of 6.45-12.55 kgf/cm^2 (low-low strength rock units).
- The free pressure value in the basalts of the Karabakir Formation (Tkb) was found to be between 561.40-568.70 kgf/cm^2 and was defined as medium-strength rock units.

RQD values for the limestones of Keban Metamorphics (PzMzk), gabbro diorites of Elazig Magmatites (Ke), and basalt levels of Karabakr Formation (Tkb) vary between 5% and 40%, indicating that they are "very poor quality" or "poor quality" rocks, respectively. Because of the Alibonca Formation's (Ta) sandstones, the Krkgeçit Formation's (Tk) conglomerate-sandstone levels, and the limestone-claystone levels vary by 5% - 25%, RQD classifies it as a "very poor quality" or "poor quality" rock. Based on these values, the rock units comprising the research area's fundamental geology are classified as "extremely poor-poor quality" rocks.

4.5 Local Seismic Soil Classification

Soil group and soil classification of the units observed in the study area were made using seismic and sounding data from the Akare Planlama report (2015) using international codes (NEHRP - UBC)" and "TS EN 1998-1 (Eurocode 8)." These are summarized in Table 4.11.

Table 4.11 Seismic Soil Classification (after Akare Planlama report (2015)

Point	Vs(30)	NEHRPUBC	TS En	Form.	Point	Vs(30)	NEHRPUBC	TS En	Form.
SIS-1	605	C	B	Qal	**SIS-26**	962	B	A	Ke
SIS-2	681	C	B	Qd	**SIS-27**	1122	B	A	Ke
SIS-3	888	B	A	Ta	**SIS-28**	916	B	A	Ta
SIS-4	660	C	B	Qd	**SIS-29**	941	B	A	Ke
SIS-5	840	B	A	Tk	**SIS-30**	988	B	A	Ke
SIS-6	684	C	B	Qal	**SIS-31**	1072	B	A	Ke
SIS-7	1009	B	A	Ke	**SIS-32**	662	C	B	Qal
SIS-8	708	C	B	Qal	**SIS-33**	684	C	B	Qal
SIS-9	676	C	B	Qal	**SIS-34**	1141	B	A	PzMzk
SIS-10	865	B	A	Tk	**SIS-35**	721	C	B	Qal
SIS-11	713	C	B	Qal	**SIS-36**	770	B	B	Tk
SIS-12	1232	B	A	PzMzk	**SIS-37**	666	C	B	Qal
SIS-13	867	B	A	Tk	**SIS-38**	680	C	B	Qal
SIS-14	1087	B	A	Ke	**SIS-39**	609	C	B	Qal
SIS-15	1707	A	A	PzMzk	**SIS-40**	675	C	B	Qal
SIS-16	1609	A	A	PzMzk	**SIS-41**	755	C	B	Tk
SIS-17	1090	B	A	Ke	**SIS-42**	705	C	B	Qal
SIS-18	1236	B	A	PzMzk	**SIS-43**	821	B	A	Tk
SIS-19	727	C	B	Qal	**SIS-44**	699	C	B	Qal
SIS-20	819	B	A	Tk	**SIS-45**	683	C	B	Qal
SIS-21	812	B	A	Tk	**SIS-46**	679	C	B	Qal
SIS-22	1938	A	A	PzMzk	**SIS-47**	856	B	A	Tk
SIS-23	727	C	B	Qal	**SIS-48**	823	B	A	Tk
SIS-24	894	B	A	Ta	**SIS-49**	631	C	B	Qal
SIS-25	913	B	A	Ta	**SIS-50**	767	B	B	Tk

Table 4.11 continued

Point	Vs(30)	NEHRPUBC	TS En	Form.	Point	Vs(30)	NEHRPUBC	TS En	Form.
SIS-51	855	B	A	Tk	SIS-81	745	C	B	Tk
SIS-52	621	C	B	Qal	SIS-82	742	C	B	Tk
SIS-53	865	B	A	Tk	SIS-83	721	C	B	Qal
SIS-54	713	C	B	Qal	SIS-84	757	C	B	Tk
SIS-55	796	B	B	Tk	SIS-85	972	B	A	Ke
SIS-56	663	C	B	Qal	SIS-86	1112	B	A	Ke
SIS-57	725	C	B	Qal	SIS-87	623	C	B	Qal
SIS-58	760	C	B	Tk	SIS-88	695	C	B	Qal
SIS-59	942	B	A	Ke	SIS-89	676	C	B	Qal
SIS-60	734	C	B	Qal	SIS-90	1180	B	A	PzMzk
SIS-61	702	C	B	Qal	SIS-91	990	B	A	Ke
SIS-62	666	C	B	Qal	SIS-92	1489	B	A	PzMzk
SIS-63	703	C	B	Qal	SIS-93	944	B	A	Ke
SIS-64	967	B	A	Ke	SIS-94	1279	B	A	PzMzk
SIS-65	643	C	B	Qal	SIS-95	806	B	A	Tk
SIS-66	807	B	A	Tk	SIS-96	795	B	B	Tk
SIS-67	1174	B	A	PzMzk	SIS-97	992	B	A	Ke
SIS-68	814	B	A	Tk	SIS-98	837	B	A	Tk
SIS-69	767	B	B	Tk	SIS-99	1248	B	A	PzMzk
SIS-70	748	C	B	Tk	SIS-100	812	B	A	Tk
SIS-71	729	C	B	Qal	SIS-101	983	B	A	Ke
SIS-72	677	C	B	Qal	SIS-102	1001	B	A	Ke
SIS-73	796	B	B	Tk	SIS-103	801	B	A	Tk
SIS-74	1205	B	A	PzMzk	SIS-104	734	C	B	Qal
SIS-75	847	B	A	Tk	SIS-105	871	B	A	Tk
SIS-76	668	C	B	Qal	SIS-106	1005	B	A	Ke
SIS-77	699	C	B	Qal	SIS-107	924	B	A	Ta
SIS-78	894	B	A	Ta	SIS-108	983	B	A	Ke
SIS-79	660	C	B	Qal	SIS-109	868	B	A	Tk
SIS-80	964	B	A	Ke	SIS-110	1225	B	A	PzMzk

4.6 Idealized Soil Profiles

The final section of this chapter uses the parameters discussed in the preceding parts to construct an idealized soil profile for each of the boreholes. Additionally, the SPT logs contained in the Akare Planlama report (2015) are utilised. This chapter presents ten of the developed idealized soil profiles (Figure 4.5, Figure 4.6, Figure 4.7 and Figure 4.8).

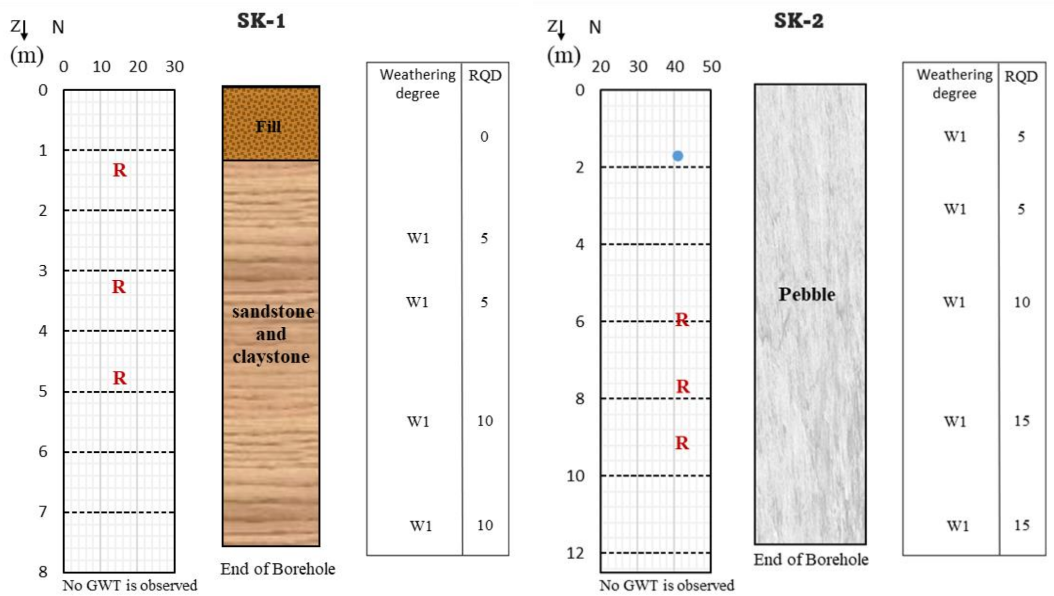

Figure 4.14. Idealized soil profiles of boreholes SK-1 and SK-2

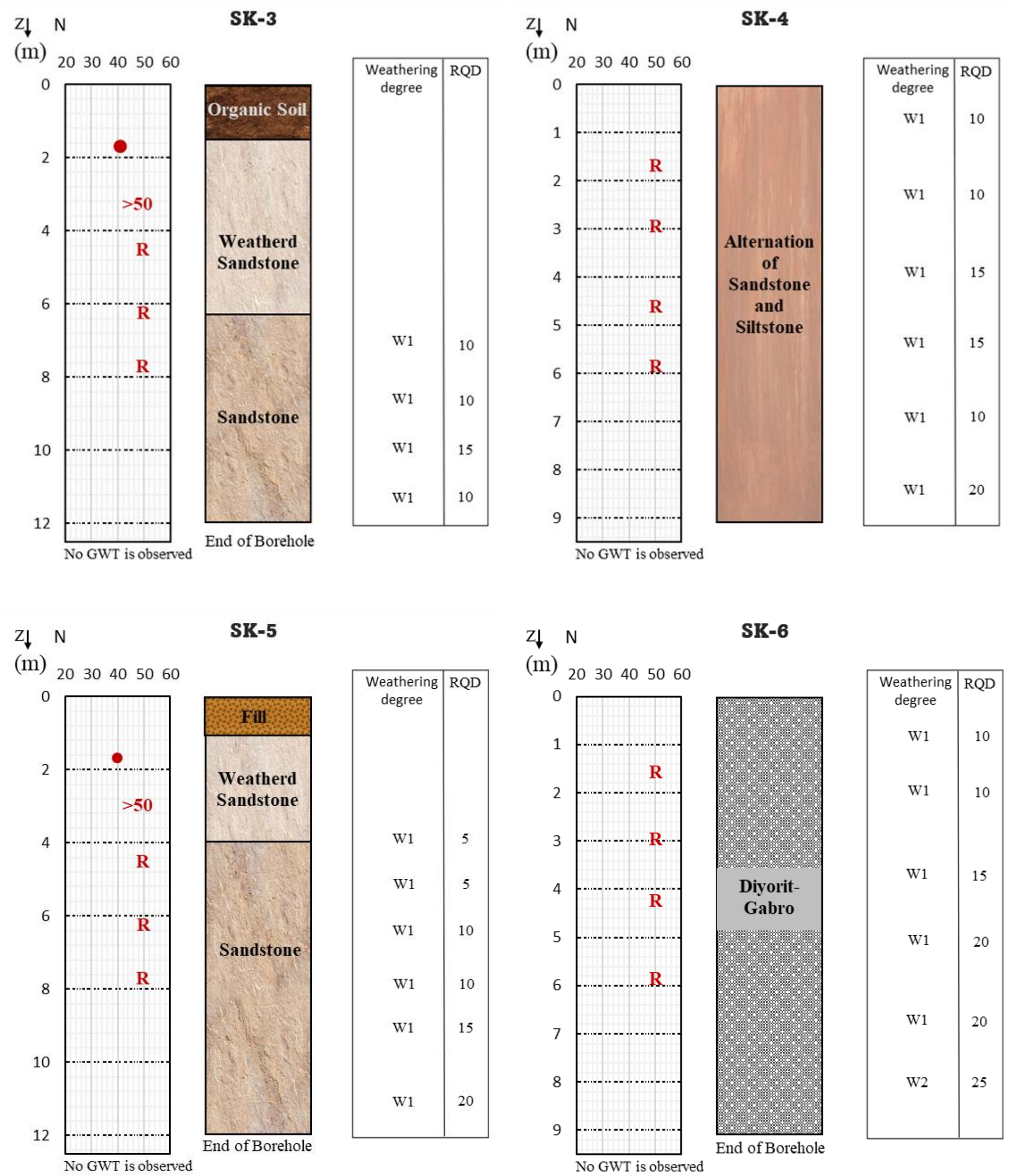

Figure 4.15. Idealized soil profiles of boreholes SK-3, SK-4, SK-5 and SK-6

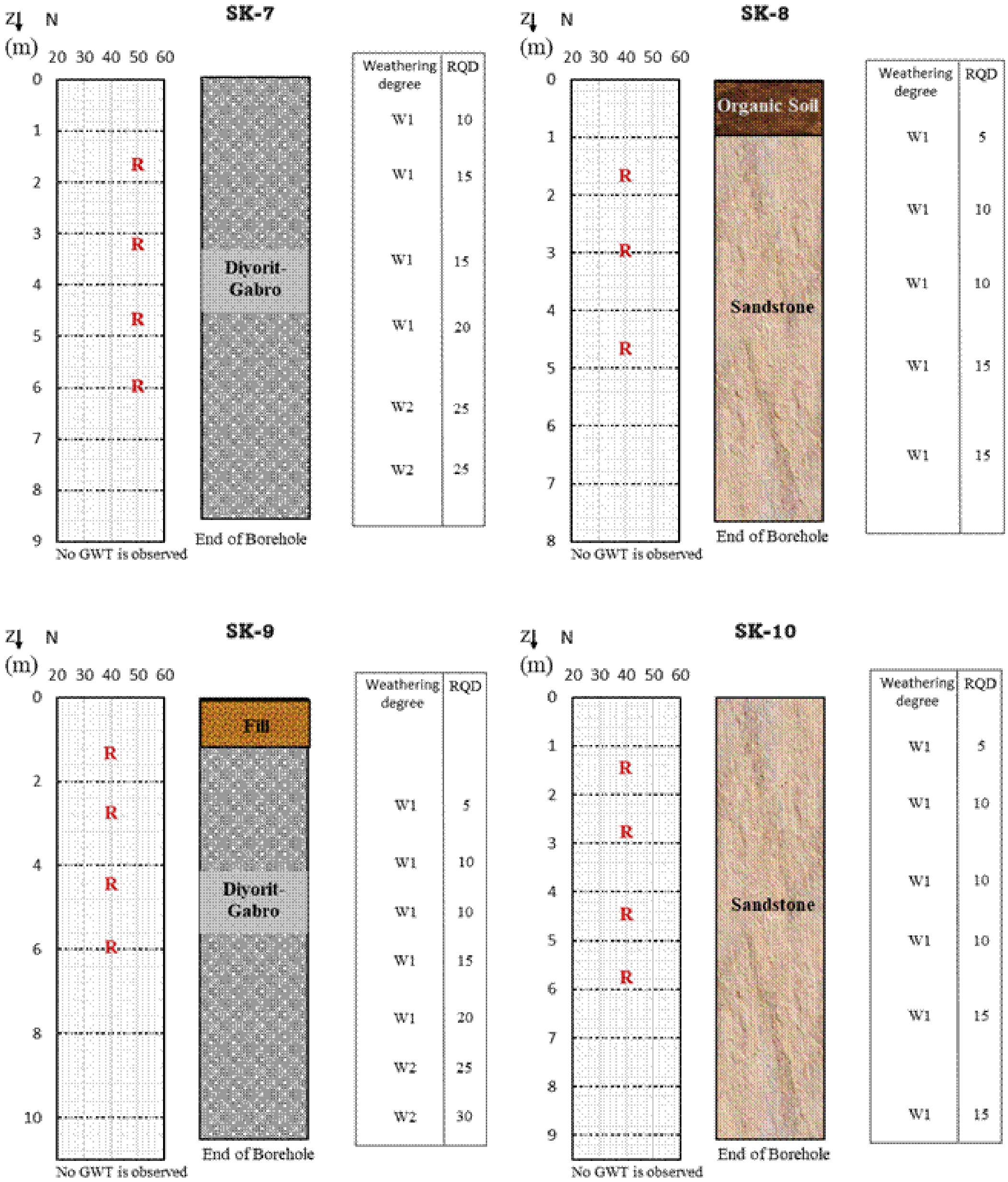

Figure 4.16. Idealized soil profiles of boreholes SK-7, SK-8, SK-9 and SK-10

CHAPTER 5

SITE RESPONSE ANALYSES

5.1 Introduction

To better understand the site effects of the 2020 Elazig-Sivrice earthquake, a total of 210 boreholes were used for one-dimensional equivalent linear site-specific seismic response analyses. The details related to those analyses are presented in this chapter; This chapter will begin with an overview of the seismic aspects of the 2020 Elazig-Sivrice event. Following that, the observed "actual" strong ground motion will be analyzed using the region's available acceleration time histories records captured during the event and the NGA-WEST2 ground motion prediction equations. Next, a globally available, locally calibrated time history record will be developed and used as a reference time history record throughout the analysis. As a prelude to site response analysis, an idealized shear wave velocity profile is created by modifying the available shear wave velocity profiles in the literature and the velocity measures for the boreholes and then tailoring them to obtain relatively deep and smooth profiles. A site response analysis will be carried out using Deepsoil software in three stages: first, (i) the original outcrop acceleration time history recorded at the strong ground motion station is de-convolved into a within-motion at bedrock, then (ii) this motion is scaled for each of the 210 boreholes. Once this has been done, (iii) an equivalent linear site response analysis is performed. The in-situ outcrop time histories, spectral acceleration plots, and PGA values for each borehole are acquired and presented in this chapter.

5.2 Preliminary Study

The epicenter of the event is reported by AFAD to be located close to Cevrimtas, a village in the region of the Sivrice district. This district had recorded the most significant PGA, calculated by AFAD to be 0.29 g. Moreover, the January 24 event was recorded by seven Strong Ground Motion Stations (SGMS) in Elazig; these SGMS are presented in Table 5.1. Additionally, to provide context for the situation, those SGMS are plotted on a Google Earth map that includes the study area's boundaries and the used boreholes; this map is shown in Figure 5.1.

Table 5.1 Strong Ground Motion Stations around the study area that captured the earthquake

Station code	**District**	**Longitude**	**Latitude**	**Vs_{30} (m/s)**	**Ec8**
2301	Elazig Center	39.19267	38.67043	407	B
2302	Maden	39.67541	38.39231	907	A
2304	Kovancılar	39.86293	38.72096	489	B
2305	Palu	40.13103	38.72778	907	A
2306	Karakoçan	40.03927	38.95945	663	B
2308	Sivrice	39.3102	38.45063	450	B
2309	Keban	38.72728	38.79913	860	A

Only one of the stations, the Elazig center (2301), is located inside the boundaries of the research region. Together with the boreholes, this station is displayed on the same map in Figure 5.1. The NGA-West GMPE is used in conjunction with the seven acceleration records gathered by the aforementioned SGMS to decide if this station (2301) may be used as-is or if it needs to be scaled prior to use.

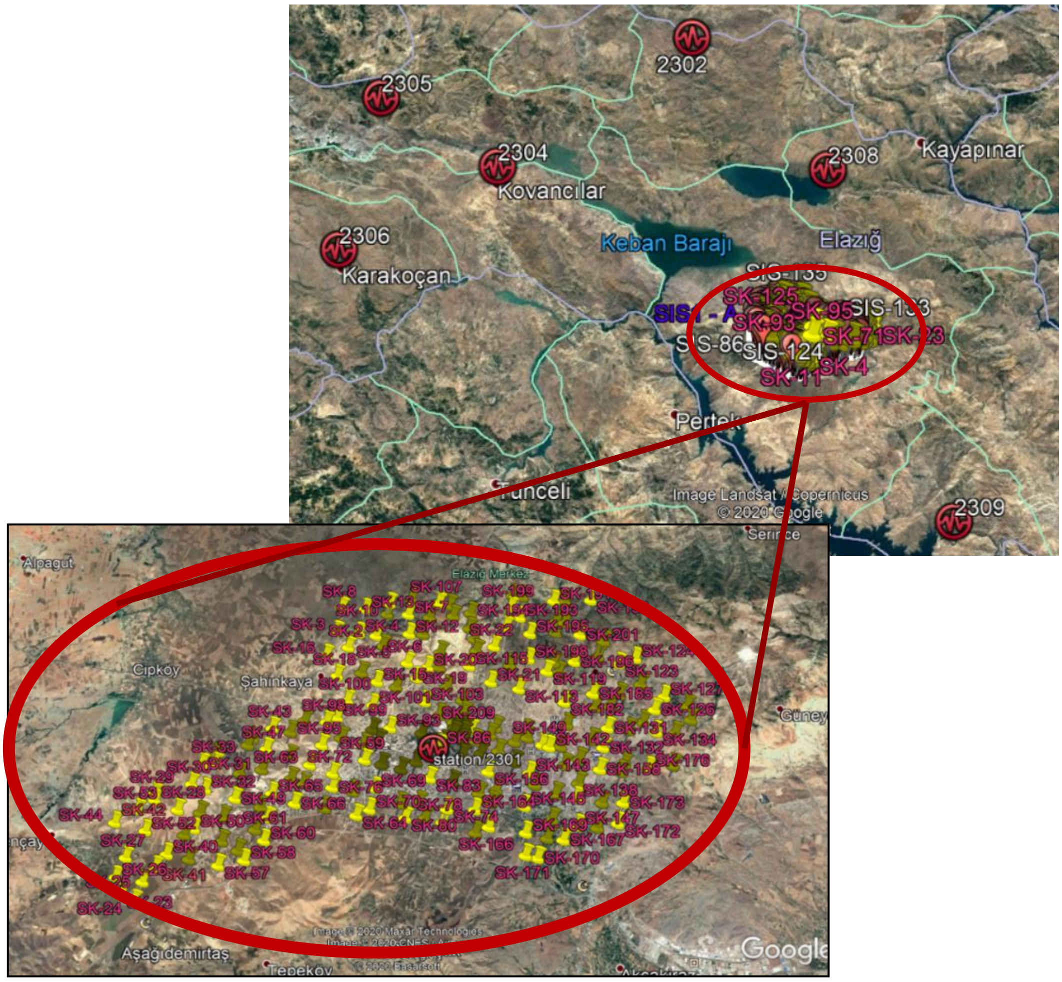

Figure 5.1. The seven SGMS that recorded the Elazig-Sivrice earthquake and the available borelogs, Google Earth, was used.

5.3 The Selection of Input Ground Motion

To begin with, the geometric mean of the PGA is calculated using Equation 5-1 which utilizes N-S and E-W components for each of the seven stations to get the geometric mean of the PGA. After that, the distance parameters named Rupture distance (R_{RUP}) and Joyner-Boore distance (R_{JB}), are obtained from AFAD. Next, Since the type of the fault's mechanism is strike-slip, and that R_{RUP} and R_{JB} distances are known, the depth to the top of the rupture (Z_{TOR}) distance can be calculated using the Pythagorean theorem as shown in Equation 5-2. The obtained distance parameters are summarized in Table 5.2. Moreover, the geometry of the strike-slip fault is illustrated by the NGA-West GMPE in their excel file, along with R_{RUP}, R_{JB}, and Z_{TOR} distances. Which is depicted in Figure 5.2.

$$PGA_{mean} = \sqrt{PGA_{N-s} \times \; PGA_{E-W}} \tag{5-1}$$

$$Z_{TOR} = \sqrt{R_{Rup}^2 - R_{JB}^2} \tag{5-2}$$

It is worth noting that within the provided stations, a couple of them had reported PGA values that are less than the significant acceleration " defined as accelerations more than 5%. " They were included in the analyses. They are, nevertheless, outliers with little engineering significance.

Table 5.2 Summary of the distance parameters and the Peak Ground Acceleration PGA values of the SGMS

Station	**District**	**PGA_{N-S} (g)**	**PGA_{E-W} (g)**	**PGA_{mean} (g)**	**R_{RUP}** (km)	**R_{JB}** (km)	**Z_{TOR}** (km)
2301	Elazig Center	0.121	0.143	0.132	30.46	30.43	1.35
2302	Maden	0.026	0.032	0.029	47.57	47.56	1.35
2304	Kovancılar	0.009	0.014	0.011	74.41	74.4	1.35
2305	Palu	0.004	0.005	0.004	95.57	95.57	1.35
2306	Karakoçan	0.004	0.006	0.005	101.94	101.93	1.35
2308	Sivrice	0.013	0.021	0.017	78.40	78.39	1.35
2309	Keban	0.240	0.298	0.268	17.89	17.86	1.35

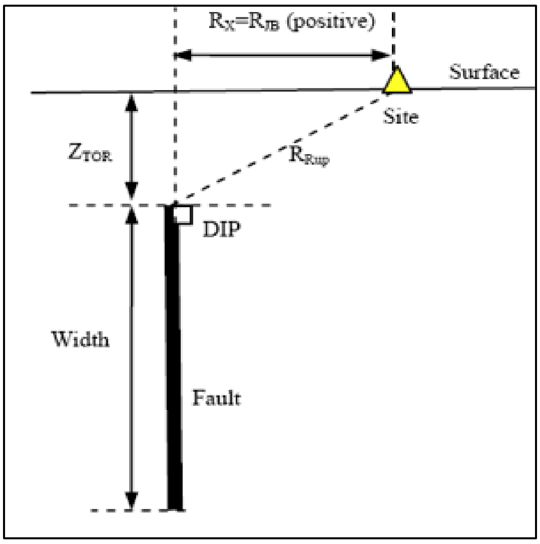

Figure 5.2. The Strike-Slip Fault Geometry definition (NGA-West GMPE)

The acceleration history record used for the analyses needs to be first calibrated. The instructions in the NGAW2 spreadsheet outline which models should be used for some specific countries. NGA-WEST2 models by Abrahamson, Silva, and Kaman (ASK14), Campbell and Bozorgnia (CB14), Chiou and Young (CY14), and Idriss (I14) will be used for the calibration. Table 5.3 summarizes the instructions for the usage of the NGA-WEST2 GMPE models based on the area code.

After specifying which GMPE will be utilized to be calibrated by the seven SGM acceleration time histories recorded in the study region, the NGA-WEST2 GMPE spreadsheet is used. The following input parameters were used as inputs:

- Moment magnitude " M_w=6.8, "
- $V_{S,30}$ " provided by AFAD, "
- R_{Rup}, R_{JB} Z_{TOR} "Table 5.2, "
- The type of Fault " Strike Slip – dip 90^o "
- The region is chosen to be Turkey.

Table 5.3 NGA-WEST2 Instructions for the use of the models depending on the region

Region	ASK14	BSSA4	CB14	CY14	I14
Global	✓	✓	✓	✓	✓
California	✓	✓	✓	✓	✓
China	Linear R term Vs30 scaling	Anelas attenuation	Anelas attenuation	Anelas attenuation	✓
Italy	✓	Anelas attenuation	Anelas attenuation	Sigma	✓
Japan	Linear R term Vs30 scaling	Anelas attenuation basin depth	Anelas. Attenuation, shallow site effects & basin effects	Basin depth sigma	✓
New Zealand	✓	✓	✓	✓	✓
Turkey	✓	Linear R term Vs30 scaling	✓	✓	✓
Taiwan	—	✓	✓	✓	✓

The shear wave velocity (V_S) used as an input to the GMPEs should be normalized to one of the stations first to perform the calibration; for this reason, the PGA is estimated twice. At each time, a different V_S value is being used. The first predicted PGA is based on the original V_S of the SGM "The V_S reported by AFAD. " The second predicted PGA is based on V_S recorded at Elazig Center Station (2301). The findings of the NGA-WEST2 GMPE for each of the SGMS are reported in Table 5.4 for the (ASK14) and (CB14) models and in Table 5.5 for the (CY14) and Idriss (I14) models.

Table 5.4 PGA estimation using the NGA-WEST2 GMPE's for ASK14 and CB14 models (to scale the PGA by $V_{s,2301} = 407$ m/s)

Station		ASK14		CB14	
Name	**Code**	**$PGA_{VS30\text{-}real}$**	**$PGA_{VS30\text{-}407}$**	**$PGA_{VS30\text{-}real}$**	**$PGA_{VS30\text{-}407}$**
Elazig Center	2301	-	-	-	-
Maden	2302	0.055	0.078	0.065	0.078
Kovancılar	2304	0.043	0.046	0.047	0.049
Palu	2305	0.023	0.033	0.028	0.035
Karakoçan	2306	0.024	0.030	0.028	0.032
Palu	2307	0.047	0.043	0.049	0.047
Sivrice	2308	0.188	0.193	0.196	0.197

Table 5.5 PGA estimation using the NGA-WEST2 GMPE's for CY14 and I14 models (to scale the PGA by $V_{s,2301} = 407$ m/s)

Station		ASK14		CB14	
Name	**Code**	**$PGA_{VS30\text{-}real}$**	**$PGA_{VS30\text{-}407}$**	**$PGA_{VS30\text{-}real}$**	**$PGA_{VS30\text{-}407}$**
Elazig Center	2301	-	-	-	-
Maden	2302	0.051	0.074	0.044	0.087
Kovancılar	2304	0.042	0.045	0.040	0.046
Palu	2305	0.023	0.034	0.016	0.032
Karakoçan	2306	0.025	0.031	0.019	0.029
Palu	2307	0.047	0.043	0.052	0.043
Sivrice	2308	0.192	0.198	0.244	0.266

After predicting the PGA using the NGA-WEST2 GMPE's. The AFAD-recorded PGAs of each of the strong ground motion stations are scaled. This scaling factor is calculated using Equation 5-3. The results of these computations are depicted in Figure 5.3. The resulting R_{JB} vs. PGA charts for ASK14, CB14, CY14, and I14 are presented in Figure 5.4, in Figure 5.5, in Figure 5.6, and in Figure 5.4. As illustrated in the figures, the ground motion prediction equations by Campbell and Bozorgnia (CB14) and Idriss (I14) provide a good match with the recorded intensities within 40 km r_{jb} distances. As a result, no further calibration was needed.

$$Scaling\ Factor = \frac{GMPE\ (PGA_{VS30,real})}{GMPE\ (PGA_{VS30,407})} \tag{5-3}$$

Station Name	Station code	ASK14		CB14		CY14		I14		To Scale PGA's to PGA vs = 407 m/s
		PGA $_{VS30\text{-}real}$	PGA $_{VS30\text{-}407}$	PGA $_{VS30\text{-}real}$	PGA $_{VS30\text{-}407}$	PGA $_{VS30\text{-}real}$	PGA $_{VS30\text{-}407}$	PGA $_{VS30\text{-}real}$	PGA $_{VS30\text{-}407}$	
Maden	2302	0.055	0.078	0.065	0.078	0.051	0.074	0.044	0.087	
Kovancılar	2304	0.043	0.046	0.047	0.049	0.042	0.045	0.040	0.046	
Palu	2305	0.023	0.033	0.028	0.035	0.023	0.034	0.016	0.032	
Karakoçan	2306	0.024	0.030	0.028	0.032	0.025	0.031	0.019	0.029	
Palu	2307	0.047	0.043	0.049	0.047	0.047	0.043	0.052	0.043	
Sivrice	2308	0.188	0.193	0.196	0.197	0.192	0.198	0.244	0.266	

$$\frac{\boxed{0.078}}{\boxed{0.055}} \times \boxed{0.029} = \boxed{0.041}$$

Station Name	Station code	PGA (g)			VS30 (m/s)	R_{rup} (km)	R_{jb} (km)	Z_{tor}	PGA scaled			
		N-S	E-W	Geometric Mean					ASK14	CB14	CY14	I14
Elazig Center	2301	0.121	0.143	0.132	407	30.46	30.43	1.35	0.132	0.132	0.132	0.132
Maden	2302	0.026	0.032	0.029	907	47.57	47.56	1.35	0.041	0.035	0.042	0.057
Kovancılar	2304	0.009	0.014	0.011	489	74.41	74.4	1.35	0.012	0.012	0.012	0.013
Palu	2305	0.004	0.005	0.004	907	95.57	95.57	1.35	0.006	0.005	0.006	0.008
Karakoçan	2306	0.004	0.006	0.005	663	101.94	101.93	1.35	0.006	0.006	0.006	0.008
Palu 2	2307	0.013	0.021	0.017	329	78.40	78.39	1.35	0.015	0.016	0.015	0.014
Sivrice	2308	0.240	0.298	0.268	450	17.89	17.86	1.35	0.275	0.270	0.276	0.292

Figure 5.3. Scaling the Peak ground acceleration for each of the SGMSs.

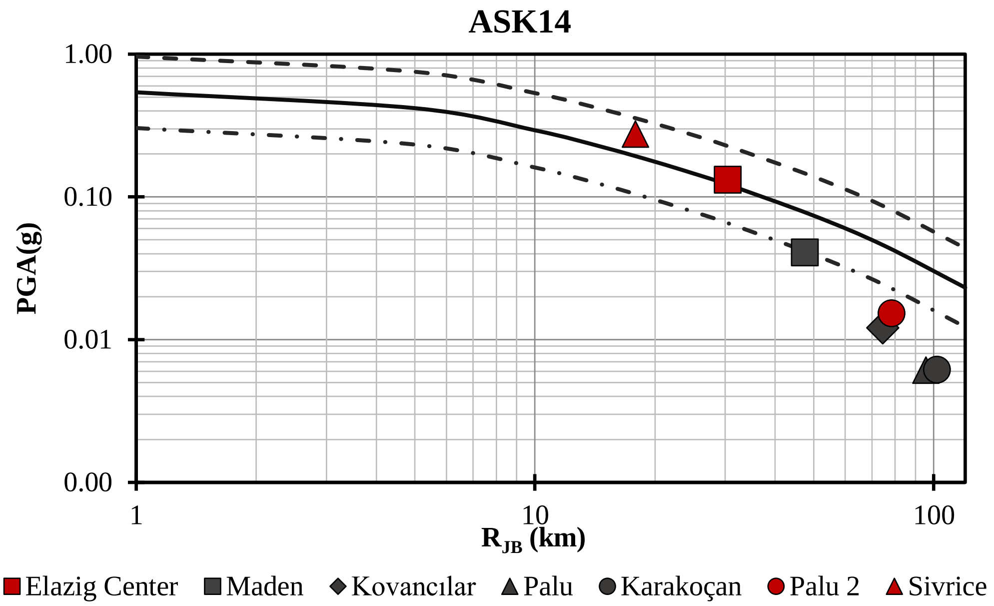

Figure 5.4. Comparison of the PGA values assessed by ASK14 at various distances to the PGA values observed at the SGM Stations for V_{S30} = 407

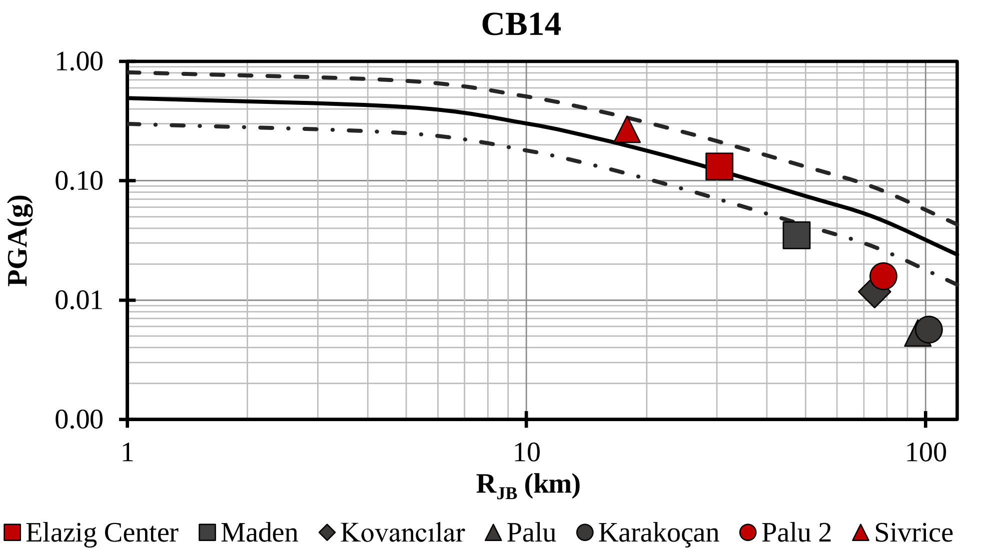

Figure 5.5. Comparison of the PGA values assessed by CB14 at various distances to the PGA values observed at the SGM Stations for V_{S30} = 407

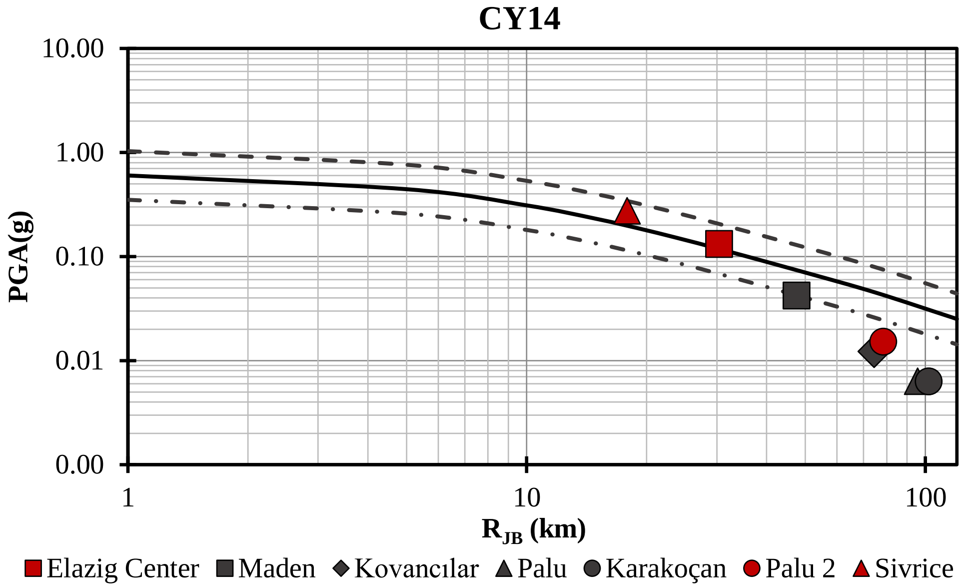

Figure 5.6. Comparison of the PGA values assessed by CY14 at various distances to the PGA values observed at the SGM Stations for V_{S30} = 407

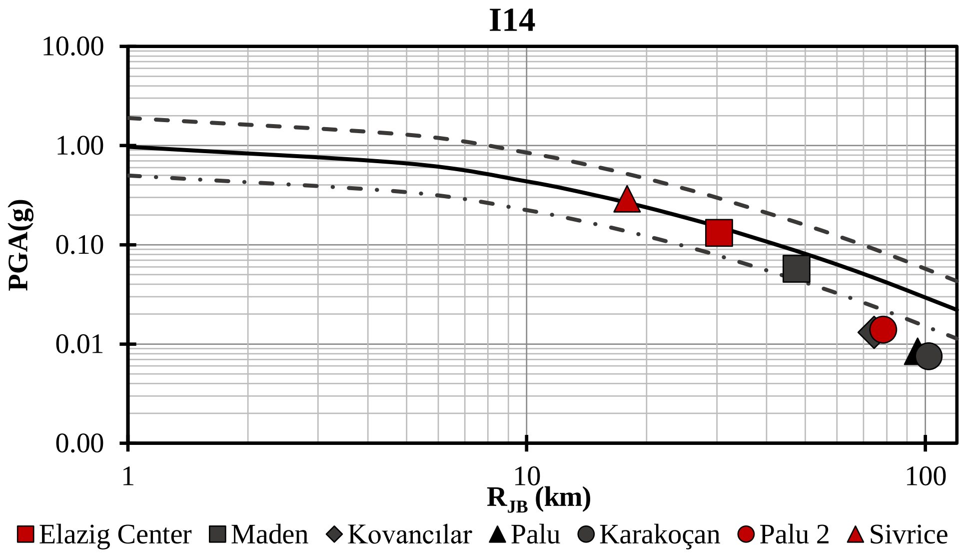

Figure 5.7. Comparison of the PGA values assessed by I14 at various distances to the PGA values observed at the SGM Stations for V_{S30} = 407

5.4 The Construction of the Idealized Shear Wave Velocity Profile

One of the most significant parameters that impact the result of the site response analyses is the shear wave velocity. For this reason, a representative, relatively deep, V_s profile must be developed before proceeding with the study. The closest accessible $V_s$profile to the area is the profile of the Elazig-Center (2301) given by AFAD. This profile will be the primary profile used for this investigation; it is 32 meters deep and has a shear wave velocity of 715 m/s at 32 m. However, this is a relatively shallow profile, and deeper profiles are required to perform a high-quality analysis. For this purpose, a literature review was conducted to identify nearby deep V_s profiles; the only profiles available were the SGM stations profiles provided by AFAD. Aside from the primary profile (Elazig-Center, 2301), a total of six profiles are accessible. These profiles are shown in Figure 5.8 to Figure 5.10. Below is a list of V_s profiles sorted according to their distance from the center of Elazig;

- The shear wave velocity profile of **Elazig Center (2301)** is the primary shear wave velocity profile as it is located in the center of the study region. This profile has a depth of 32 meters and a shear wave velocity value of 715 m/s at 32 m. This profile is shown in Figure 5.8.

- The shear wave velocity profile of **Sivrice (2308)** is located around 27 km away from the center of the study area. It is a deep profile, having a total depth of around 100 meters, with its maximum shear wave velocity Vs = 1276 m/s at around 79 m. This profile can be considered for utilizing an idealized shear wave velocity profile. It is shown in Figure 5.8.

- The third closest shear wave velocity profile to the center of Elazig is the profile of **Keban (2309)**, which is located around 42 km away from the city center. This strong ground motion station did not capture the acceleration of the 2020 Elazig-Sivrice earthquake. However, a shear wave velocity profile for this station has been prepared by AFAD. This station's shear wave velocity profile is relatively shallow, with a total depth of 36 meters, having its maximum velocity (V_s = 223 m/s) measured at 29 m depth. This profile is shown in Figure 5.9.

- The fourth profile in the list is located around 52 km away from Elazig center. This profile is the profile of the strong ground motion station **Maden (2302)**. This profile is also considered a relatively shallow profile with a total depth of 41 m and a maximum shear wave velocity of 1750 m/s starting at a depth of 32 m. This profile is plotted in Figure 5.9.

- Around 59 km away from the center of the region of interest, the shear wave velocity profile of the **Kovanclarl (2304)** Strong Ground Motion Station exists. This profile is considered to be relatively deep, with a total depth of 78 meters and a maximum shear wave velocity of 1286 m/s starting at 61 m. This shear wave velocity profile is illustrated in Figure 5.10.

- The **Palu (2305)** strong ground motion station is the last considered shear wave velocity profile. Although it is the furthest between the aforelisted profiles, that is 82 km away from the center of Elazig. However, it is the deepest profile among them, with a total depth of around 150 meters, having its maximum shear wave velocity $V_s = 3377$ m/s starting at 116 m. The shear wave velocity profile of Palu is shown in Figure 5.10.

The Keban (2309) and Maden (2302) Strong Ground Motion Stations are excluded from the aforementioned shear wave profiles. True, those two profiles are believed to be relatively close to Elazig's center. Those are, however, short profiles. In other words, the Elazig center (2301) profile already exists, and the 2301 station profile is nearly the same depth as 2309 and 2302. The remaining shear wave velocity profiles will be used to construct the idealized shear wave velocity profile.

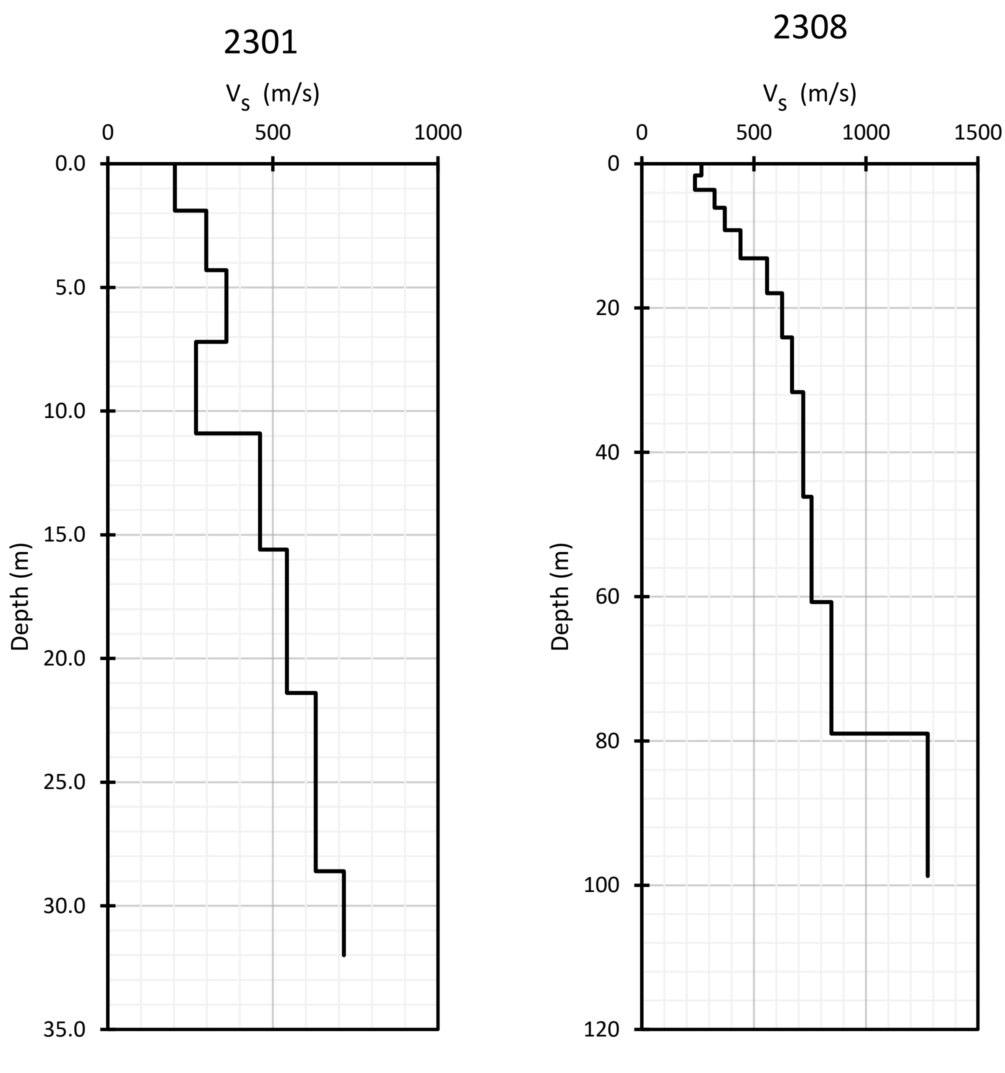

(A) (B)

Figure 5.8. Shear wave velocity profile plots of Strong Ground Motion Station 2301, Elazig Center and 2308, Sivrice

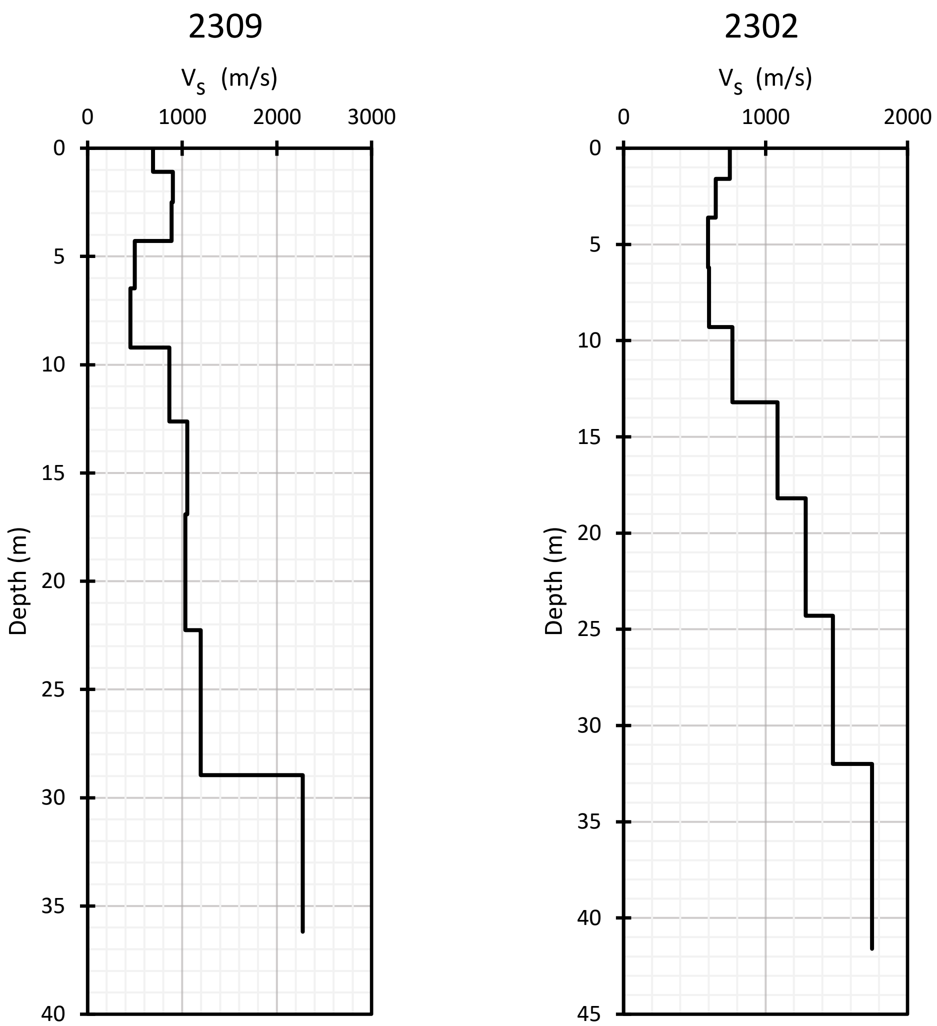

(A) (B)

Figure 5.9. Shear wave velocity profile plots of Strong Ground Motion Station 2309, Keban and 2302, Maden

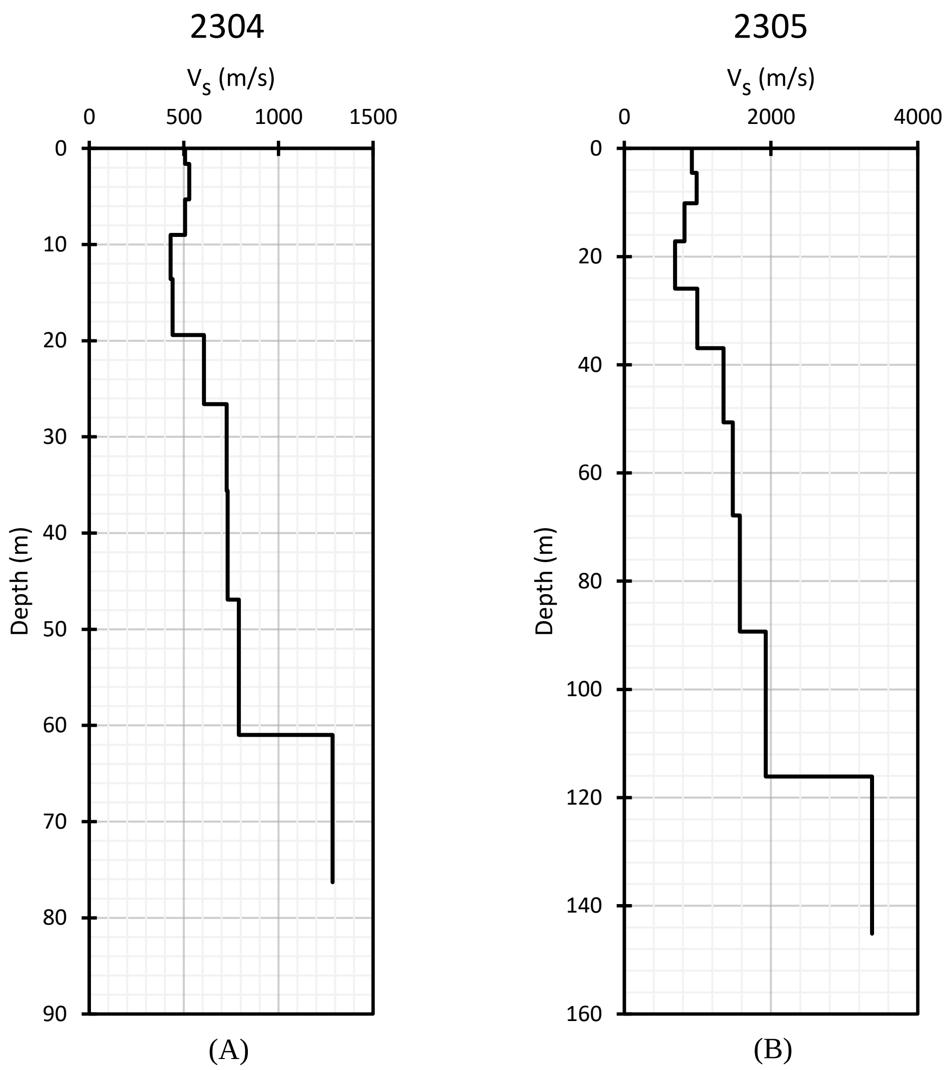

Figure 5.10. Shear wave velocity profile plots of Strong Ground Motion Station 2304, Kovancılarl and 2305, Palu

To construct an idealized V_s profile, several nearby available profiles are going to be tailored in a way that they will be consistent with the primary $V_s$profile (2301) as illustrated in Figure 5.11 During the tailoring process, **Elazig Center (2301)** profile is used as the primary profile; in other words, the idealized V_s profile will start with Elazig Center (2301), then just underneath **Sivrice (2308)** is being used up to 83 meters, then **Palu (2305)** V_s profile will be used up to 145.5 meters ($V_s = 3377$ m/s), that is where bedrock is assumed to exist in the Elazig center. Following is the detailed explanation of the construction of the idealized shear wave velocity profile:

- The first profile is that of Elazig Center (2301). This profile ends at 32 m with a shear wave velocity of 715 m/s.
- The second profile is Sivrice (2308). This profile will be extracted starting at the last recorded depth of station 2301 (32 m), and it has a consistent shear wave velocity value, that is 720 m/s (the 2301 had 715 m/s at the same depth). The deepest shear wave velocity value recorded for the current station is 1276 m/s, assigned at depths between 79 and 100 m. This profile will be used for up to 83 m.
- The last profile that is going to be used for the tailoring process is the shear wave velocity profile of SGMS Palu (2305). This station has a relatively comparable shear wave velocity value to the last assigned shear wave velocity profile (2310). In other words, in the newly constructed profile, the last used depth is 83 m, with a 1276 m/s shear wave velocity value, while station 2305 at the same depth has a shear wave velocity value of 1575 m/s. This profile is going to be used up to 145.5 m ($V_s = 3377$ m/s). As mentioned previously, this shear wave velocity will be considered as V_s, the bedrock of Elazig for this study.

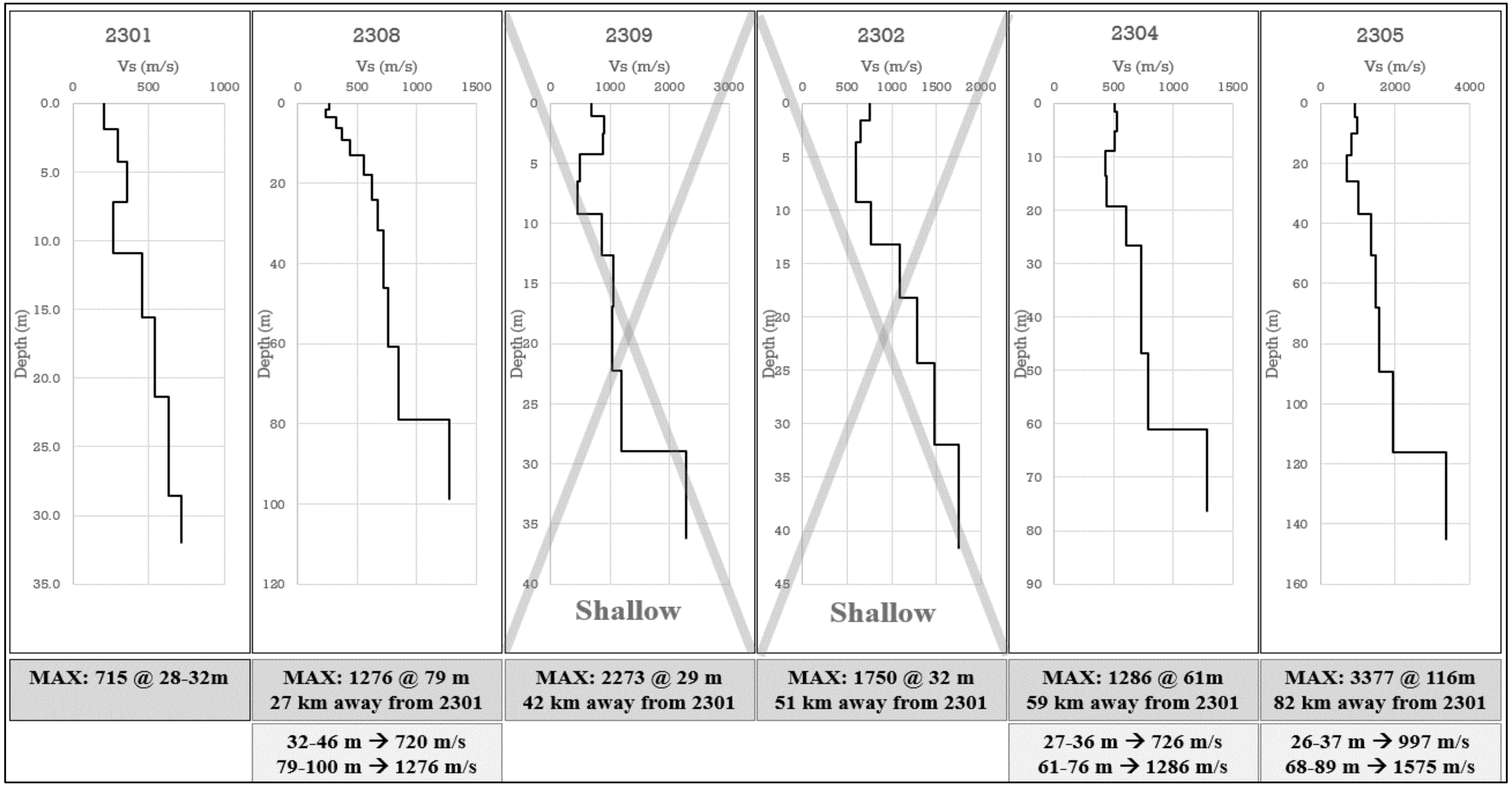

Figure 5.11. Comparison of the available SGM station's shear wave velocity profiles.

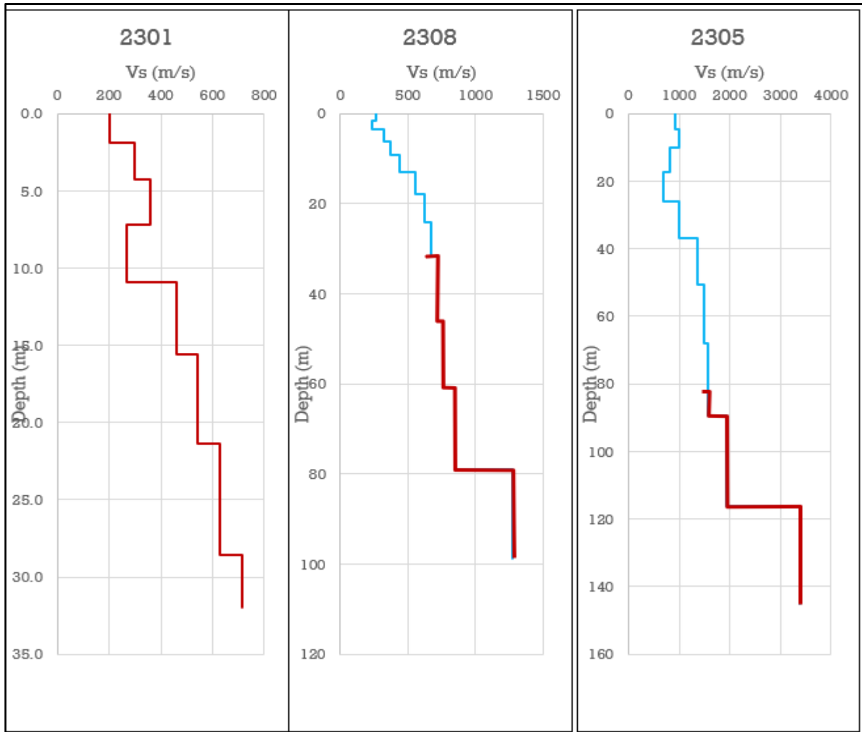

28-32 m → 715 m/s	MAX: 1276 @ 79 m 27 km away from 2301	MAX: 3377 @ 116m 82 km away from 2301
	32-46 m → 720 m/s 79-100 m → 1276 m/s	26-37 m → 997 m/s 68-89 m → 1575 m/s

Depth m	VS m/s	
0.0	203	2301
1.9	203	
1.9	298	
4.3	298	
4.3	359	
7.2	359	
7.2	267	
10.9	267	
10.9	461	
15.6	461	
15.6	542	
21.4	542	
21.4	630	
28.6	630	
28.6	715	
32.0	715	
32	720	2308
46	720	
46	757	
61	757	
61	846	
79	846	
79	1276	
83	1276	
83	1575	2305
89	1575	
89	1927	
116	1927	
116	3377	
145	3377	

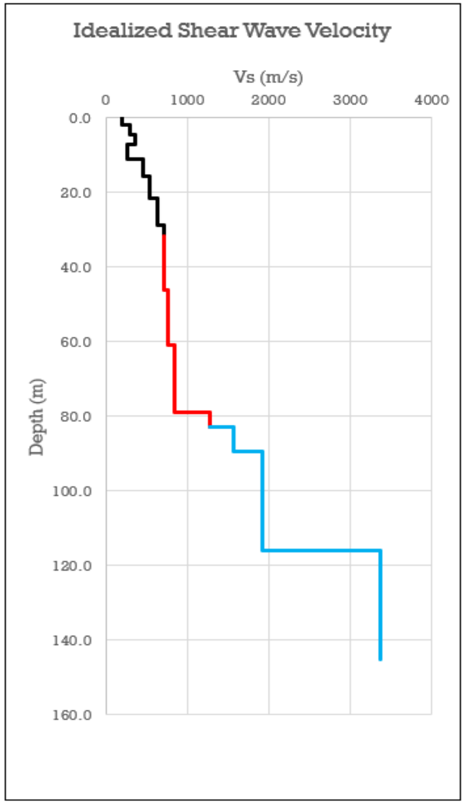

Figure 5.12. The used SGMS V_s profiles for the construction of the idealized shear wave velocity profile

5.5 Performing Site Response Analysis

An idealized shear wave velocity profile and representative soil profiles have now been established; at this point, the equivalent linear site-specific seismic response analysis can be performed with all the inputs necessary to do this analysis.

AFAD has documented an outcrop time history record on the surface of Elazig Center's (2301) SGM station. To use this data, one must first deconvolve the acceleration time history to establish the bedrock motion associated with the recorded surface motion; the acceleration time history record is "propagated" downward from the ground's surface detection point to the bedrock. This procedure is referred to as "Step 1" in Figure 5.13.

Prior to performing the equivalent linear site response analysis, it is necessary to scale the deconvolved bedrock motion for each borehole in the research region using an appropriate scaling factor; in order to do so, the PGA for each individual borehole will be predicted using the NGA-WEST2 GMPE's. The scaling procedure is represented by the designation "Step 2."The deconvolved-scaled bedrock motion is then propagated in the upper direction "convolved " and used in the third step of performing site response analysis. This convolution process is the reversal of the preceding step, "Step 1." It should be noted that the outcrop motion was used in the first stage, whereas "within motion" was used in the third step. The outcropping motion is then obtained from the bedrock motion propagating upward through the representative soil profile. The third and last step is called "Step 3."

Figure 5.13 illustrates these three processes in further detail. The following subsections conduct site response analysis on 210 locations located inside the Elazig Center.

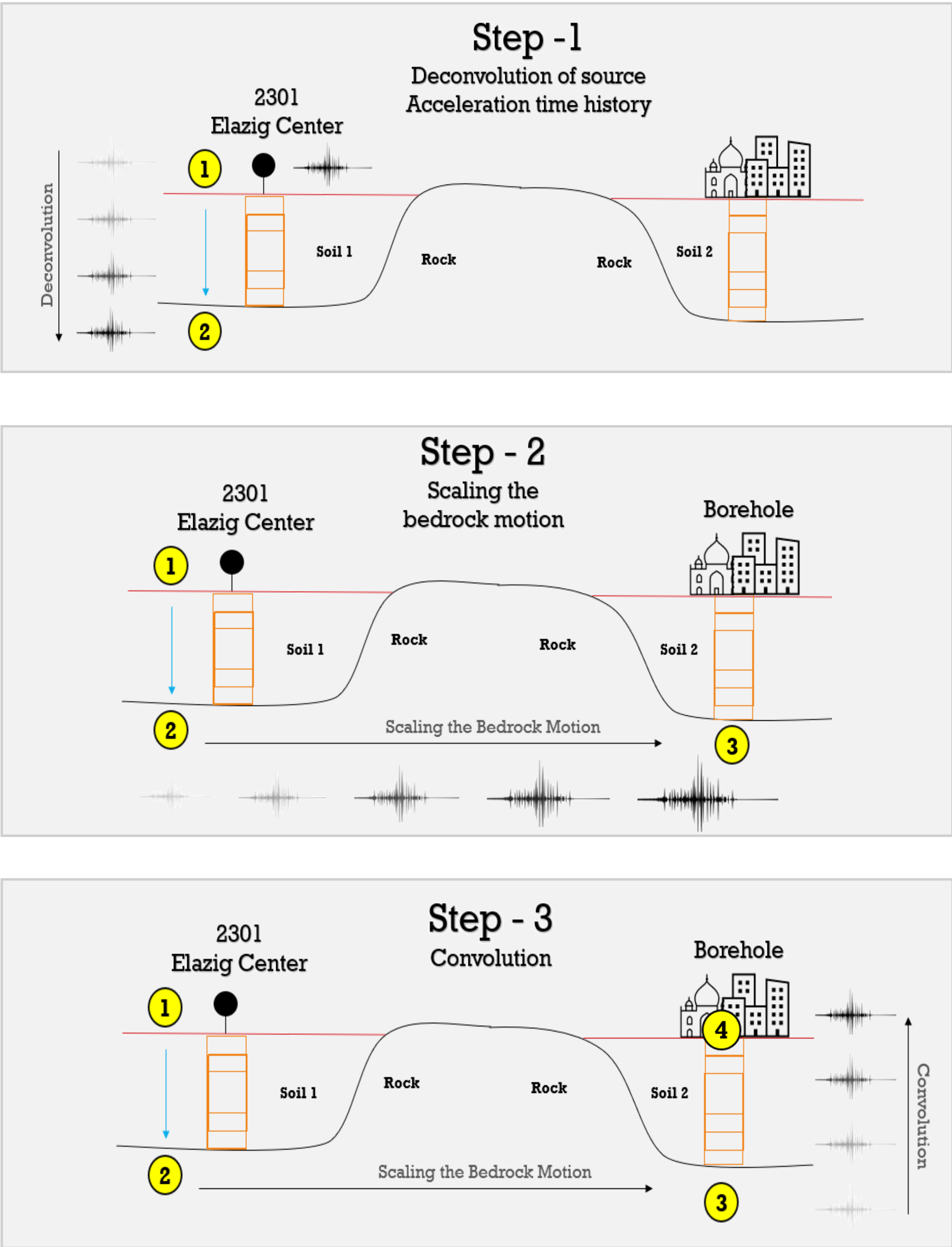

Figure 5.13. The procedures for conducting site response analysis

5.5.1 Deconvolution of The Recoded Acceleration Time History at Elazig Center (2301)

The Elazig Center (2301) SGMS reorded the event; the recorded time history is referred to as "an outcrop rock motion" because it is recorded at the ground surface and the column beneath the SGMS is composed of rock; this motion is plotted in Figure 5.14 using Deepsoil software. The Elazig Center (2301) station's soil profile is reported in Table 5.6, while the station's V_s is plotted in Figure 5.15.

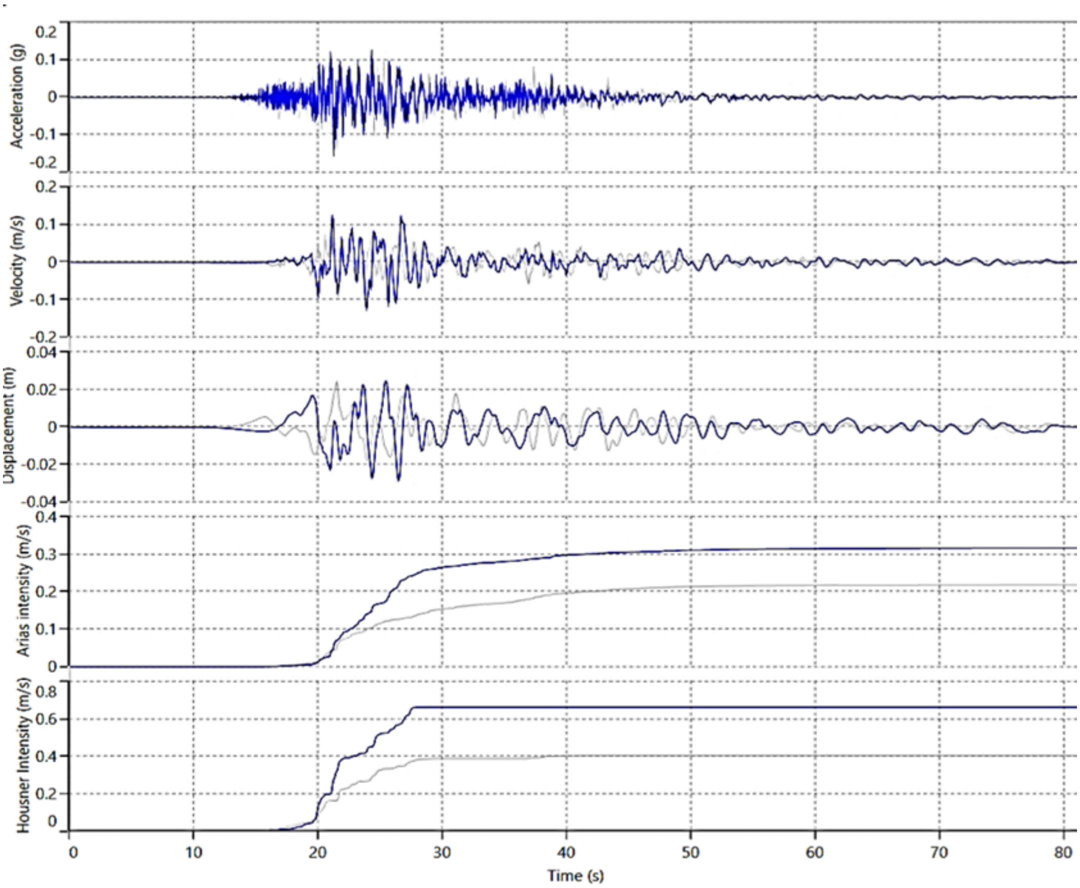

Elazig Center (2301) North — Elazig Center (2301) East

Figure 5.14. Housner intensity, arias intensity, acceleration, velocity, and displacement time histories that are recorded at the SGMS Elazig-Center (2301).

Table 5.6 The soil properties used for the analysis of Elazig Center (2301) SGMS

Depth (m)	Layer Name	Thickness (m)	Unit wight (kN/m3)	Vs (m/s)	PI
1.9	Silty Clay	1.9	18.4	203	21
3	Silty Clay	1.1	18.4	298	15
4.5	Silty Clay	3.4	18.4	298	19
6	Clayey Gravelly Sand	2.6	18.4	298	-
7.2	Clayey Gravelly Sand	4.6	18.4	359	-
9	Claystone - Siltstone	4.4	19	359	13
10.9	Claystone - Siltstone	6.5	19	267	8
12	Claystone - Siltstone	5.5	19	267	-
15.6	Clayey Gravelly Sand	10.1	20	461	-
21.4	Weathered silt stone	11.3	20	542	-
28.6	Rock	17.3	21	630	-
32	Rock	14.7	21.5	715	-
46.1	Rock	31.44	22	720	-
60.7	Rock	29.3	23	757	-
79	Rock	49.69	24	846	-
83	Rock	33.31	24.5	1276	-
89.3	Rock	55.99	24.5	1575	-
116.1	Rock	60.13	25	1927	-
145.2	Rock	85.02	25	3377	-

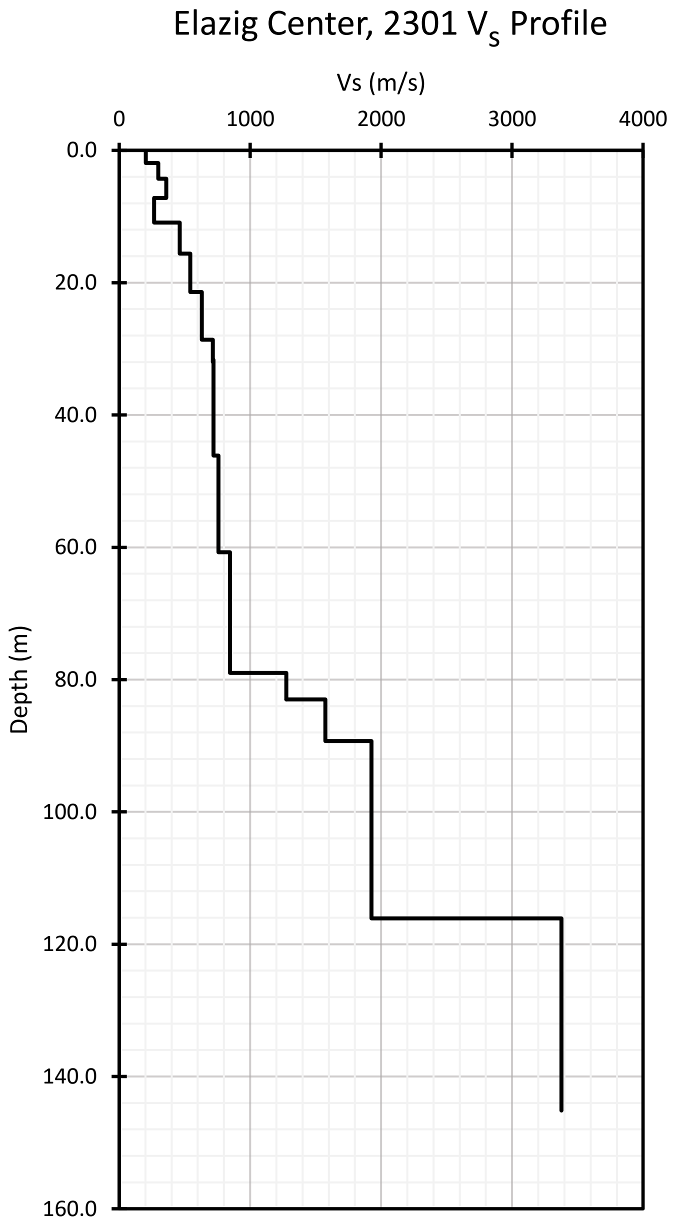

Figure 5.15. The adopted shear wave velocity profile for the SGMS Elazig Center (2301)

To conduct an equivalent linear site response analysis, picking the normalized shear modulus and damping degradation curves from a reference curve is necessary. There are numerous references to degradation curves in the literature. The reference curves used in this work are Seed and Idriss (1970), Vucetic and Dobry (1991), and Rollins et al. (2020). The class of soil layer dictates the degradation reference curves to be utilized.

That is, for sand, Seed and Idriss (1970) curves are used. Within this reference, there are three possibilities: Seed and Idriss upper limit, Seed and Idriss mean, and Seed and Idriss lower limit. The layer's effective stress decides the option to be used. To elaborate, the Seed and Idriss alternatives are listed below, along with their respective effective stress levels.

- The lower limit of Seed and Idriss (1970) is applied to layers with effective stress levels below 100 kPa.
- For layers with effective stress levels ranging from 100 to 300 kPa, Seed and Idriss mean (1970) are utilized.
- At effective stress levels greater than 100 kPa, we adopt Seed and Idriss' Upper Limit (1970).

For clayey soils, on the other hand, the modulus and damping degradation curves proposed by Vucetic and Dobry (1991) are used. This reference was chosen for its ease of usage, as the plasticity index is the sole input parameter required for this reference.

Finally, Rollins et al. (2020) have been accepted as the standard reference for gravel. It is necessary to know two factors in order to use this reference: the effective stress and the uniformity coefficient (C_u). For this reason, using the USGS soil classification charts, an assumption is made for C_u. The following are the equations that were used to create the reference curves developed by Rollins and his colleagues:

$$D = 26.05 \left(\frac{\gamma}{1+\gamma} \right)^{0.375} C_u^{0.08} \ \sigma'^{-0.07} \quad (5\text{-}4)$$

$$G/G_{max} = \frac{1}{\left\{ 1 + \left[\frac{\gamma}{0.0046(C_u)^{-0.197}(\sigma'_o)^{0.52}} \right]^{0.84} \right\}} \quad (5\text{-}5)$$

given that:

$$G_{max} = \rho \, V_s^2 \quad (5\text{-}6)$$

Where in the above equations, D is denoting the damping ratio, γ is the shear strain, and σ'_o is the effective stress. C_u is the uniformity coefficient, G is the shear modulus, ρ is the density of the soil, and V_S is the shear wave velocity.

The investigation was conducted using Deepsoil software; after defining the bedrock and inputting the layer parameters, a motion should be chosen; in this example, the north and east components of the Elazig Center (2301) acceleration time history records are chosen. Figure 5.16 shows the record acquired from AFAD.

The effective shear strain must be specified as indicated in Equation 5-7, where M is the event's moment magnitude.

$$Effective\ Shear\ Strain\ Ratio\ (SSR) = \frac{M-1}{10} \quad (5\text{-}7)$$

Finally, the east and north output components of the outcrop acceleration time history motion of the Elazig center (2301) station are exported. After being scaled, this motion will be employed as a within motion for the rest of the analyses. The findings of motion plots are shown in Figure 5.16.

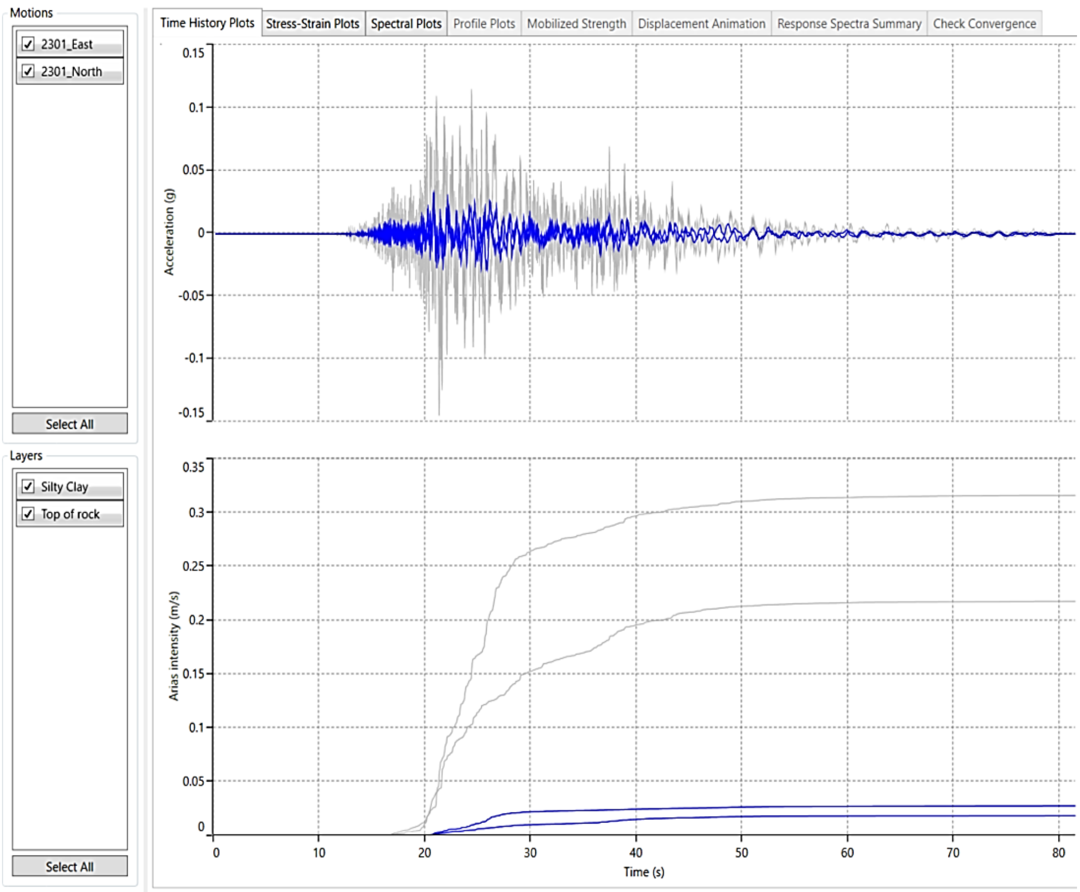

Figure 5.16. The output motion plots of the convolution using Deepsoil software.

5.5.2 Seismic Demand Parameters for the Boreholes

In order to perform site-specific seismic site response analyses for each of the 210 boreholes, instead of using the same acceleration time history and shear wave velocity profile for all of the boreholes, a "borehole-specific" acceleration time history and shear wave velocity profiles will be constructed.

5.5.2.1 Borehole-Specific Acceleration Time History Generation

A "borehole-specific" acceleration time history is developed by scaling the main bedrock motion that was obtained in the previous section, "the de-convoluted motion, " and developing new acceleration time history records to be used for the site response analyses.

In order to scale the bedrock motion, a scaling factor is obtained using the NGA-WEST2 GMPE's. As mentioned previously, to use the NGA-WEST2 spreadsheet, some parameters, such; as the distance parameters; R_{RUP}, R_{JB}, and Z_{TOR} are needed. For the SGMS in Section 5.3, R_{RUP} and R_{JB} were obtained from AFAD and the Z_{TOR} was calculated using Equation 5-2 and was found out to be 1.35 for all the SGMS. However, for the local boreholes, this is not the case, as there is no available data for the (R_{RUP}) and (R_{JB}) in the literature. However, since (Z_{TOR}) distance was found out to be the same for all the SGMS that are surrounding the study area, it is assumed to be the same as well for all the boreholes (that is $Z_{TOR} = 1.35$). The (R_{JB}) distance is measured as the closest distance to the fault ruptures in the surface; the faults that are located in the region are plotted in google earth and shown in a single figure together with the borders of the study region in Figure 5.17, where the pink polygon represents the study area, and the red lines refer to the fault. The coordinates of the closest two faults to the study region are measured and presented in Table 5-7.

Table 5.7 The coordinates of the closest two fault lines to the study region

Fault 1, East	**Fault** 1, North	**Fault** 2, East	**Fault** 2, North
520341.6	4252619	520767.3	4251386.4
522517.3	4253684	520015.4	4251031.2
524796.9	4254778	519834.6	4250947.6
528215.7	4256458	519666.2	4250867.5
538614.3	4261446	519522.6	4250800.8
544061.4	4263904	515788.9	4249045.6

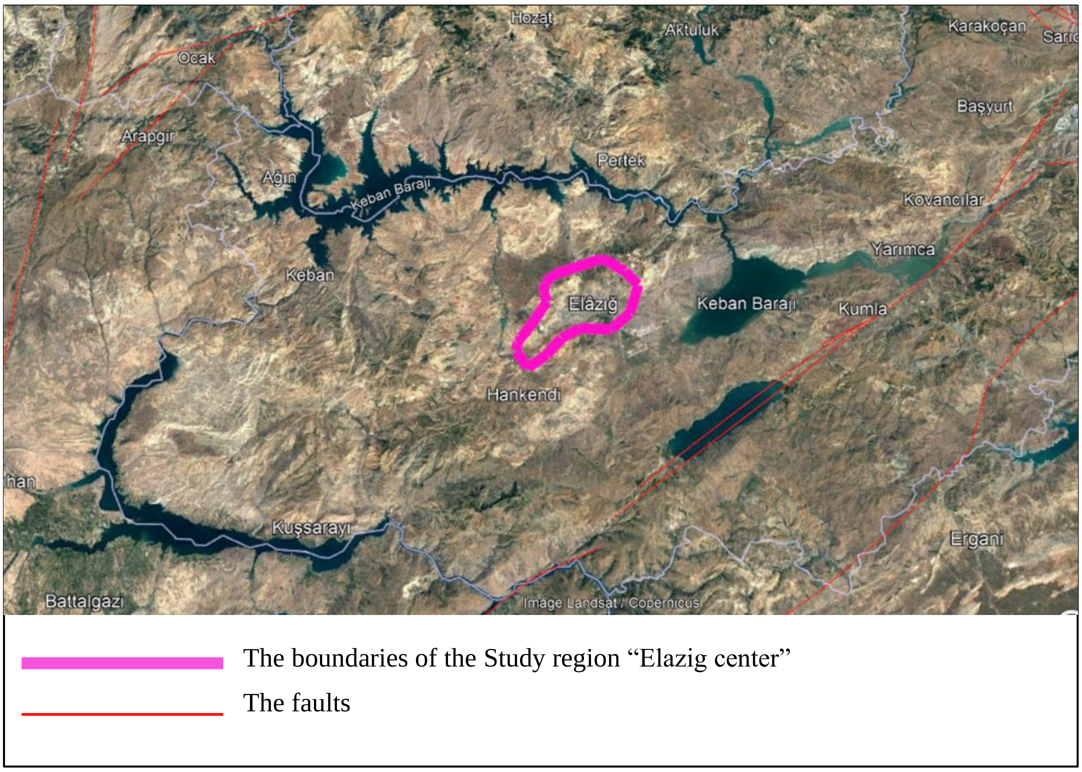

Figure 5.17. The location of the study area with respect to the earthquake faults

After measuring the closest distance to the faults for each of the boreholes and assigning it to the (R_{JB}), the (R_{RUP}) is then calculated from R_{JB} and Z_{TOR} using Equation 5.17. Next, after obtaining the distance parameters, the NGA-WEST2 GMPE spreadsheet is used to predict the PGA of each of the boreholes. In the NGA-WEST2 spreadsheet CB14 model was used to PGA of the bedrock for each borehole. The following input parameters were used as inputs in the NGA-WEST2:

- Moment magnitude $M_w = 6.8$,
- $V_{S,rock}$ specified in Chapter 4,
- $Z_{TOR} = 1.35$, R_{JB} is measured and R_{RUP} is calculated.
- The type of Fault is Strike-Slip – dip 90^{o}
- The region is chosen to be Turkey.

To obtain a scaling factor, the predicted PGA at the bedrock of the boreholes is divided by the predicted bedrock PGA for the SGMS obtained from the previous sections (0.097 g). This scaling factor is used to scale the actual acceleration time history recorded at the SGMS Elazig-Center (2301).

To reduce the workload, and to also reduce the probability of making mistakes, the process is automated, and a short code is written using excel visual basic, where the R_{JB} is measured using a line equation and the coordinates of the closest two faults to the study region, which are presented in Table 5-7, This distance measurement is then assigned to the R_{JB}, which in turn is being used then for the calculation of the R_{RUP}. Next, using the seismic parameters of the earthquake and the obtained distance measurements as input parameters in the NGA-WEST2 spreadsheet, the PGA prediction values at the bedrock are obtained. Finally, the recorded initial motions at the SGMS are scaled, and a new motion is assigned for each borehole. The calculated distance parameters, the calculated scaling factors, and the obtained PGA values at the bedrock for all the boreholes are presented in Table 5.8.

Table 5.8 The calculated Joyner-Boore (R_{JB}), the Rupture distance (R_{RUP}) distances

SK NO	R_{jb} (km)	Z_{tor}	R_{rup} (Km)	$PGA_{GMPE.rock}$	Scaling Factor	$PGA_{scaled,rock}$
SK-1	29.94	1.35	29.97	0.0990	1.0203	0.0536
SK-2	31.01	1.35	31.04	0.0955	0.9842	0.0517
SK-3	31.72	1.35	31.75	0.0932	0.9612	0.0505
SK-4	31.39	1.35	31.42	0.0942	0.9716	0.0510
SK-5	31.10	1.35	31.13	0.0952	0.9812	0.0515
SK-6	29.78	1.35	29.81	0.0995	1.0260	0.0539
SK-7	31.50	1.35	31.53	0.0939	0.9682	0.0509
SK-8	32.54	1.35	32.57	0.0908	0.9361	0.0492
SK-9	31.77	1.35	31.80	0.0931	0.9598	0.0504
SK-10	32.13	1.35	32.16	0.0920	0.9485	0.0498
SK-11	31.16	1.35	31.18	0.0950	0.9793	0.0514
SK-12	30.77	1.35	30.80	0.0962	0.9920	0.0521
SK-13	32.20	1.35	32.23	0.0918	0.9464	0.0497
SK-14	30.65	1.35	30.68	0.0966	0.9959	0.0523
SK-15	29.46	1.35	29.49	0.1007	1.0376	0.0545
SK-16	30.97	1.35	31.00	0.0956	0.9853	0.0518
SK-17	29.08	1.35	29.11	0.1020	1.0517	0.0552
SK-18	30.11	1.35	30.14	0.0984	1.0144	0.0533
SK-19	29.16	1.35	29.19	0.1017	1.0484	0.0551
SK-20	29.43	1.35	29.46	0.1008	1.0387	0.0546
SK-21	28.27	1.35	28.30	0.1050	1.0825	0.0569
SK-22	29.45	1.35	29.48	0.1007	1.0378	0.0545
SK-23	24.78	1.35	24.81	0.1201	1.2379	0.0650
SK-24	24.45	1.35	24.49	0.1217	1.2545	0.0659
SK-25	25.00	1.35	25.04	0.1190	1.2266	0.0644
SK-26	25.42	1.35	25.45	0.1170	1.2065	0.0634
SK-27	25.97	1.35	26.01	0.1145	1.1804	0.0620
SK-28	27.61	1.35	27.65	0.1076	1.1089	0.0582
SK-29	27.83	1.35	27.86	0.1067	1.1000	0.0578
SK-30	27.78	1.35	27.81	0.1069	1.1021	0.0579
SK-31	28.40	1.35	28.43	0.1045	1.0774	0.0566
SK-32	27.46	1.35	27.49	0.1082	1.1152	0.0586
SK-33	28.26	1.35	28.30	0.1050	1.0827	0.0569
SK-34	27.69	1.35	27.72	0.1073	1.1058	0.0581
SK-35	28.57	1.35	28.61	0.1039	1.0707	0.0562

Table 5.8 Continued

SK NO	R_{jb} (km)	Z_{tor}	R_{rup} (Km)	$PGA_{GMPE.rock}$	Scaling Factor	$PGA_{scaled,rock}$
SK-36	28.77	1.35	28.80	0.1031	1.0633	0.0559
SK-37	26.73	1.35	26.77	0.1112	1.1462	0.0602
SK-38	26.14	1.35	26.18	0.1137	1.1724	0.0616
SK-39	25.30	1.35	25.33	0.1176	1.2122	0.0637
SK-40	25.68	1.35	25.71	0.1158	1.1940	0.0627
SK-41	25.35	1.35	25.39	0.1173	1.2095	0.0635
SK-42	27.04	1.35	27.08	0.1099	1.1328	0.0595
SK-43	28.94	1.35	28.97	0.1025	1.0569	0.0555
SK-44	27.26	1.35	27.29	0.1090	1.1236	0.0590
SK-45	27.59	1.35	27.62	0.1077	1.1099	0.0583
SK-46	28.59	1.35	28.62	0.1038	1.0700	0.0562
SK-47	28.26	1.35	28.29	0.1050	1.0829	0.0569
SK-48	26.32	1.35	26.36	0.1129	1.1643	0.0612
SK-49	26.87	1.35	26.90	0.1106	1.1404	0.0599
SK-50	26.25	1.35	26.29	0.1133	1.1676	0.0613
SK-51	26.36	1.35	26.39	0.1128	1.1628	0.0611
SK-52	26.67	1.35	26.71	0.1114	1.1487	0.0603
SK-53	27.45	1.35	27.48	0.1082	1.1157	0.0586
SK-54	25.57	1.35	25.60	0.1163	1.1992	0.0630
SK-55	25.63	1.35	25.66	0.1160	1.1964	0.0628
SK-56	25.10	1.35	25.13	0.1185	1.2219	0.0642
SK-57	24.80	1.35	24.84	0.1199	1.2366	0.0650
SK-58	24.72	1.35	24.75	0.1204	1.2410	0.0652
SK-59	26.89	1.35	26.92	0.1105	1.1394	0.0599
SK-60	25.18	1.35	25.21	0.1181	1.2180	0.0640
SK-61	25.89	1.35	25.93	0.1148	1.1839	0.0622
SK-62	25.95	1.35	25.98	0.1146	1.1815	0.0621
SK-63	27.26	1.35	27.30	0.1090	1.1235	0.0590
SK-64	25.12	1.35	25.15	0.1184	1.2211	0.0641
SK-65	26.68	1.35	26.71	0.1114	1.1487	0.0603
SK-66	26.11	1.35	26.15	0.1139	1.1739	0.0617
SK-67	26.58	1.35	26.61	0.1118	1.1529	0.0606
SK-68	26.98	1.35	27.01	0.1102	1.1356	0.0597
SK-69	25.84	1.35	25.87	0.1151	1.1866	0.0623
SK-70	25.19	1.35	25.23	0.1181	1.2173	0.0639

Table 5.8 Continued

SK NO	R_{jb} (km)	Z_{tor}	R_{rup} (Km)	$PGA_{GMPE.rock}$	Scaling Factor	$PGA_{scaled,rock}$
SK-71	26.22	1.35	26.26	0.1134	1.1688	0.0614
SK-72	26.74	1.35	26.78	0.1111	1.1457	0.0602
SK-73	25.29	1.35	25.33	0.1176	1.2125	0.0637
SK-74	24.46	1.35	24.49	0.1217	1.2542	0.0659
SK-75	26.69	1.35	26.73	0.1113	1.1478	0.0603
SK-76	26.29	1.35	26.33	0.1131	1.1657	0.0612
SK-77	25.66	1.35	25.70	0.1159	1.1947	0.0628
SK-78	24.07	1.35	24.11	0.1236	1.2743	0.0669
SK-79	24.37	1.35	24.41	0.1221	1.2586	0.0661
SK-80	24.57	1.35	24.60	0.1211	1.2486	0.0656
SK-81	25.08	1.35	25.12	0.1186	1.2226	0.0642
SK-82	24.94	1.35	24.97	0.1193	1.2300	0.0646
SK-83	25.64	1.35	25.68	0.1160	1.1956	0.0628
SK-84	26.32	1.35	26.36	0.1129	1.1644	0.0612
SK-85	27.41	1.35	27.44	0.1084	1.1173	0.0587
SK-86	26.51	1.35	26.54	0.1121	1.1560	0.0607
SK-87	27.41	1.35	27.45	0.1084	1.1171	0.0587
SK-88	26.08	1.35	26.11	0.1140	1.1756	0.0618
SK-89	26.83	1.35	26.86	0.1108	1.1421	0.0600
SK-90	26.71	1.35	26.75	0.1113	1.1471	0.0603
SK-91	27.24	1.35	27.27	0.1091	1.1246	0.0591
SK-92	27.85	1.35	27.88	0.1066	1.0992	0.0577
SK-93	27.72	1.35	27.76	0.1071	1.1044	0.0580
SK-94	27.85	1.35	27.88	0.1066	1.0992	0.0577
SK-95	27.79	1.35	27.83	0.1068	1.1015	0.0579
SK-96	27.73	1.35	27.76	0.1071	1.1043	0.0580
SK-97	28.59	1.35	28.62	0.1038	1.0700	0.0562
SK-98	28.57	1.35	28.60	0.1039	1.0710	0.0563
SK-99	28.62	1.35	28.65	0.1037	1.0690	0.0562
SK-100	29.12	1.35	29.16	0.1018	1.0499	0.0551
SK-101	28.69	1.35	28.72	0.1034	1.0661	0.0560
SK-102	28.84	1.35	28.87	0.1029	1.0605	0.0557
SK-103	28.28	1.35	28.31	0.1050	1.0823	0.0569
SK-104	27.68	1.35	27.71	0.1073	1.1063	0.0581
SK-105	27.50	1.35	27.53	0.1080	1.1137	0.0585

Table 5.8 Continued

SK NO	R_{jb} (km)	Z_{tor}	R_{rup} (Km)	$PGA_{GMPE.rock}$	Scaling Factor	$PGA_{scaled,rock}$
SK-106	26.69	1.35	26.72	0.1114	1.1481	0.0603
SK-107	31.58	1.35	31.61	0.0937	0.9656	0.0507
SK-108	31.39	1.35	31.42	0.0943	0.9718	0.0510
SK-109	30.35	1.35	30.38	0.0976	1.0062	0.0529
SK-110	30.97	1.35	31.00	0.0956	0.9855	0.0518
SK-111	32.04	1.35	32.07	0.0923	0.9512	0.0500
SK-112	29.92	1.35	29.95	0.0991	1.0212	0.0536
SK-113	27.75	1.35	27.78	0.1070	1.1034	0.0580
SK-114	29.30	1.35	29.34	0.1012	1.0432	0.0548
SK-115	29.04	1.35	29.07	0.1021	1.0530	0.0553
SK-116	29.50	1.35	29.54	0.1005	1.0360	0.0544
SK-117	28.56	1.35	28.59	0.1039	1.0711	0.0563
SK-118	28.64	1.35	28.67	0.1036	1.0680	0.0561
SK-119	28.05	1.35	28.09	0.1058	1.0911	0.0573
SK-120	28.27	1.35	28.30	0.1050	1.0824	0.0569
SK-121	27.89	1.35	27.92	0.1065	1.0976	0.0577
SK-122	28.00	1.35	28.03	0.1060	1.0931	0.0574
SK-123	27.57	1.35	27.60	0.1077	1.1108	0.0583
SK-124	27.58	1.35	27.61	0.1077	1.1103	0.0583
SK-125	26.67	1.35	26.71	0.1114	1.1488	0.0603
SK-126	25.71	1.35	25.74	0.1157	1.1926	0.0626
SK-127	26.04	1.35	26.08	0.1142	1.1771	0.0618
SK-128	25.42	1.35	25.46	0.1170	1.2063	0.0634
SK-129	26.56	1.35	26.59	0.1119	1.1538	0.0606
SK-130	26.25	1.35	26.29	0.1132	1.1675	0.0613
SK-131	25.56	1.35	25.60	0.1163	1.1994	0.0630
SK-132	24.97	1.35	25.00	0.1192	1.2285	0.0645
SK-133	25.30	1.35	25.33	0.1176	1.2123	0.0637
SK-134	24.96	1.35	24.99	0.1192	1.2289	0.0646
SK-135	25.02	1.35	25.06	0.1189	1.2257	0.0644
SK-136	23.20	1.35	23.24	0.1283	1.3224	0.0695
SK-137	24.74	1.35	24.78	0.1202	1.2397	0.0651
SK-138	23.58	1.35	23.62	0.1262	1.3008	0.0683
SK-139	24.05	1.35	24.09	0.1237	1.2755	0.0670
SK-140	24.81	1.35	24.85	0.1199	1.2363	0.0649

Table 5.8 Continued

SK NO	R_{jb} (km)	Z_{tor}	R_{rup} (Km)	$PGA_{GMPE.rock}$	Scaling Factor	$PGA_{scaled,rock}$
SK-141	25.42	1.35	25.46	0.1170	1.2062	0.0634
SK-142	25.51	1.35	25.55	0.1166	1.2017	0.0631
SK-143	24.85	1.35	24.89	0.1197	1.2341	0.0648
SK-144	24.41	1.35	24.45	0.1219	1.2566	0.0660
SK-145	23.81	1.35	23.85	0.1250	1.2884	0.0677
SK-146	23.92	1.35	23.95	0.1244	1.2828	0.0674
SK-147	22.68	1.35	22.72	0.1312	1.3525	0.0710
SK-148	22.45	1.35	22.49	0.1326	1.3665	0.0718
SK-149	25.65	1.35	25.69	0.1159	1.1952	0.0628
SK-150	26.04	1.35	26.07	0.1142	1.1773	0.0618
SK-151	26.02	1.35	26.06	0.1143	1.1780	0.0619
SK-152	25.88	1.35	25.91	0.1149	1.1847	0.0622
SK-153	26.50	1.35	26.54	0.1122	1.1564	0.0607
SK-154	26.46	1.35	26.49	0.1124	1.1584	0.0608
SK-155	25.98	1.35	26.02	0.1144	1.1799	0.0620
SK-156	25.29	1.35	25.33	0.1176	1.2125	0.0637
SK-157	26.28	1.35	26.31	0.1131	1.1665	0.0613
SK-158	24.29	1.35	24.33	0.1225	1.2628	0.0663
SK-159	23.13	1.35	23.17	0.1287	1.3264	0.0697
SK-160	24.61	1.35	24.64	0.1209	1.2466	0.0655
SK-161	25.35	1.35	25.39	0.1173	1.2097	0.0635
SK-162	24.67	1.35	24.71	0.1206	1.2431	0.0653
SK-163	24.24	1.35	24.28	0.1227	1.2654	0.0665
SK-164	24.17	1.35	24.21	0.1231	1.2691	0.0667
SK-165	23.43	1.35	23.46	0.1270	1.3096	0.0688
SK-166	23.48	1.35	23.52	0.1267	1.3065	0.0686
SK-167	22.38	1.35	22.42	0.1329	1.3704	0.0720
SK-168	22.58	1.35	22.62	0.1318	1.3584	0.0714
SK-169	22.95	1.35	22.99	0.1297	1.3367	0.0702
SK-170	22.05	1.35	22.09	0.1349	1.3910	0.0731
SK-171	22.24	1.35	22.28	0.1338	1.3791	0.0724
SK-172	22.39	1.35	22.43	0.1329	1.3701	0.0720
SK-173	23.00	1.35	23.04	0.1294	1.3340	0.0701
SK-174	24.21	1.35	24.25	0.1229	1.2669	0.0665
SK-175	24.00	1.35	24.04	0.1240	1.2781	0.0671

Table 5.8 Continued

SK NO	R_{jb} (km)	Z_{tor}	R_{rup} (Km)	$PGA_{GMPE.rock}$	Scaling Factor	$PGA_{scaled,rock}$
SK-176	23.86	1.35	23.90	0.1247	1.2857	0.0675
SK-177	23.72	1.35	23.76	0.1254	1.2931	0.0679
SK-178	27.94	1.35	27.98	0.1063	1.0955	0.0575
SK-179	29.81	1.35	29.84	0.0994	1.0251	0.0538
SK-180	30.62	1.35	30.65	0.0967	0.9972	0.0524
SK-181	25.33	1.35	25.36	0.1174	1.2107	0.0636
SK-182	26.85	1.35	26.88	0.1107	1.1411	0.0599
SK-183	26.08	1.35	26.12	0.1140	1.1753	0.0617
SK-184	26.38	1.35	26.41	0.1127	1.1619	0.0610
SK-185	26.83	1.35	26.86	0.1108	1.1420	0.0600
SK-186	24.77	1.35	24.80	0.1201	1.2384	0.0651
SK-187	25.51	1.35	25.54	0.1166	1.2021	0.0631
SK-188	30.96	1.35	30.99	0.0956	0.9857	0.0518
SK-189	31.11	1.35	31.14	0.0951	0.9807	0.0515
SK-190	30.30	1.35	30.33	0.0978	1.0078	0.0529
SK-191	30.45	1.35	30.48	0.0973	1.0028	0.0527
SK-192	30.09	1.35	30.12	0.0985	1.0150	0.0533
SK-193	30.22	1.35	30.25	0.0980	1.0105	0.0531
SK-194	30.02	1.35	30.05	0.0987	1.0176	0.0535
SK-195	29.51	1.35	29.54	0.1005	1.0359	0.0544
SK-196	28.09	1.35	28.12	0.1057	1.0897	0.0572
SK-197	30.90	1.35	30.93	0.0958	0.9877	0.0519
SK-198	28.65	1.35	28.68	0.1036	1.0678	0.0561
SK-199	30.69	1.35	30.72	0.0965	0.9947	0.0523
SK-200	29.29	1.35	29.32	0.1013	1.0439	0.0548
SK-201	28.94	1.35	28.97	0.1025	1.0570	0.0555
SK-202	27.29	1.35	27.32	0.1089	1.1222	0.0590
SK-203	29.52	1.35	29.56	0.1004	1.0352	0.0544
SK-204	29.66	1.35	29.69	0.0999	1.0303	0.0541
SK-205	28.47	1.35	28.50	0.1043	1.0748	0.0565
SK-206	27.11	1.35	27.14	0.1096	1.1300	0.0594
SK-207	26.93	1.35	26.97	0.1103	1.1375	0.0597
SK-208	26.99	1.35	27.02	0.1101	1.1351	0.0596
SK-209	26.86	1.35	26.90	0.1106	1.1406	0.0599
SK-210	26.56	1.35	26.60	0.1119	1.1537	0.0606

5.5.2.2 Borehole-Specific Shear wave velocity profiles

Instead of using the idealized shear wave velocity profile obtained in Section 5.4 for all boreholes, one can further modify this profile and obtain a "borehole-specific" shear wave velocity profile to get more realistic results.

In Chapter 4, shear wave velocity parameters (the shear wave velocity at the bedrock; $V_{s,rock}$, the average shear wave velocity at the upper 7 meters; $V_{s,7}$, and the average shear wave velocity at the upper 30 meters; $V_{s,30}$) were assigned to each of the boreholes and summarized in Table 4.9. In this chapter, the obtained shear wave velocity data will serve as a precious tool to adjust the idealized shear wave velocity profile of the region (generated in Section 5.4) to obtain shear wave velocity profile that presents that specific location, which is referred to as "borehole-specific shear wave velocity profiles" in this chapter.

To prepare the location-specific shear wave velocity profiles, first of all, the upper 7 meters are scaled by considering the upper 7 meters of the idealized shear wave velocity profile obtained in Section 5.4; next, by keeping the scaled upper 7 meters unchanged, the remained 23 meters of the idealized shear wave velocity profile are scaled in order to satisfy the $V_{s,30}$ value that is specified for the borehole.

At this point, the upper 30 meters are constructed, the remained profile is either kept the same "but making it smoother" as the idealized shear wave velocity profile obtained in Section 5.4 with a maximum shear wave velocity value of 3377 m/s at 145 m or scaled depending on the assigned $V_{s,rock}$ For the borehole in chapter 3. In other words, if the bedrock shear wave velocity assigned for the borehole is greater than 3377 m/s then the idealized shear wave velocity profile underneath 30 meters is scaled so the assigned average $V_{s,rock}$ for the borehole is satisfied. Figure 5.20 compares the idealized shear wave velocity profile and the obtained profile for two of the borehole (SK-1 and SK-20).

To better explain how "borehole-specific shear wave velocity profiles" are obtained in detail, the used code script for this purpose is presented in Figure 5.21.

Depth m	Vs m/s			
	SK-20	SK-1	Idealized	
0	244	294	203	2301
1.9	244	294	203	
1.9	358	432	298	
4.3	358	432	298	
4.3	431	520	359	
7.2	431	520	359	
7.2	1383	797	267	
10.9	1383	797	267	
10.9	2388	1376	461	
15.6	2388	1376	461	
15.6	2808	1617	542	
21.4	2808	1617	542	
21.4	3264	1880	630	
28.6	3264	1880	630	
28.6	3704	2134	715	
32	3704	2134	715	
32	3879	2309	720	2308
46	3879	2309	720	
46	4054	2484	757	
61	4054	2484	757	
61	4229	2659	846	
79	4229	2659	846	
79	4404	2834	1276	
83	4404	2834	1276	
83	4579	3009	1575	2305
89	4579	3009	1575	
89	4754	3184	1927	
116	4754	3184	1927	
116	4929	3377	3377	
145	4929	3377	3377	

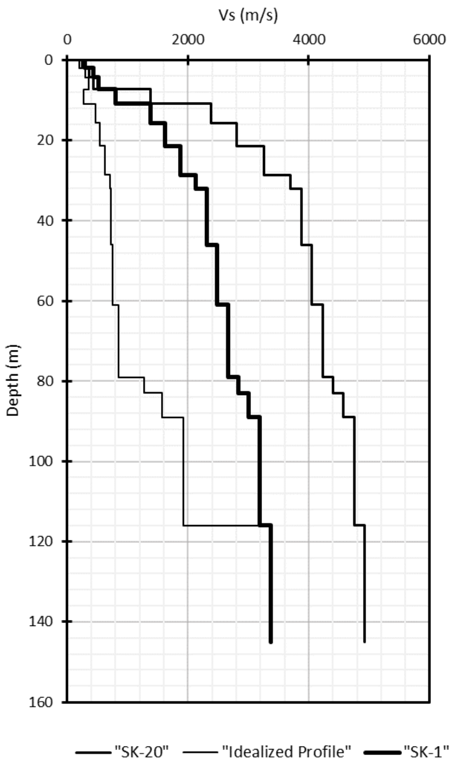

For SK-1:

$V_{s,7} = 330\ ms/s$

$V_{s,30} = 983\ ms/s$

$V_{s,rock} = 2471\ ms/s$

For SK-20:

$V_{s,7} = 398\ ms/s$

$V_{s,30} = 889\ ms/s$

$V_{s,rock} = 889\ ms/s$

For the idealized profile:

$V_{s,7} = 274.6\ ms/s$

$V_{s,30} = 407\ ms/s$

Figure 5.18. Comparison of the idealized shear wave velocity profile and the obtained profile for two boreholes (SK-1 and SK-20)

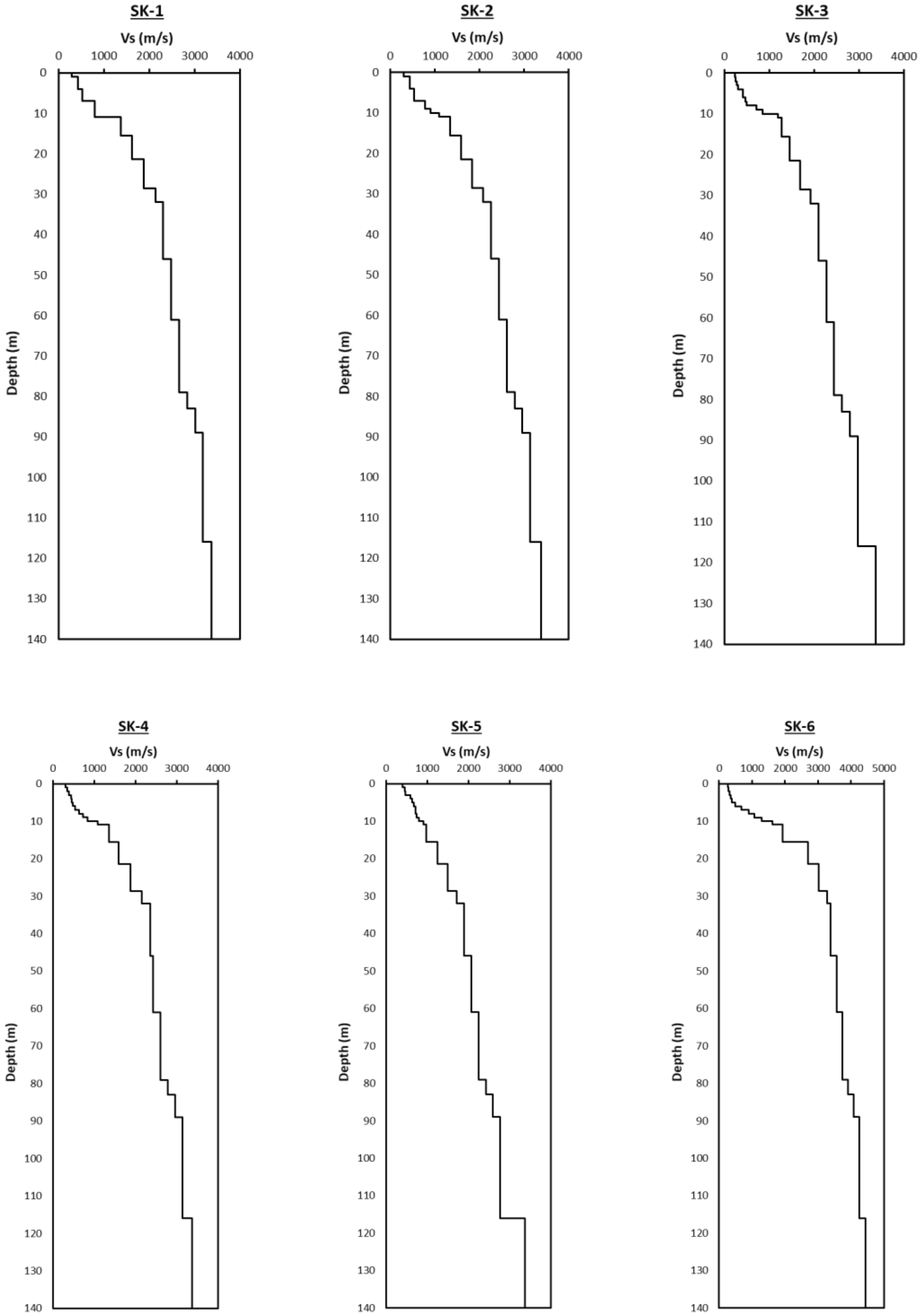

Figure 5.19. Full depth shear wave velocity profiles (SK-1 through SK-6)

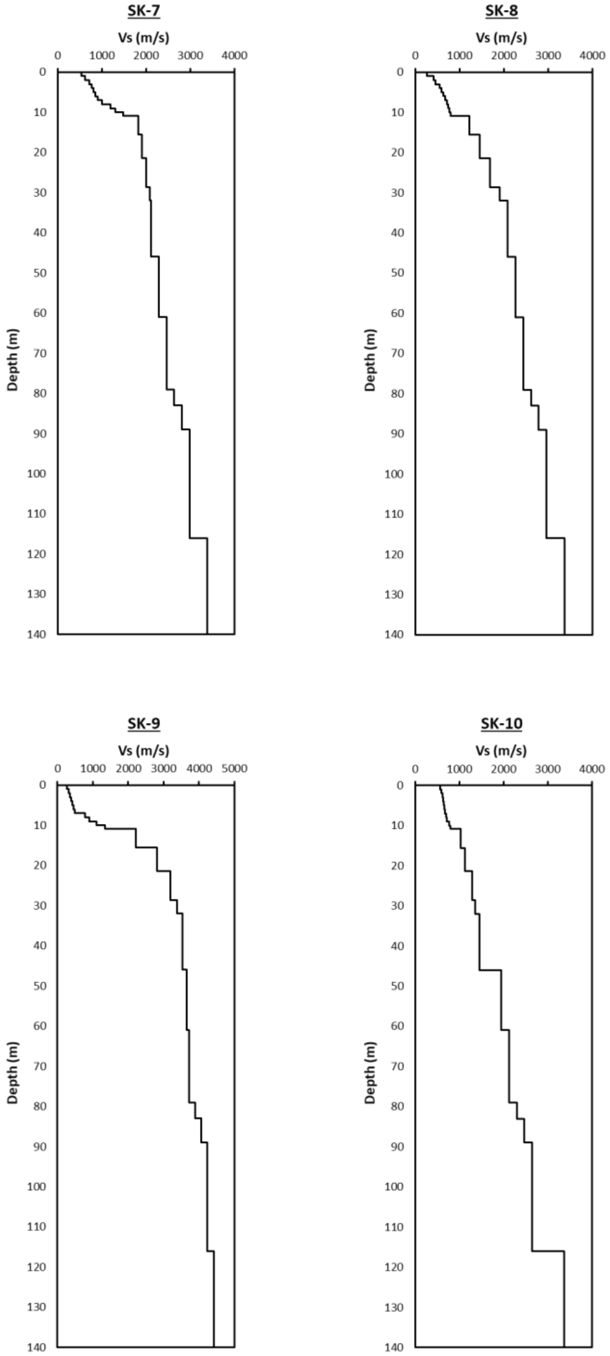

Figure 5.20. Full depth shear wave velocity profiles (SK-7 through SK-10)

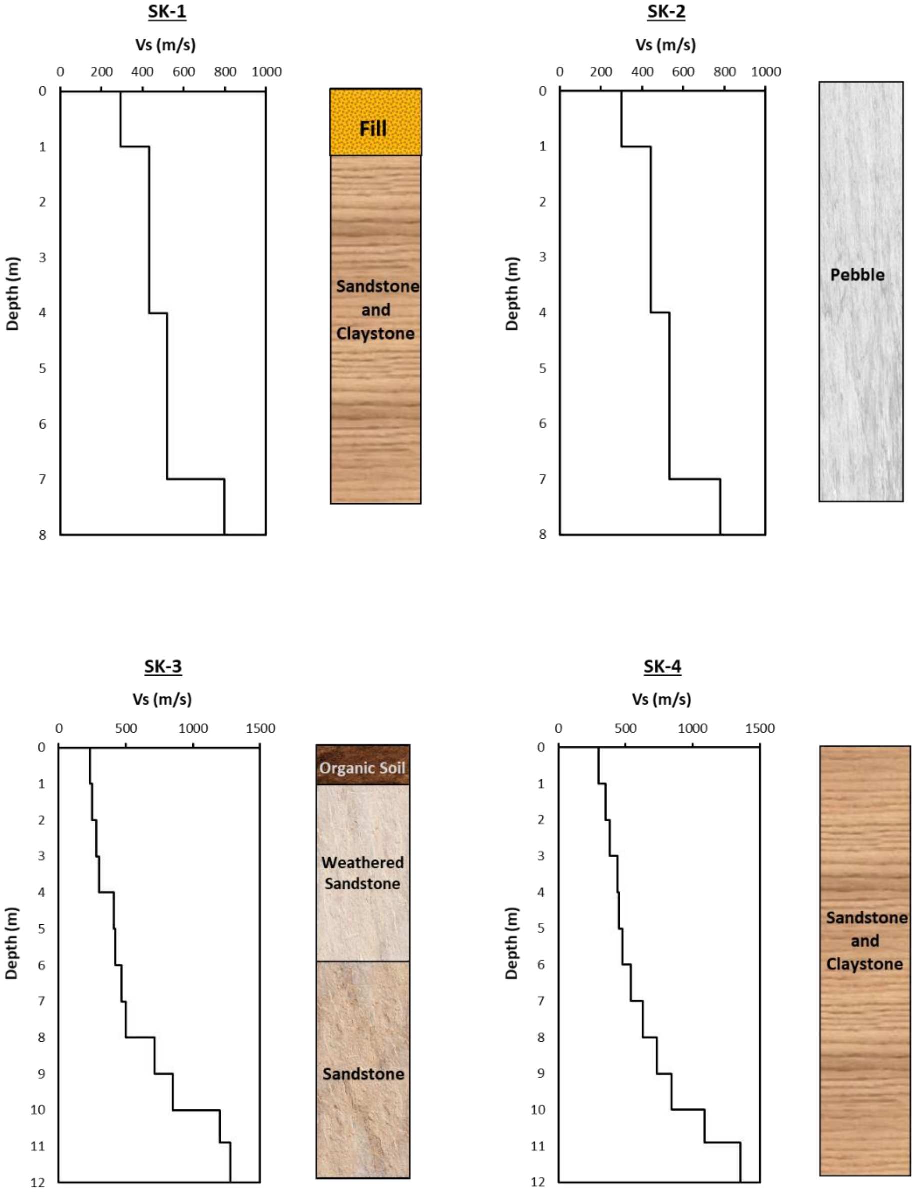

Figure 5.21. Shallow soil and shear wave velocity profiles (SK-1 through SK-4)

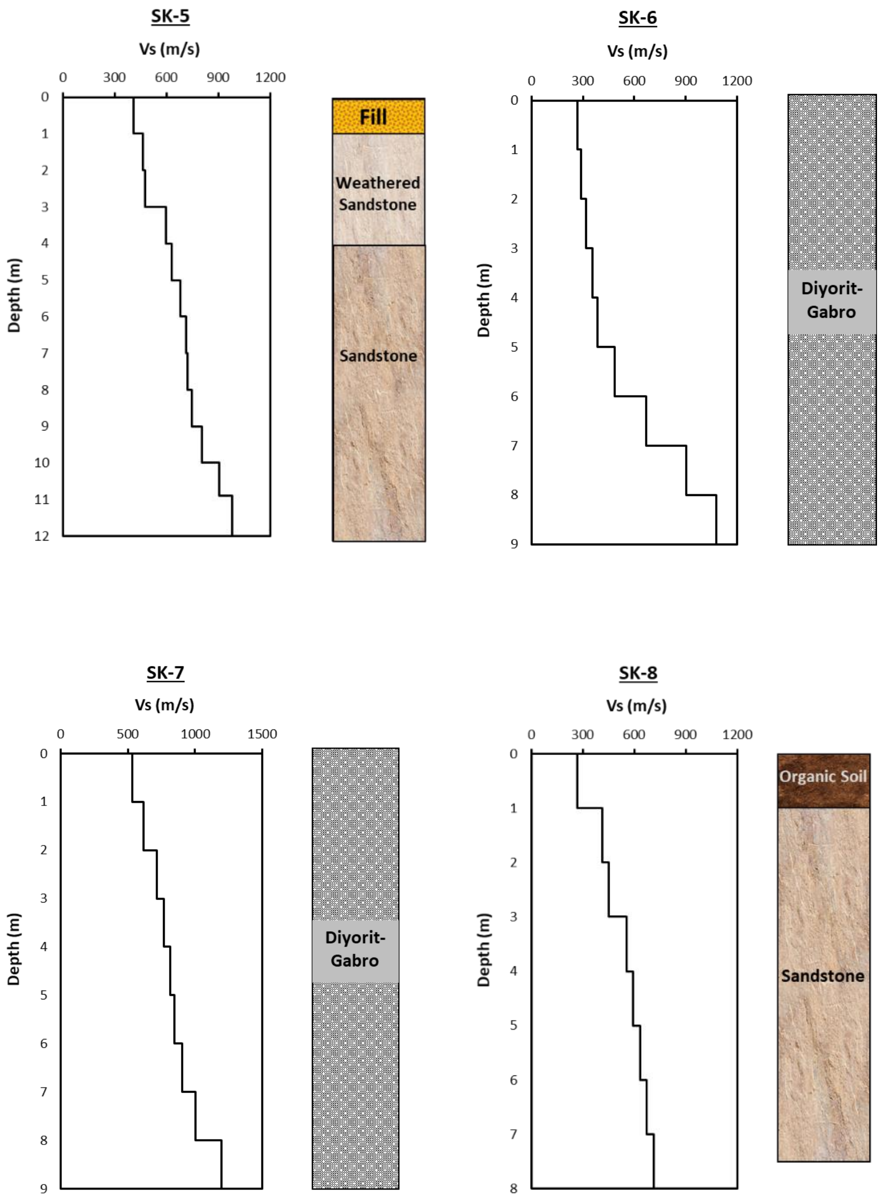

Figure 5.22. Shallow soil and shear wave velocity profiles (SK-5 through SK-8)

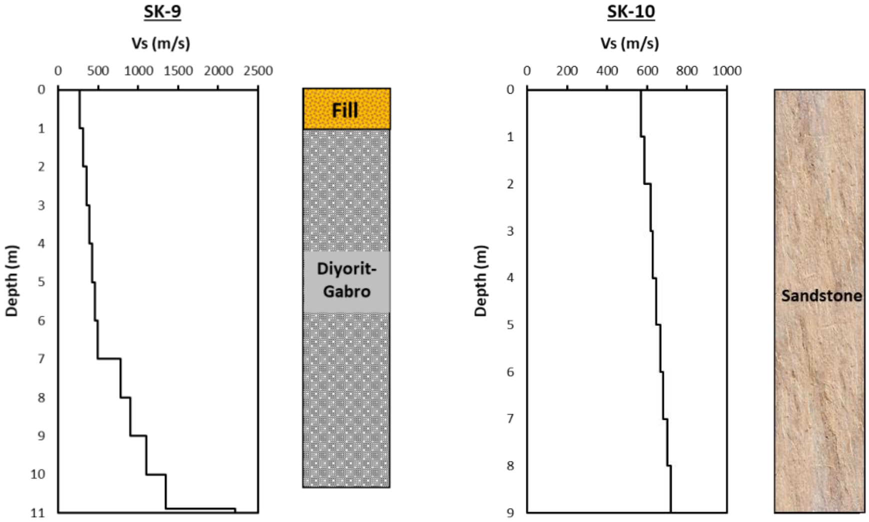

Figure 5.23. Shallow soil and shear wave velocity profiles (SK-9 and SK-10)

5.5.3 Seismic Site Response (Convolution)

Deepsoil software with Equivalent linear approach in the frequency domain is used. The steps followed in section 5.5.1 are repeated for each borehole using the borehole specific time history and shear wave velocity profiles.

As an output, the Acceleration Time History at the ground surface is obtained along with the spectral plot. For illustration purposes, results from three different boreholes are provided in Figure 5.24, Figure 5.25, and Figure 5.26. The spectral plots for all the boreholes are provided from Figure 5.27 to Figure 5.40.

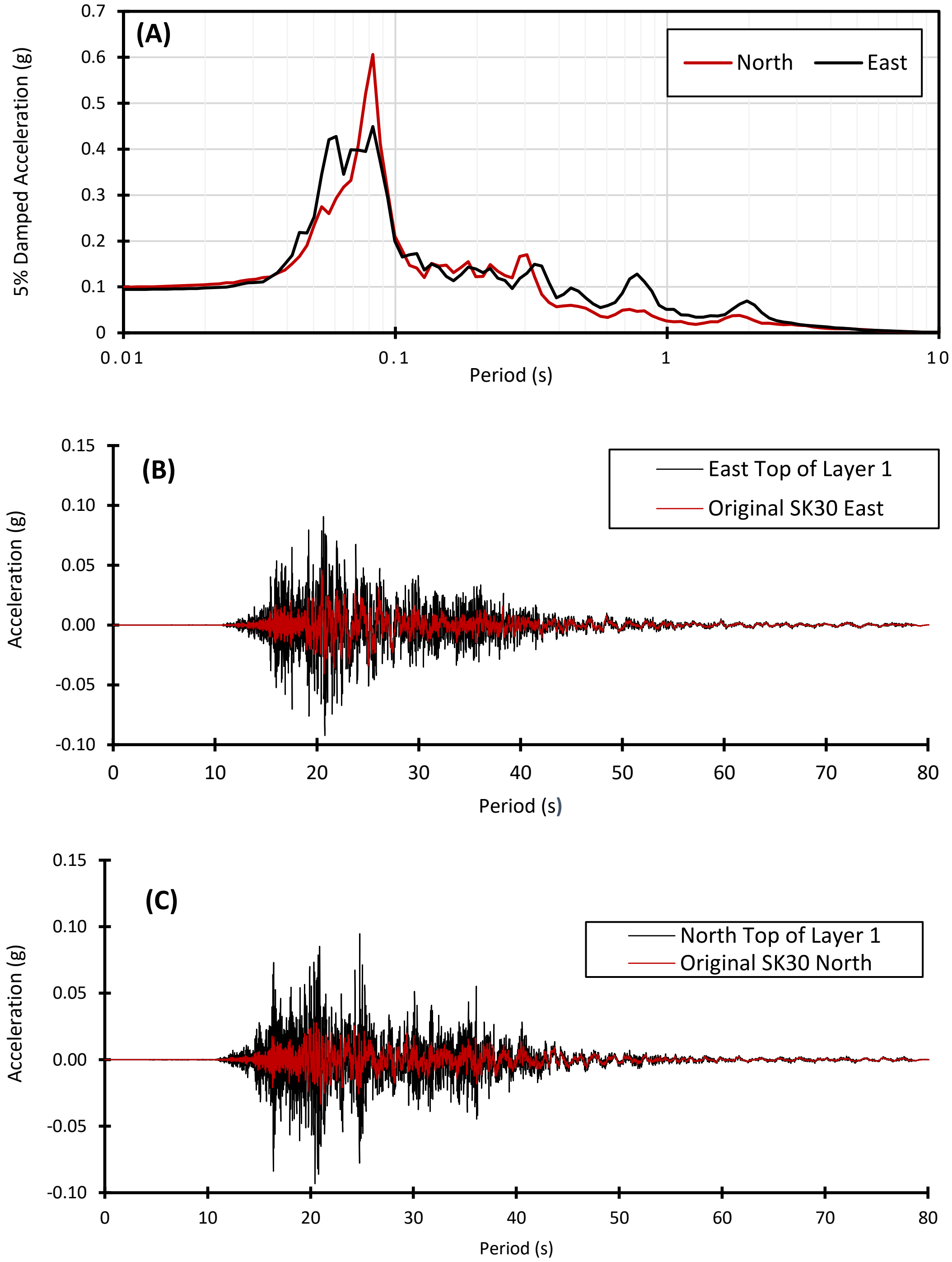

Figure 5.24. (a) the east (b) the north components of the acceleration time history and the spectral plots of SK-30

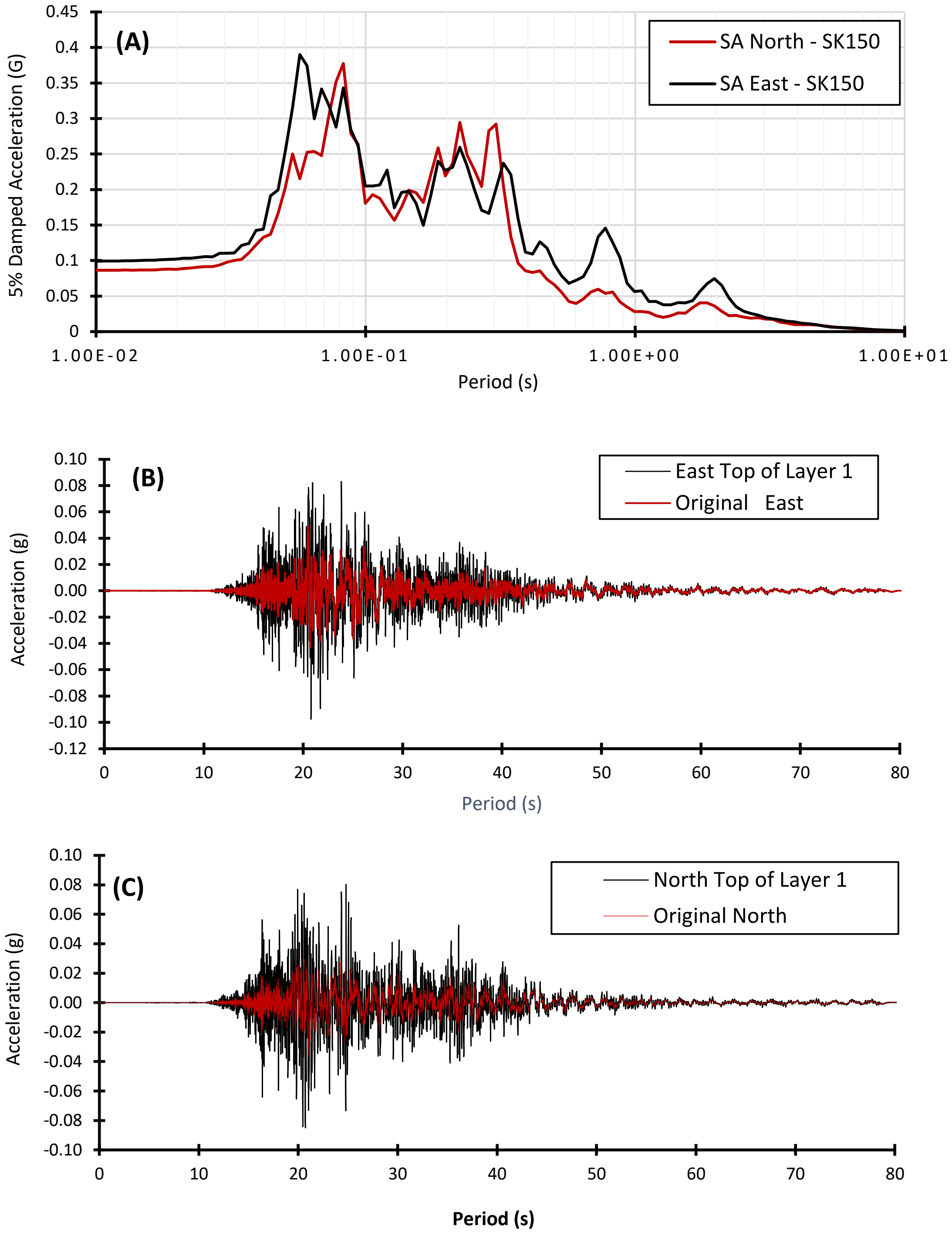

Figure 5.25. (a) the east (b) the north components of the acceleration time history and the spectral plots of SK-150

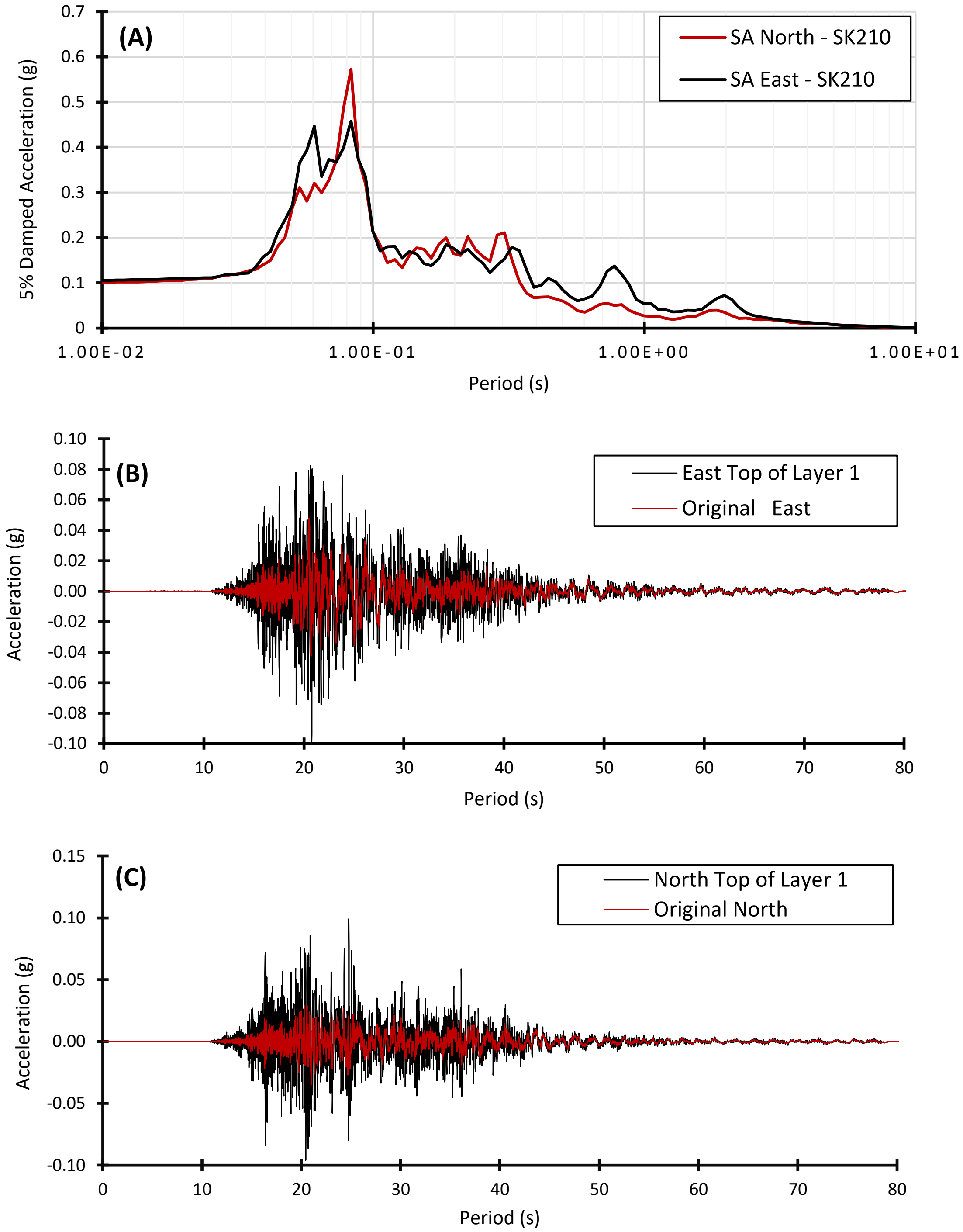

Figure 5.26. (a) the east (b) the north components of the acceleration time history and the spectral plots of SK-210

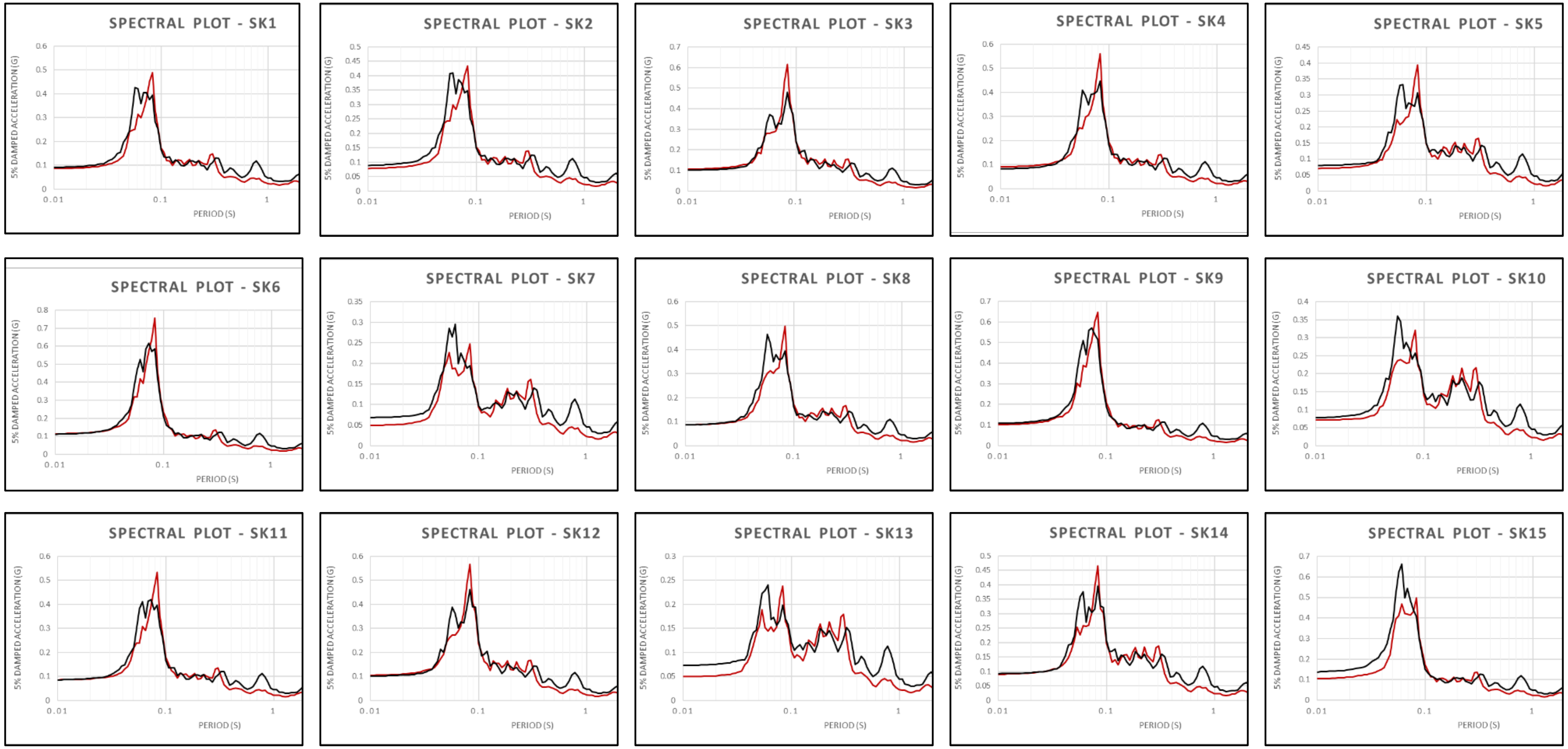

Figure 5.27. Spectral Acceleration SA charts of SK-1 to SK-15 (5% Damped acceleration (g) vs. Period (s))

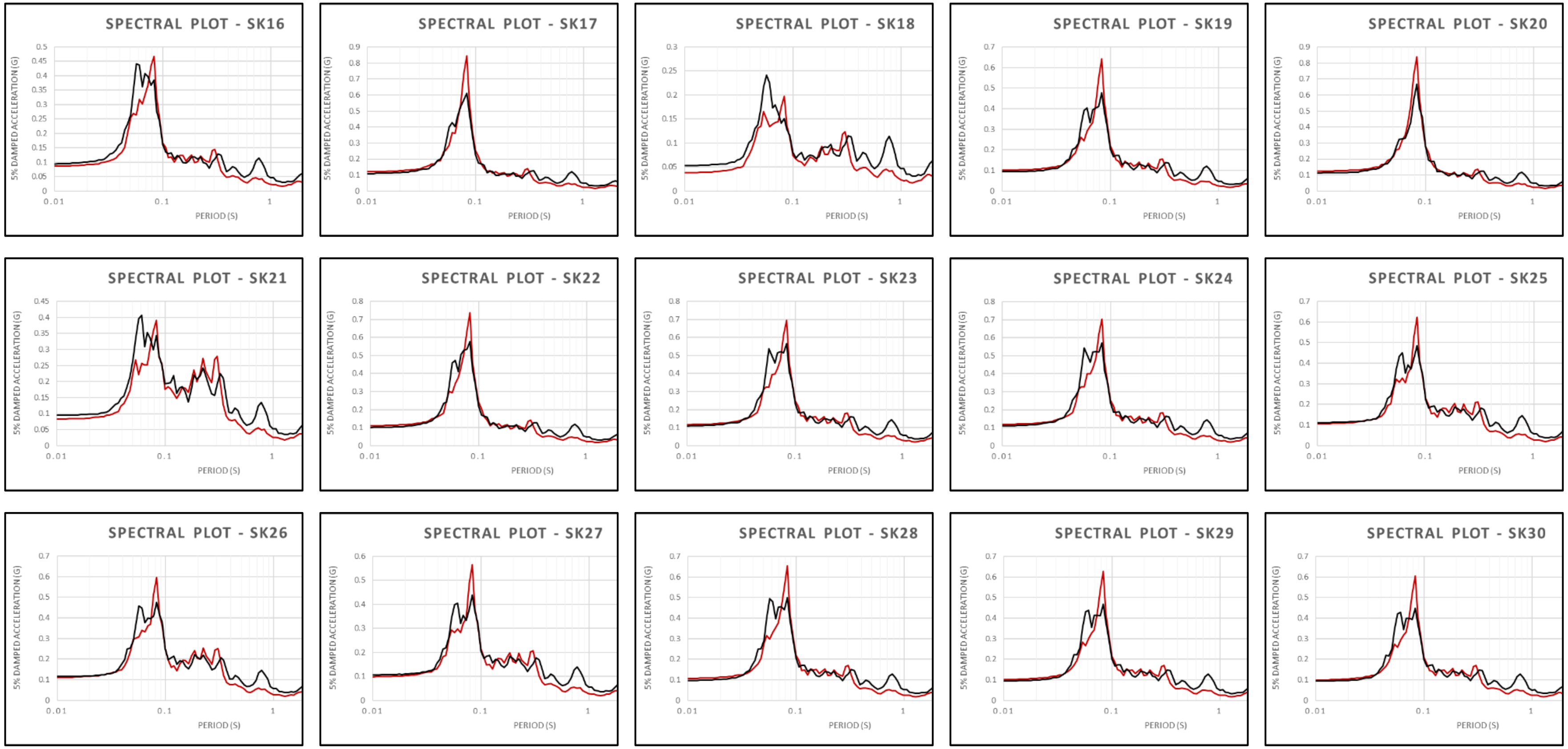

Figure 5.28. Spectral Acceleration SA charts of SK-16 to SK-30 (5% Damped acceleration (g) vs. Period (s))

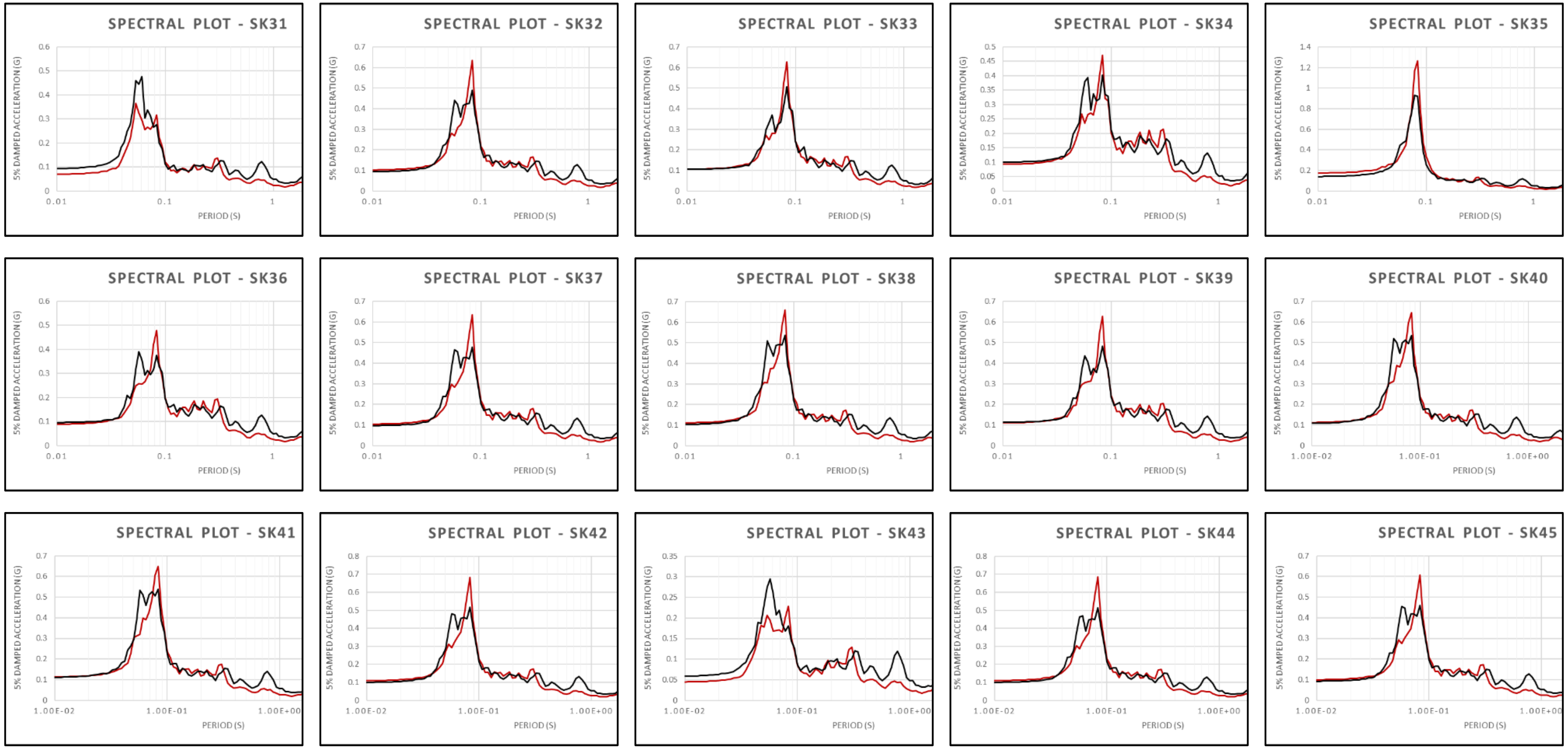

Figure 5.29. Spectral Acceleration SA charts of SK-31 to SK-45 (5% Damped acceleration (g) vs. Period (s))

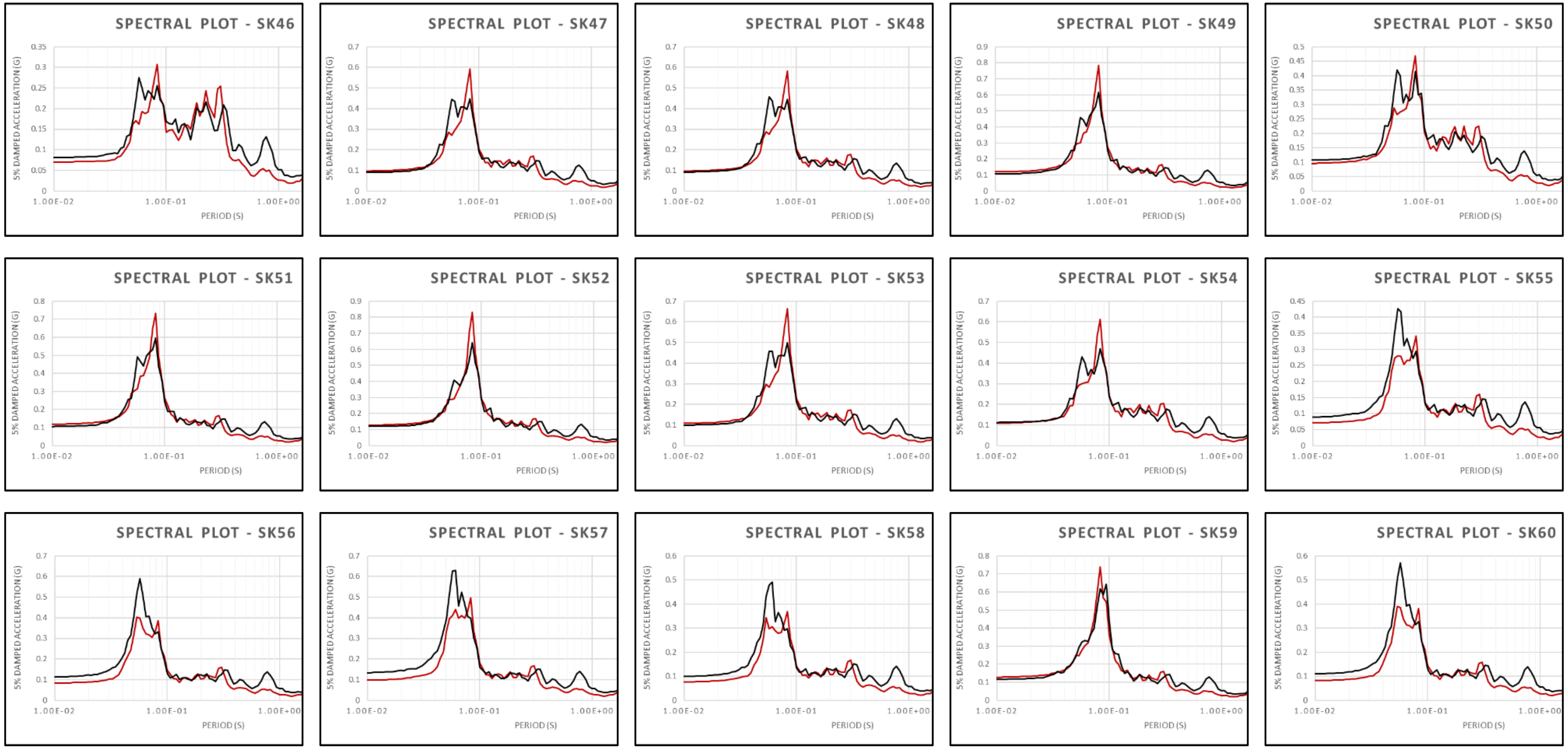

Figure 5.30. Spectral Acceleration SA charts of SK-46 to SK-60 (5% Damped acceleration (g) vs. Period (s))

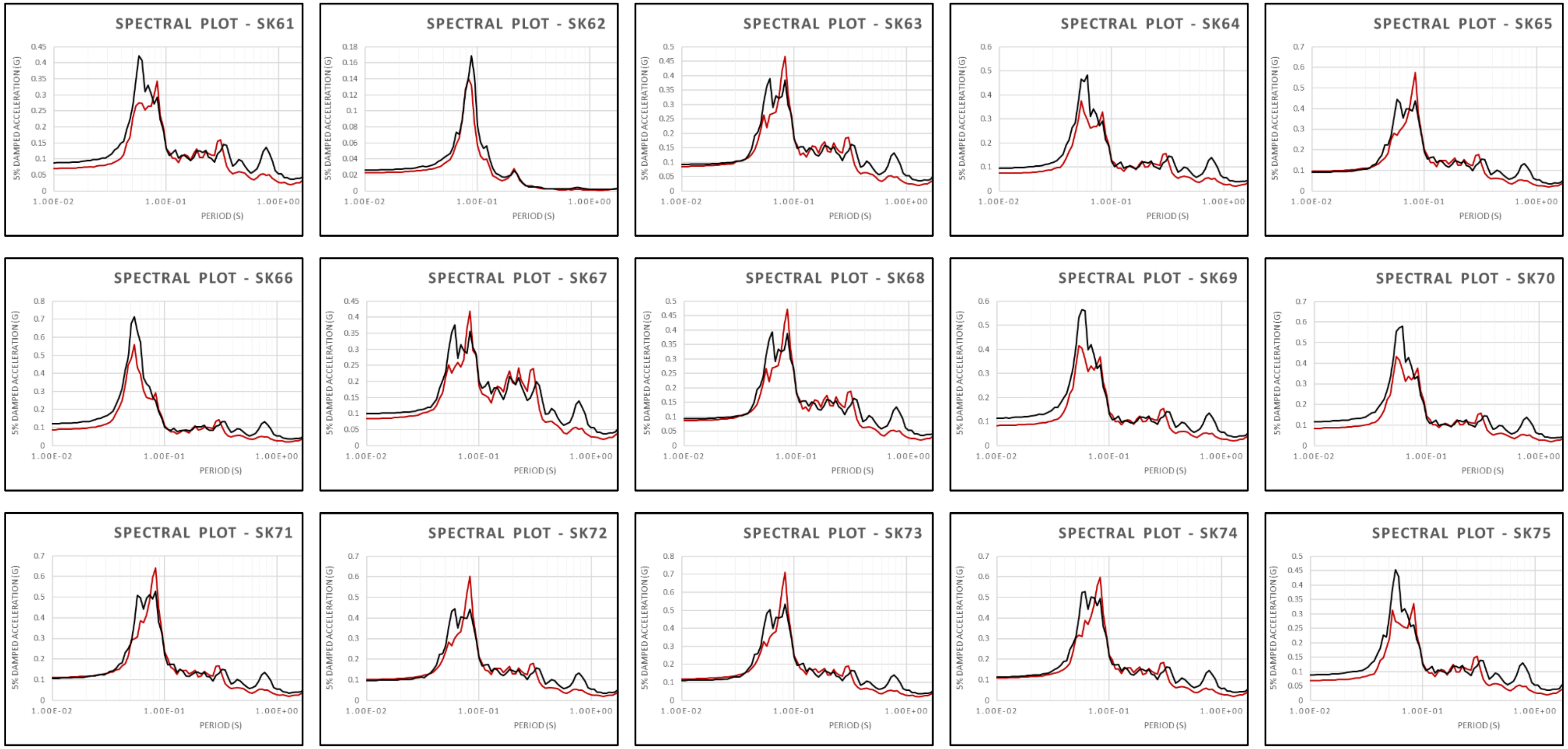

Figure 5.31. Spectral Acceleration SA charts of SK-61 to SK-75 (5% Damped acceleration (g) vs. Period (s))

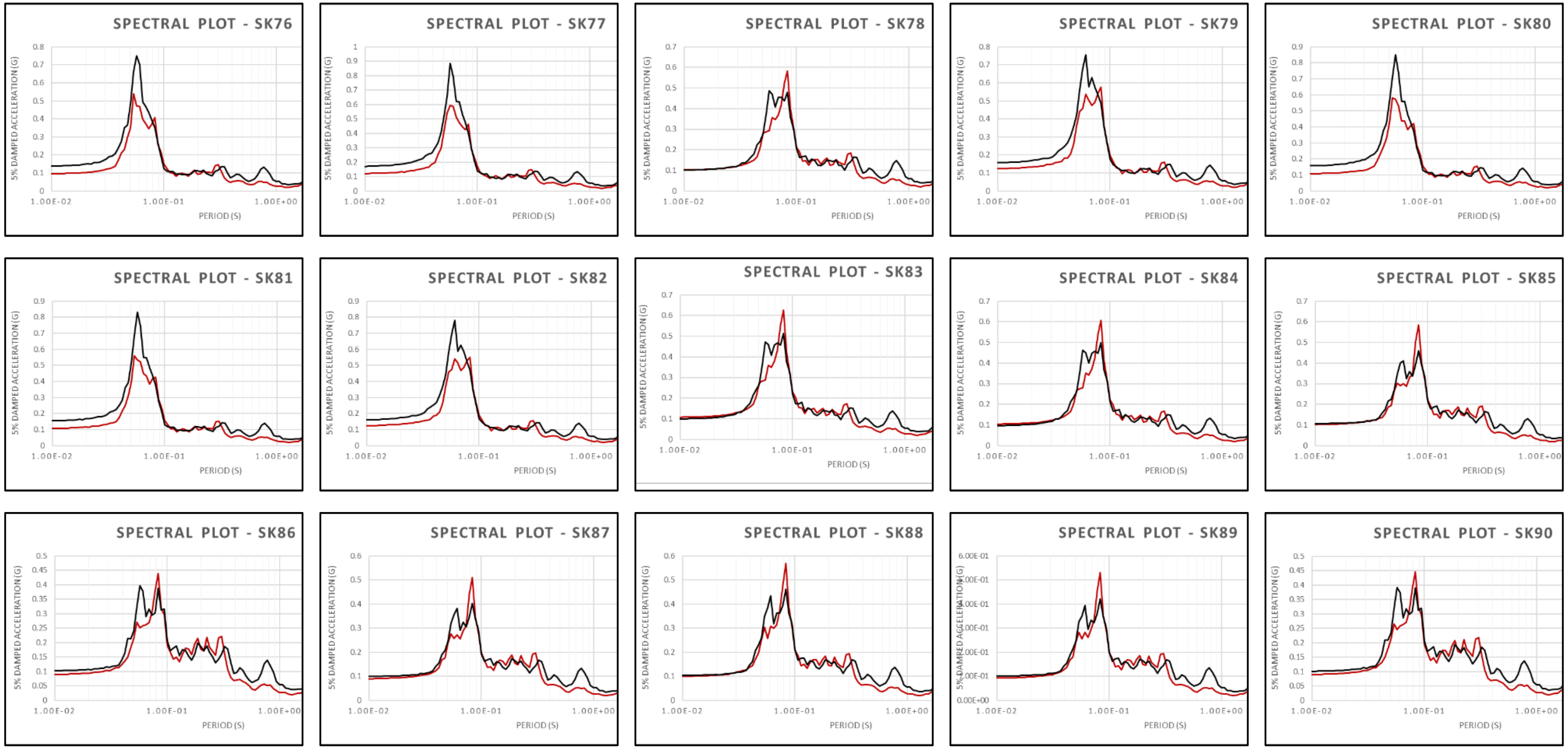

Figure 5.32. Spectral Acceleration SA charts of SK-76 to SK-90 (5% Damped acceleration (g) vs. Period (s))

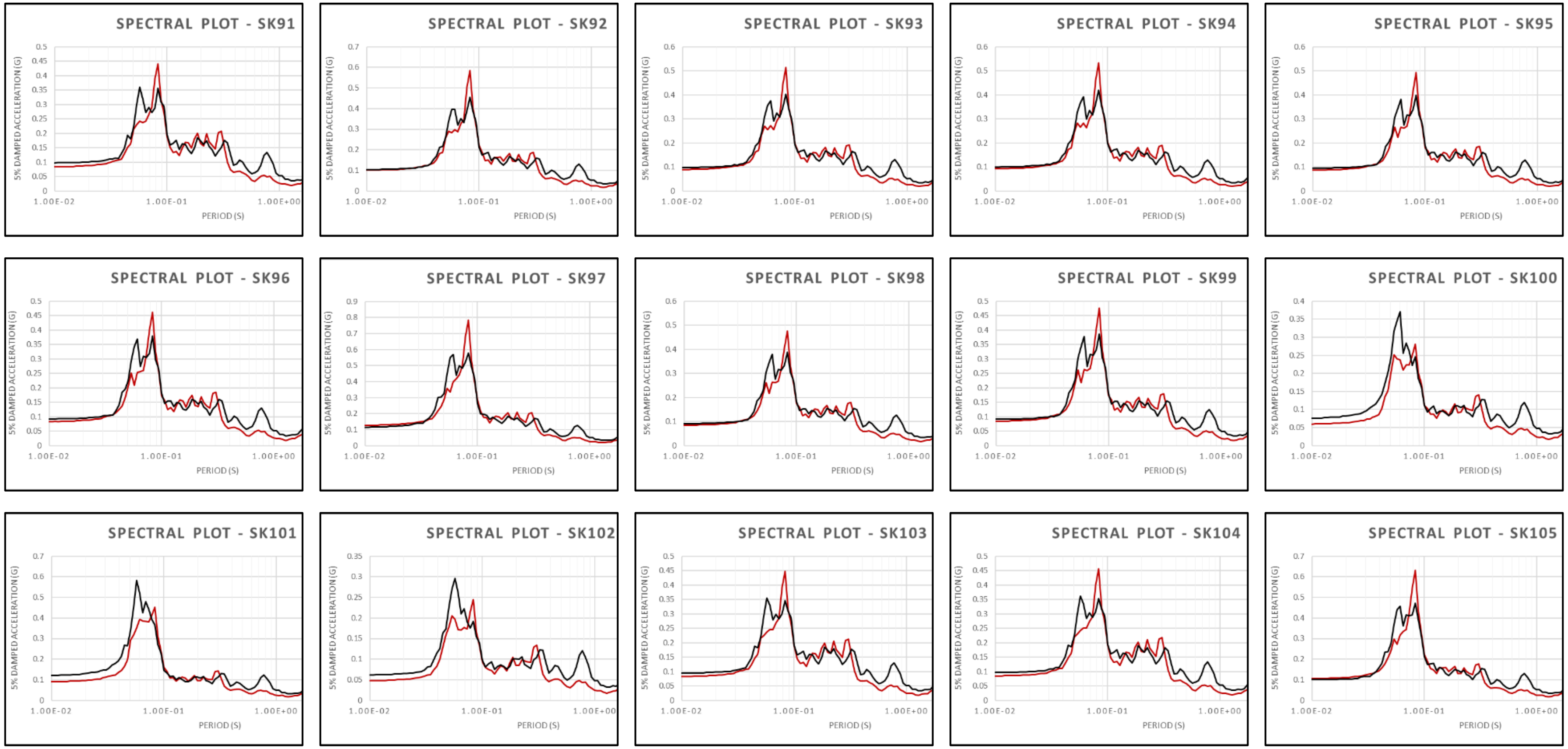

Figure 5.33. Spectral Acceleration SA charts of SK-91 to SK-105 (5% Damped acceleration (g) vs. Period (s))

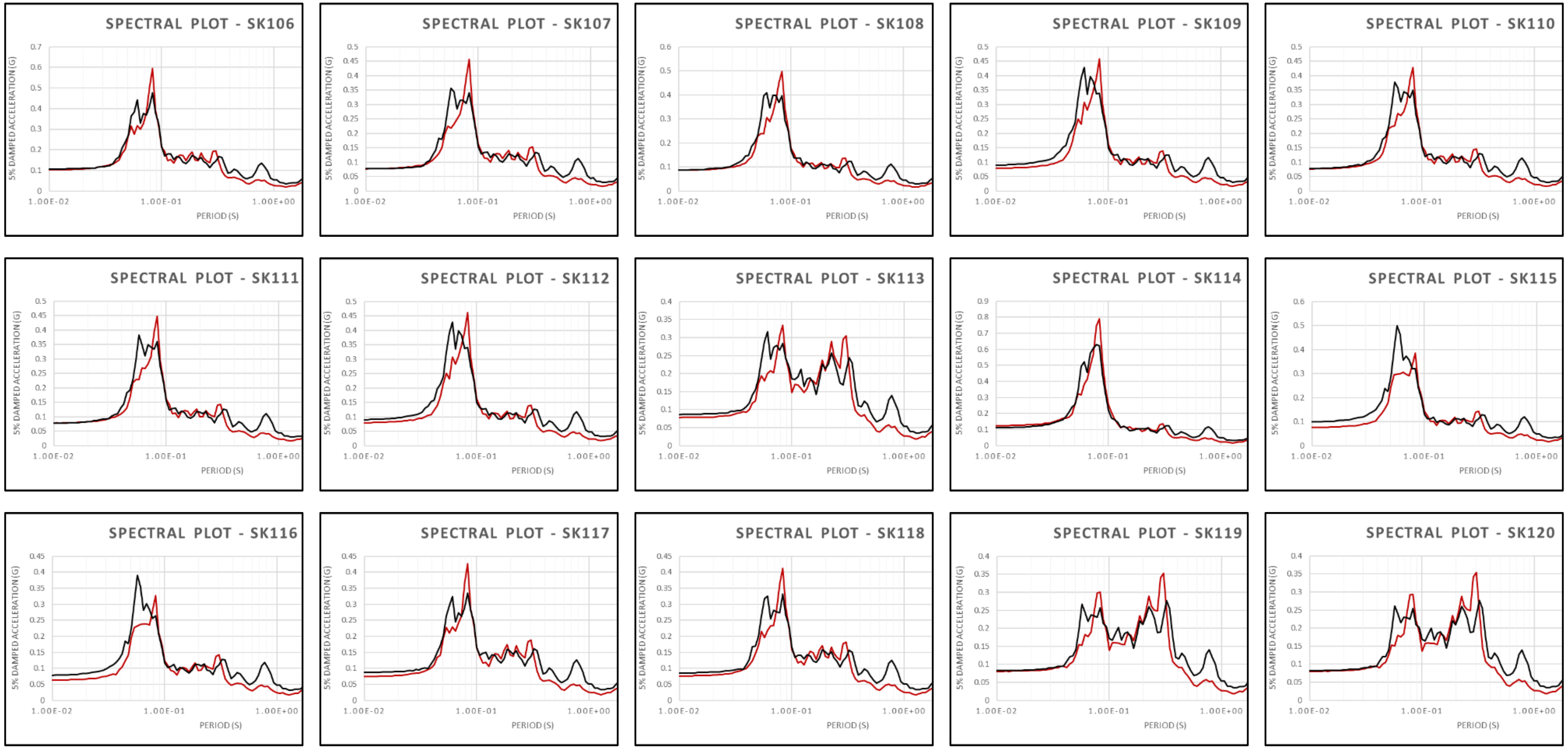

Figure 5.34. Spectral Acceleration SA charts of SK-106 to SK-120 (5% Damped acceleration (g) vs. Period (s))

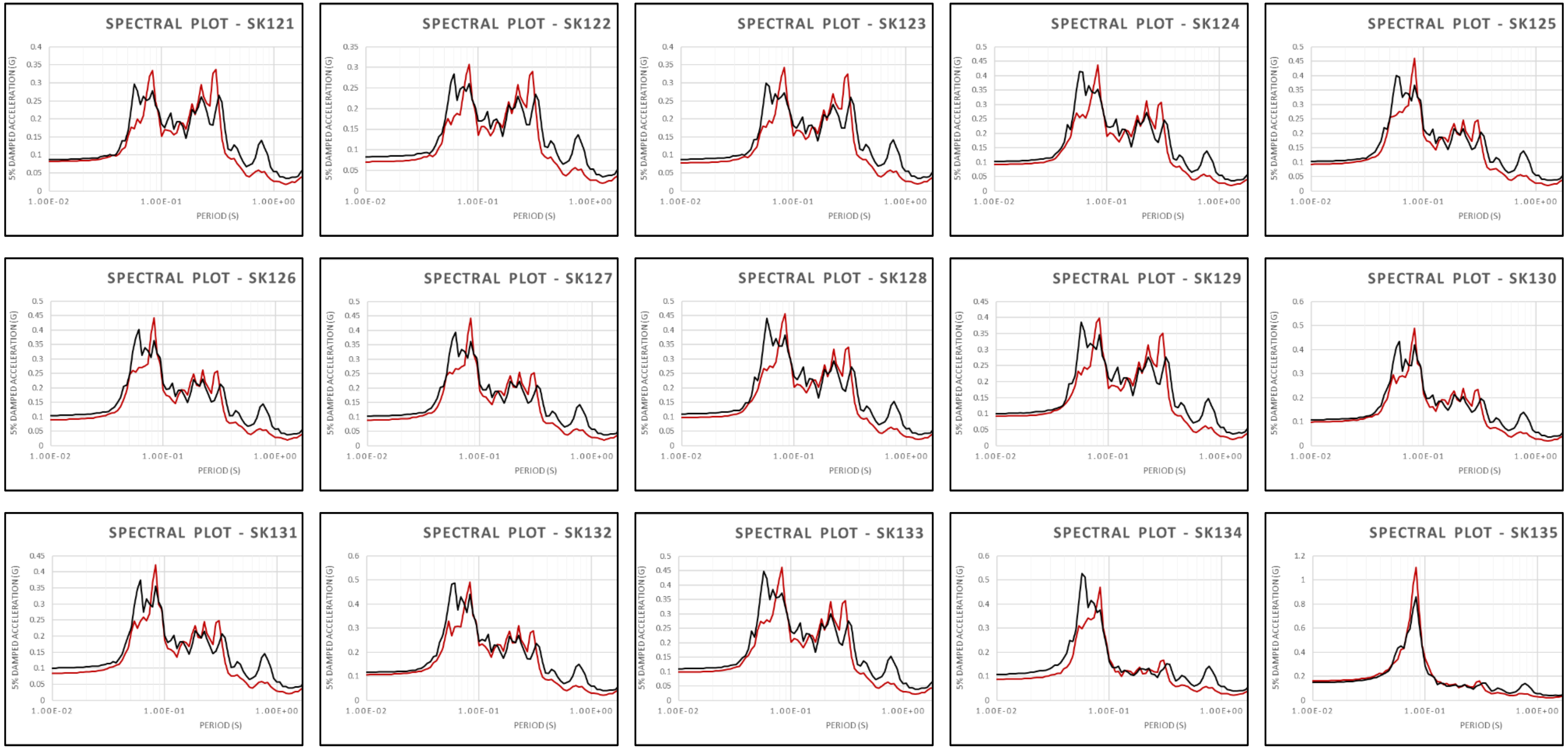

Figure 5.35. Spectral Acceleration SA charts of SK-121 to SK-135 (5% Damped acceleration (g) vs. Period (s))

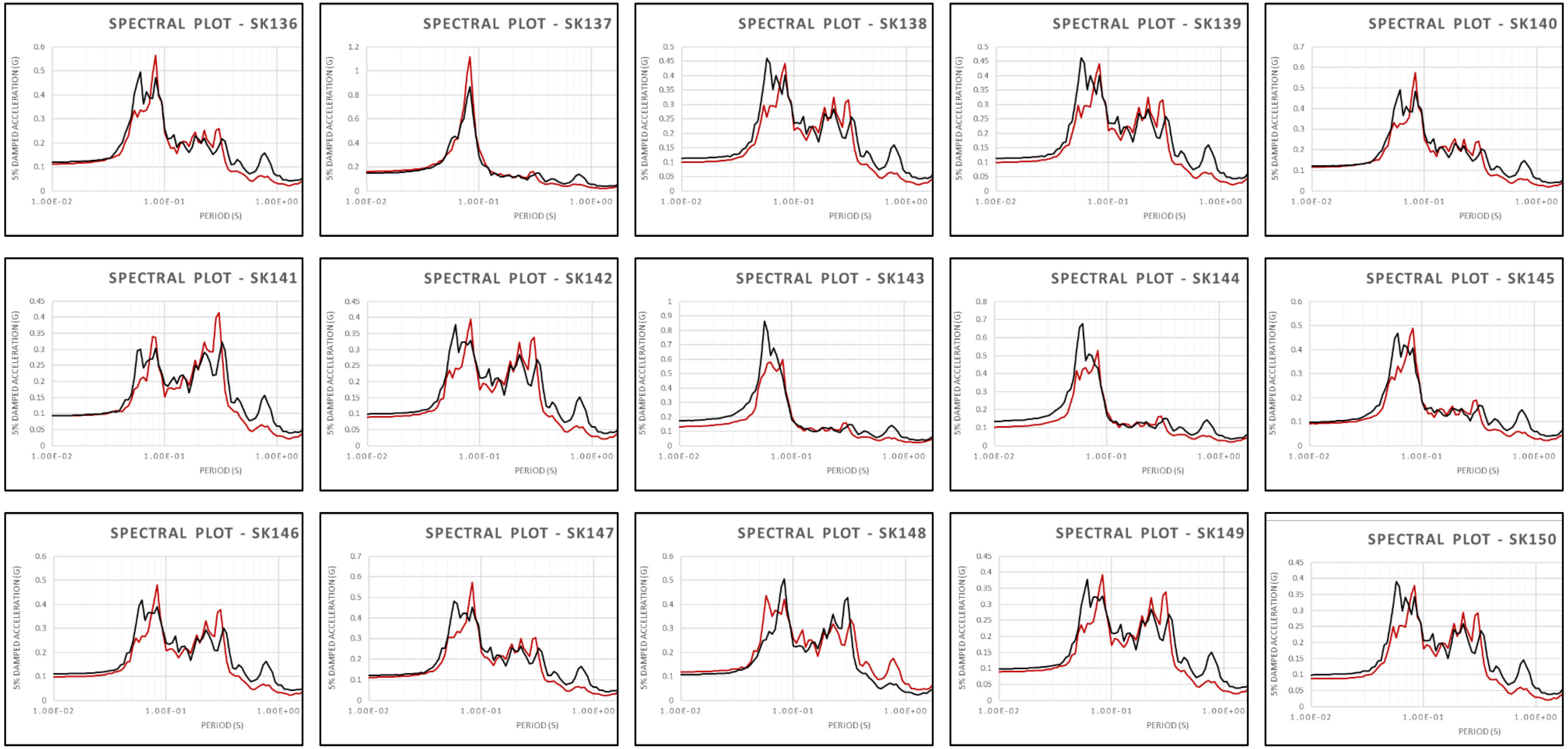

Figure 5.36. Spectral Acceleration SA charts of SK-136 to SK-150 (5% Damped acceleration (g) vs. Period (s))

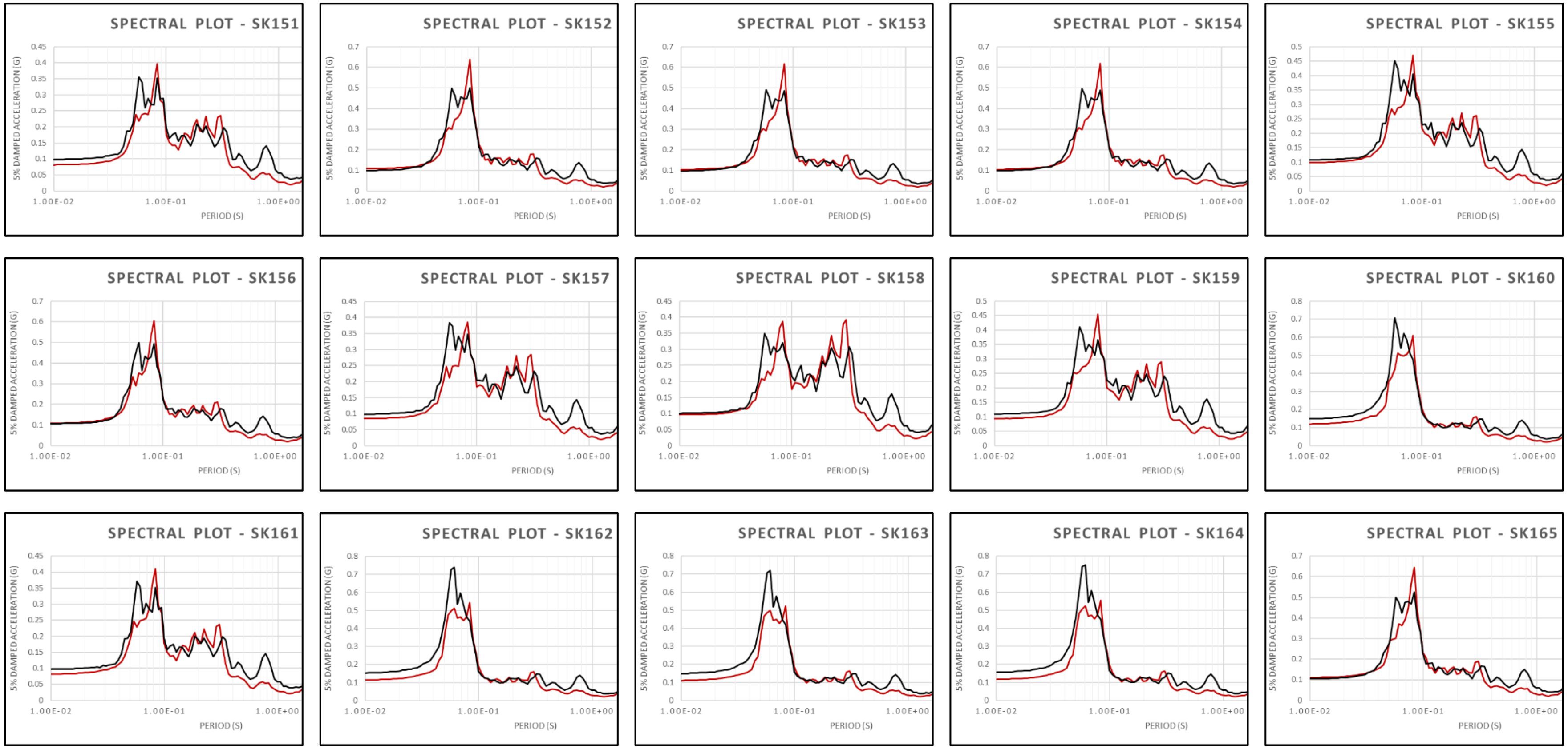

Figure 5.37. Spectral Acceleration SA charts of SK-151 to SK-165 (5% Damped acceleration (g) vs. Period (s))

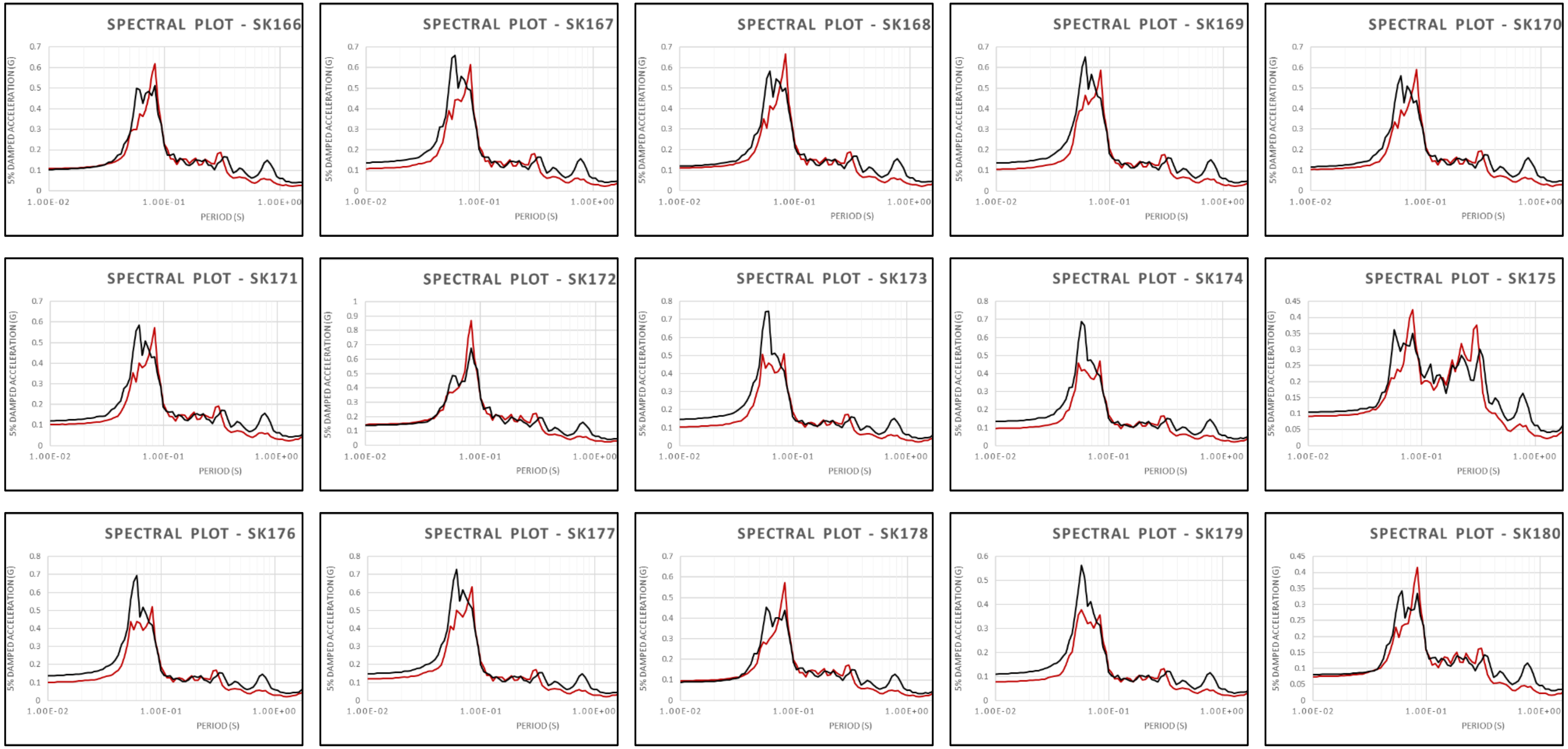

Figure 5.38. Spectral Acceleration SA charts of SK-166 to SK-180 (5% Damped acceleration (g) vs. Period (s))

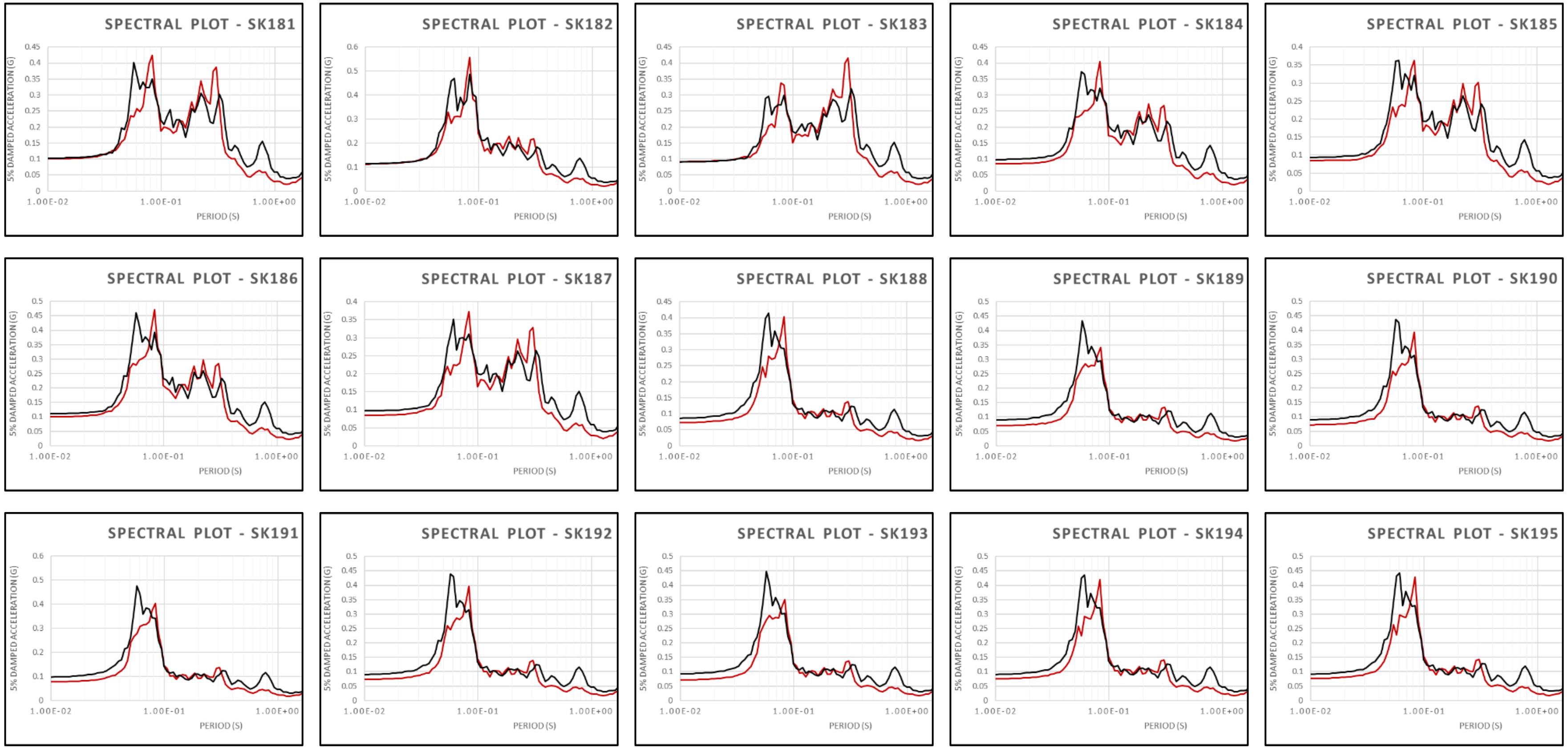

Figure 5.39. Spectral Acceleration SA charts of SK-181 to SK-195 (5% Damped acceleration (g) vs. Period (s))

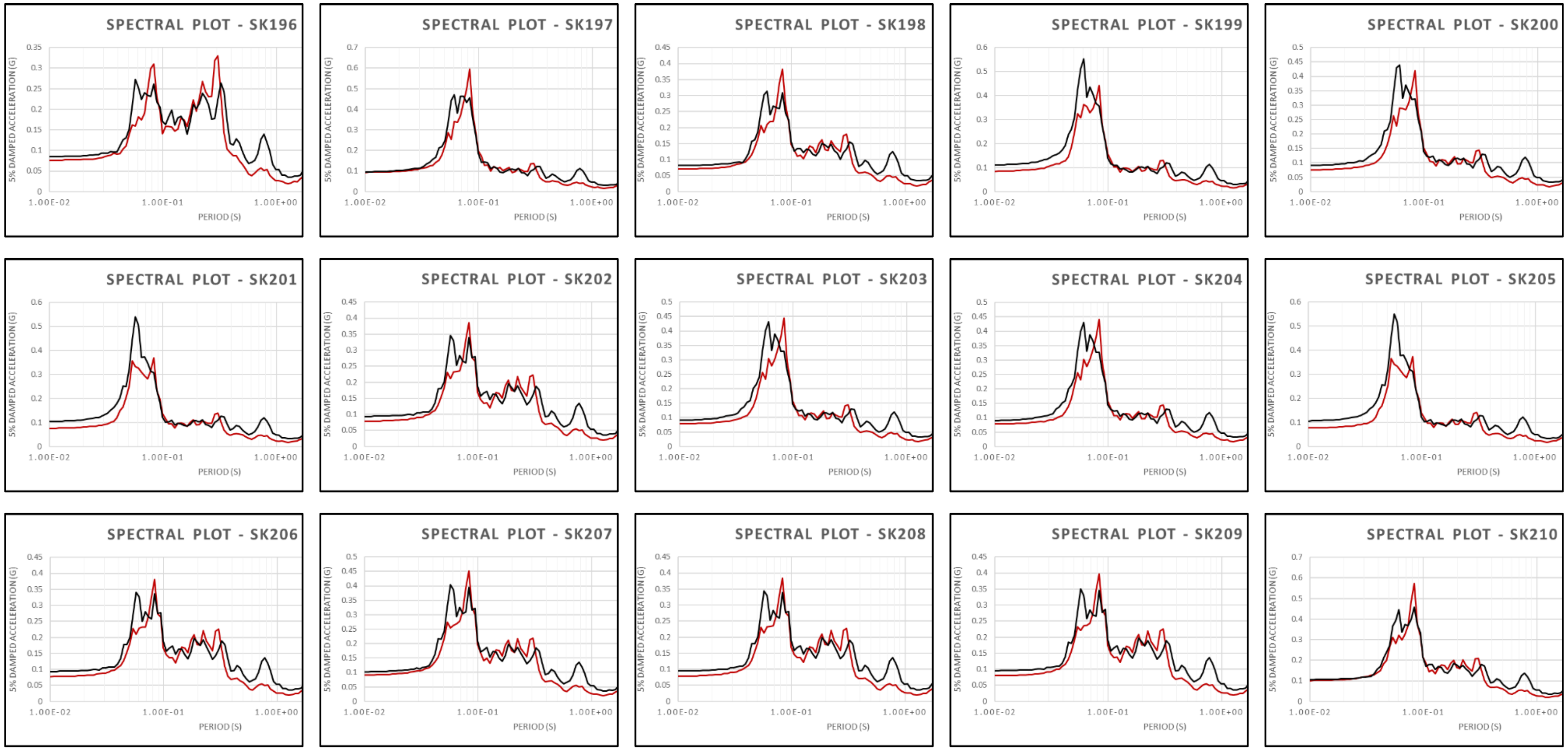

Figure 5.40. Spectral Acceleration SA charts of SK-196 to SK-210 (5% Damped acceleration (g) vs. Period (s))

CHAPTER 6

LIQUEFACTION ASSESSMENT

6.1 Introduction

During earthquakes, one of the geo-phenomenon that may result in structural damage is soil liquefaction, a process in which soil transforms into a "viscous liquid" and lose their strength. Cetin et al. (2020) traveled to Elazig in search of liquefied soil areas just after the occurrence of the earthquake. Along the boundaries of Lake Hazar, a range of surface indicators of seismic-induced soil liquefaction have been documented, including water boils, excessive settlement, and lateral spreading deformations (outside the borders of the region included in this study). Cetin et al. (2020) noted that no evidence of these surface manifestations was found in any of the other possibly liquefiable alluvial sites evaluated; in other words, a limited number of locations and soil strata may be liquefiable. However, none were affected by this incident.

This chapter will cover liquefaction susceptibility and triggering assessments utilizing the seismic findings after the 2020 Elazig-Sivrice earthquake. In the first part of this chapter, all available boreholes will be examined to find potentially liquefiable soils. Following that, a liquefaction assessment will be carried out adopting the Cetin et al. 2004 assessment method.

Cetin et al. (2018) explained the procedures for liquefaction triggering assessments in a detailed manner. They provided a recommended flowchart for Liquefaction triggering assessments which will be followed to perform the analyses in this chapter. The flowchart of Cetin et al. (2018) is provided in Figure 6.1.

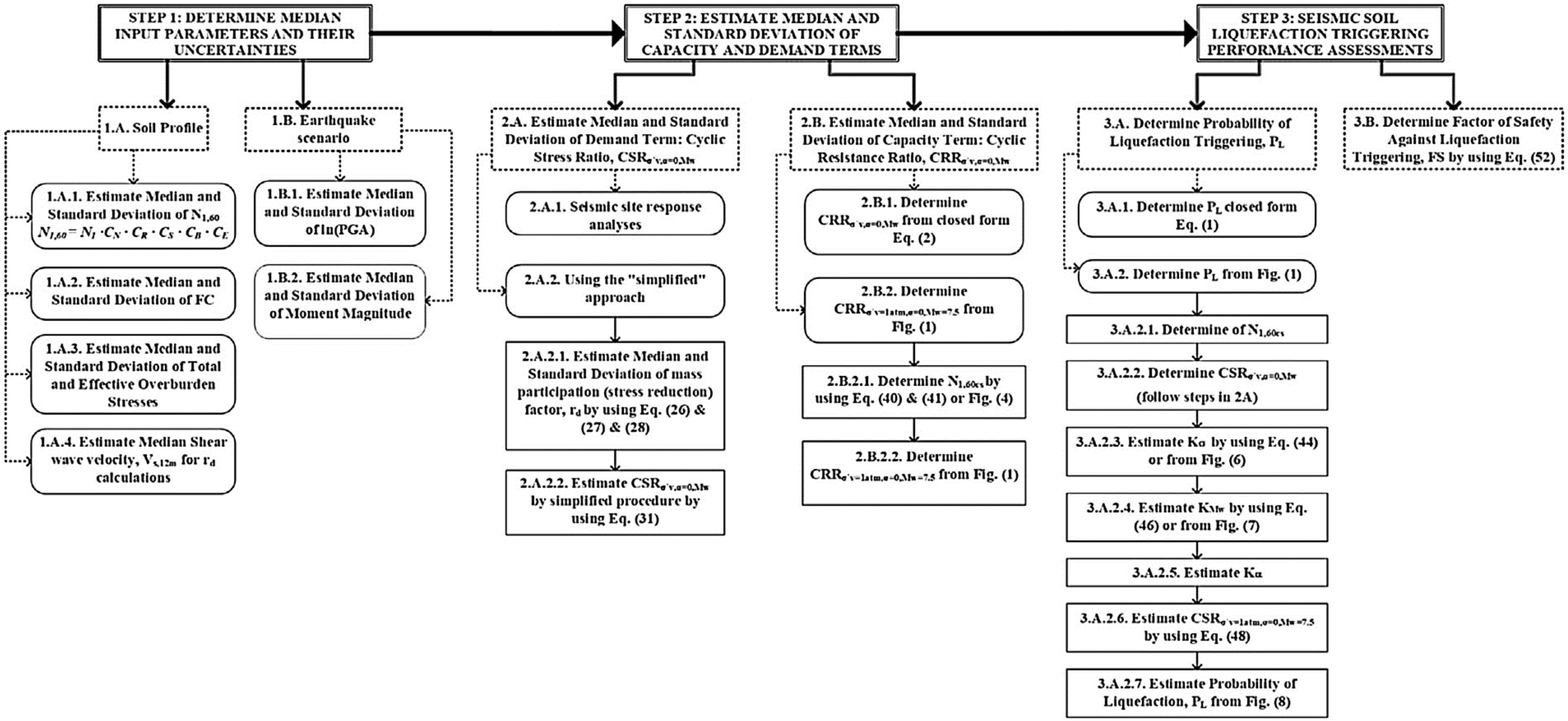

Figure 6.1. Recommended use of the proposed Cetin et al. liquefaction triggering assessment methodology (Cetin et al., 2018)

6.2 Identifying Potentially Liquefiable Boreholes

For the purpose of conducting liquefaction triggering analysis, local borelogs from Elazig – center's local site research database catalogs were used (borrowed from Akare Planlama, 2015). The purpose of this section is to identify boreholes that contain cohesionless soil layers underneath the water table level with relatively low SPT blow counts.

Although a total of 210 borehole samples were investigated looking for potentially liquefiable soils, there were "fortunately" only limited numbers of boreholes that meet the criteria for liquefaction initiation. That is because, within the geological setting, Elazig-center's plastic-cohesive soil layers are the dominant feature. To clarify, the consistency limit chart is plotted and provided in Figure 6.1

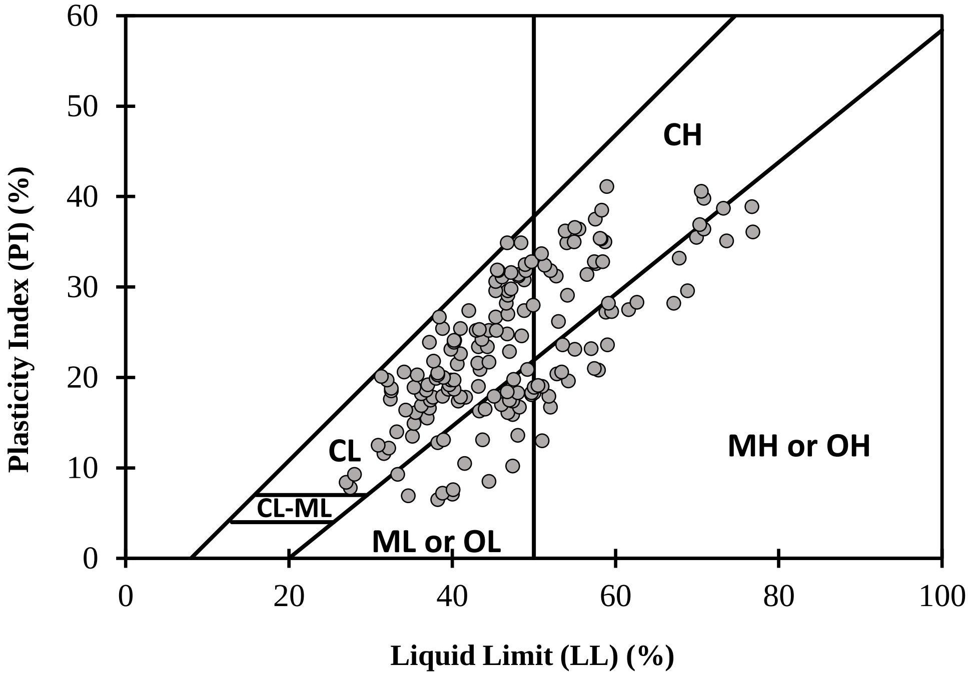

Figure 6.2. Plasticity chart of soils from Elazig-Center (ASTM D2487-17e1)

Seed et al. (2003) liquefaction susceptibility chart is used to identify the potentially liquefiable soils. First, dry boreholes located above the groundwater table level are eliminated. Next, all remaining data is plotted on Seed et al.'s liquefaction susceptibility chart (2003) provided in Figure 6.3, and boreholes located outside Zone A (the region highlighted in blue in Figure 6.3) and outside Zone B (the region highlighted in red in Figure 6.3) are eliminated.

At this point, only three boreholes remain in Zone B, namely, SK-83, SK-88, and SK-73 (provided as green circles in Figure 6.3) and seven nonplastic boreholes, namely, SK-138, SK-141, SK-142, SK-148, SK-161, SK-171, and SK-172 (provided as yellow circles in Figure 6.3).

Finally, the boreholes SK-83, SK-88, and SK-73, plotted in green in Figure 6.3, are also eliminated as they do not satisfy the water content criteria "$Zone\ B: Test\ if\ w\_c \geq 0.85\ (LL)$" provided in Seed et al.'s liquefaction susceptibility chart

As previously stated, in only a few boreholes there are soil layers which are prone to liquefaction. After carefully investigating through all the 210 boreholes one by one, only seven boreholes were chosen for the liquefaction assessment; the following boreholes were found out to have layer prone to liquefaction; (SK-138, SK-141, SK-142, SK-148, SK-161, SK-171, and SK-172). Those boreholes are suspected to be prone to liquefaction after eliminating the boreholes of soils with a plasticity index $PI > 7$, low SPT blow counts, and lay above the groundwater table level.

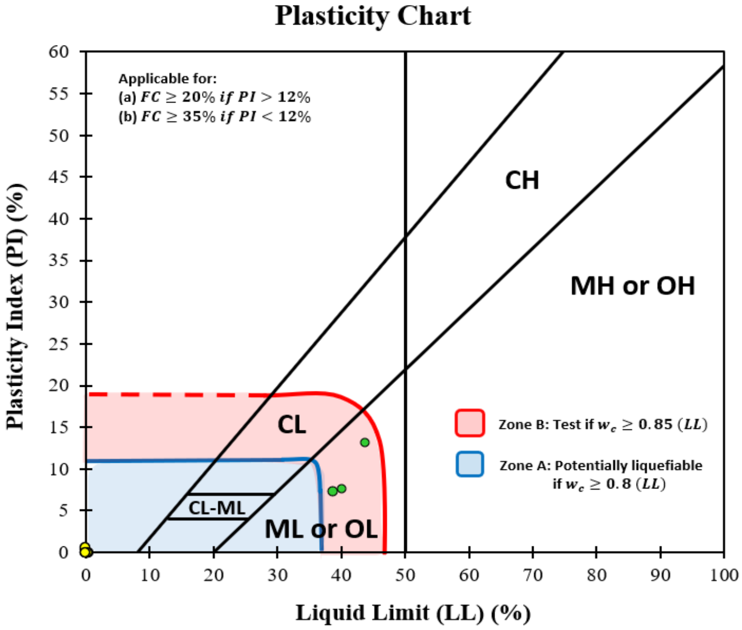

Figure 6.3. Liquefaction susceptibility chart (after Seed et al., 2003)

An important note to deliver at this point is that, although the boreholes that entirely lay above the groundwater table level were eliminated, as stated previously, within the potentially liquefied boreholes mentioned, only five boreholes were reported to have a groundwater table in the survey report used as a reference in this study (Akare Planlama, 2015). The boreholes with groundwater table levels reported are (SK-138, SK-141, SK-142); the groundwater table level of the remaining boreholes is assumed based on the elevation difference between them and the boreholes with a known groundwater table level. All liquefaction triggering analyses in this chapter are based on this assumption; however, if the water table level changes, or if any of the assumptions are shown to be not valid, the results presented in this chapter may be affected. The assumptions underlying the groundwater table level were thoroughly addressed in Chapter 4. The water table level of the potentially liquefiable boreholes is given in Table 6.1.

Finally, it should also be noted that all the analyses performed depend on the validity of the data borrowed from Elazig-Center Municipality Geological-Geotechnical Survey Report Based on Zoning Plan (Akare Planlama, 2015).

Table 6.1 The groundwater table level at the boreholes used for the liquefaction assessment.

Borehole	GWT (m)	Source
SK-138	10.00	Reported (Akare Planlama, 2015)
SK-141	13.00	Reported (Akare Planlama, 2015)
SK-142	12.00	Reported (Akare Planlama, 2015)
SK-148	0.00	Assumed (Elevation difference)
SK-161	0.00	Assumed (Elevation difference)
SK-171	0.00	Assumed (Elevation difference)
SK-172	0.00	Assumed (Elevation difference)

Other than the groundwater table level, there are several important parameters to consider while conducting liquefaction assessments, including the consistency limits (only non-plastic soils are susceptible to liquefaction) and fines contents of the soil sample. For this aim, the survey report of Akare Planlama (2015) is used as a reference, and the parameters required are taken from this report in order to complete the analysis.

According to the contents of the Akare Planlama (2015) survey report, a number of laboratory experiments were reported to have been performed in order to determine the index and physical properties of the units observed in the study area, including 248 Atterberg Limits, 248 sieve analyses, 248 water content experiments, and 248 soil class definitions. Table 6.2 summarizes all of the acquired characteristics (fine contents, plastic limitations, and USCS soil classification).

Table 6.2 The fines contents, Plasticity limits, and USCS classification of potentionally liquefiable soils in Elazig-Center

Borehole	Depth (m)	FC (%)	PL (%)	USCS
SK-138	3.00-3.50	85.3	18.4	CL
	1.50-8.00	82.8	18.2	CL
	10.50-11.00	94.2	19.1	CL
	15.00-15.45	46.9	NP	SM
SK-141	3.00-3.50	38.4	NP	SM
	6.00-6.50	88.7	16.1	CL
	7.50-8.00	78.2	20.9	CL
	12.00-12.45	40.6	NP	SM
	19.5-19.95	94.9	38.9	MH
SK-142	3.00-3.50	93.6	24.2	CL
	6.00-6.50	96.6	17.2	CL
	7.50-8.00	44.9	NP	SM
	18.00-18.45	49.0	NP	SM
SK-148	3.00-3.50	90.1	11.7	CL
	9.00-9.45	52.4	NP	ML
SK-161	3.00-3.50	88.0	18.4	CL
	4.50-4.95	41.9	NP	SM
SK-171	1.50-1.95	39.5	NP	SM
SK-172	3.00-3.50	95.4	23.9	CL
	7.50-7.95	36.9	NP	GM

6.3 Determination of the Input Parameters

Prior to performing liquefaction triggering assessments for Elazig-Center, input parameters for the assessments should be specified; (i) the soil profile parameters (ii) the earthquake parameters. This will be explained in detail in the following sections.

6.3.1 The Standard Penetration Test

Following the procedures recommended by Cetin et al. (2018), the first step is to estimate the corrected SPT-N blow counts of the boreholes to be used in the assessment.

In this study, simplified approaches will be used to conduct liquefaction triggering assessments using typical in-situ field test results in the form of SPT (standard penetration test). However, the raw SPT N values need to be corrected prior to use, NCEER (1997) suggested the following correction to the raw SPT-N values:

$$N_{1,60} = N_m C_N C_E C_B C_R C_S \tag{6-1}$$

Where; N_m stands for the raw SPT-N value measured, C_N for the overburden correction, C_E for the energy correction, C_B for the borehole diameter correction, C_R for the rod length correction and C_S for the sampling method correction.

The correction parameters used in Equation (6.1) are suggested by NCEER (1997) and are summarized in Table 6.3.

Table 6.3 The SPT corrections recommendations for liquefaction assessments NCEER (1997)

Factor	Term	Equipment Variable	Correction
Overburden Pressure	C_N	-	Pa/σ_v' $C_N \leq 2$
Energy Ratio	C_E	Safety Hummer Donut Hummer	0.60 - 1.17 0.45 – 1.00
Borehole Diameter	C_B	65-115 mm 150 mm 200 mm	1.00 1.05 1.15
Rod Length	C_R	3-4 m 4-6 m 6-10 m 10-30 m > 30 m	0.75 0.85 0.95 1.0 < 1.0
Sampling Method	C_S	Standard Sampler Sampler without liners	1.0 1.15-1.30

Because Cetin et al. (2004) will be adapted for the liquefaction evaluation in this specific study, it is essential to note that Cetin et al. (2004) used the same set of SPT corrections as NCEER in their analysis (1997). A slight discrepancy exists between the two studies, as Cetin et al. (2004) updated the short rod correction factor, which is represented in Figure 6.2, as opposed to the other NCEER (1997).

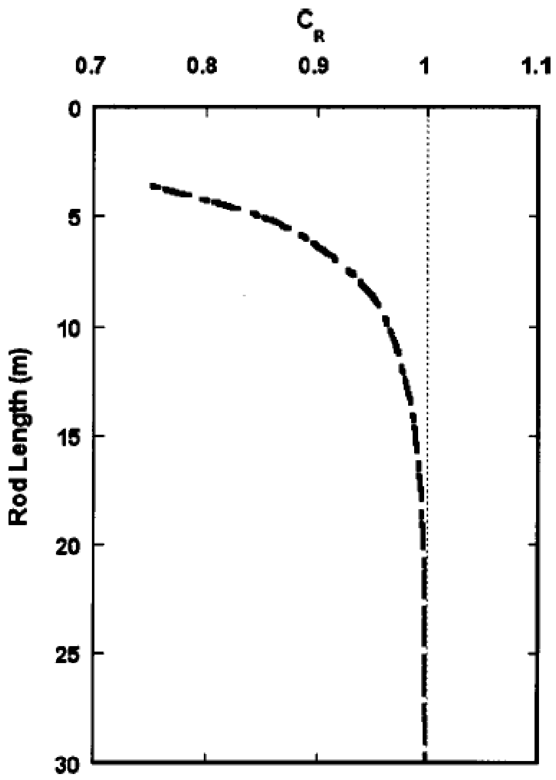

Figure 6.4. Rod length correction recommendation by Cetin et al. (2004)

The SPT data available for the research area (retrieved from Akare Planlama, 2015) have no precise information about the specifications of the standard penetration test performed to get this data; for this reason, the following assumptions are made for this specific study:

- The rod length is assumed to be: $SPT\ Depth + 1.5\ m$.
- The borehole diameter is accepted to be $< 15\ cm$.
- The hummer energy is assumed to be 45%.
- A Standard sampler is assumed to be used $(C_s = 1)$.

6.3.1.1 The estimation of $N_{1,60}$

For the estimation of the $N_{1,60}$ the correction parameters presented in Equation 6-1 will be first determined. Prior to starting, all the equations used for this section are referred to the original work of Cetin et al. (2018).

To start, the overburden correction factor C_N is determined using Equation 6-2:

$$C_N = \left(\frac{P_a}{\sigma'_{vo}}\right)^{0.5} \leq 2.0 \tag{6-2}$$

where σ'_{vo} and P_a are the effective stress and is the atmospheric pressure, respectively; $P_a = 100$ kPa (1 atm) both σ'_{vo} and P_a should be used with the same units.

Next, the rod correction parameter C_R is calculated. As previously stated, The rod length (d) used for the determination of the rod correction factor is assumed for this specific study to be the depth of the SPT with an addition of 1.5 m; Equations 6-3 and Equation 6-4 are used for the calculation of the rod correction factor:

$$\mathrm{C_R} = 0.48 + 0.225\ln(\mathrm{d})\,;\ \mathrm{d} < 10\ \mathrm{m}\ (\mathrm{T}-1) \tag{6-3}$$

$$\mathrm{C_R} = 0.48\,;\ 10 < \mathrm{d} < 30\ \mathrm{m}\ (\mathrm{T}-1) \tag{6-4}$$

where d is the rod length starting from the top of the SPT sampler to the sticking point.

Next, for the sampler and borehole correction factors (C_S and C_B), no correction is being applied, that is because, as stated previously, a standard sampler is assumed to be used ($C_S = 1$), and the borehole diameter is accepted to be less than 15 cm ($C_B = 1$).

Finally, for the hummer energy correction factor C_E, Equation 6-5 is used. Please note that, as mentioned previously, the hummer energy that is used for this study is assumed to be 45%.

$$C_E = \frac{ER}{60\%} \tag{6-5}$$

where ER (efficiency ratio) is the proportion or percentage of the theoretical SPT impact hammer energy actually delivered to the sampler, represented as percentage.

The raw SPT values, the calculated correction factors, and the estimated $N_{1,60}$ of the boreholes used for the assessment (SK-138, SK-141, SK-142, SK-148, SK-161, SK-171, and SK-172) are summarized in Table 6.4.

For the purpose of providing a feeling of the situation, the soil profiles of Boreholes SK-138, SK-141, SK-142, and SK-148 are depicted in Figure 6.4, together with the SPT-N blow counts.

Table 6.4 The raw SPT-N blow count and the $N_{1,60}$ values of the boreholes used in teh liquefaction assessment

Borehole	Mid-depth (m)	Thickness (m)	N_{45}	Rod-length (m)	σ_v (kPa)	σ'_v (kPa)	C_N	C_R	C_E	$N_{1,60}$
SK-138	1.725	0.45	12	3.23	31.4	31.4	1.78	0.75	0.75	12
	3.725	0.45	16	5.23	67.8	67.8	1.21	0.85	0.75	12
	4.725	0.45	21	6.23	86.0	86.0	1.08	0.95	0.75	16
	6.225	0.45	26	7.73	113.3	113.3	0.94	0.95	0.75	17
	8.225	0.45	30	9.73	149.7	149.7	0.82	0.95	0.75	17
	9.225	0.45	35	10.73	167.9	167.9	0.77	1	0.75	20
	10.725	0.45	33	12.23	195.6	188.4	0.73	1	0.75	18
	12.225	0.45	48	13.73	223.6	201.8	0.70	1	0.75	25
	13.725	0.45	61	15.23	251.7	215.1	0.68	1	0.75	31
	15.225	0.45	68	16.73	279.7	228.5	0.66	1	0.75	34
	16.725	0.45	74	18.23	307.8	241.8	0.64	1	0.75	36
	18.225	0.45	79	19.73	344.9	264.2	0.62	1	0.75	36

Table 6.4 Continued

Borehole	Mid-depth (m)	Thickness (m)	N_{45}	Rod-length (m)	σ_v (kPa)	σ'_v (kPa)	C_N	C_R	C_E	$N_{1,60}$
	1.725	0.45	14	3.23	31.4	31.4	1.78	0.75	0.75	14
	3.725	0.45	16	5.23	67.8	67.8	1.21	0.85	0.75	12
	4.725	0.45	21	6.23	86.0	86.0	1.08	0.95	0.75	16
	6.725	0.45	26	8.23	122.4	122.4	0.90	0.95	0.75	17
	8.225	0.45	31	9.73	149.7	149.7	0.82	0.95	0.75	18
	9.225	0.45	37	10.73	167.9	167.9	0.77	1	0.75	21
SK-141	10.725	0.45	41	12.23	195.6	195.2	0.72	1	0.75	22
	12.225	0.45	46	13.73	223.6	222.5	0.67	1	0.75	23
	13.725	0.45	51	15.23	251.7	215.1	0.68	1	0.75	26
	15.225	0.45	58	16.73	279.7	228.5	0.66	1	0.75	29
	16.725	0.45	67	18.23	307.8	241.8	0.64	1	0.75	32
	18.225	0.45	73	19.73	335.8	255.1	0.63	1	0.75	34
	19.725	0.45	81	21.23	363.9	268.5	0.61	1	0.75	37

Table 6.4 Continued

Borehole	Mid-depth (m)	Thickness (m)	N_{45}	Rod-length (m)	σ_v (kPa)	σ'_v (kPa)	C_N	C_R	C_E	$N_{1,60}$
	1.725	0.45	12	3.23	31.4	31.4	1.78	0.75	0.75	12
	3.725	0.45	14	5.23	67.8	67.8	1.21	0.85	0.75	11
	4.725	0.45	16	6.23	86.0	86.0	1.08	0.95	0.75	12
	6.725	0.45	25	8.23	122.4	122.4	0.90	0.95	0.75	16
	7.725	0.45	26	9.23	140.6	140.6	0.84	0.95	0.75	16
	9.225	0.45	31	10.73	167.9	167.9	0.77	1	0.75	18
SK-142	11.225	0.45	40	12.73	204.9	204.3	0.70	1	0.75	21
	12.225	0.45	37	13.73	223.6	201.8	0.70	1	0.75	20
	13.725	0.45	46	15.23	251.7	215.1	0.68	1	0.75	24
	15.225	0.45	53	16.73	279.7	228.5	0.66	1	0.75	26
	16.725	0.45	65	18.23	307.8	241.8	0.64	1	0.75	31
	18.225	0.45	73	19.73	335.8	255.1	0.63	1	0.75	34
	19.725	0.45	>50	21.23	363.9	268.5	0.61	1	0.75	>50

Table 6.4 Continued

Borehole	Mid-depth (m)	Thickness (m)	N_{45}	Rod-length (m)	σ_v (kPa)	σ'_v (kPa)	C_N	C_R	C_E	$N_{1,60}$
SK-148	1.725	0.45	12	3.23	31.4	108.4	0.96	0.75	0.75	6
	3.725	0.45	18	5.23	67.8	126.2	0.89	0.85	0.75	10
	4.725	0.45	21	6.23	86.0	135.1	0.86	0.95	0.75	13
	6.225	0.45	26	7.73	113.3	148.4	0.82	0.95	0.75	15
	7.725	0.45	32	9.23	140.6	161.8	0.79	0.95	0.75	18
	9.225	0.45	44	10.73	167.9	175.1	0.76	1	0.75	25
SK-161	1.725	0.45	24	3.23	31.4	108.4	0.96	0.75	0.75	13
	3.725	0.45	33	5.23	67.8	126.2	0.89	0.85	0.75	19
	4.725	0.45	44	6.23	86.0	135.1	0.86	0.95	0.75	27
	6.225	0.45	>50	7.73	113.3	148.4	0.82	0.95	0.75	>50
SK-171	1.725	0.45	30	3.23	31.4	108.4	0.96	0.75	0.75	16
SK-172	1.725	0.45	16	3.23	31.4	108.4	0.96	0.75	0.75	9
	3.725	0.45	24	5.23	67.8	126.2	0.89	0.85	0.75	14
	4.725	0.45	28	6.23	86.0	135.1	0.86	0.95	0.75	17
	6.225	0.45	35	7.73	113.3	148.4	0.82	0.95	0.75	20
	7.725	0.45	45	9.23	140.6	161.8	0.79	0.95	0.75	25

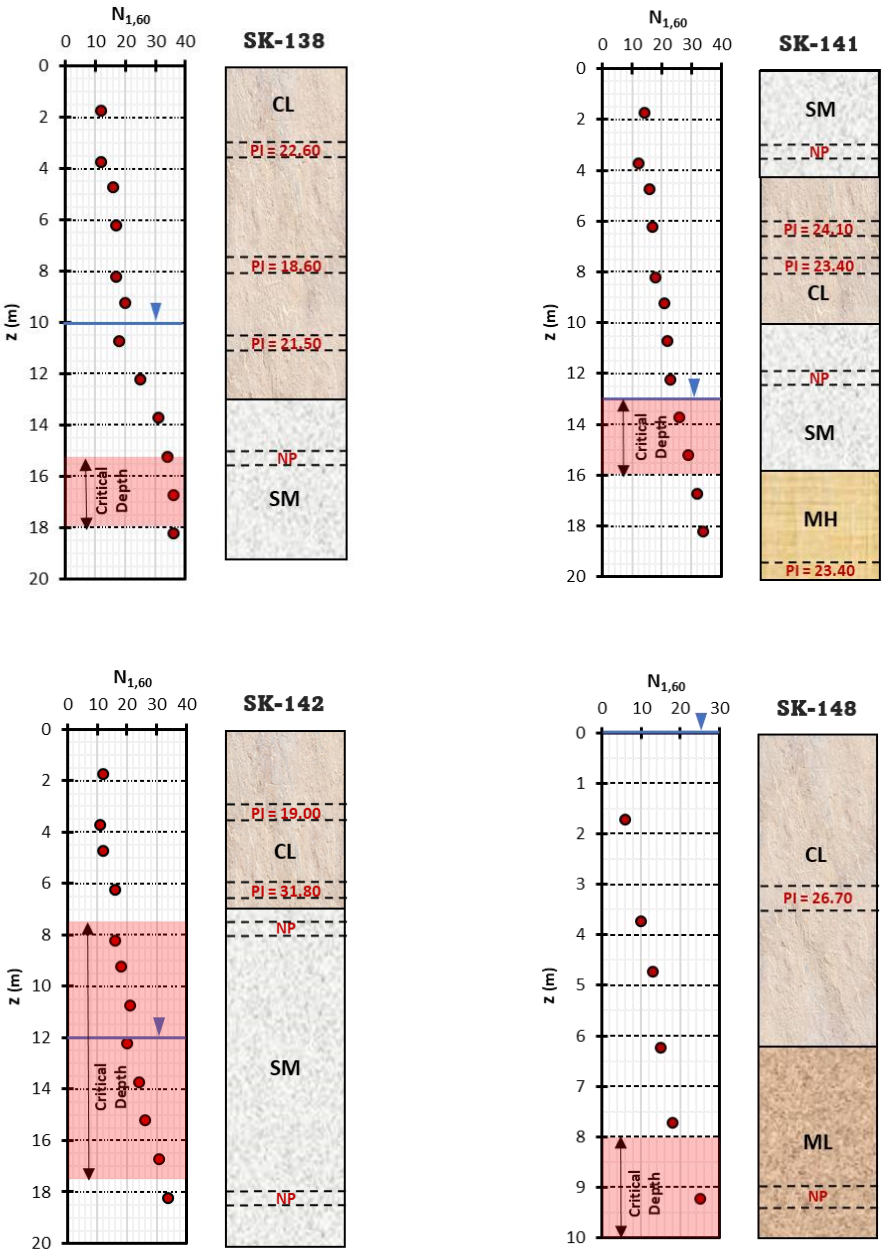

Figure 6.5. The soil profiles and SPT-N blow counts for SK-138, SK-141, SK-142, and SK-148.

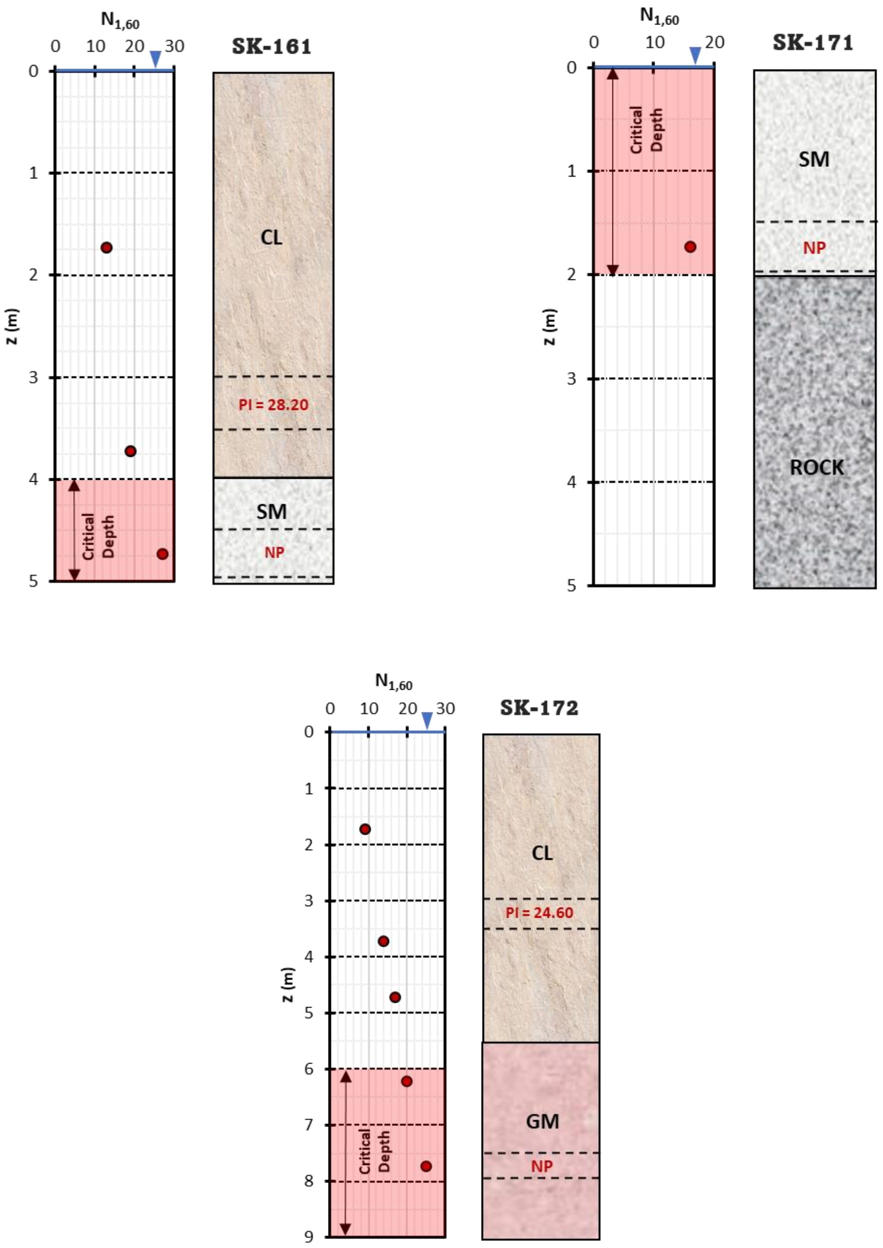

Figure 6.6. The soil profiles and SPT-N blow counts for SK-138, SK-141, SK-142, and SK-148.

6.3.1.2 Estimation of $V_{S,12}$ Values

Accurate measurement of the shear wave velocity in the top 12 m is necessary for the Cetin et al. (2004) relationship. The apparent travel durations through each sub-layer are calculated to a depth of 12 m and then divided by the distance traveled, as provided in Equation 6-6, to estimate V_{s12m}.

$$V_{s12m} = \frac{12\ m}{\sum \frac{H_i}{V_{s,i}}} \tag{6-6}$$

Equation 6-6 is calculated using the boreholes-specific shear wave velocity profiles prepared in the previous chapter. Moreover, the calculated values of V_{s12m} of the boreholes used for the liquefaction assessment in Elazig-Center are summarized in Table 6.5.

Table 6.5 Summary of the V_{s12m} values for the boreholes used in the liquefaction assessment.

Borehole	$\boldsymbol{V_{s12m}\ (m/s)}$
SK-138	449
SK-141	531
SK-142	472
SK-148	460
SK-161	587
SK-171	590
SK-172	437

6.3.2 Estimation of Seismic Input parameters

Only two seismic parameters are needed for liquefaction triggering assessment: the moment magnitude M_w and the Peak Ground Acceleration PGA. Since the site-effects of a real event is being studied, the moment magnitude is already known ($M_w = 6.8$). The results from the equivalent linear site response analyses performed in the previous chapter are utilized for the Peak Ground Acceleration. Table 6.6 summarizes the PGA values obtained from the site response analyses results for each of the boreholes at a depth of non-plastic layers.

Table 6.6 Summary of PGA values obtained from site response analyses at non-plastic depths

Borehole	**Mid-depth (m)**	PGA_{East} **(g)**	PGA_{North} **(g)**	PGA_{Mean} **(g)**
SK-138	15.2	0.084	0.072	0.078
SK-141	13.7	0.084	0.079	0.081
SK-142	12.2	0.075	0.071	0.073
SK-148	9.2	0.091	0.085	0.088
SK-161	4.7	0.086	0.072	0.079
SK-171	1.7	0.115	0.099	0.107
SK-172	7.7	0.070	0.057	0.063

6.4 Estimation of the Capacity and Demand Terms

In liquefaction triggering assessments, the cyclic stress ratio CSR is referred to as the demand term, and it can be calculated from Equation 6-7, whereas the capacity term is the cyclic resistance ratio CRR and is estimated using Equation 6-11.

$$CSR = \left(\frac{\tau_{av}}{\sigma'_{vo}}\right) = 0.65\left(\frac{a_{max}}{g}\right)\left(\frac{\sigma_{vo}}{\sigma'_{vo}}\right) r_d \tag{6-7}$$

where r_d refers to the mass participation factor, and it can be calculated from Equation 6-8 and Equation 6-9:

For $d < 20$ m:

$$r_d = \frac{\left[1 + \frac{-23.013 - 2.949 \cdot a_{max} + 0.999 \cdot M_w + 0.0525 \cdot V^*_{s,12}}{16.258 + 0.201 \cdot e^{0.341 \cdot (-d + 0.0785 \cdot V^*_{s,12} + 7.586)}}\right]}{\left[1 + \frac{-23.013 - 2.949 \cdot a_{max} + 0.999 \cdot M_w + 0.0525 \cdot V^*_{s,12}}{16.258 + 0.201 \cdot e^{0.341 \cdot (0.0785 \cdot V^*_{s,12} + 7.586)}}\right]} \pm \sigma_{\varepsilon_{r_d}} \tag{6-8}$$

For $d \geq 20$ m:

$$r_d = \frac{\left[1 + \frac{-23.013 - 2.949 \cdot a_{max} + 0.999 \cdot M_w + 0.0525 \cdot V^*_{s,12}}{16.258 + 0.201 \cdot e^{0.341 \cdot (-20 + 0.0785 \cdot V^*_{s,12} + 7.586)}}\right]}{\left[1 + \frac{-23.013 - 2.949 \cdot a_{max} + 0.999 \cdot M_w + 0.0525 \cdot V^*_{s,12}}{16.258 + 0.201 \cdot e^{0.341 \cdot (0.0785 \cdot V^*_{s,12} + 7.586)}}\right] - 0.046 \cdot (d - 20)} \pm \sigma_{\varepsilon_{r_d}} \tag{6-9}$$

where;

$$d < 12m\ (\approx 40ft) \rightarrow \sigma_{\varepsilon_{r_d}}(d) = \mathrm{d}^{0.8500}.\,0.0198 \qquad (6\text{-}10)$$

$$d \geq 12m\ (\approx 40ft) \rightarrow \sigma_{\varepsilon_{r_d}}(d) = 12^{0.8500}.\,0.0198 \qquad (6\text{-}11)$$

$$CRR = exps\left[\frac{\begin{array}{c} N_{1,60}\,.\,(1+\theta_1.FC) - \ \theta_6.\ln\,(M_w) \\ -\theta_3.\ln\left(\frac{\sigma_v'}{P_a}\right) + \ \theta_4.FC + \ \theta_5 + \sigma_\epsilon.\varphi^{-1}(PL) \end{array}}{\theta_6}\right] \qquad (6\text{-}12)$$

$$P_L = exps\left[\frac{\begin{array}{c} N_{1,60}\,.\,(1+\theta_1.FC) - \ \theta_2.\ln\,(CSR_{\alpha=0}) \\ -\theta_2.\ln(M_w) - \theta_3.\ln\left(\frac{\sigma_v'}{P_a}\right) + \ \theta_4.FC + \ \theta_5 \end{array}}{\theta_6}\right] \qquad (6\text{-}13)$$

$$N_{1,60\,,CS} = N_{1,60} \ + \ \Delta\,N_{1,60} \qquad (6\text{-}14)$$

$$\Delta\,N_{1,60} \ = FC\,.\left(\theta_1 + N_{1,60} \ + \ \theta_4\right),\ \text{lim: } (5\% \ \leq \mathrm{FC} \leq 35\%) \qquad (6\text{-}15)$$

Finally, after determining the demand and capacity terms, the safety factor against liquefaction can be estimated, defined as the ratio of capacity to demand terms. This is shown in Equation 6-16

$$FS = \frac{CRR}{CSR} \tag{6-16}$$

The model coefficients of CEA2018 provided in Equation 6-12 are listed in Table 6.7. Moreover, the calculated values of the cyclic stress ratio CSR and the cyclic resistance ratio CRR of the boreholes prone to liquefaction and at the critical depth are presented in Table 6.8.

Table 6.7 The coefficients used for the calculation of the cyclic resistance ratio

σ_ε	θ_1	θ_2	θ_3	θ_4	θ_5	θ_6	θ_7	θ_8
2.95	0.0017	27.352	3.958	0.089	16.084	11.771	0.392	2.950

Table 6.8 The demand, capacity and factor of safety results for the liquefaction assessment

Borehole	**Mid-depth (m)**	**$N_{1,60,cs}$**	**K_{σ}**	**K_{MW}**	**K_{α}**	**r_d (m)**	**CSR**	**$CSR_{corrected}$**	**CRR**	**FS**
SK-138	16.5	40	0.75	1.256	1	1.004	0.0645	0.0689	0.0645	0.860
SK-141	14.5	34	0.73	1.256	1	1.000	0.0561	0.0608	0.0561	0.892
SK-142	12.5	29	0.76	1.256	1	1.001	0.0487	0.0508	0.0487	0.804
SK-148	9.0	26	1.08	1.256	1	1.000	0.1171	0.0865	0.1171	1.000
SK-161	4.5	32	1.36	1.256	1	1.000	0.1051	0.0615	0.1051	0.946
SK-171	6.5	20	1.20	1.256	1	1.000	0.1424	0.0943	0.1424	1.000
SK-172	7.5	27	1.15	1.256	1	1.000	0.0839	0.0583	0.0839	0.728

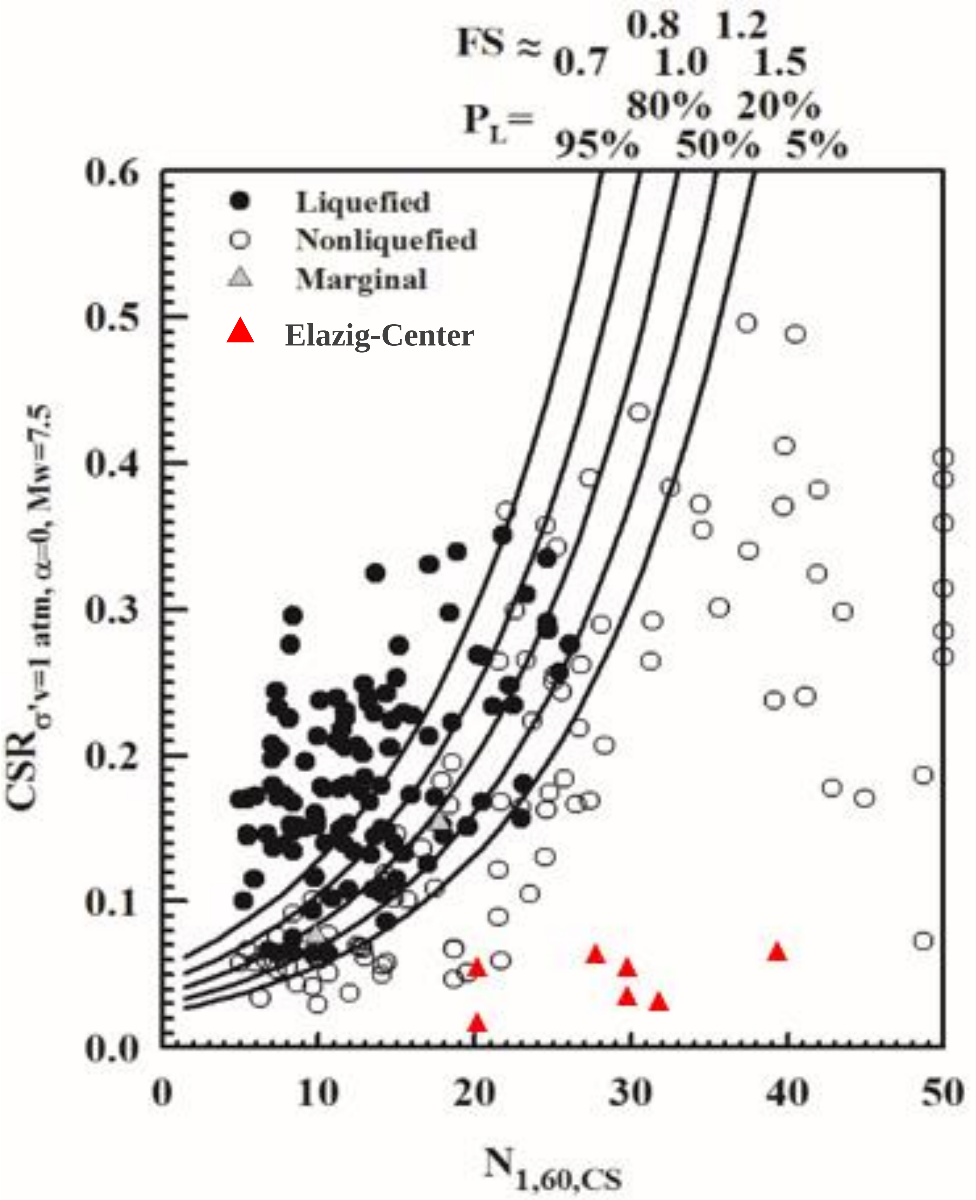

Figure 6.7. Liquefaction triggering assessment results plotted on Cetin et al. (2018) database

Although no liquefaction is expected in Elazig-Center based on the results of the analysis, the author was eager to conduct the analyses and report the results in this study.

CHAPTER 7

ZONATION OF THE STUDY REGION

7.1 Introduction

Nowadays, earthquake damage is easier to monitor, anticipate, and prepare for, thanks to technological advancements such as satellite imaging, GIS software, and computers. Those powerful tools will enhance and conclude the work done in this thesis. In this chapter, zonation maps for the collected geotechnical data and the results of the performed seismic analyses are presented to provide a reference for engineering purposes and define the seismic demand of the region.

Zonation maps will be constructed for mainly two sets of categories; (i) for the collected/generated geodata (ii) for the estimated seismic parameters after performing seismic response analyses and liquefaction triggering assessments, "namely, PGA maps S_a maps. Originally, within the scope of these stıdies liquefaction zonation maps were intended to be developed. However, fortunately, after conducting the assessments, Elazig-Center, under the current conditions, was concluded to be composed of mostly non-liquefiable soils or soils with very low probability of liquefaction.

Generally speaking, for each of the mentioned parameters, three different types of maps are created; the first is a scatter discrete data map with real (actual) values distributed over the geological settings Elazig-Center. Second , contour maps are generated over the geological map of the study region where the real values are predicted. Finally, the zonation maps are constructed without contour lines or geological settings, which will provide a general overview of the distribution of the selected engineering parameter. Please note that when preparing these maps, due to smoothing algorithms used by the software the loss in resolution of the actual data is possible.

7.2 Zonation Overview

GIS software has improved significantly over the last two decades, making it feasible to model diverse natural phenomena in ways that were previously unimaginable. The software program ArcGIS Pro v. 2.9.1 is used for GIS purposes in this specific study.

Through raster analysis techniques, GIS may be used to depict a range of natural phenomena. These approaches split the phenomena under investigation into a grid system and assign a strength rating to each occurrence's value characteristics.

Typically, data in tables are merely numbers that do not convey the whole picture and do not indicate the geographical link or pattern depicted until the data is referenced and graphically mapped. With this concept in mind, the potential for GIS becomes clear, as billions of records exist in such tables around the world that may contain a geographical reference or address but have not been integrated into a GIS. Thus the pattern and meaning inherent in such data are typically not fully utilized and are frequently unusable within such table, except to a trained eye that uses the data frequently enough to recognize such patterns.

7.3 Mapping Elazig-Center

While conducting this study, first geotechnical data was compiled from the literature, and subsequent seismic analyses were conducted. Both the geotechnical and seismic data serve as precious engineering sources; for this reason, the first part of this chapter will focus on generating maps out of the geodata compiled as discussed in previous chapters. Next, zonation maps will be generated.

7.3.1 Geodata Zonation Maps

To begin with, in this study, the primary source of the compiled data was from the Elazig (Central) Municipality Geological-Geotechnical Survey Report Based on Zoning Plan (Akare Planlama, 2015). Data were analyzed, and assumptions were made while acquiring the missing geotechnical data; the details regarding the assumptions and the way the data is generated are presented in Chapter-4; this chapter will serve for demonstration purposes only.

7.3.1.1 Zonation Maps for the Groundwater Table level

Only five boreholes were reported to have a Ground Water Table in Elazig-center:

- The borehole SK-138, with a recorded water table level at 10 m depth.
- The borehole SK-139, with a recorded water table level at 12 m depth.
- The borehole SK-140, with a recorded water table level at 14 m depth.
- The borehole SK-141, with a recorded water table level at 13 m depth.
- The borehole SK-142, with a recorded water table level at 12 m depth.

The groundwater table level (GWT) for the remaining boreholes is assumed considering the elevation difference between the above boreholes with known GWT values and the related ones.

The zonation map of GWT of Elazig Center is constructed utilizing the kriging interpolation algorithm in the software ArcGIS Pro v. 2.9.1 and provided. The discrete-scatter points are provided in Figure 7.1, while the predicted zonation map of the GWT is given in Figure 7.2.

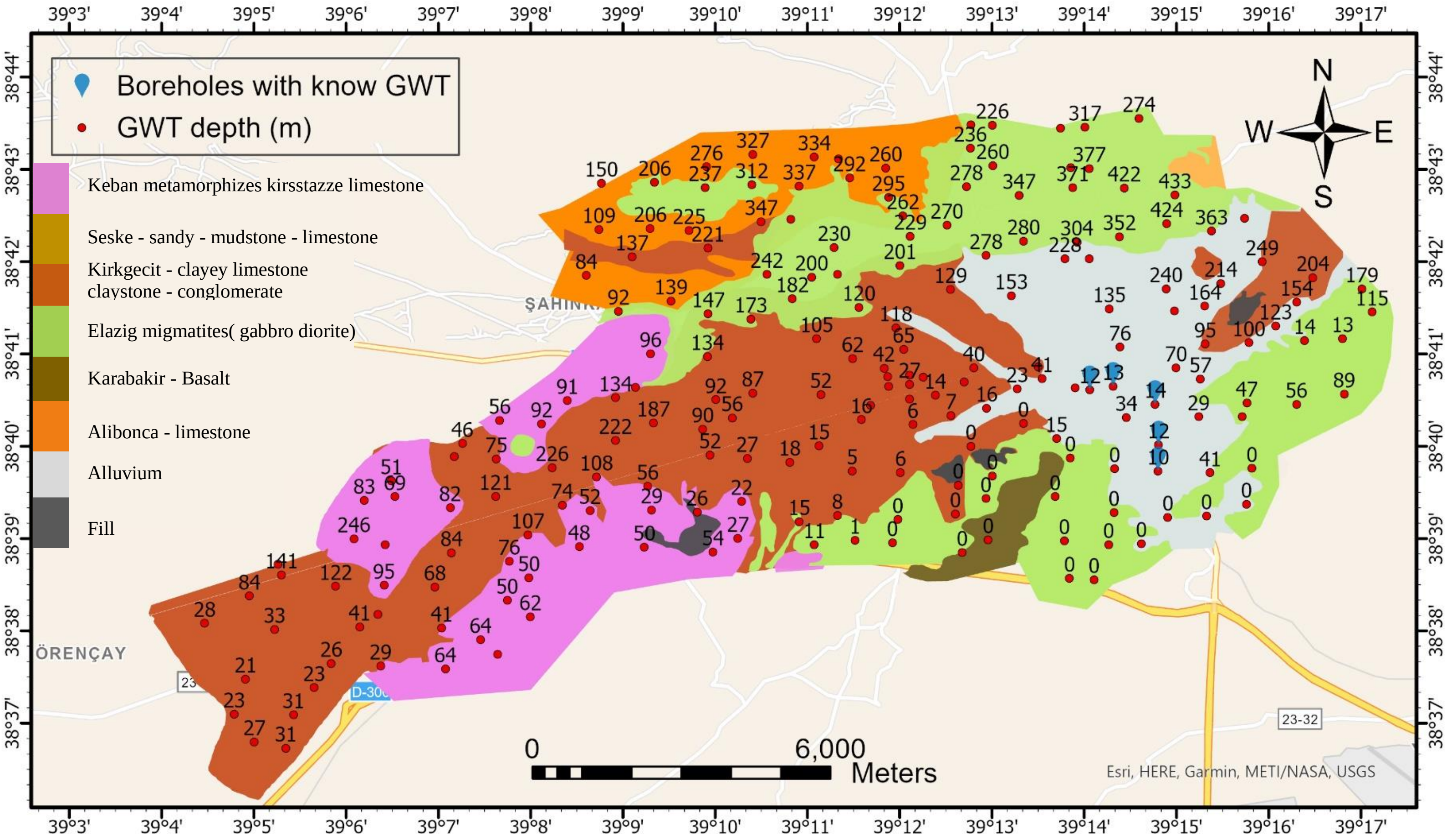

Figure 7.1. Discrete GWT values plotted on the geological Map of Elazig-Center

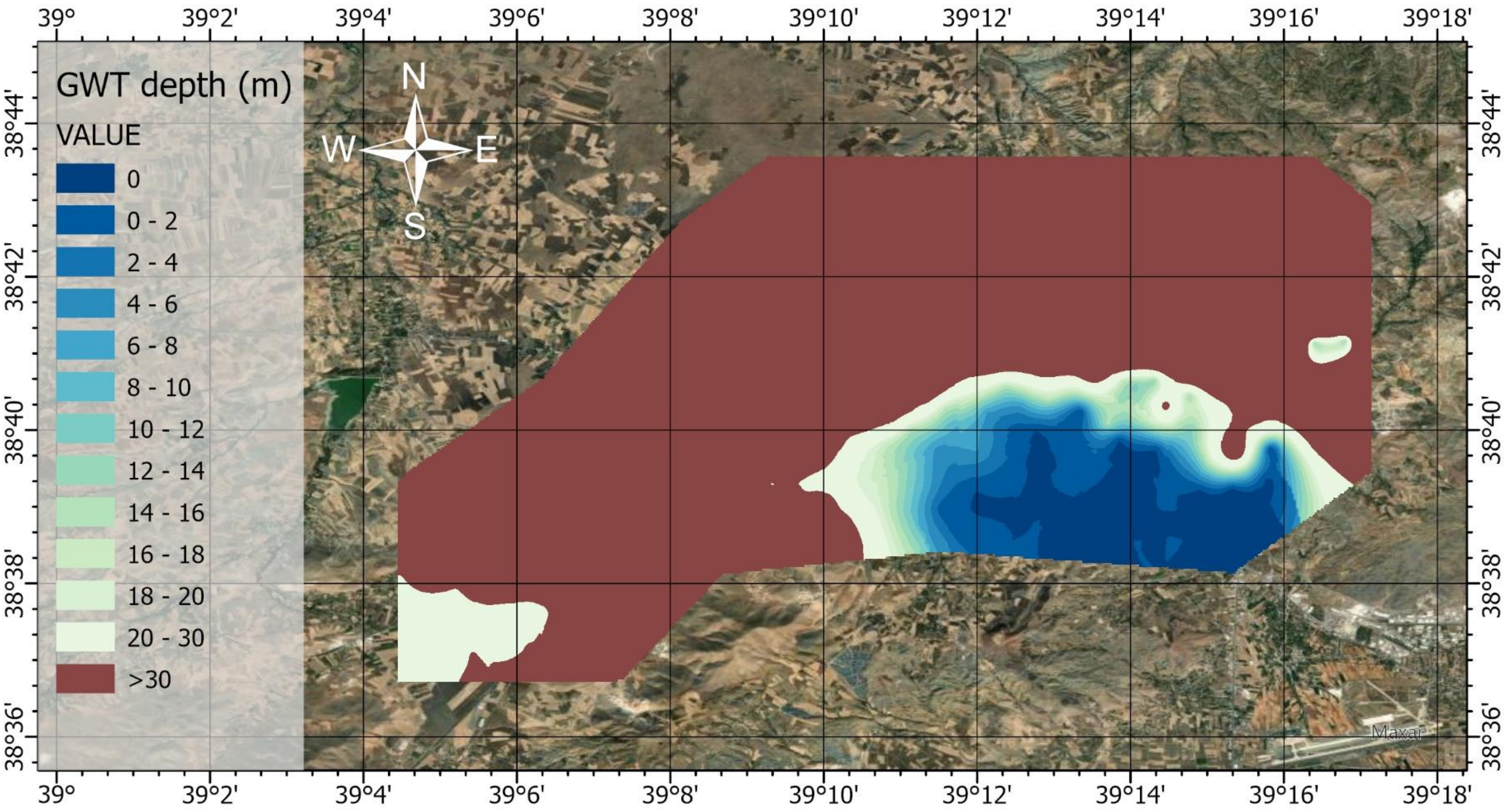

Figure 7.2. Zonation of GWT values in Elazig Center utilizing the kriging interpolation algorithm

7.3.1.2 Zonation Maps SPT-N blow counts

The standard penetrations test (SPT) is a prominent and well-known in-situ test in the geotechnical engineering discipline. The SPT tests are one of the in-situ tests done as part of Akare Planlama's (2015) study. The data sets for this thesis were obtained mostly from the reported SPT data.

In this section, zonation maps will be prepared considering the average SPT-N values for the upper seven meters in Elazig-Center. However, the SPT data available for the research region (retrieved from Akare Planlama, 2015) does not contain any particular information regarding the parameters of the standard penetration test conducted to get this data; as a result, the raw data is displayed on the maps instead of the corrected data.

Mainly three maps will be prepared for the SPT-N values:

- Scatter discrete data map with raw SPT-N values distributed over the geological settings Elazig-Center (Figure 7.3)
- Contour maps for raw SPT-N generated over the geological map of the study region, the Empirical Bayesian Kriging interpolation algorithm was used for the generation of the map (Figure 7.4).
- Zonation maps for raw SPT-N generated using kriging interpolation and adopting the Exponential Semi-variogram model (Figure 7.5).

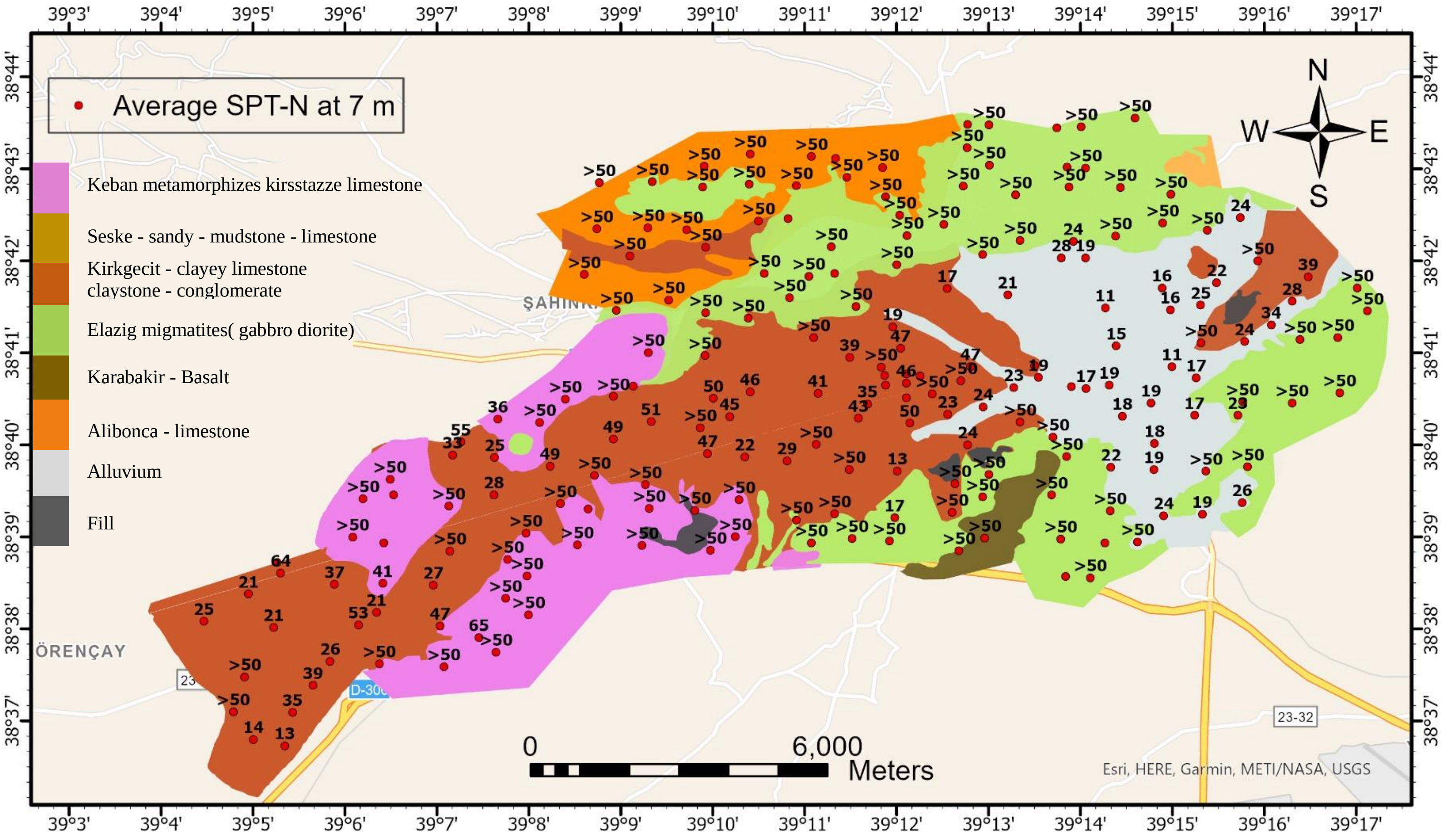

Figure 7.3. The average raw SPT-N values in the upper 7 meters plotted in the geological map of Elazig-Center

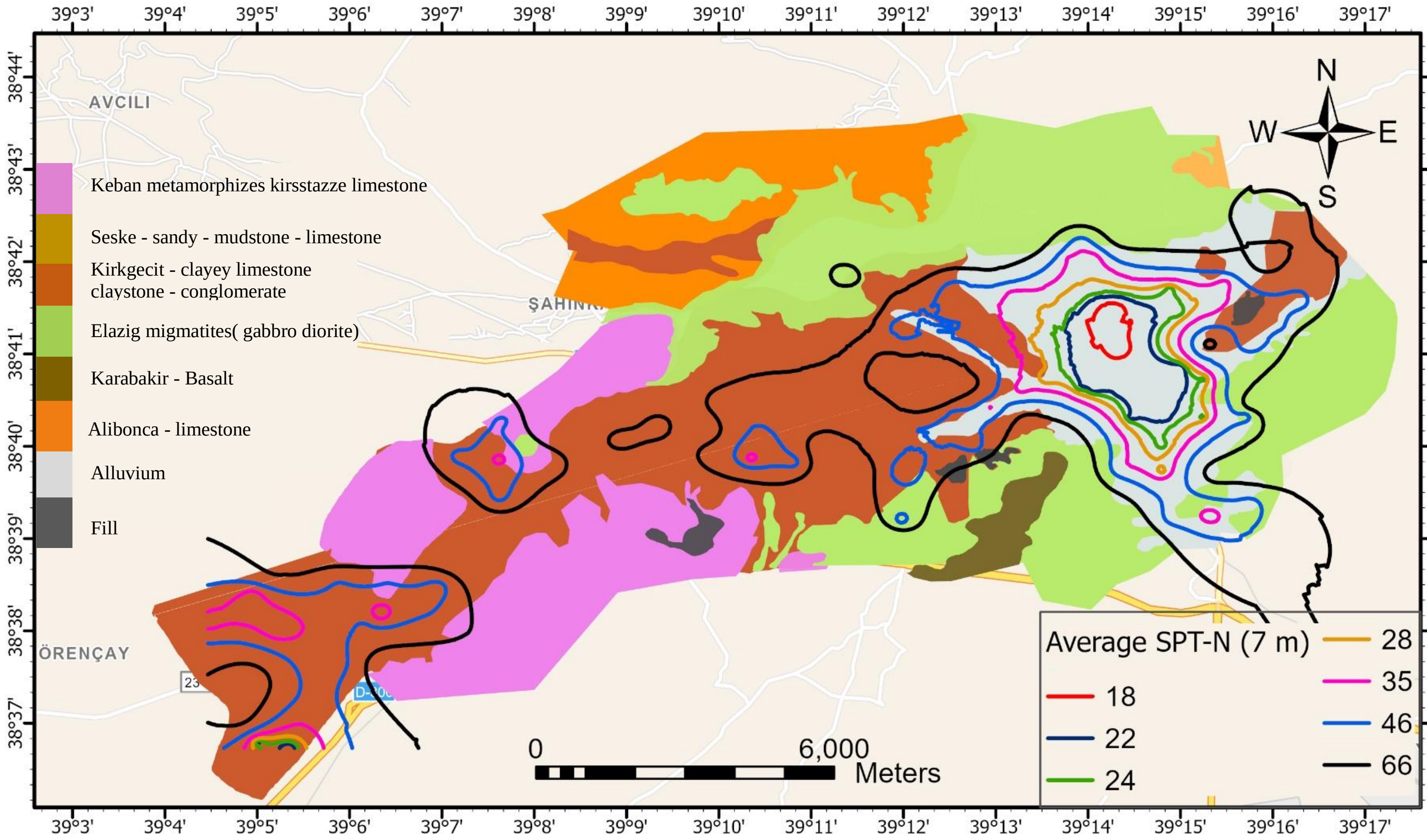

Figure 7.4. The contours for the average raw SPT-N values in the upper 7 meters plotted in the geological map of Elazig-Center

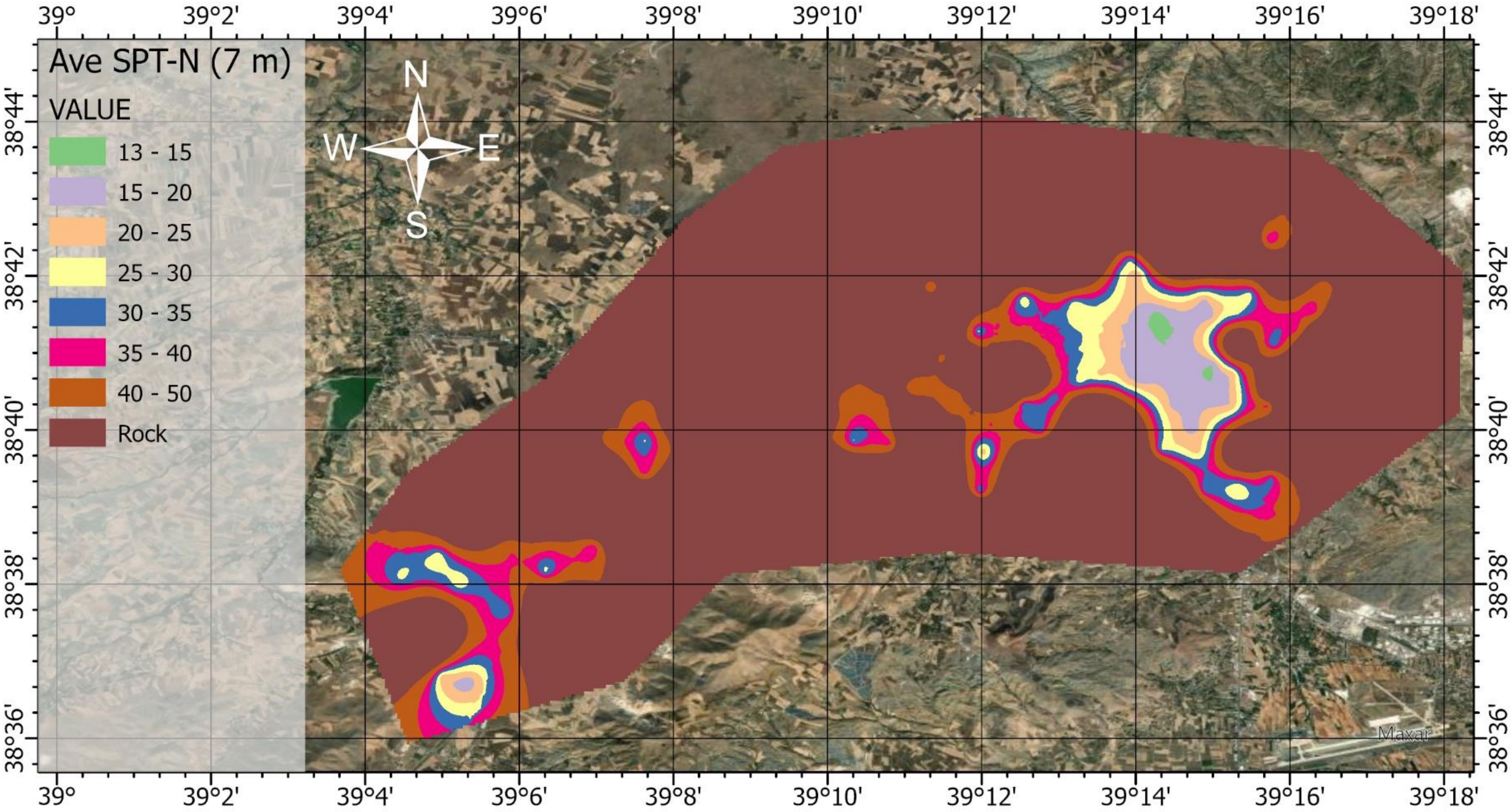

Figure 7.5. Zonation of the average raw SPT-N values in the upper 7 meters in Elazig Center utilizing the kriging interpolation algorithm

7.3.1.3 Zonation Maps Pressuremeter Test Results

Akare Planlama (2015) conducted a total of 50 pressuremeter experiments in ten distinct boreholes to ascertain the mechanical characteristics of the soil strata during the drilling studies (SK23, SK49, SK52, SK89, SK91, SK95, SK113, SK132, SK138, SK142). The experiment is based on the inflation of a cylindrical tube with a diameter of 74 mm that is dropped to the necessary depth in the drilled boreholes and is composed of three cells, as well as the borehole's radial stress.

The elastic modulus (E_m) from the pressuremeter test is obtained in Akare Planlama (2015) at various depths (3m, 6m, 9m, 12m and 15m). In this section, maps for E_m will be generated for all measured depth.

Please note that, since the test is performed in only ten boreholes, only the Scatter - discrete data map is prepared. The E_m data is plotted on the geological map of Elazig-Center and the results are provided in Figure 7.6, Figure 7.7, Figure 7.8, Figure 7.9, and Figure 7.10, at 3m, 6m, 9m, 12m and 15m depth respectively.

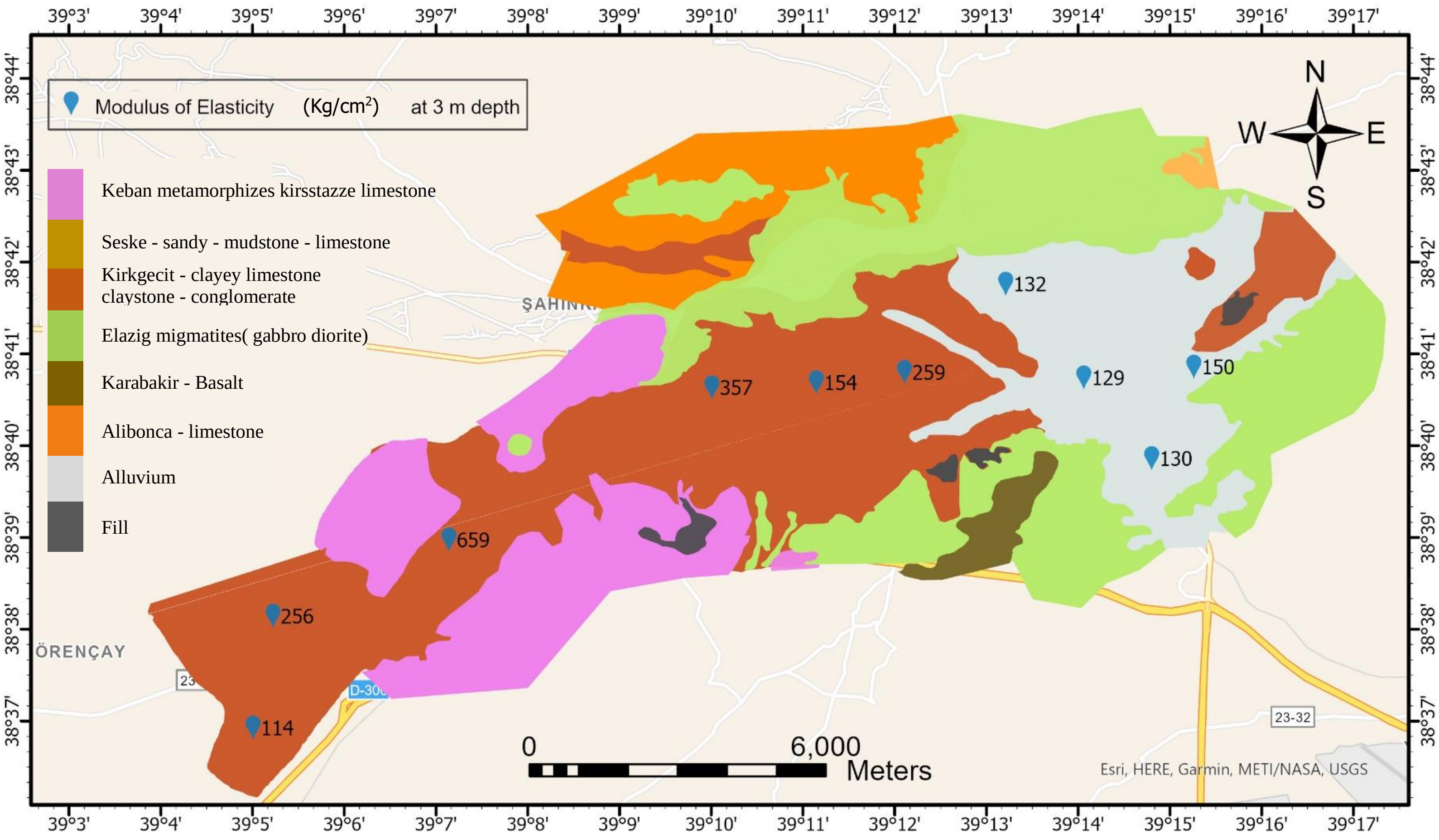

Figure 7.6. Discrete E_m values obtained from the pressuremeter test at 0-3 m depth and plotted on the geological Map of Elazig-Center

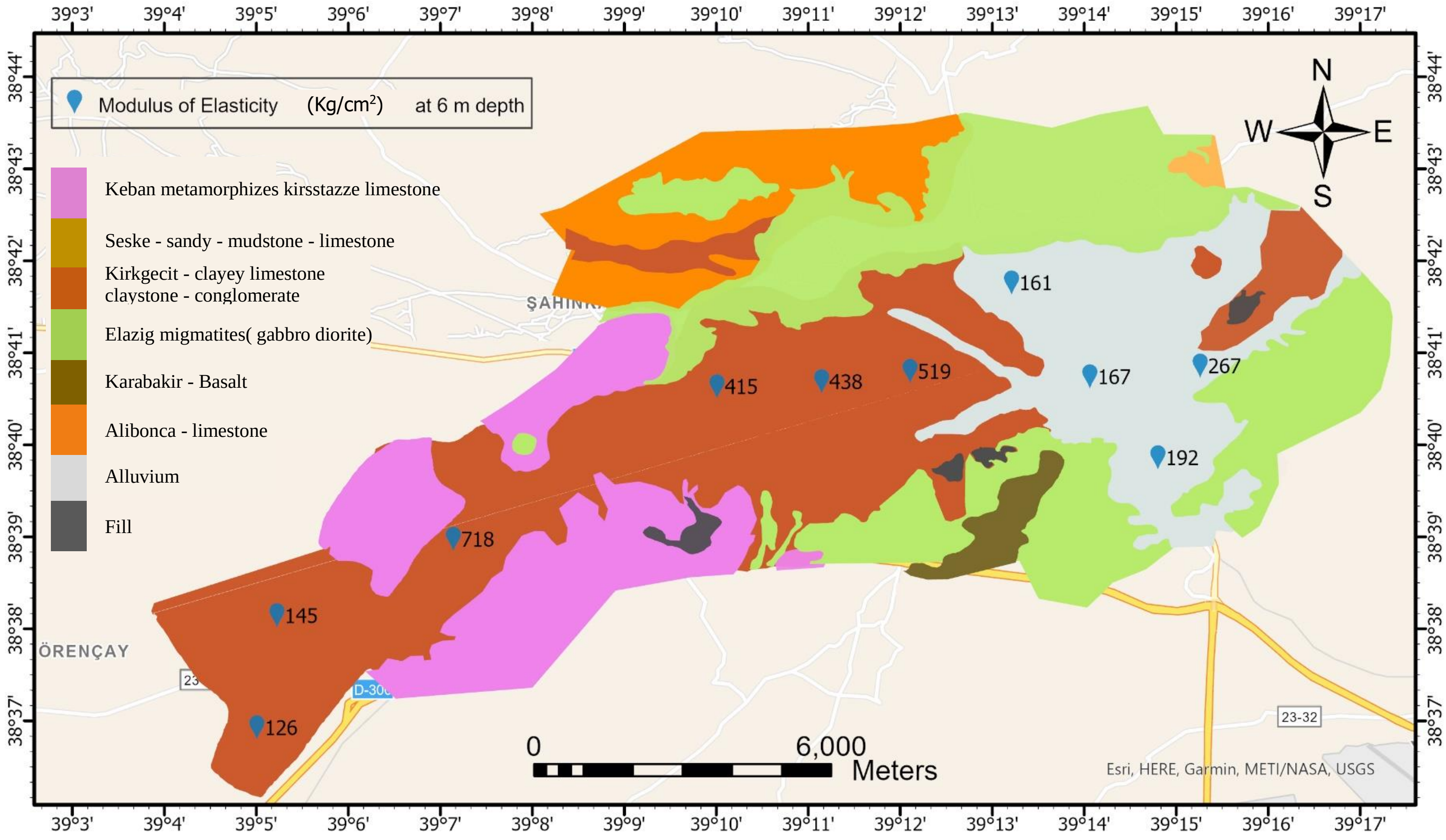

Figure 7.7. Discrete E_m values obtained from the pressuremeter test 3-6 m depth and plotted on the geological Map of Elazig-Center

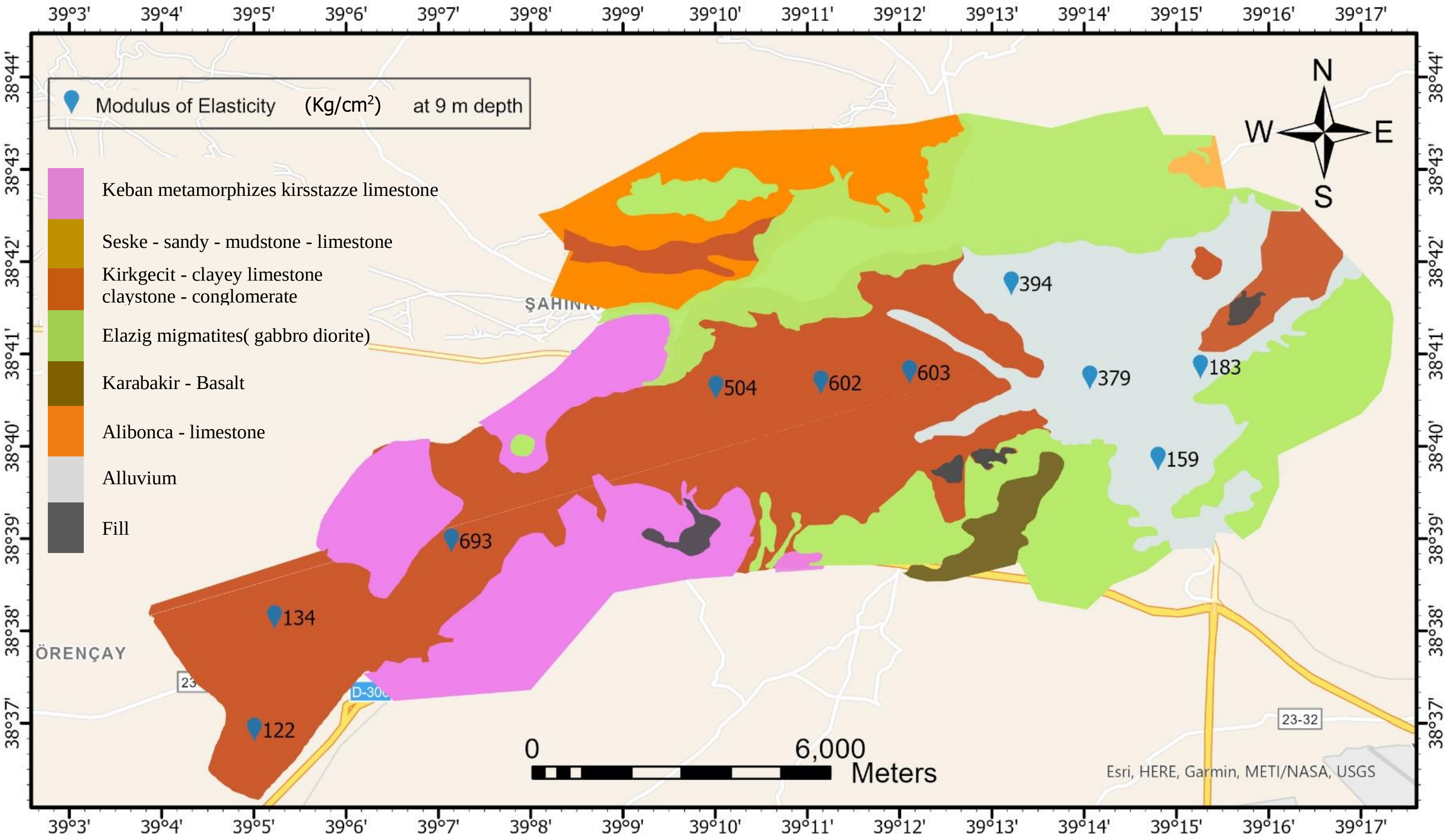

Figure 7.8. Discrete E_m values obtained from the pressuremeter test at 6-9 m depth and plotted on the geological Map of Elazig-Center

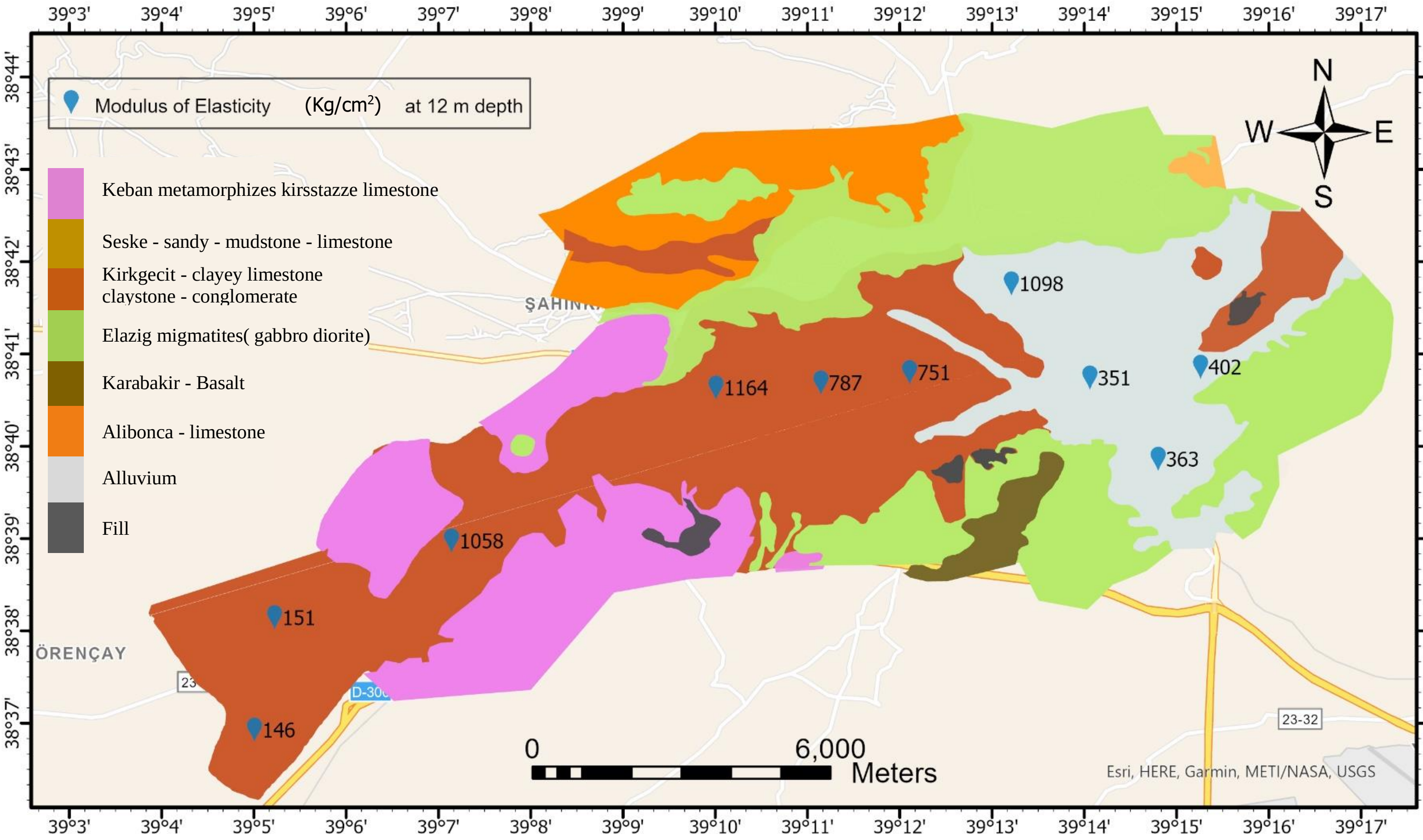

Figure 7.9. Discrete E_m values obtained from the pressuremeter test at 9-12 m depth and plotted on the geological Map of Elazig-Center

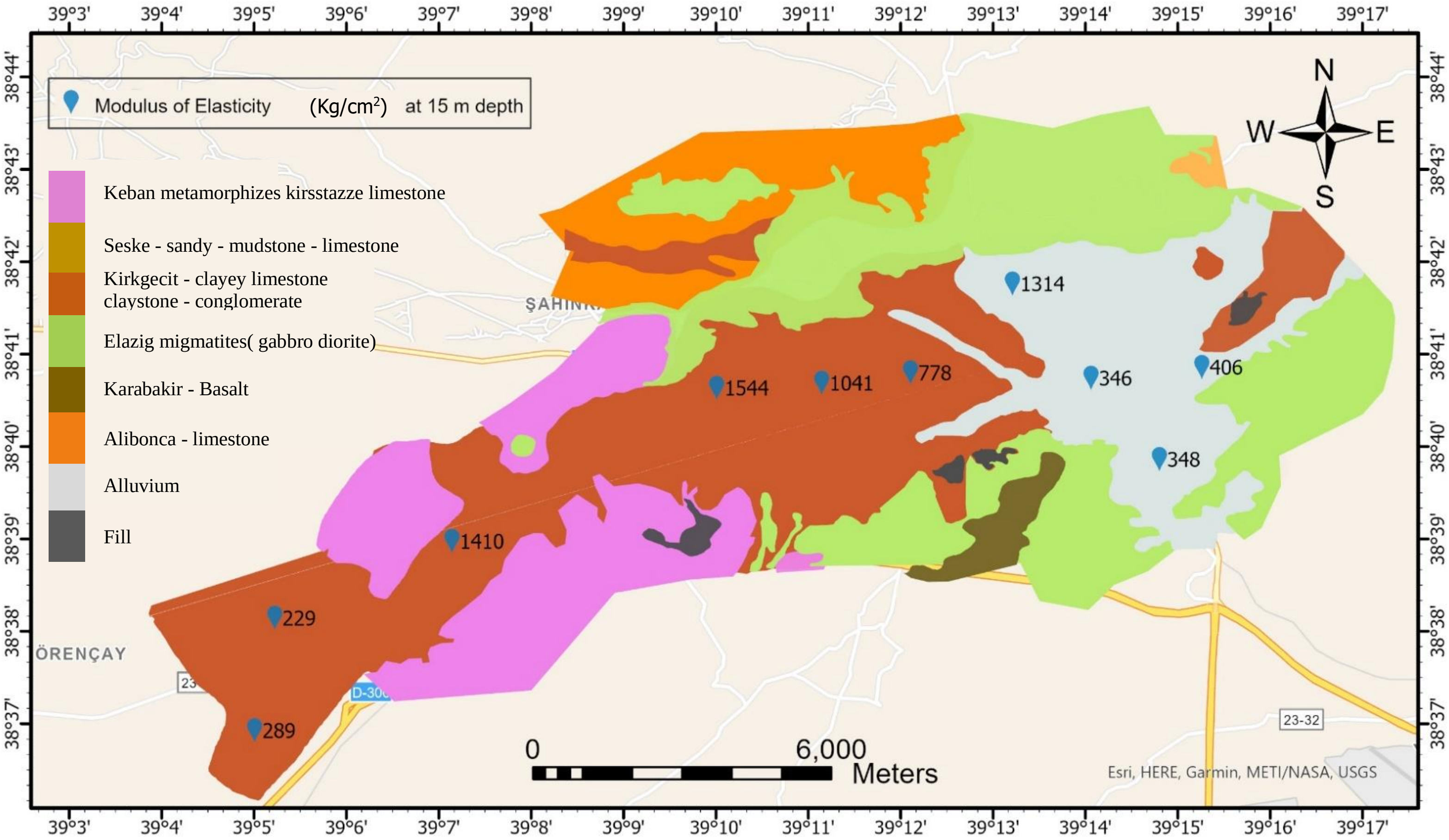

Figure 7.10. Discrete E_m values from the pressuremeter test at 12-15 m depth and plotted on the geological Map of Elazig-Center

7.3.1.4 Zonation Maps of the Shear Wave Velocity Data

According to Akare Planlama (2015), P and S wave velocity measurements were taken in the study area, and 170 profiles were reported. In this section zonation maps will be prepared considering the seismic refraction test results reported. The maps will be generated for seismic refraction Layer-1 results (varying between 5 m and 11 m), for the seismic refraction Layer-2 results (presenting the shear wave velocity values for rocks) and maps for V_{s30}.

Following the same methodoly, three type of maps are prepared for each of the three outputs ($V_{s-layer1}$, $V_{s-layer2}$, and V_{s30}):

- Scatter discrete data map plotted on the geological settings of Elazig-Center for $V_{s-layer1}$, $V_{s-layer2}$, and V_{s30} shown in Figure with raw SPT-N values distributed over the geological settings Elazig-Center given in Figure 7.6, Figure 7.8, and Figure 7.9 respectively.
- Contour maps plotted on the geological settings of Elazig-Center for $V_{s-layer1}$, $V_{s-layer2}$, and V_{s30} shown in Figure with raw SPT-N values distributed over the geological settings Elazig-Center given in Figure 7.10, Figure 7.11, and Figure 7.12 respectively.
- Zonation maps for $V_{s-layer1}$, $V_{s-layer2}$, and V_{s30} shown in Figure with raw SPT-N values distributed over the geological settings Elazig-Center given in Figure 7.13, Figure 7.14, and Figure 7.5 respectively.

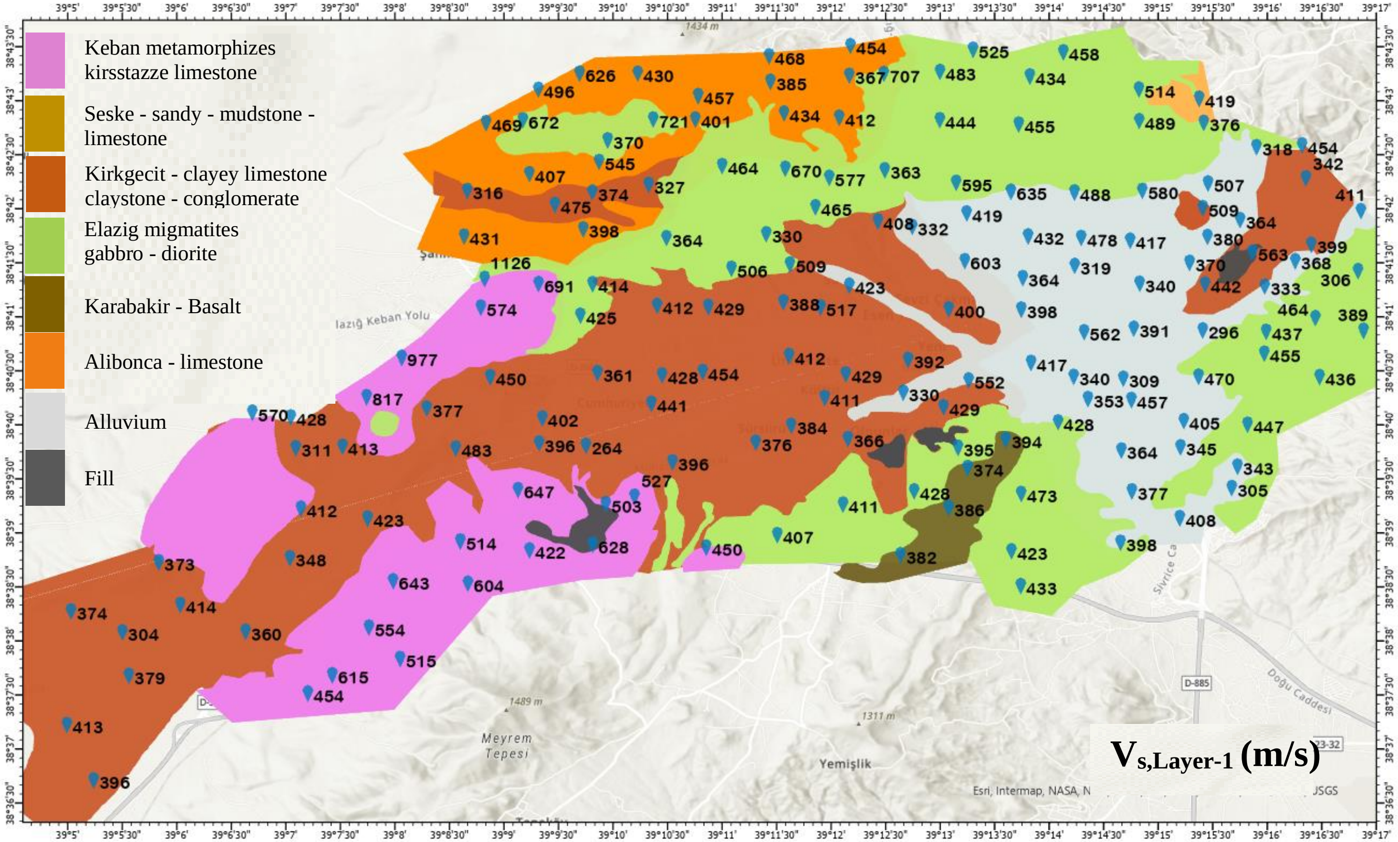

Figure 7.11. Vs measured for the first layer using seismic refraction tests and plotted on the geological map of Elazig-Center

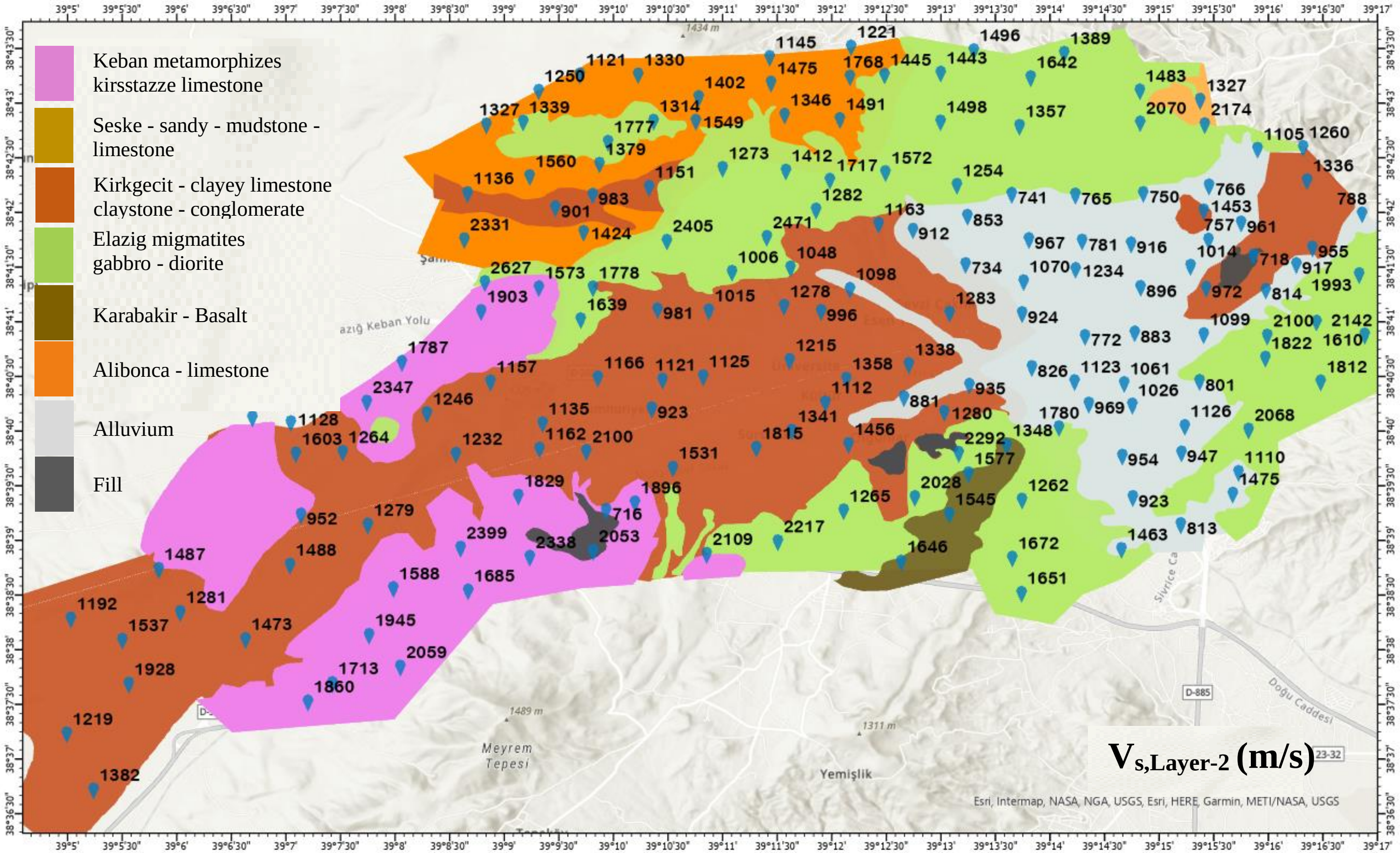

Figure 7.12. Vs measured for the second layer using seismic refraction tests and plotted on the geological map of Elazig-Center

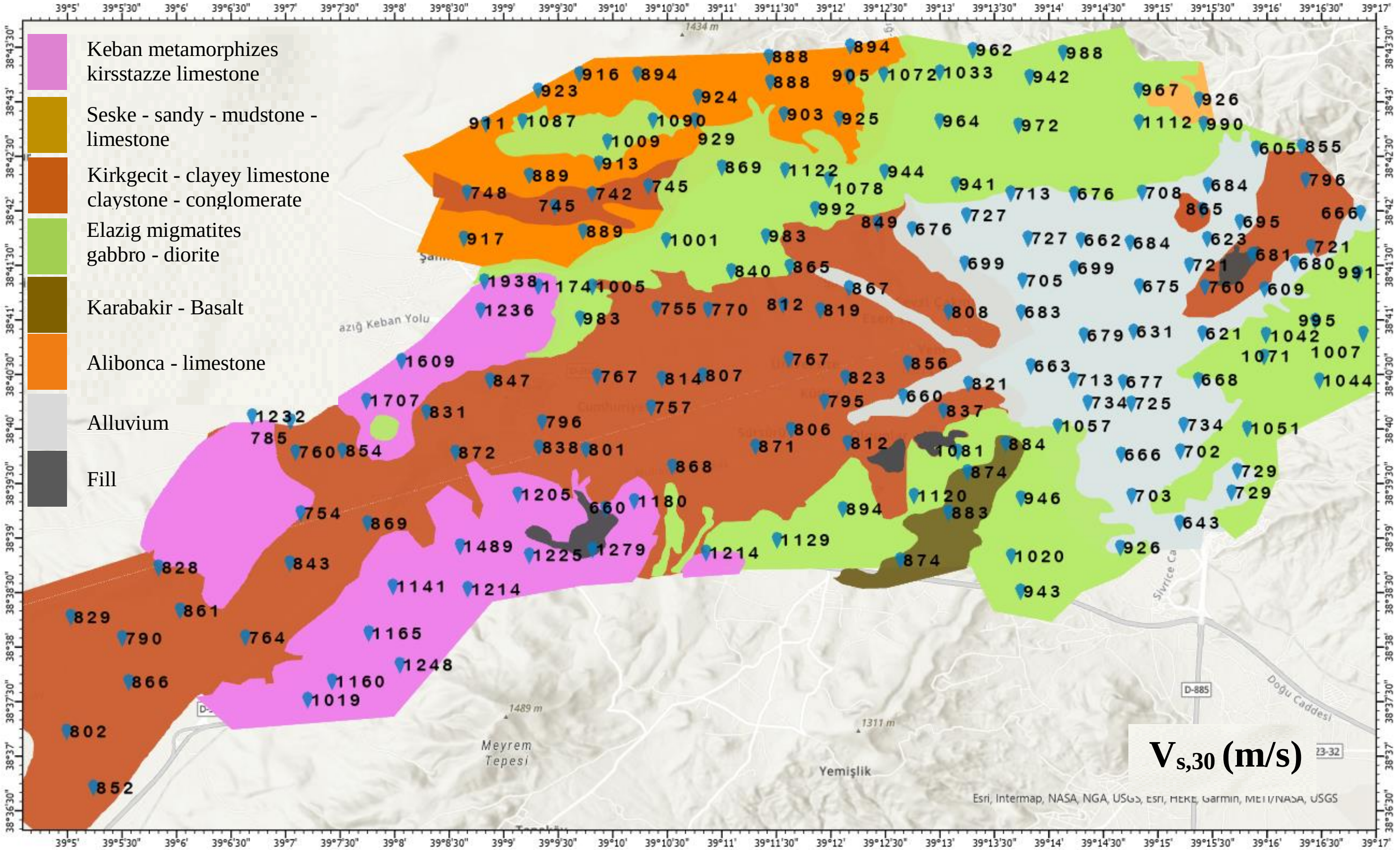

Figure 7.13. Vs_{30} plotted on the geological map of Elazig-Center

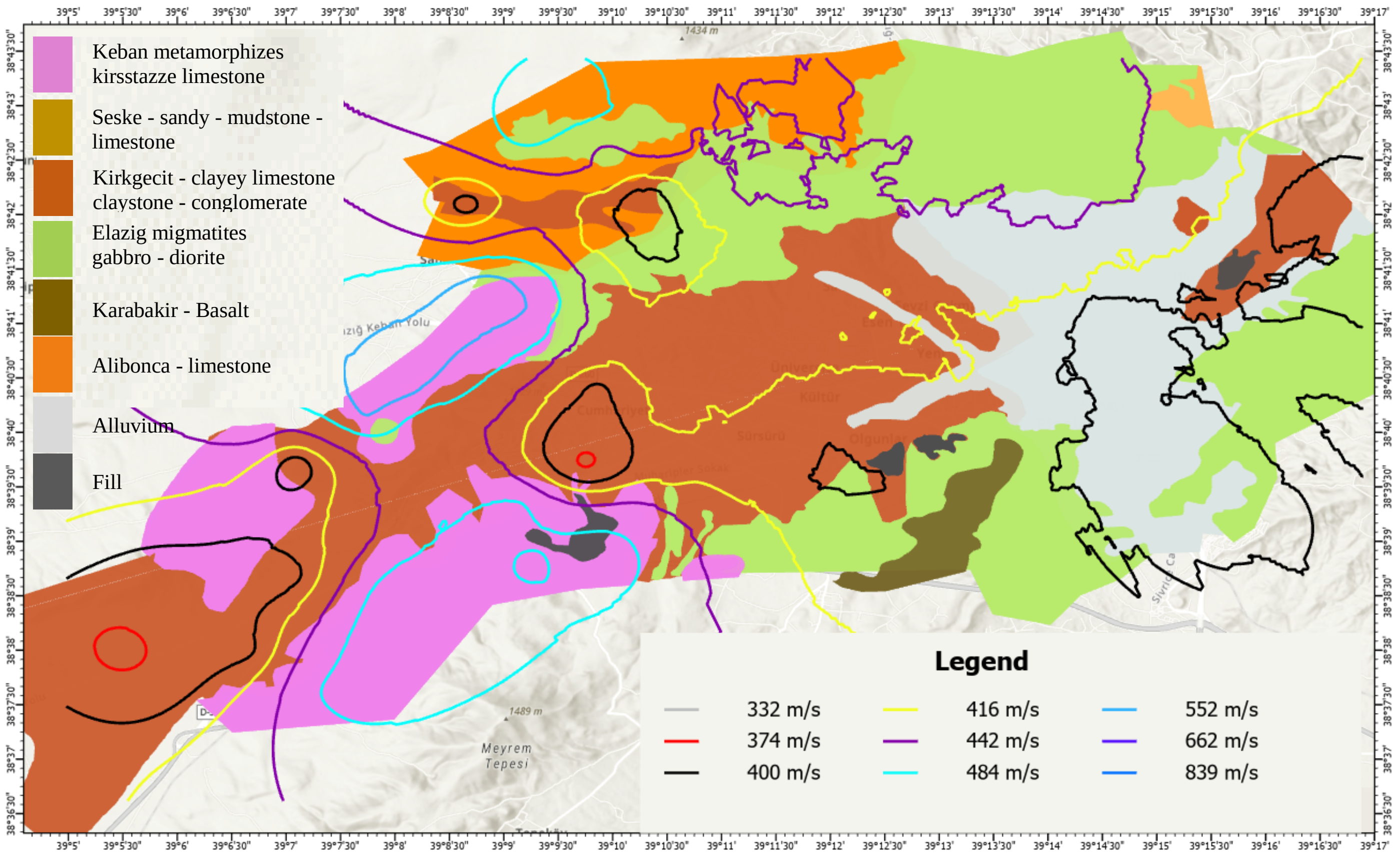

Figure 7.14. Contours for Vs measured for the first layer using seismic refraction tests and plotted on the geological map of Elazig-Center

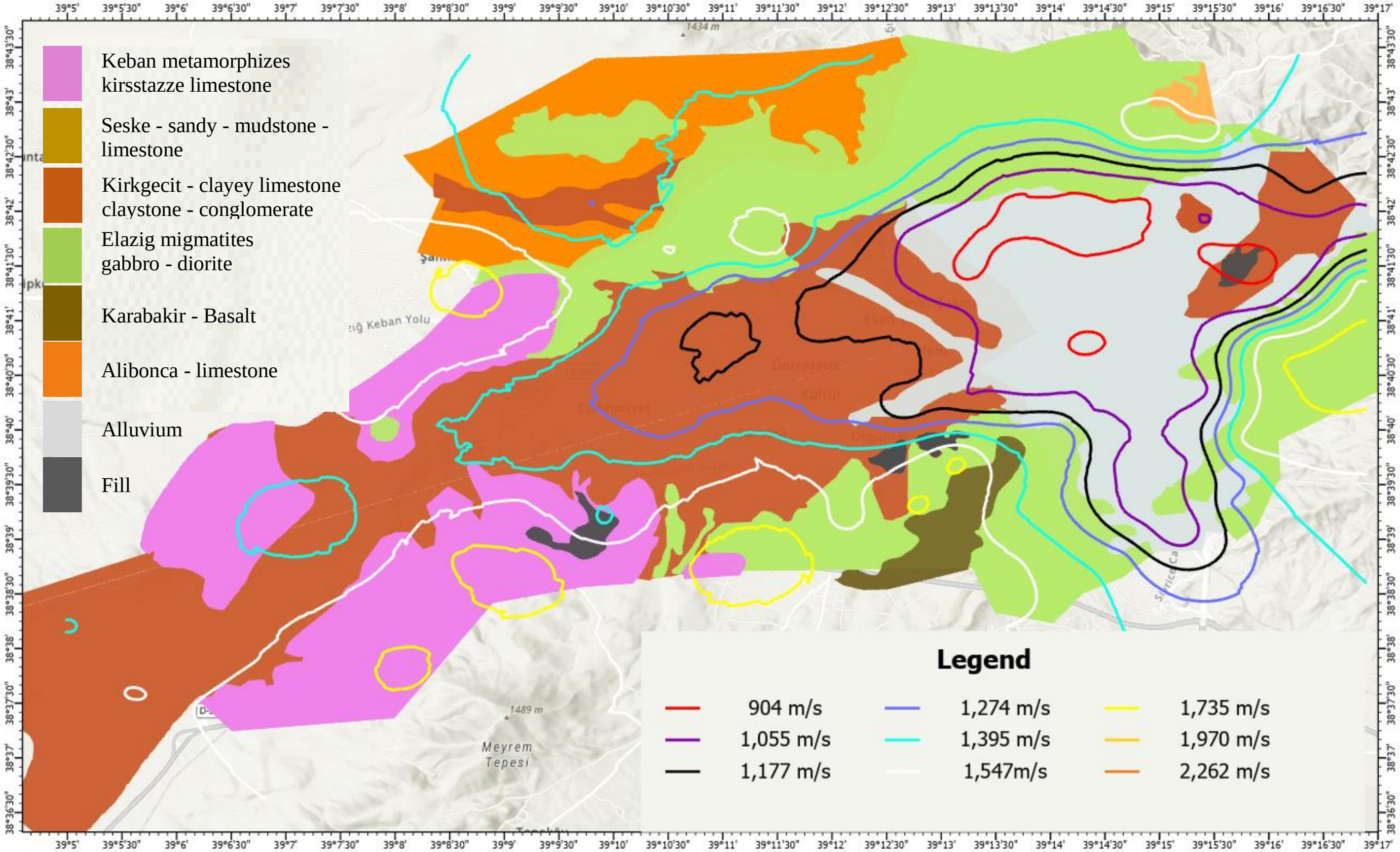

Figure 7.15. Contours for Vs measured for the 2nd layer using seismic refraction tests and plotted on the geological map of Elazig-Center

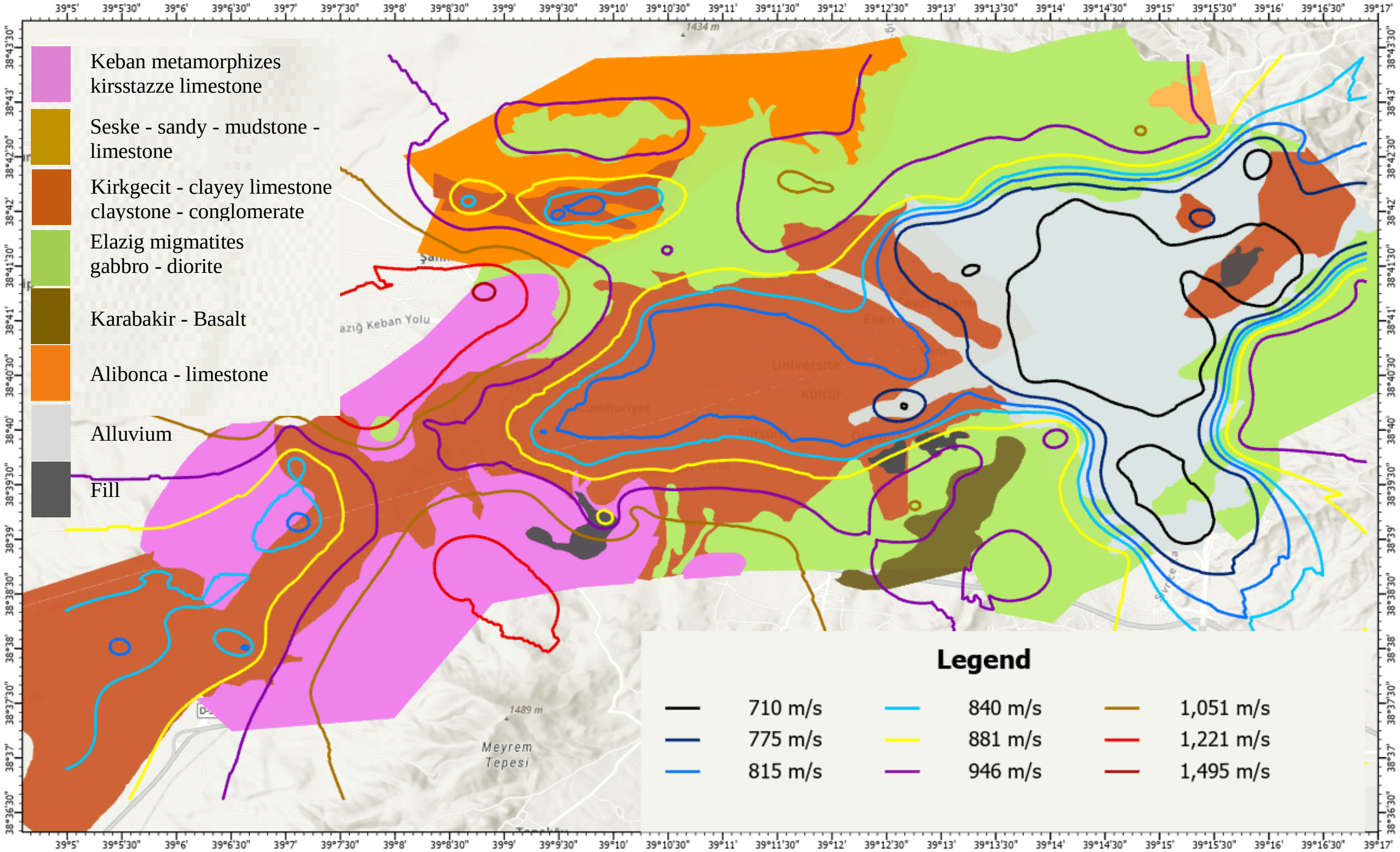

S

Figure 7.16. Contours for Vs_{30} plotted on the geological map of Elazig-Center

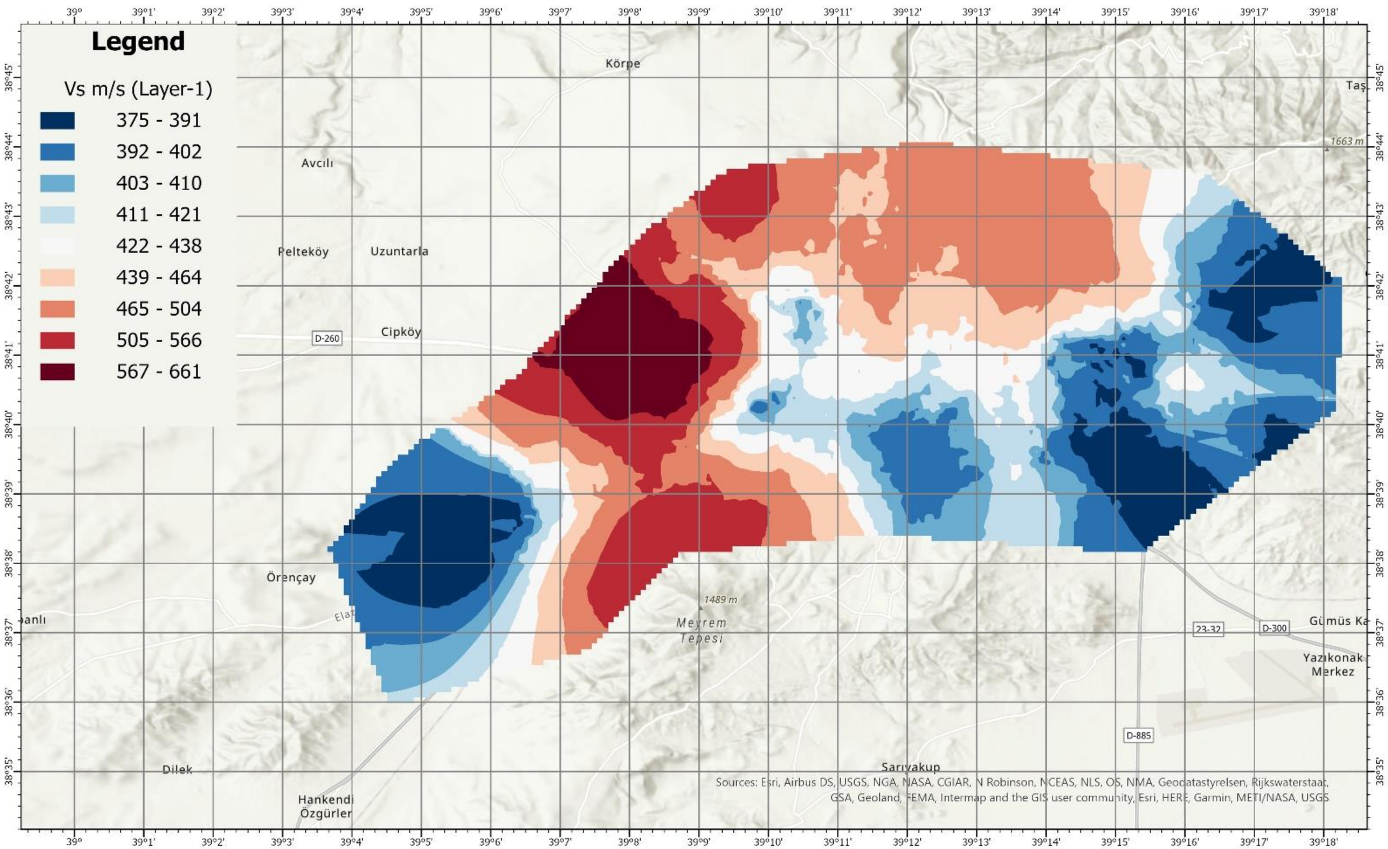

Figure 7.17. Shear wave velocity zonation for the 1st layer measured using seismic refraction tests on Elazig - Center

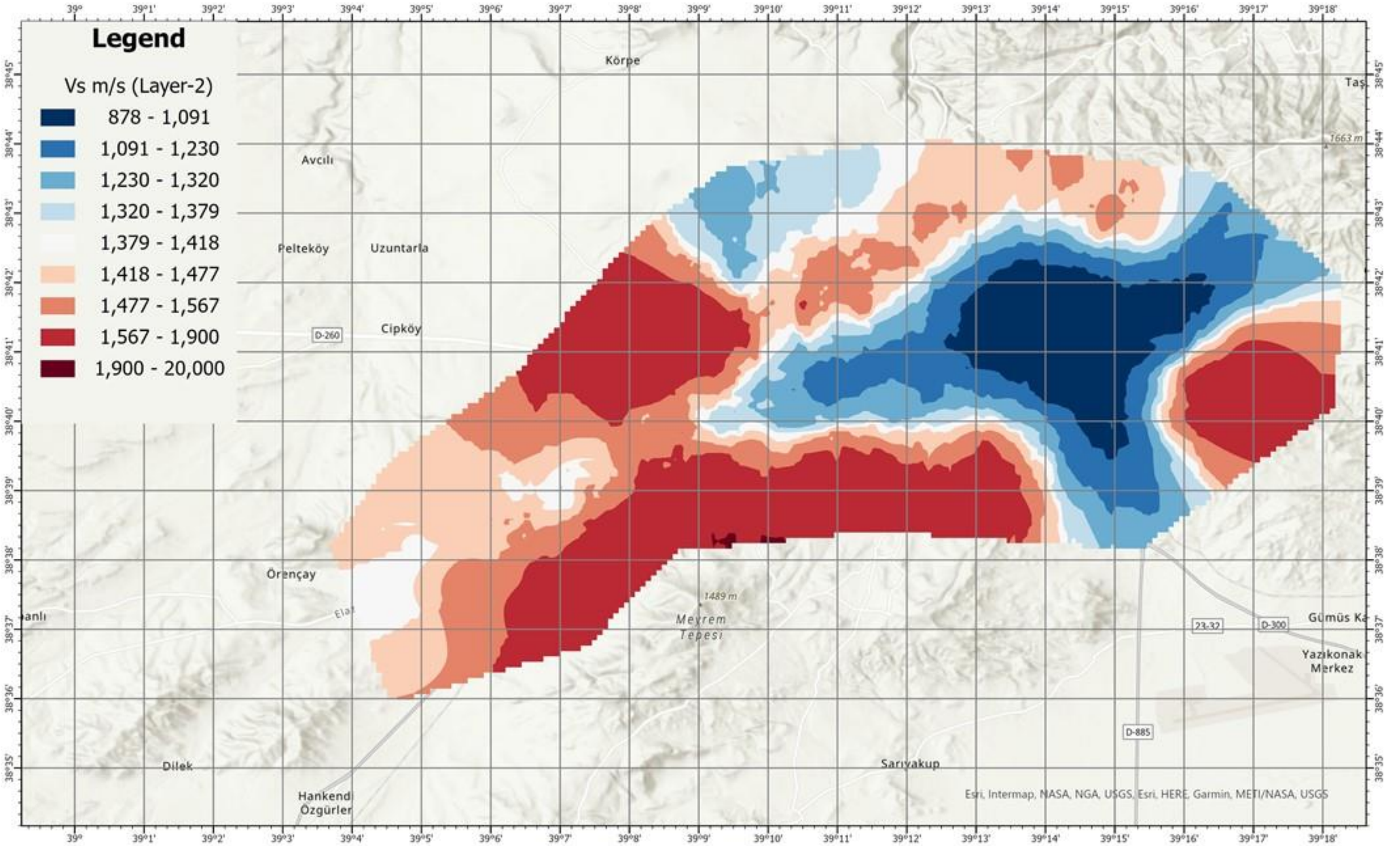

Figure 7.18. Shear wave velocity zonation for the 2nd layer measured using seismic refraction tests on Elazig - Center

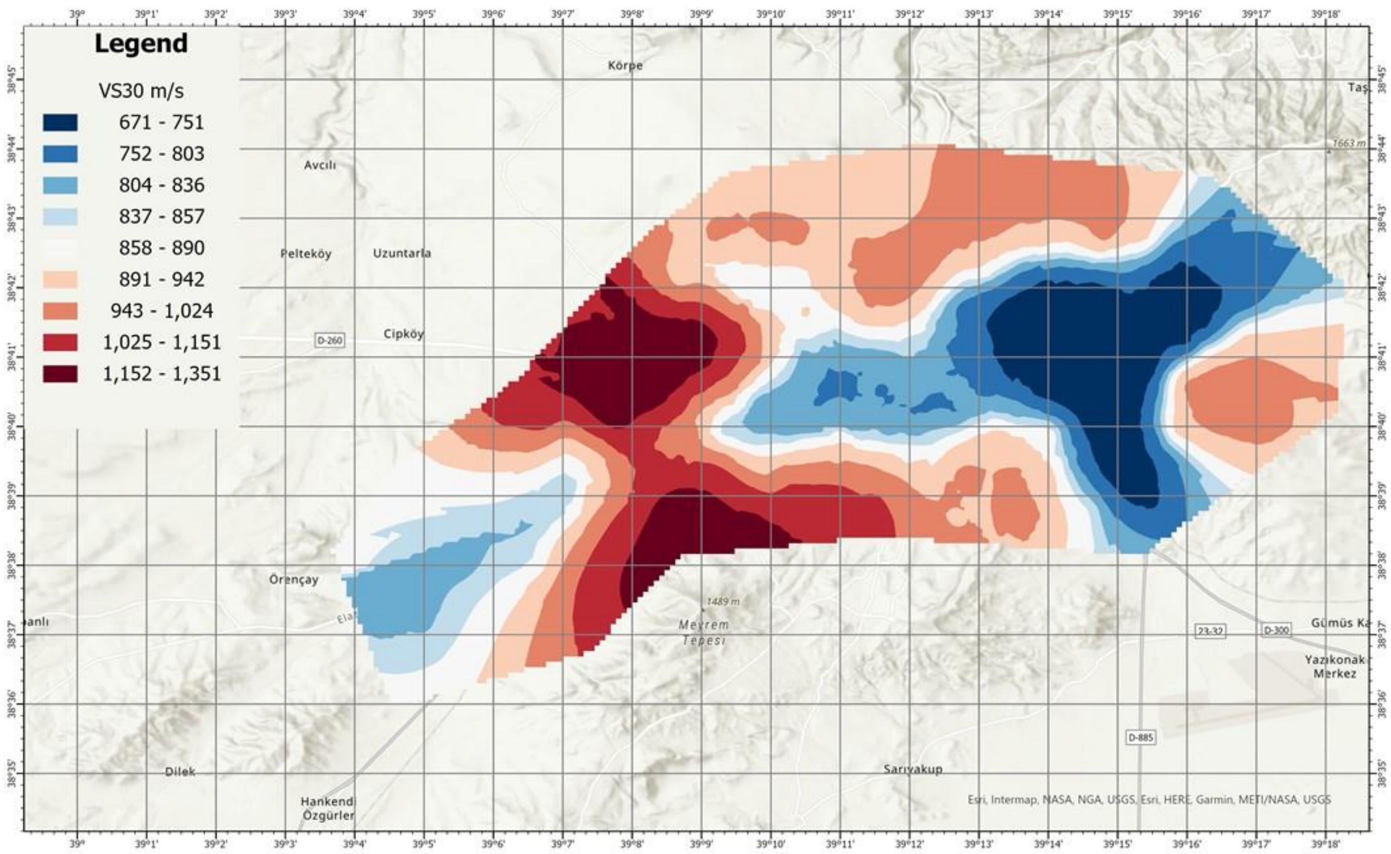

Figure 7.19. Vs_{30} zonation on Elazig - Center

7.3.2 Seismic Zonation Maps

Seismic zonation models "also known as seismic hazard risk models," have been developed, in this section, utilizing raster computing methods, using the ArcGIS software tool, to provide information on locations of considerable ground motion danger during an earthquake in the center of Elazig.

This section will include the seismic zonation maps prepared for the peak ground acceleration PGA, Spectral acceleration Sa at different periods, and liquefaction hazard maps.

7.3.2.1 Peak Ground Acceleration Maps

In this research, site-specific seismic response analyses were conducted in Chapter-5; one of the most significant outputs one may get from such analyses is the peak ground acceleration PGA.

To help envision how the PGA values are distributed over the study area and better understand the region's seismicity, seismic zonation maps are prepared using the ArcGIS software tool. Their main maps are prepared

- Scatter discrete PGA and amplification maps where the real output values obtained from the site response analyses were plotted on the geological settings Elazig-Center (Figure 7.20)
- Contour maps for the interpolated PGA values generated over the geological map of the study region; the Empirical Bayesian Kriging interpolation algorithm was used for the generation of the map (Figure 7.21).
- Zonation maps for the PGA values and PGA amplifications were generated using kriging interpolation and adopting the Exponential Semi-variogram model (Figure 7.22).

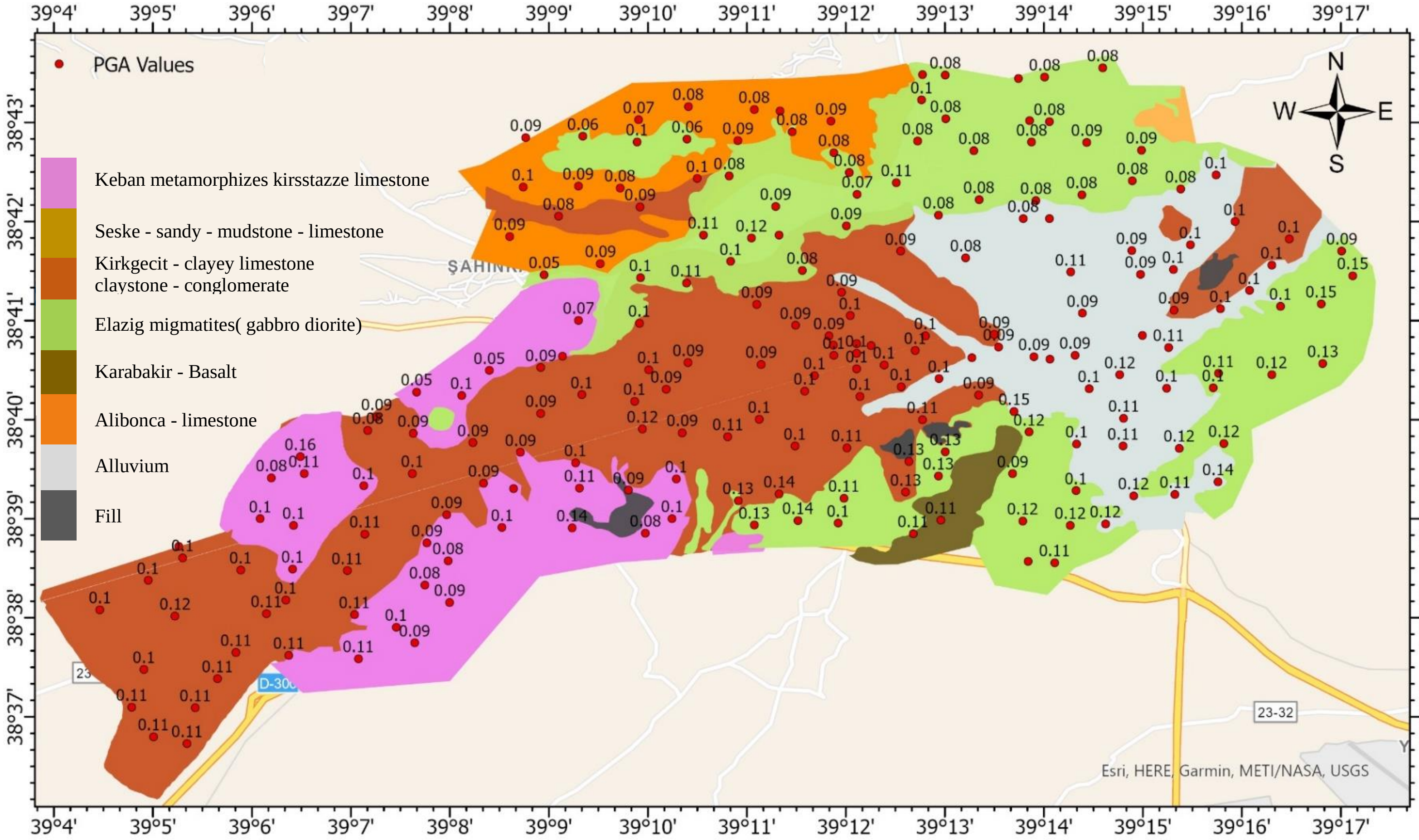

Figure 7.20. Discrete PGA values plotted on the geological Map of Elazig-Center

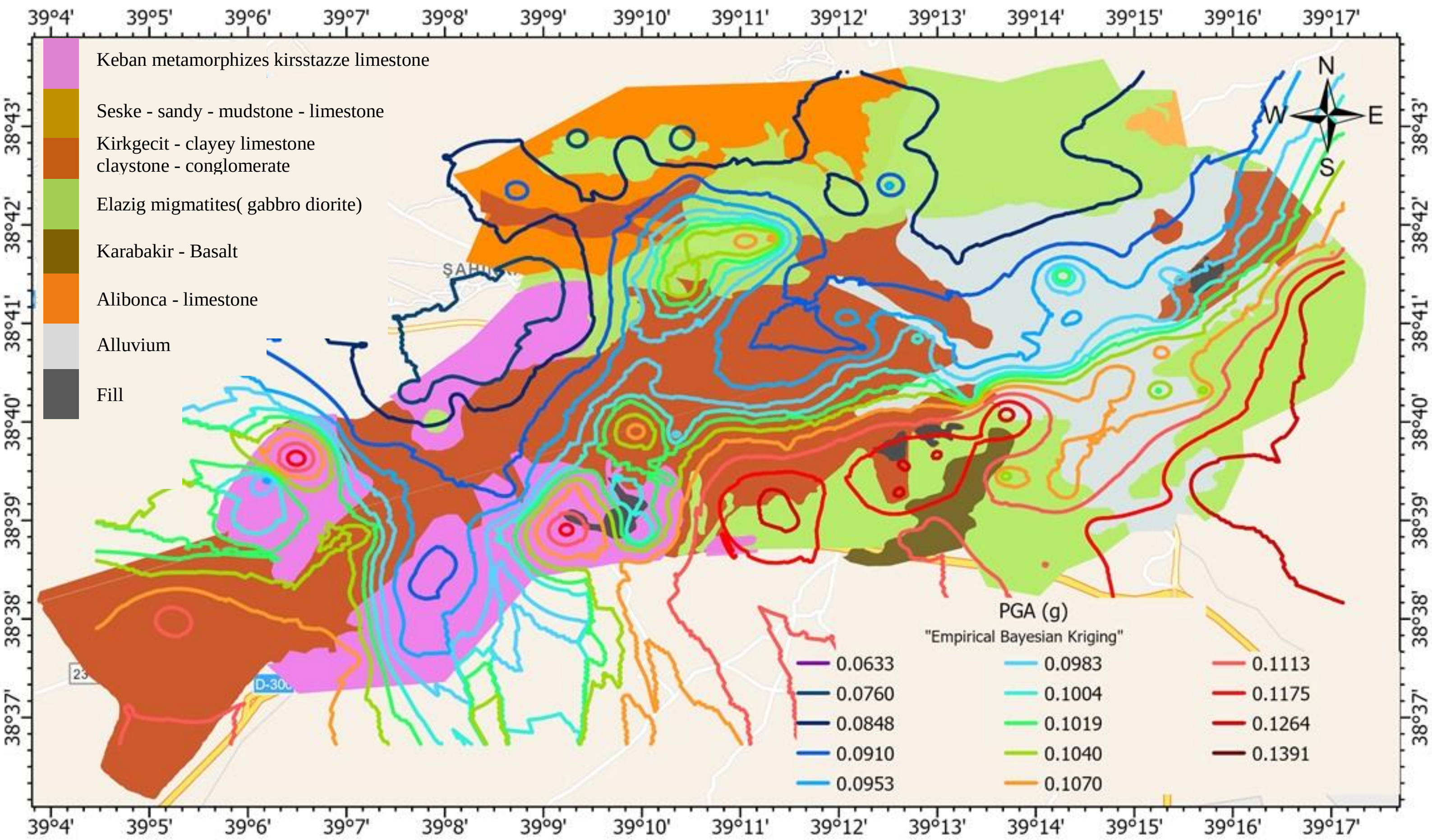

Figure 7.21. PGA contours plotted on the geological Map of Elazig-Center using empirical bayesian kriging

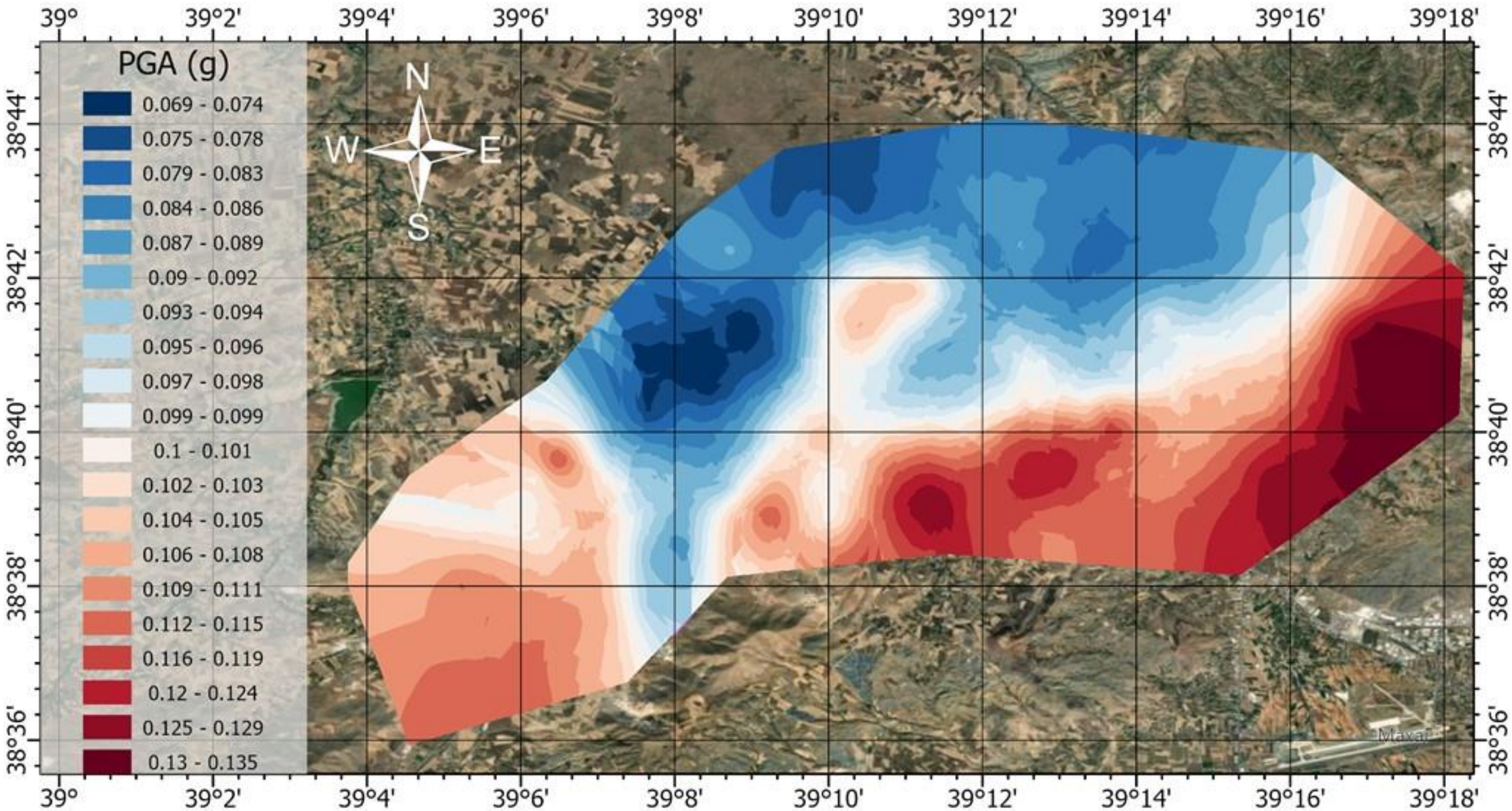

Figure 7.22. PGA (g) zonation map of Elazig-Center

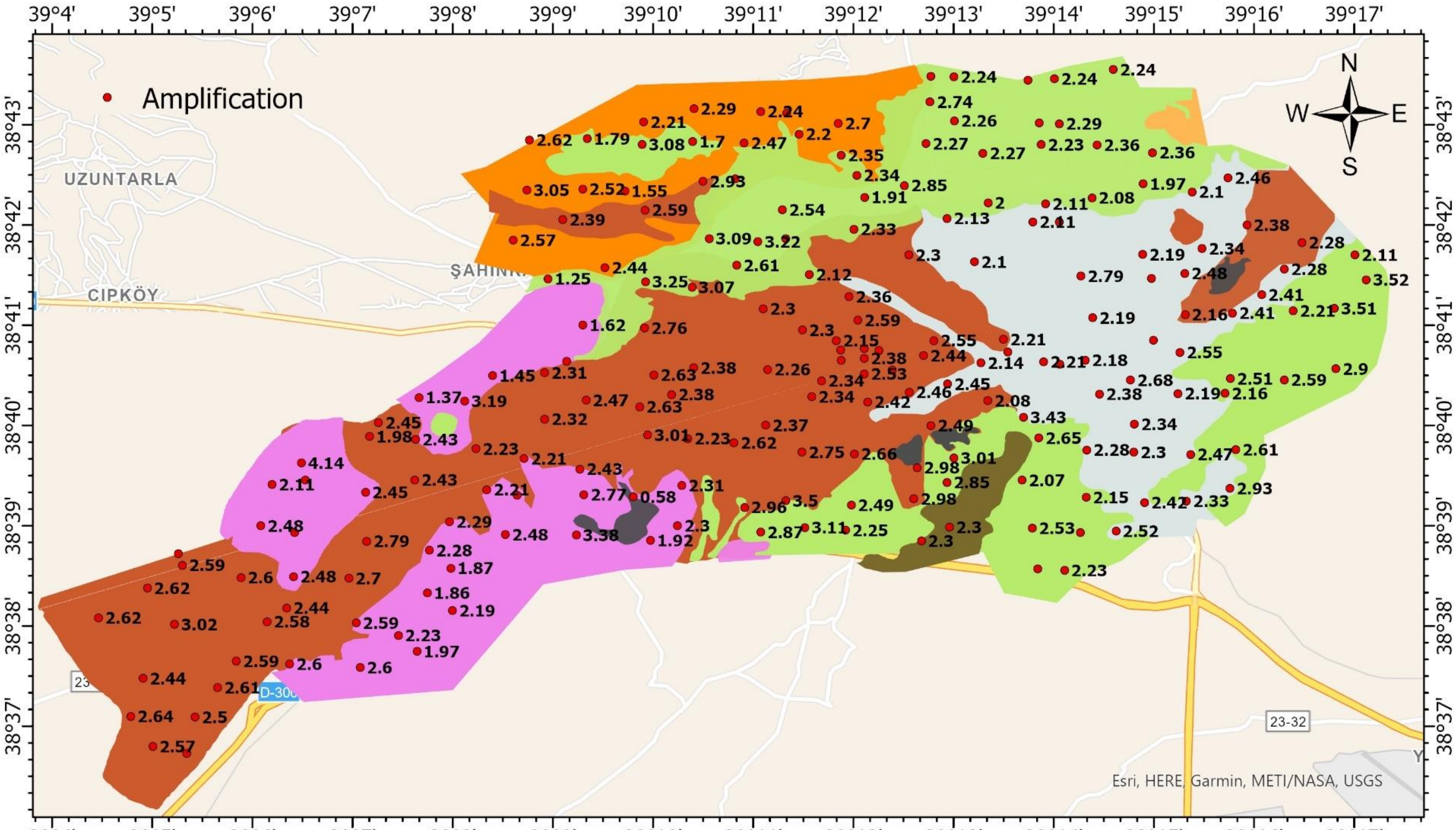

Figure 7.23. Discrete PGA Amplification values plotted on the geological Map of Elazig-Center

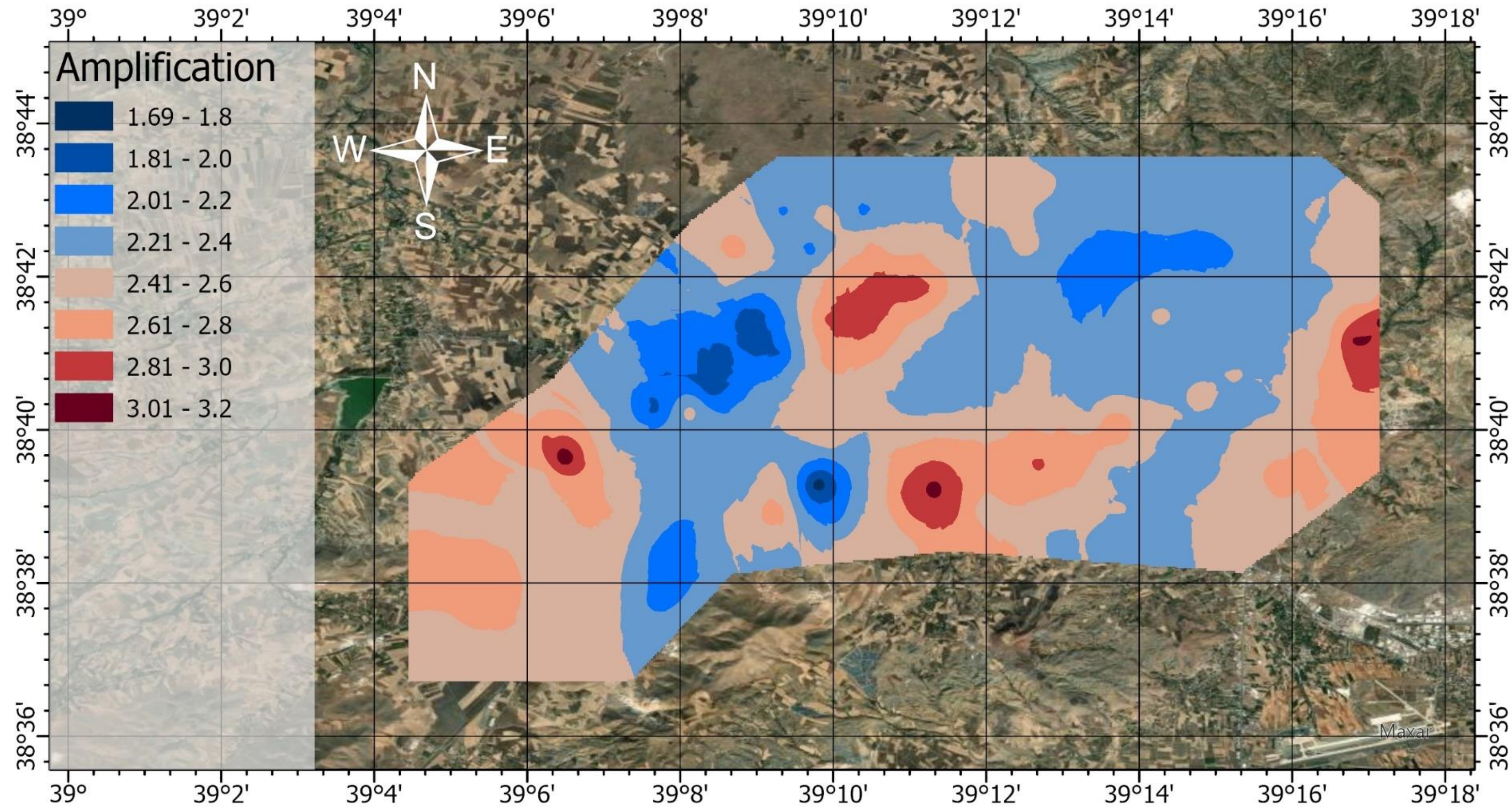

Figure 7.24. PGA amplification zonation map of Elazig-Center

7.3.2.2 Spectral Acceleration Maps

A building's ability to withstand shaking at its foundation relies, of course, on the quality of the structure. However, It is crucial to keep in mind that the building's height is a major consideration. In other words, the frequency at which it naturally tends to vibrate is its fundamental period or natural frequency. High-rise buildings (which have a low natural frequency) have a completely different response than shorter buildings (with a much higher natural frequency).

When the natural frequency of the ground motion corresponds with the structure's natural frequency, buildings have a high likelihood of achieving (partial) resonance. Resonance increases the swing of the structure, and if the period of amplification is long enough, amplification of ground motion might result in damage or destruction. Specific ground conditions may result in resonance and severe amplification of the seismic signal; however, this may have little effect if the frequencies at which this happens are much beyond the normal frequency range of the building.

As a result, determining the spectral acceleration or the seismic amplification at various frequencies or periods is critical. The Sa values are determined in Chapter-5, conducting site response analyses at various locations. In this section, to provide a big picture of the situation, Sa zonation maps are provided (for T=0.1 s, T=0.2 s, T=0.3 s, T=0.4 s, T=0.5 s, T=0.6 s, T=0.7 s, T=0.8 s, T=0.9 s, T=1 s, T=1.5 s, T=2 s, T=3 s, T=4, s and T=5 s.)

In general, two types of maps are provided for the spectral acceleration plots; discrete scattered maps plotted on the geological settings Elazig-Center, and zonation maps generated using kriging interpolation methodology.

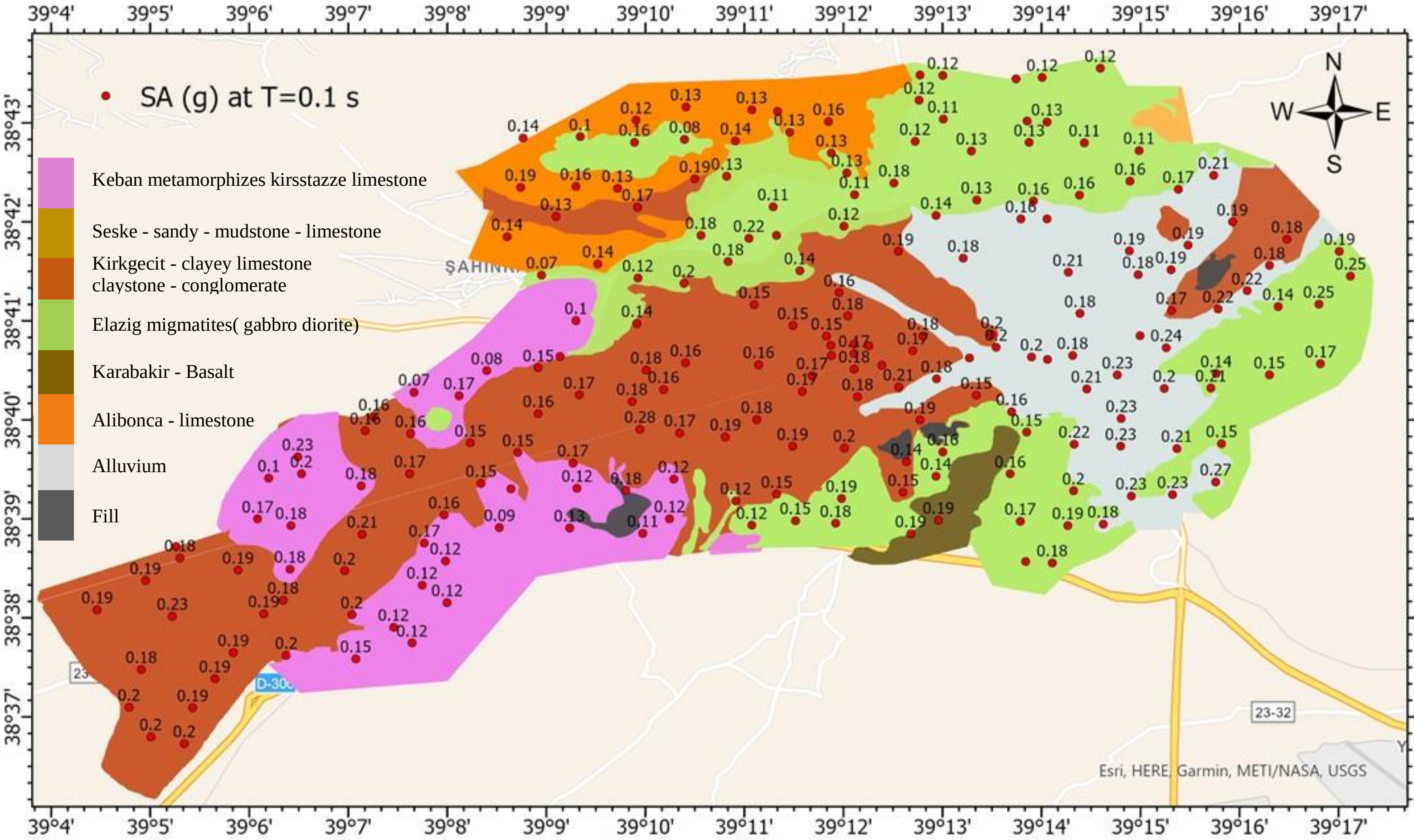

Figure 7.25. Discrete SA values at T=0.1 (s) plotted on the geological Map of Elazig-Center

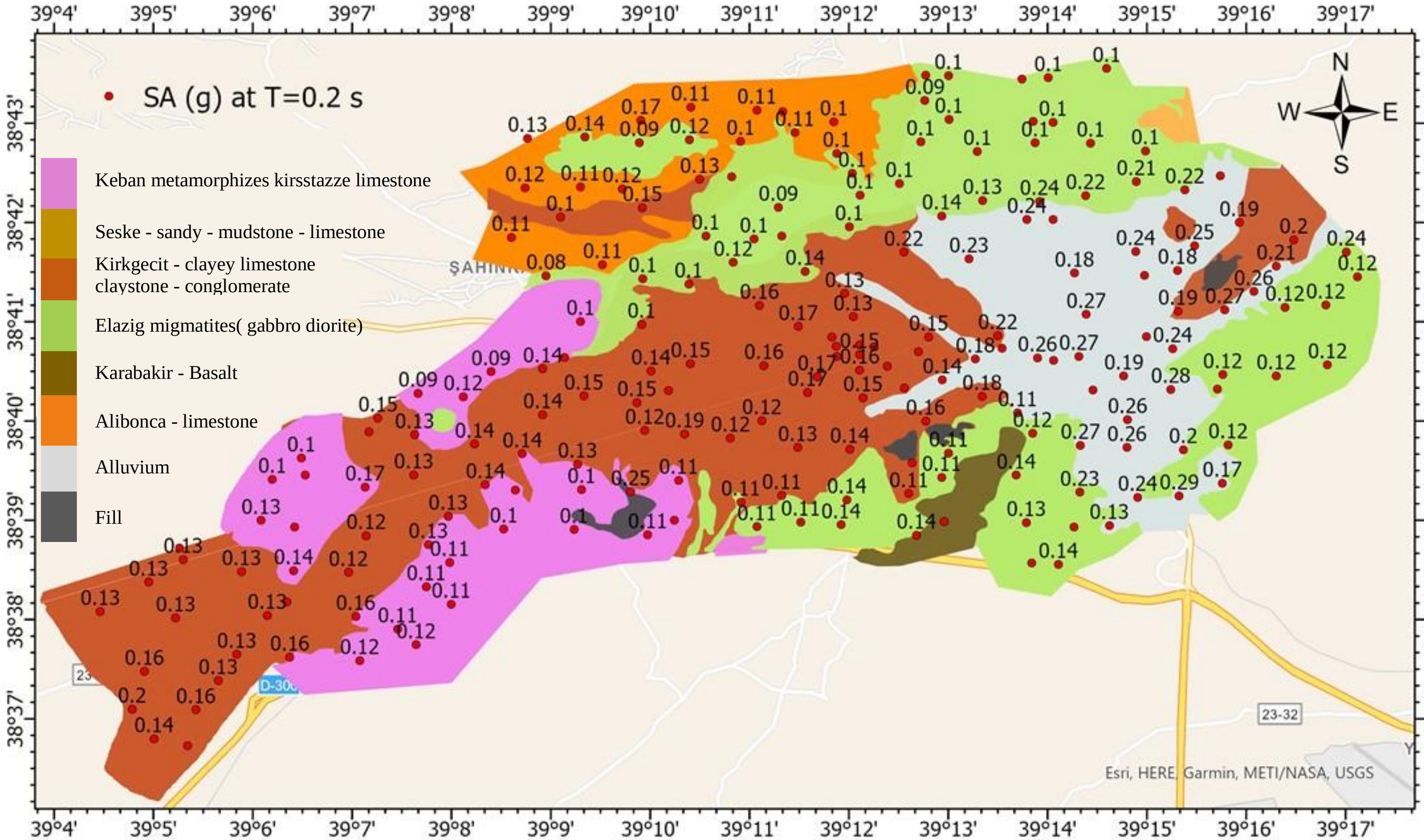

Figure 7.26. Discrete SA values at T=0.2 (s) plotted on the geological Map of Elazig-Center

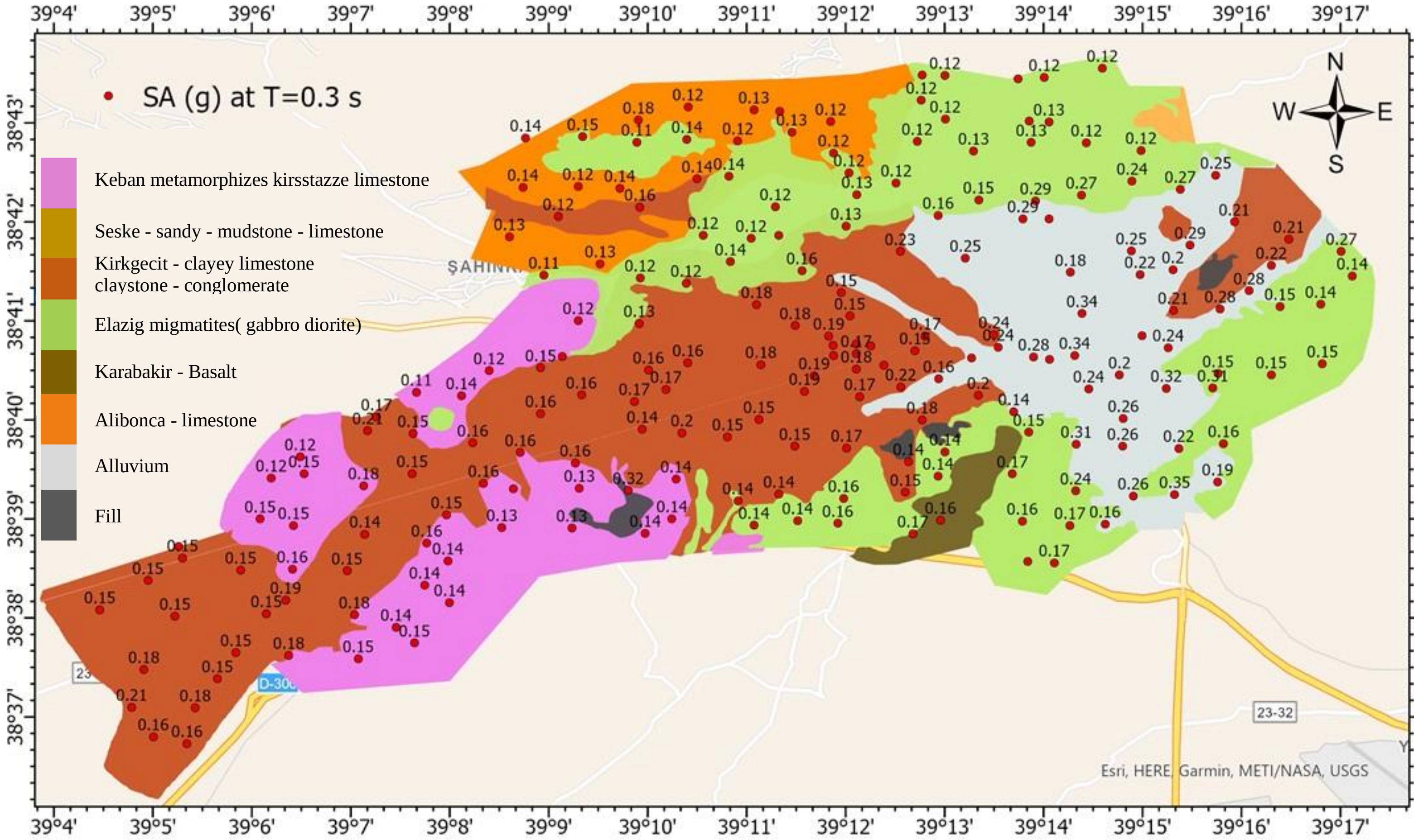

Figure 7.27. Discrete SA values at T=0.3 (s) plotted on the geological Map of Elazig-Center

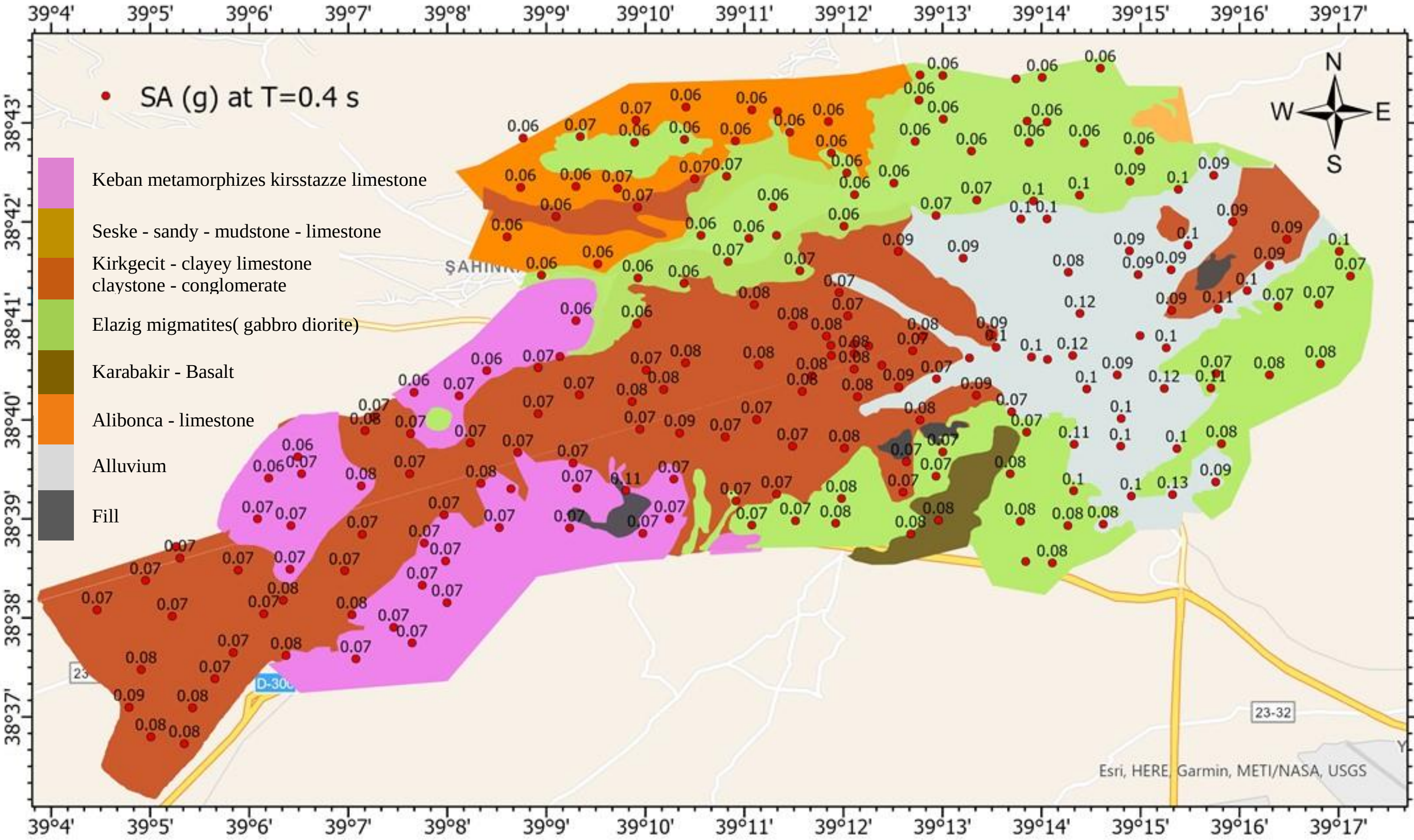

Figure 7.28. Discrete SA values at T=0.4 (s) plotted on the geological Map of Elazig-Center

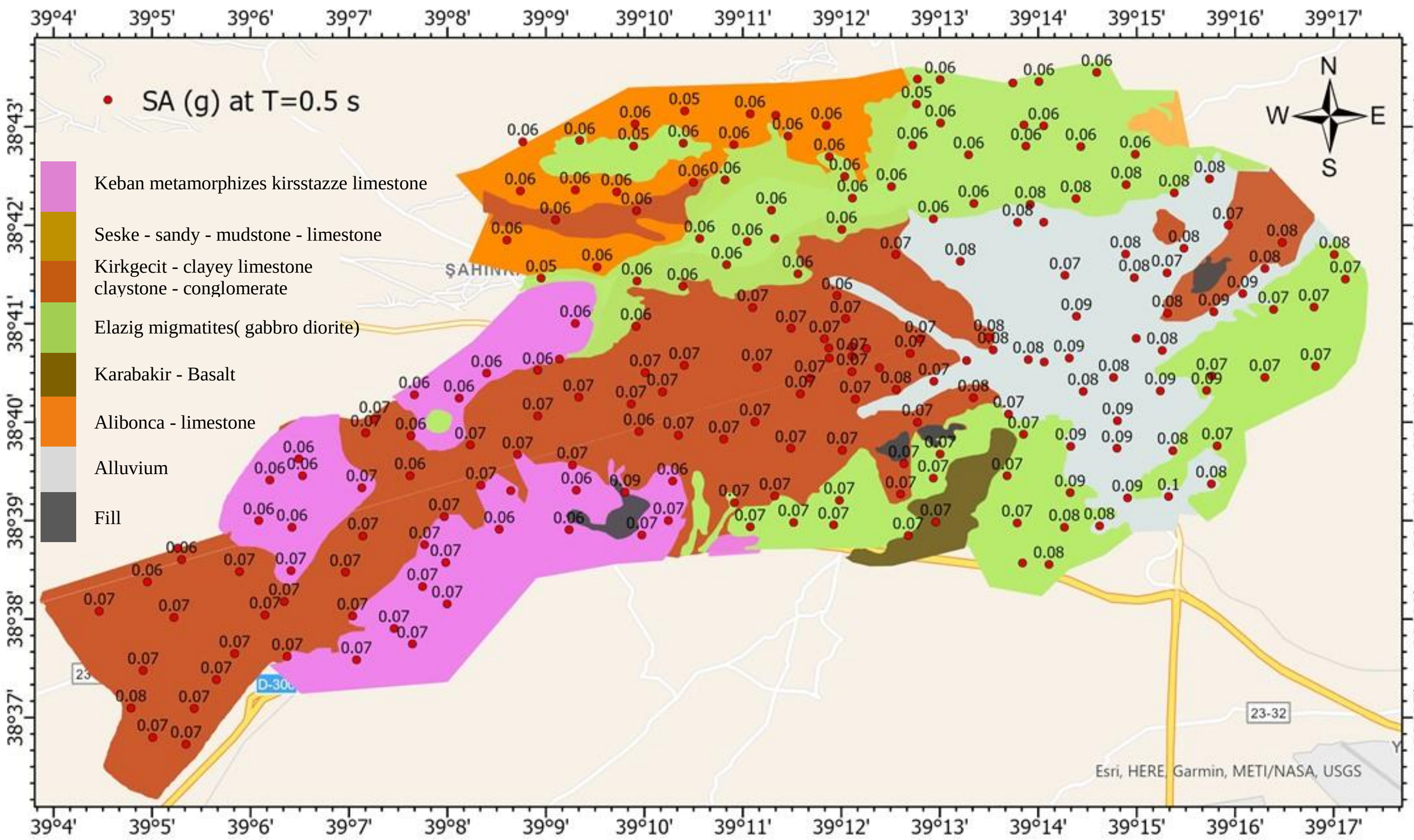

Figure 7.29. Discrete SA values at T=0.5 (s) plotted on the geological Map of Elazig-Center

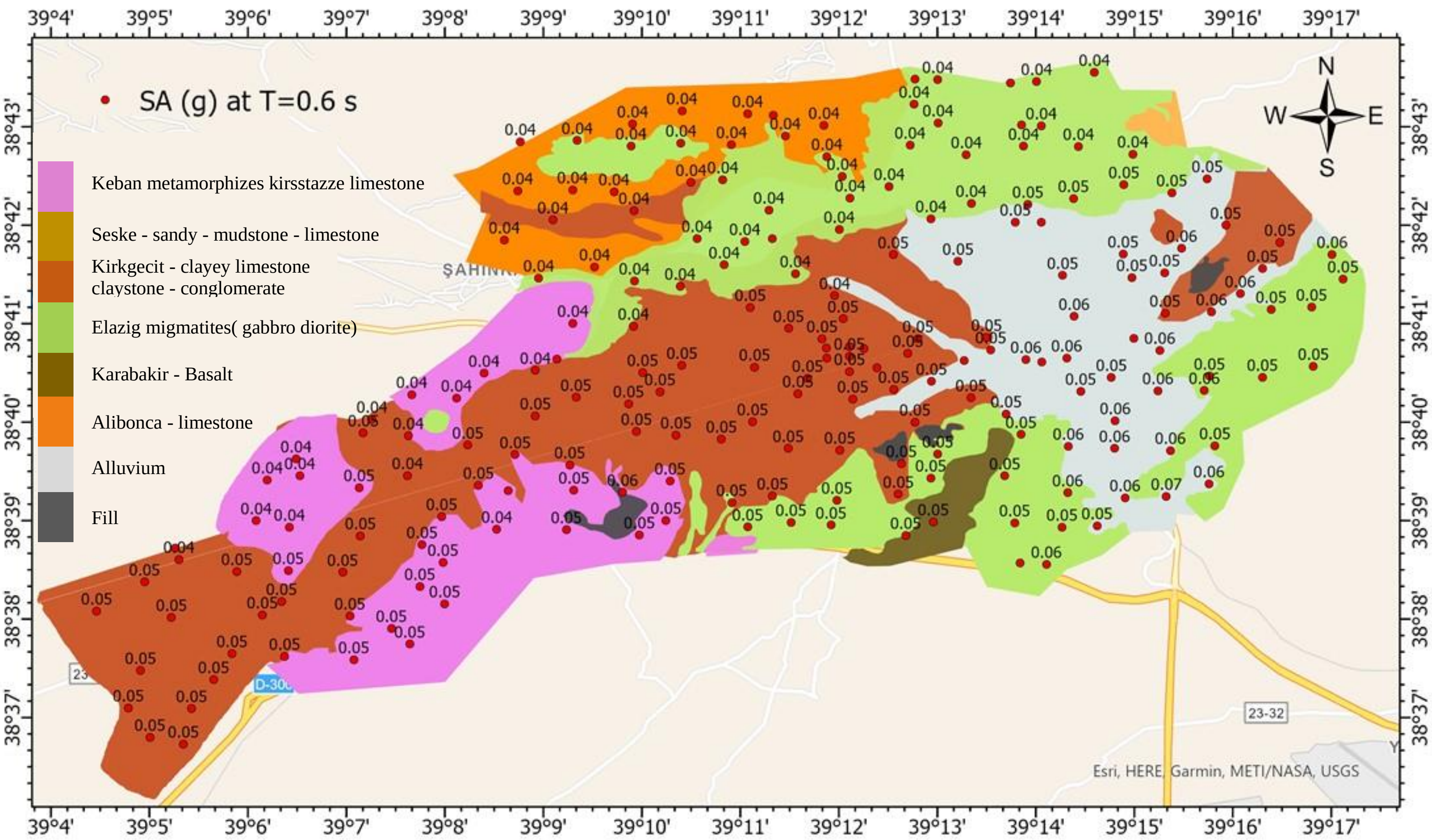

Figure 7.30. Discrete SA values at T=0.6 (s) plotted on the geological Map of Elazig-Center

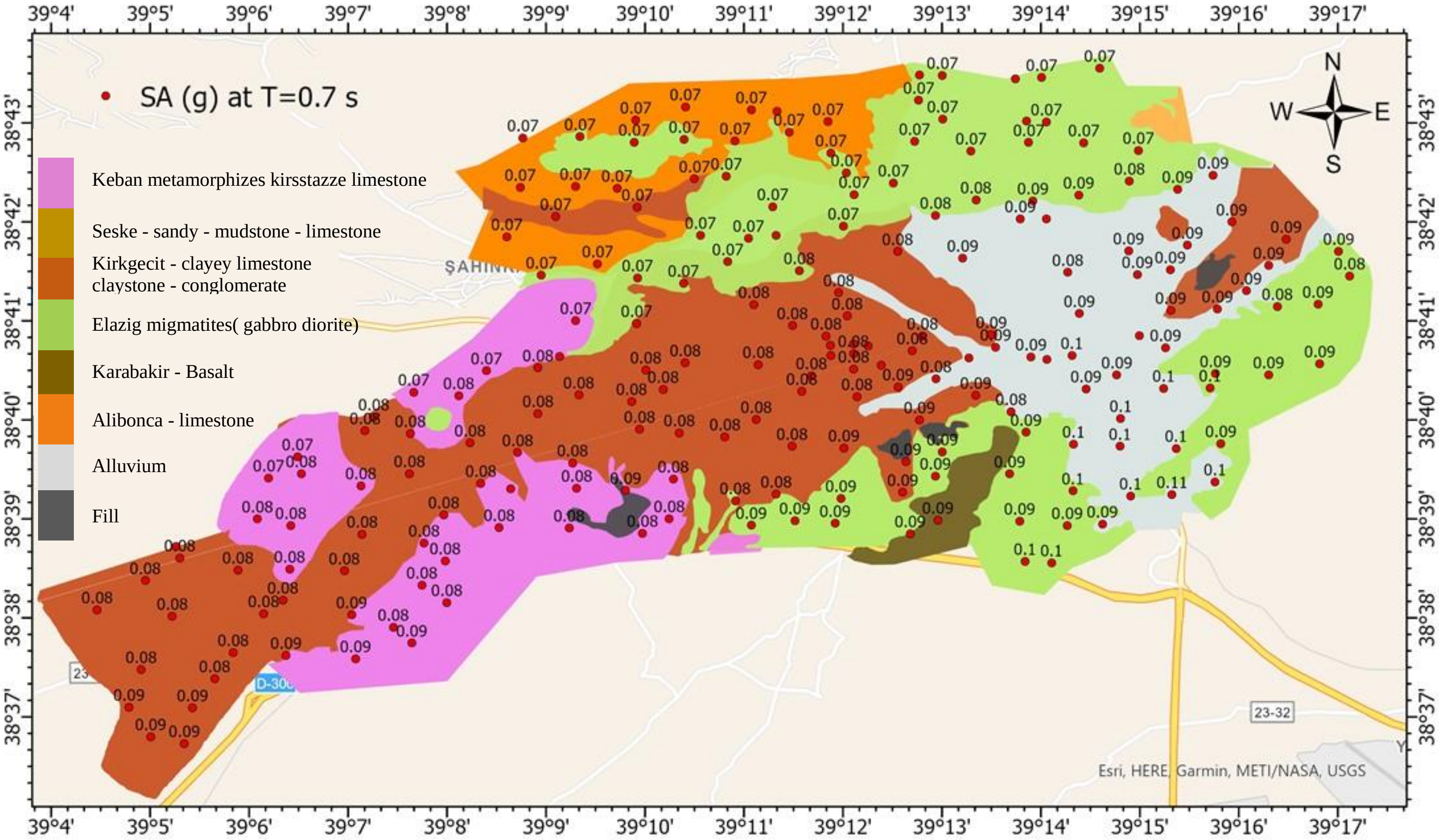

Figure 7.31. Discrete SA values at T=0.7 (s) plotted on the geological Map of Elazig-Center

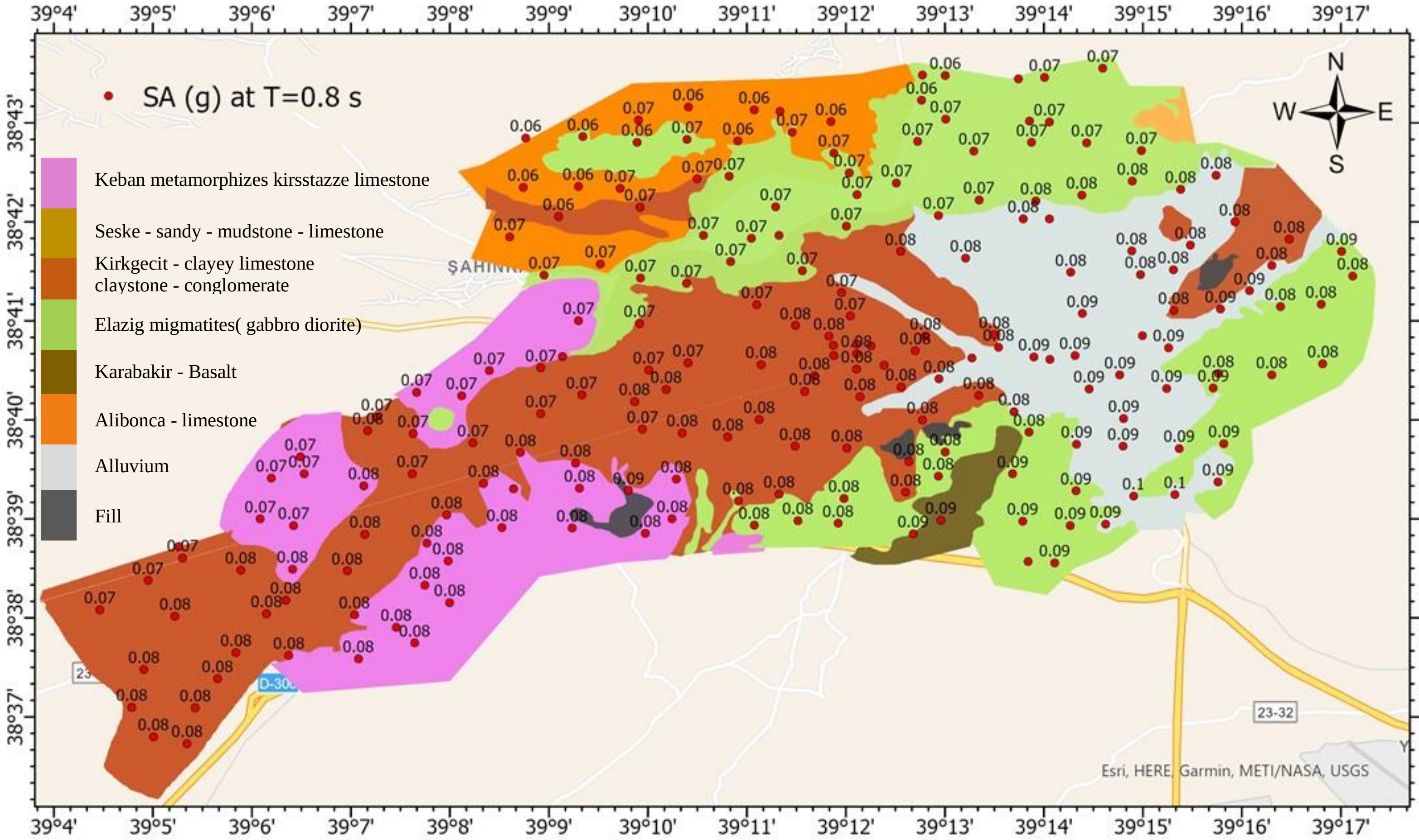

Figure 7.32. Discrete SA values at T=0.8 (s) plotted on the geological Map of Elazig-Center

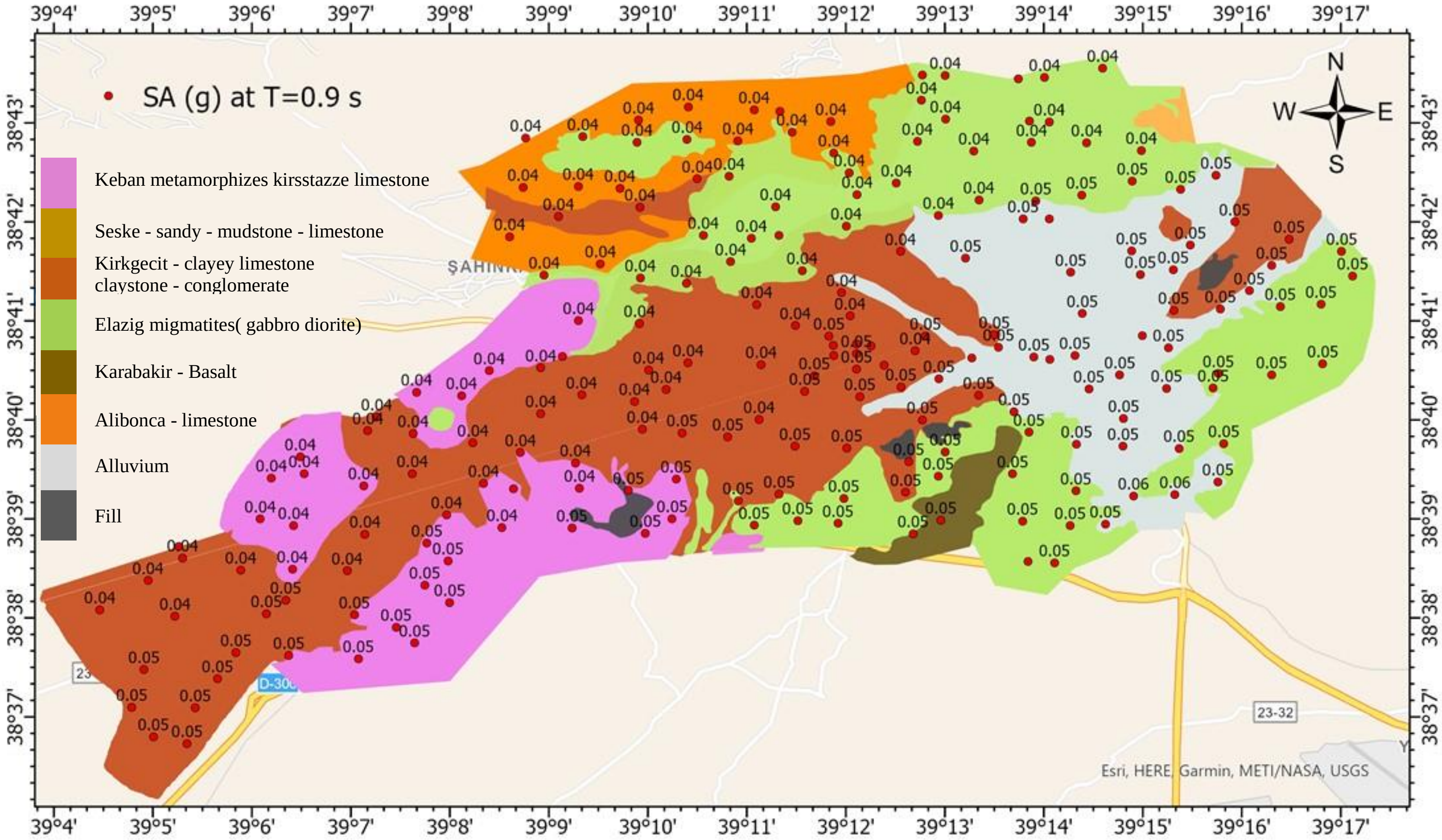

Figure 7.33. Discrete SA values at T=0.9 (s) plotted on the geological Map of Elazig-Center

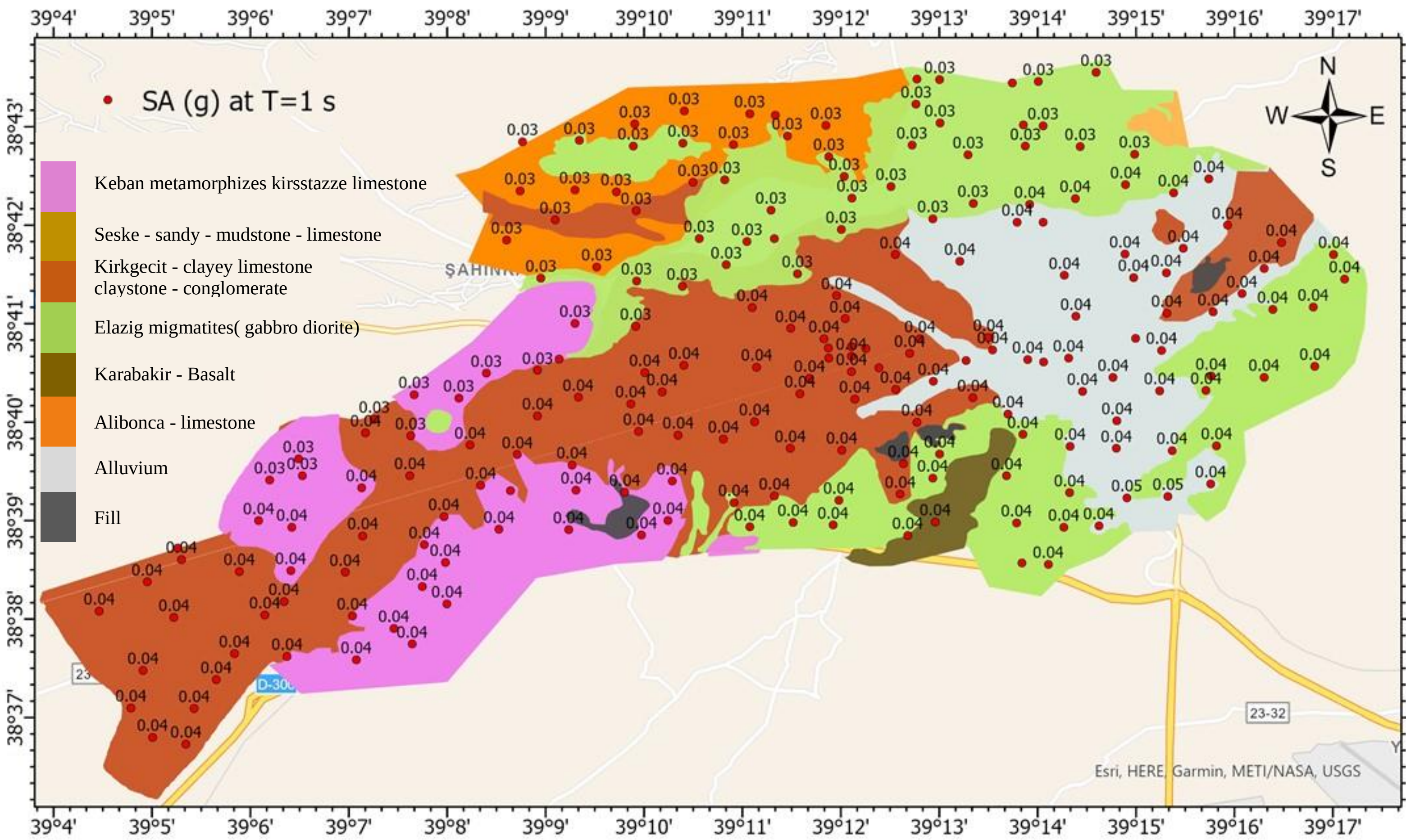

Figure 7.34. Discrete SA values at T=1 (s) plotted on the geological Map of Elazig-Center

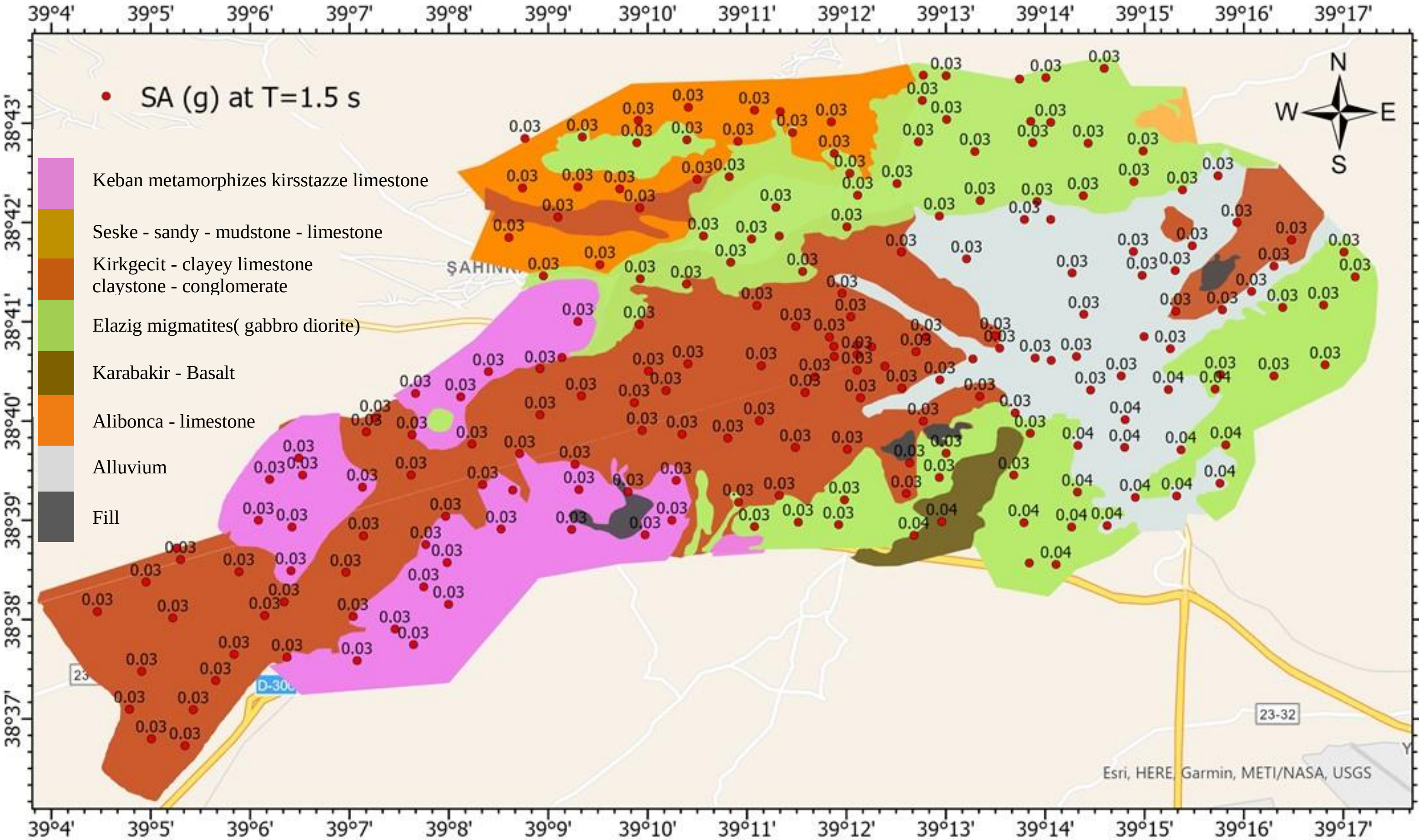

Figure 7.35. Discrete SA values at T=1.5 (s) plotted on the geological Map of Elazig-Center

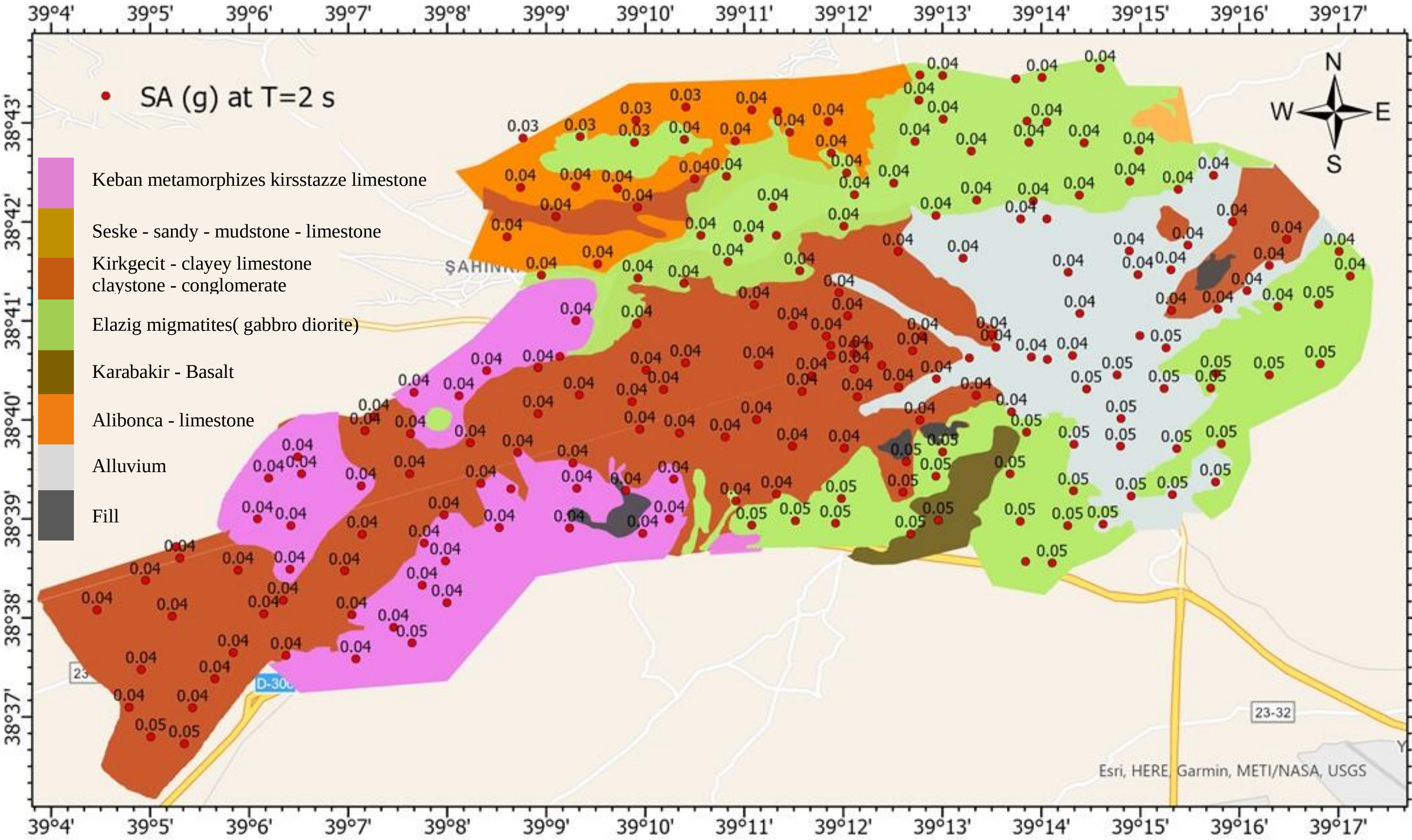

Figure 7.36. Discrete SA values at T=2 (s) plotted on the geological Map of Elazig-Center

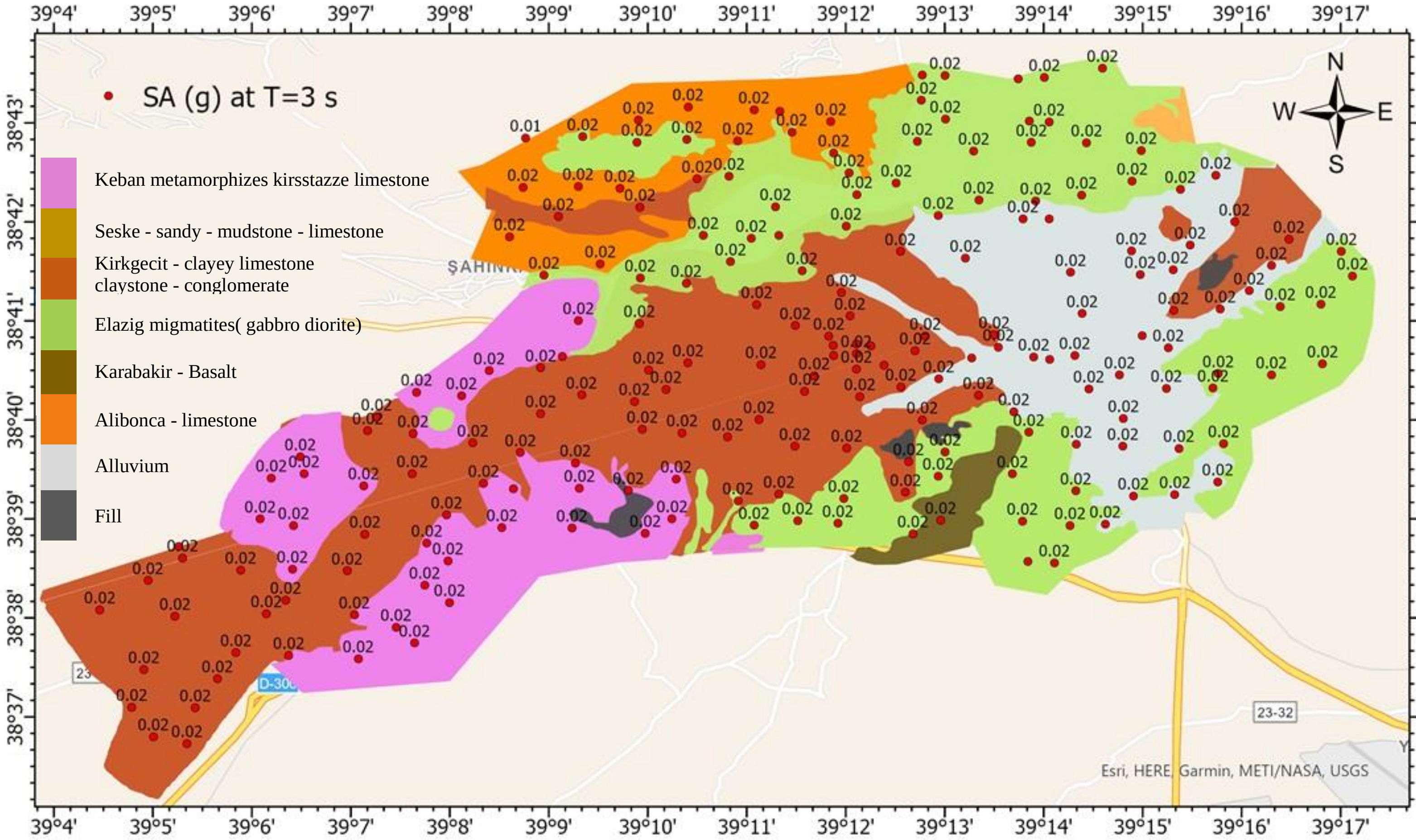

Figure 7.37. Discrete SA values at T=3 (s) plotted on the geological Map of Elazig-Center

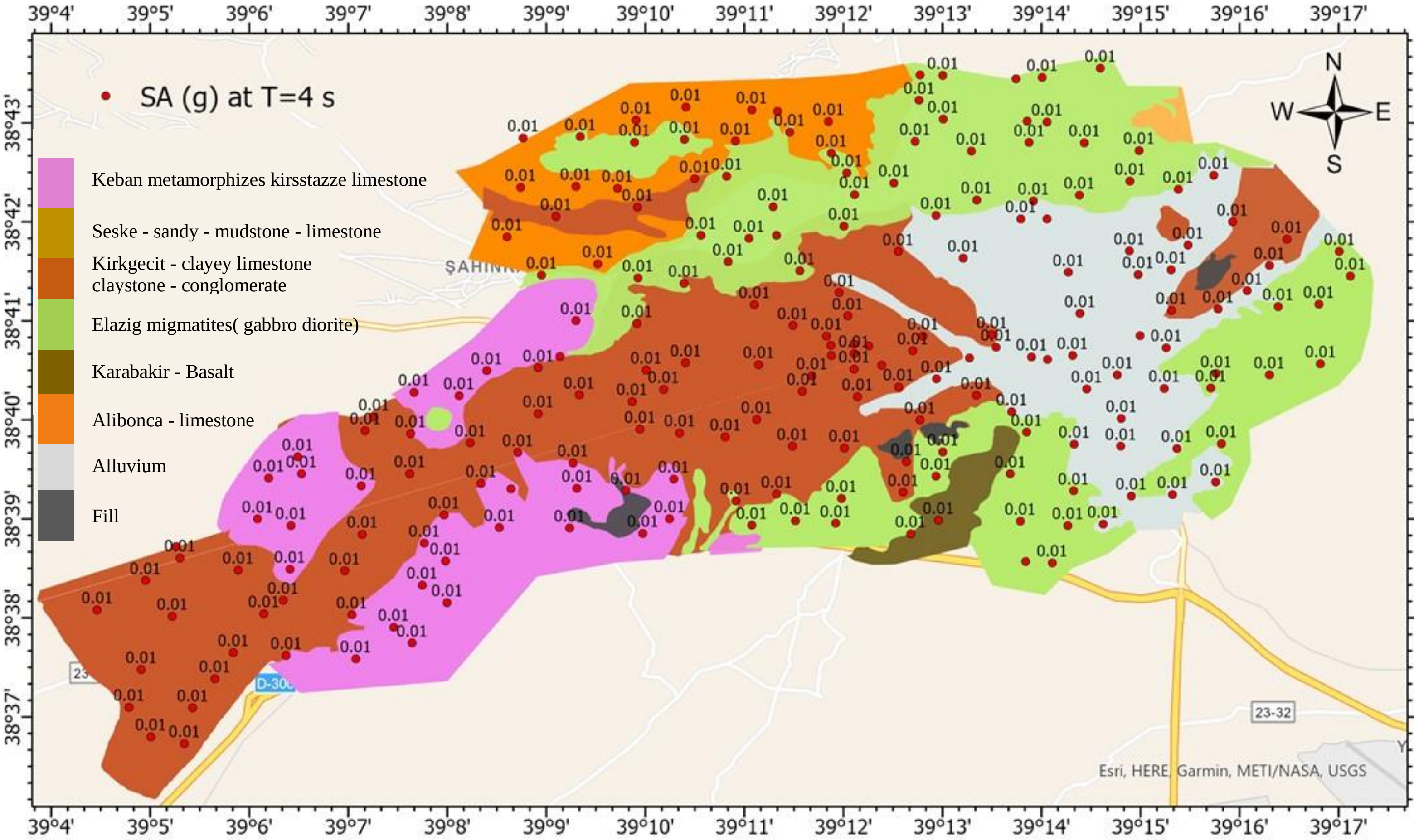

Figure 7.38. Discrete SA values at T=4 (s) plotted on the geological Map of Elazig-Center

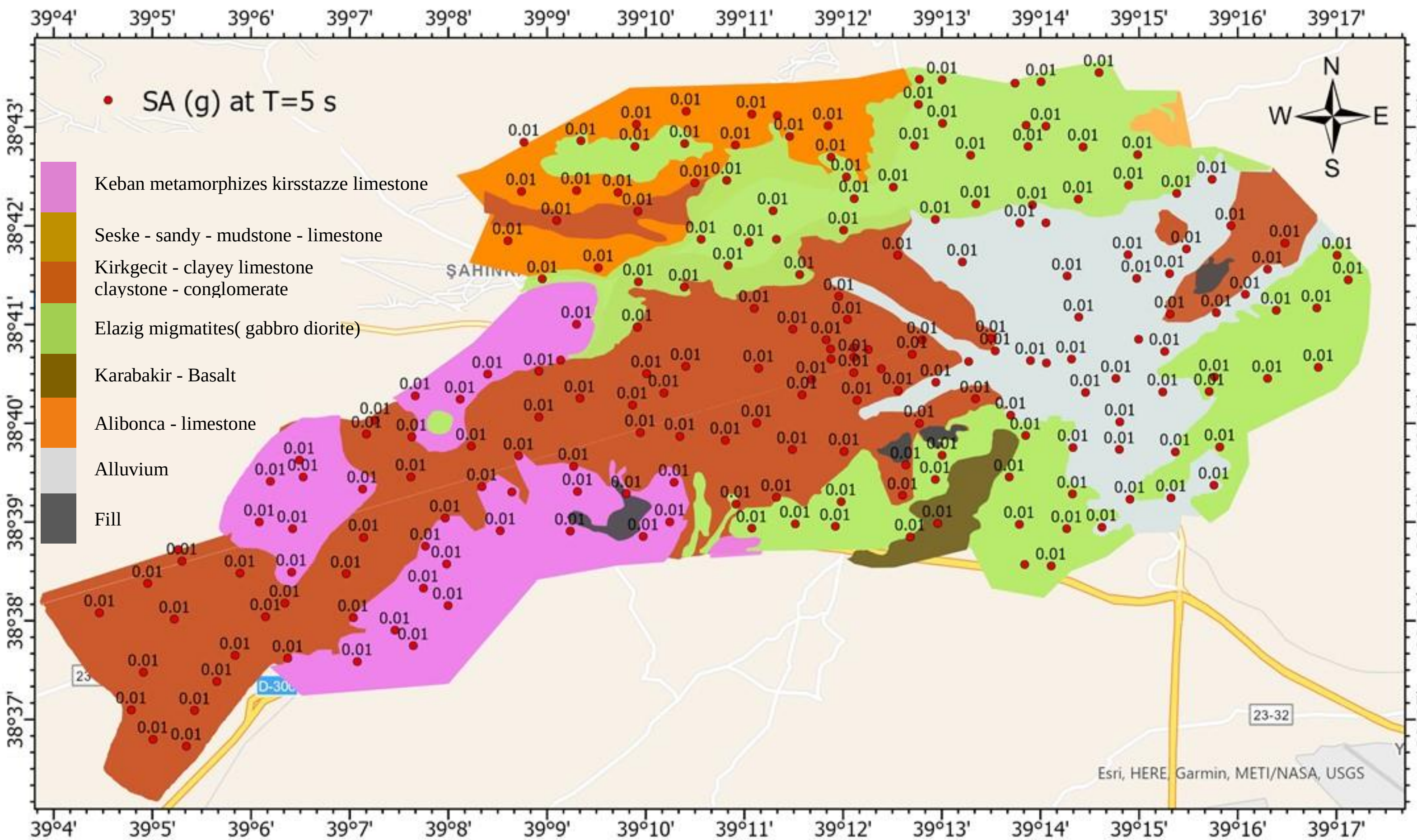

Figure 7.39. Discrete SA values at T=5 (s) plotted on the geological Map of Elazig-Center

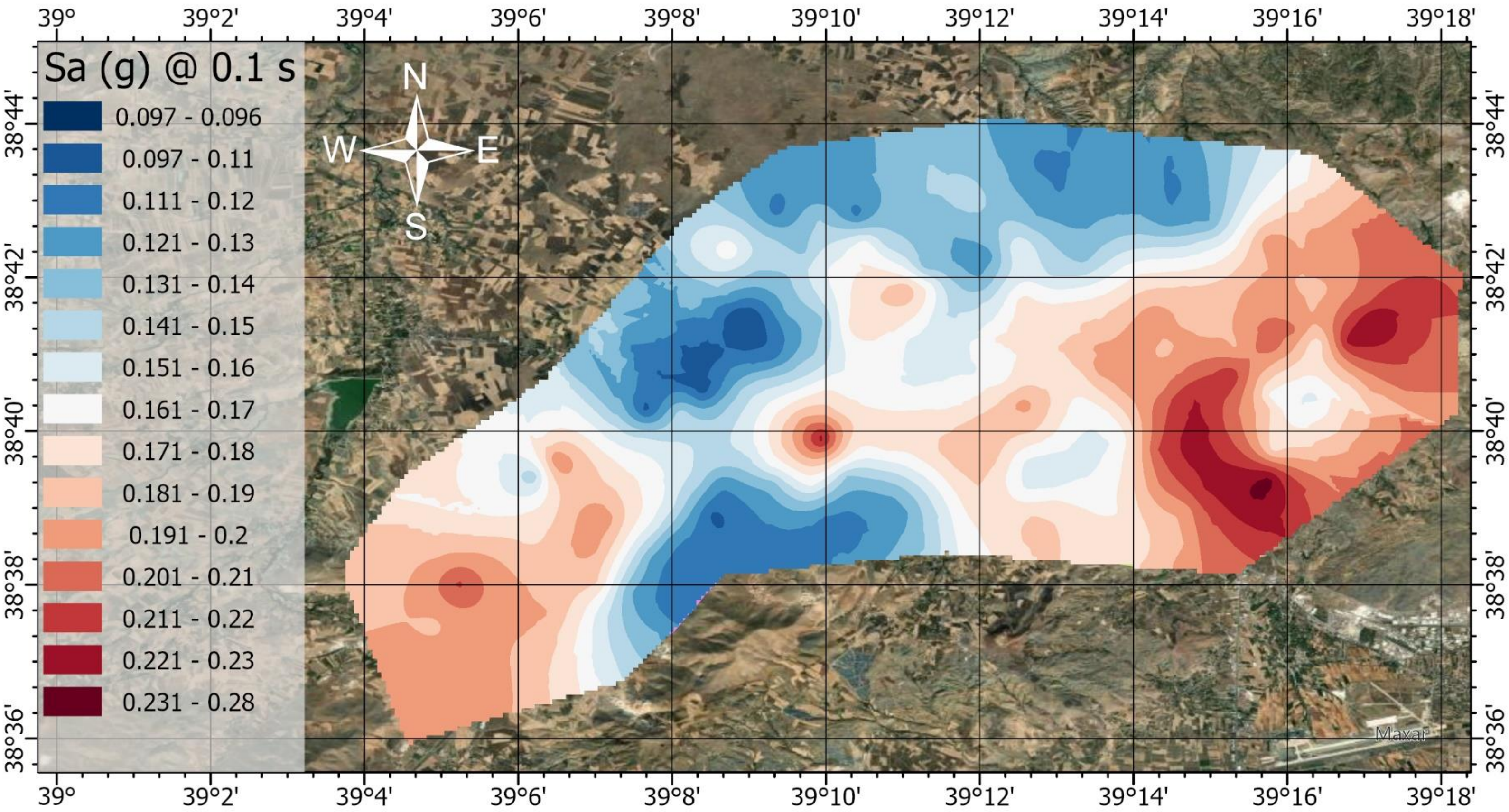

Figure 7.40. Spectral acceleration Sa (g) zonation map of Elazig-Center at Period T=0.1 s

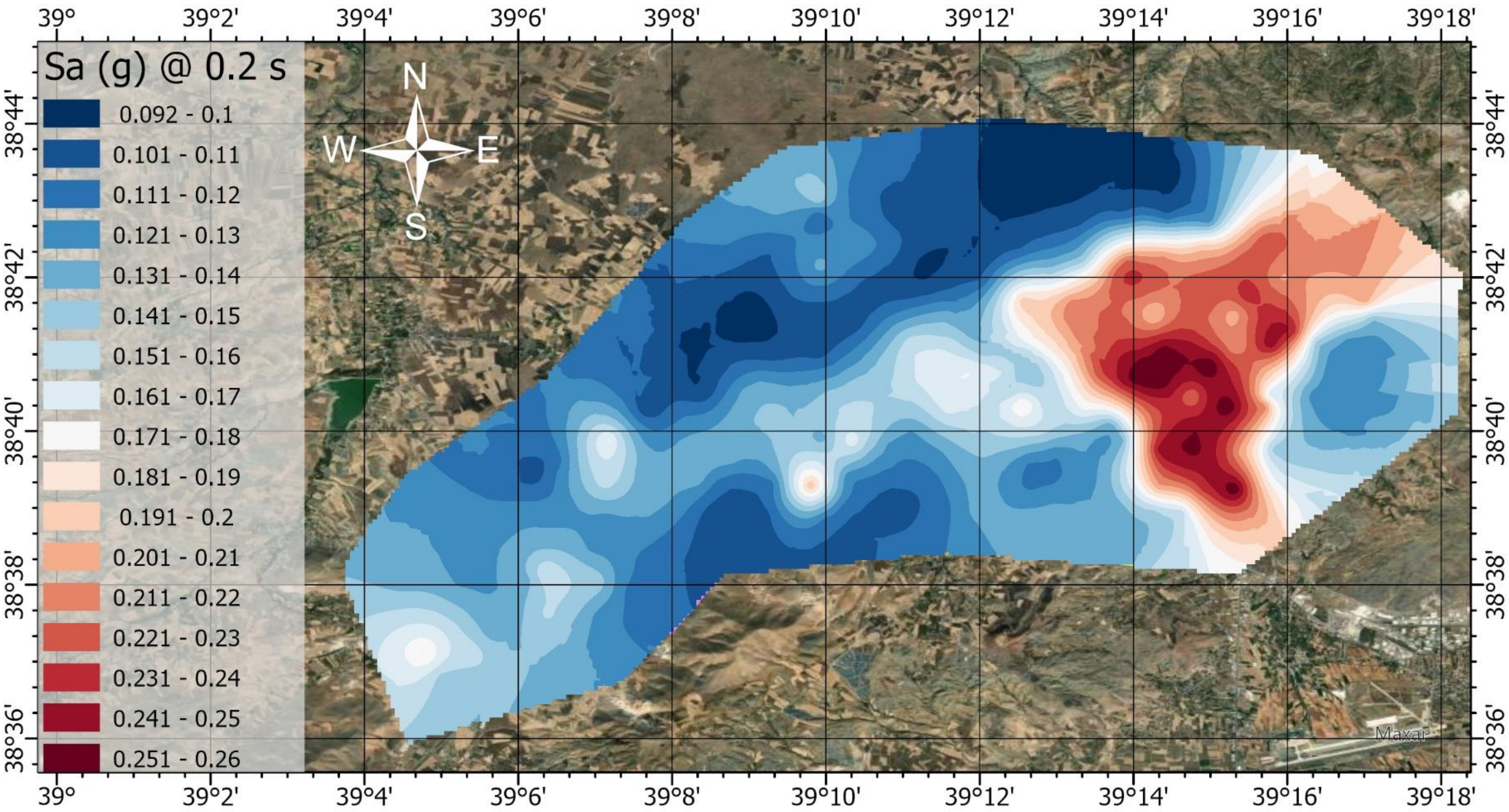

Figure 7.41. Spectral acceleration Sa (g) zonation map of Elazig-Center at Period T=0.2 s

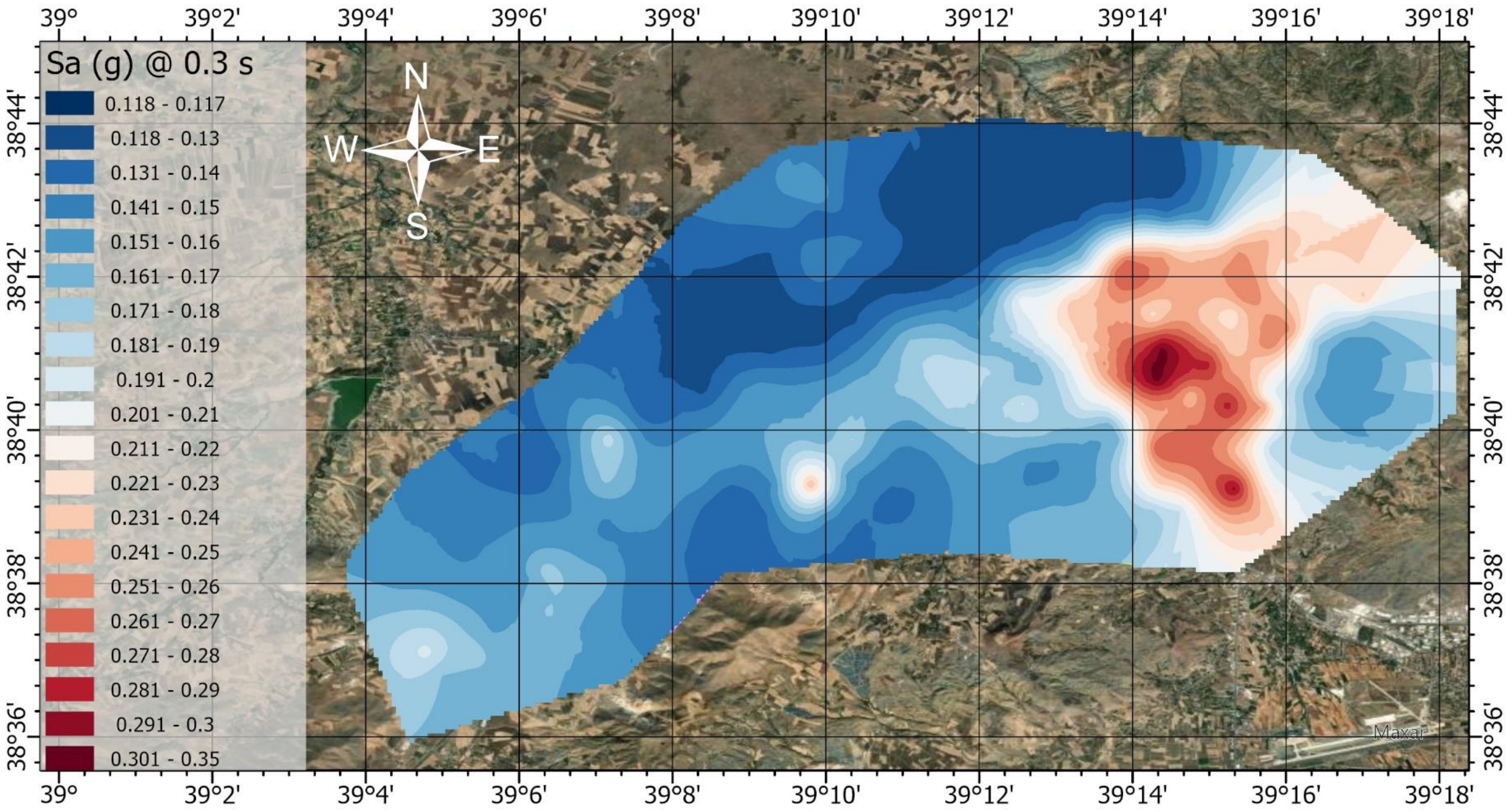

Figure 7.42. Spectral acceleration Sa (g) zonation map of Elazig-Center at Period T=0.3 s

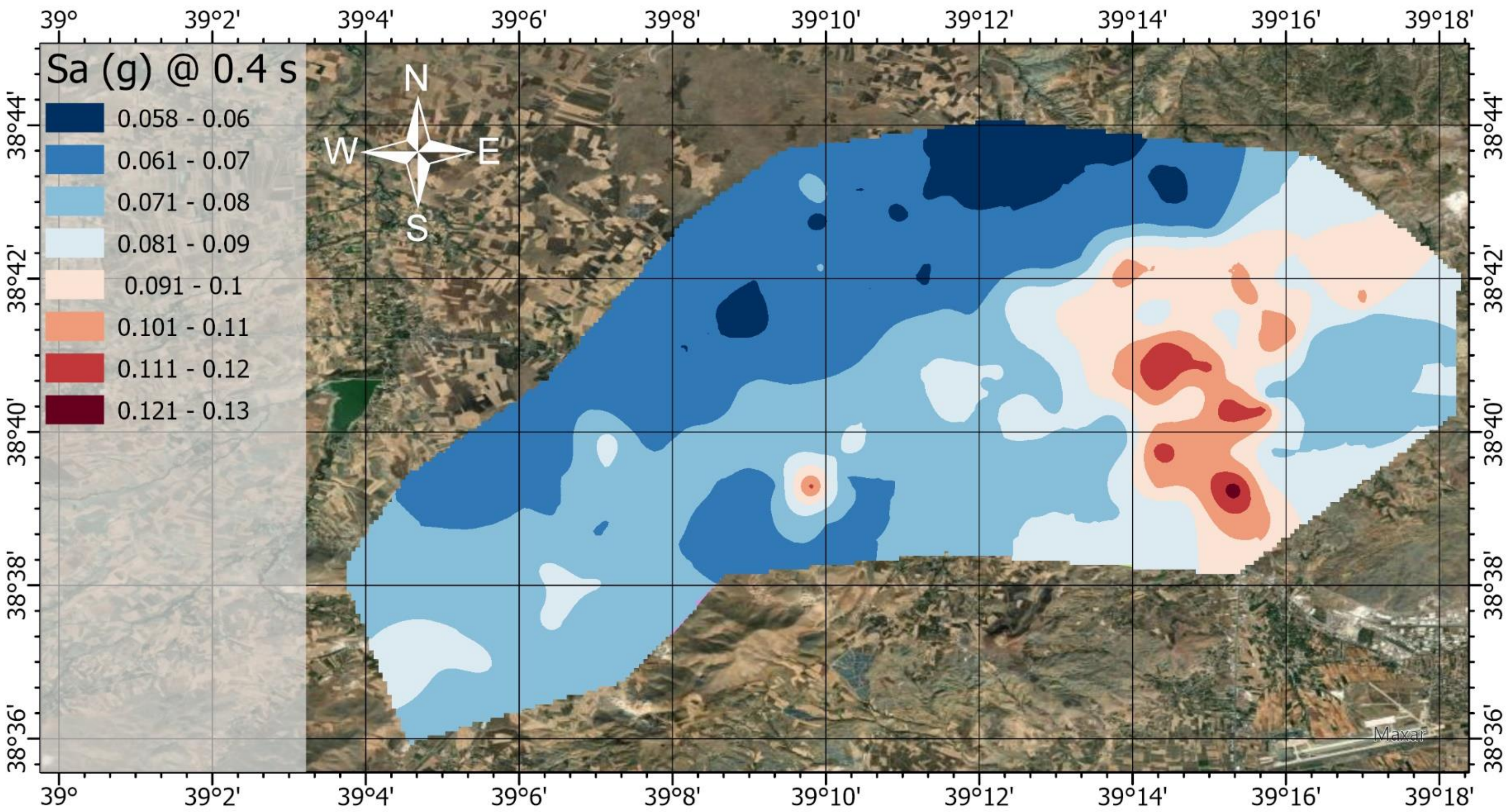

Figure 7.43. Spectral acceleration Sa (g) zonation map of Elazig-Center at Period T=0.4 s

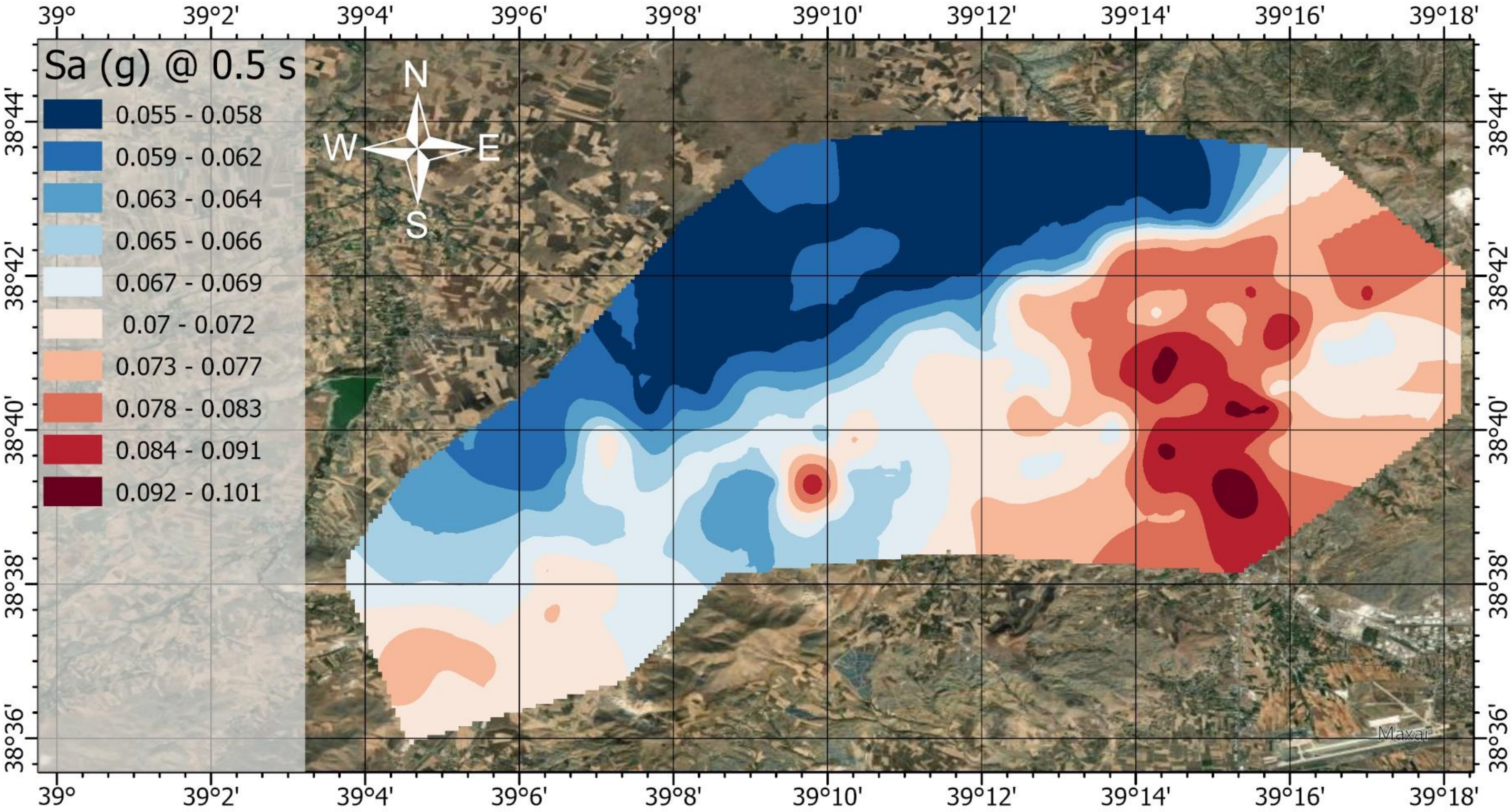

Figure 7.44 Spectral acceleration Sa (g) zonation map of Elazig-Center at Period T=0.5 s

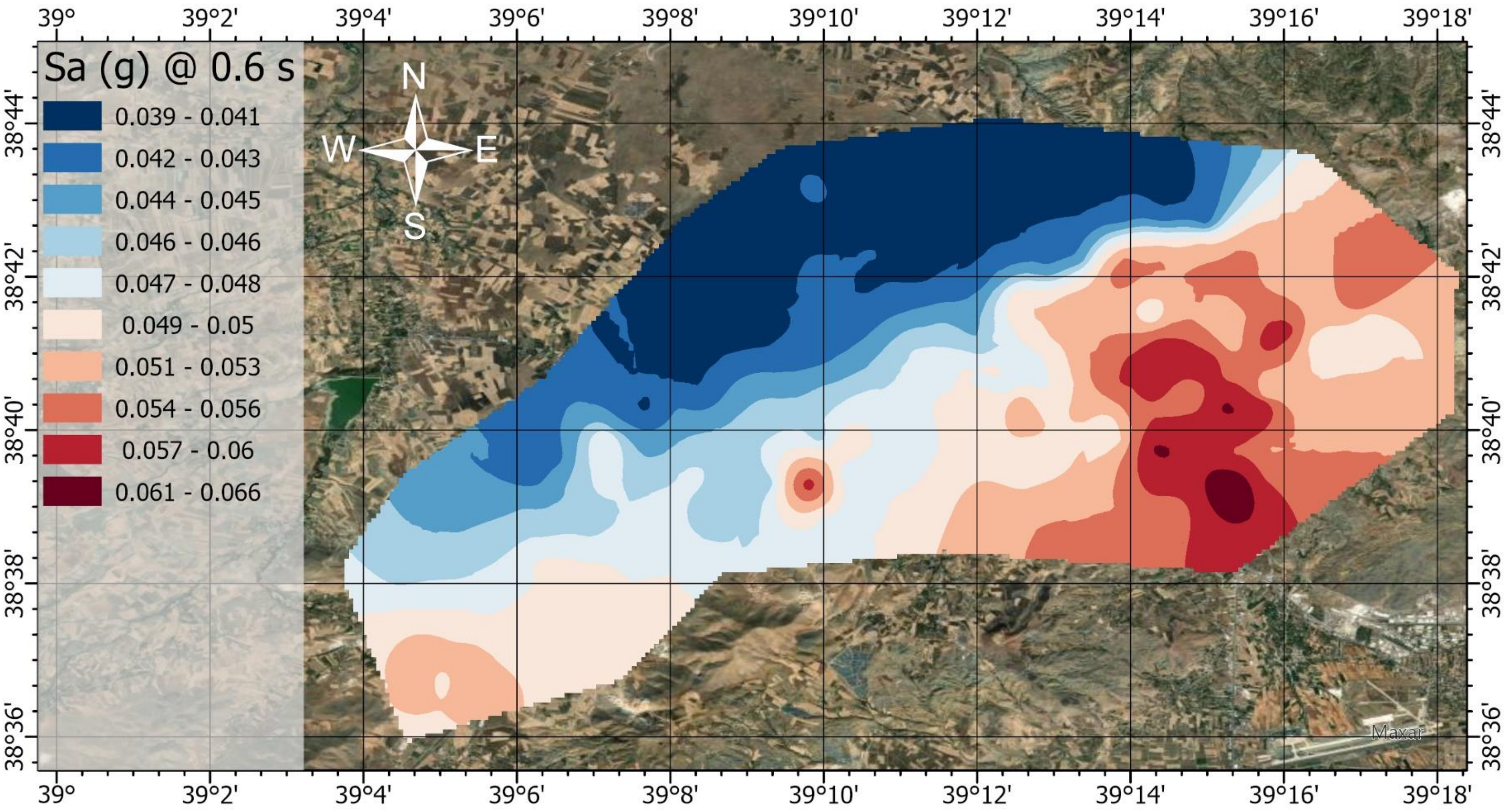

Figure 7.45 Spectral acceleration Sa (g) zonation map of Elazig-Center at Period T=0.6 s

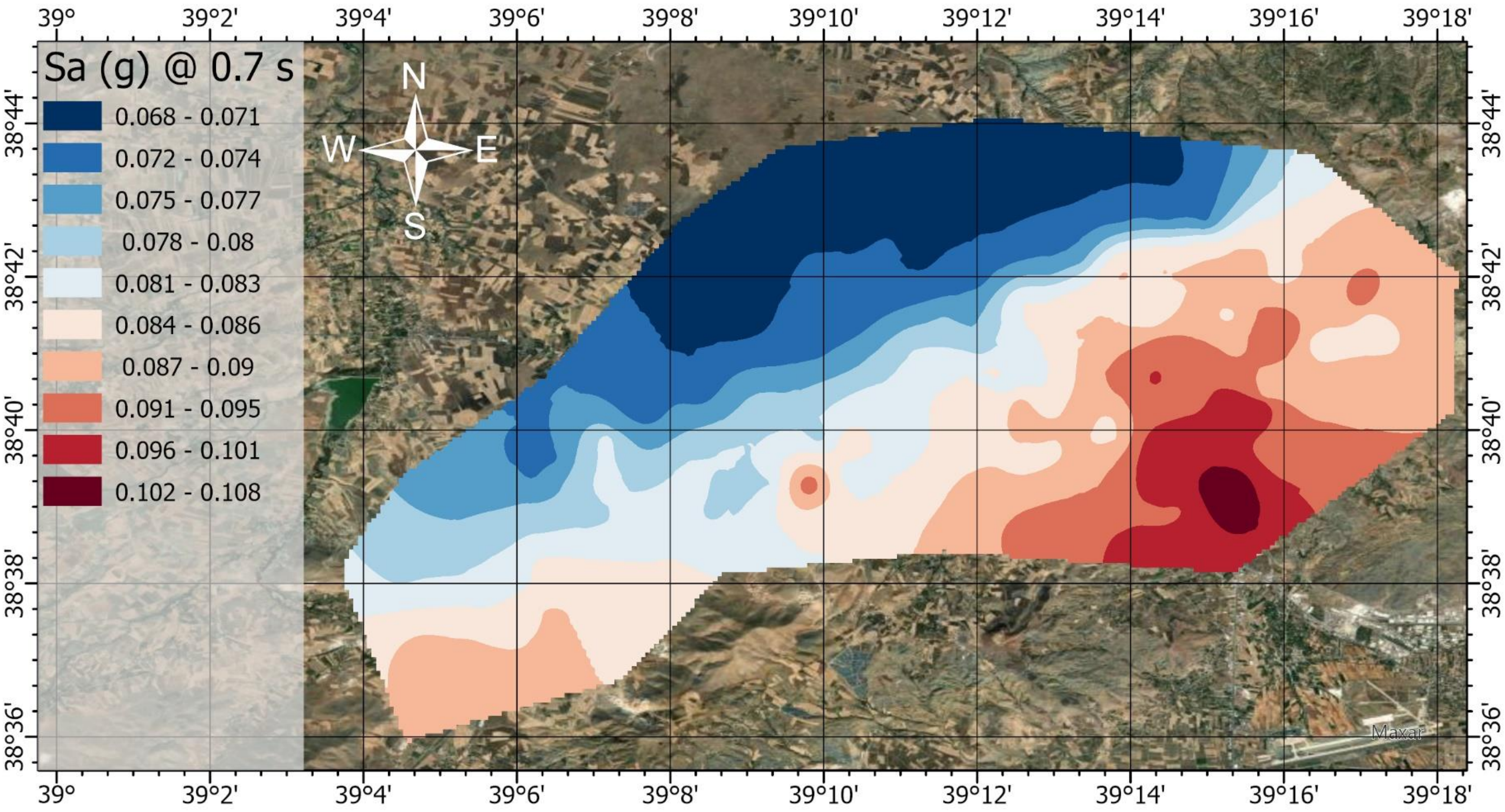

Figure 7.46 Spectral acceleration Sa (g) zonation map of Elazig-Center at Period T=0.7 s

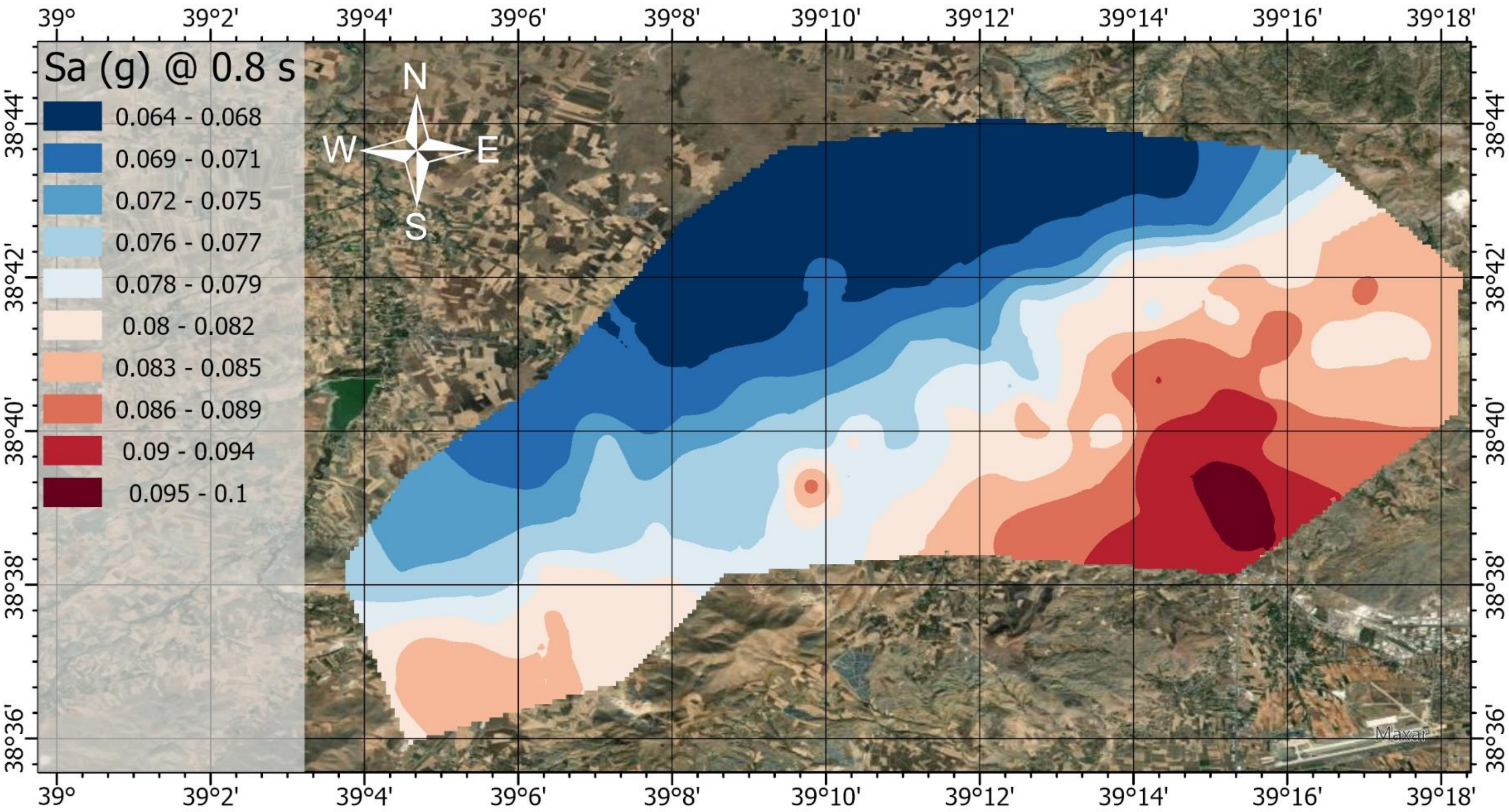

Figure 7.47 Spectral acceleration Sa (g) zonation map of Elazig-Center at Period T=0.8 s

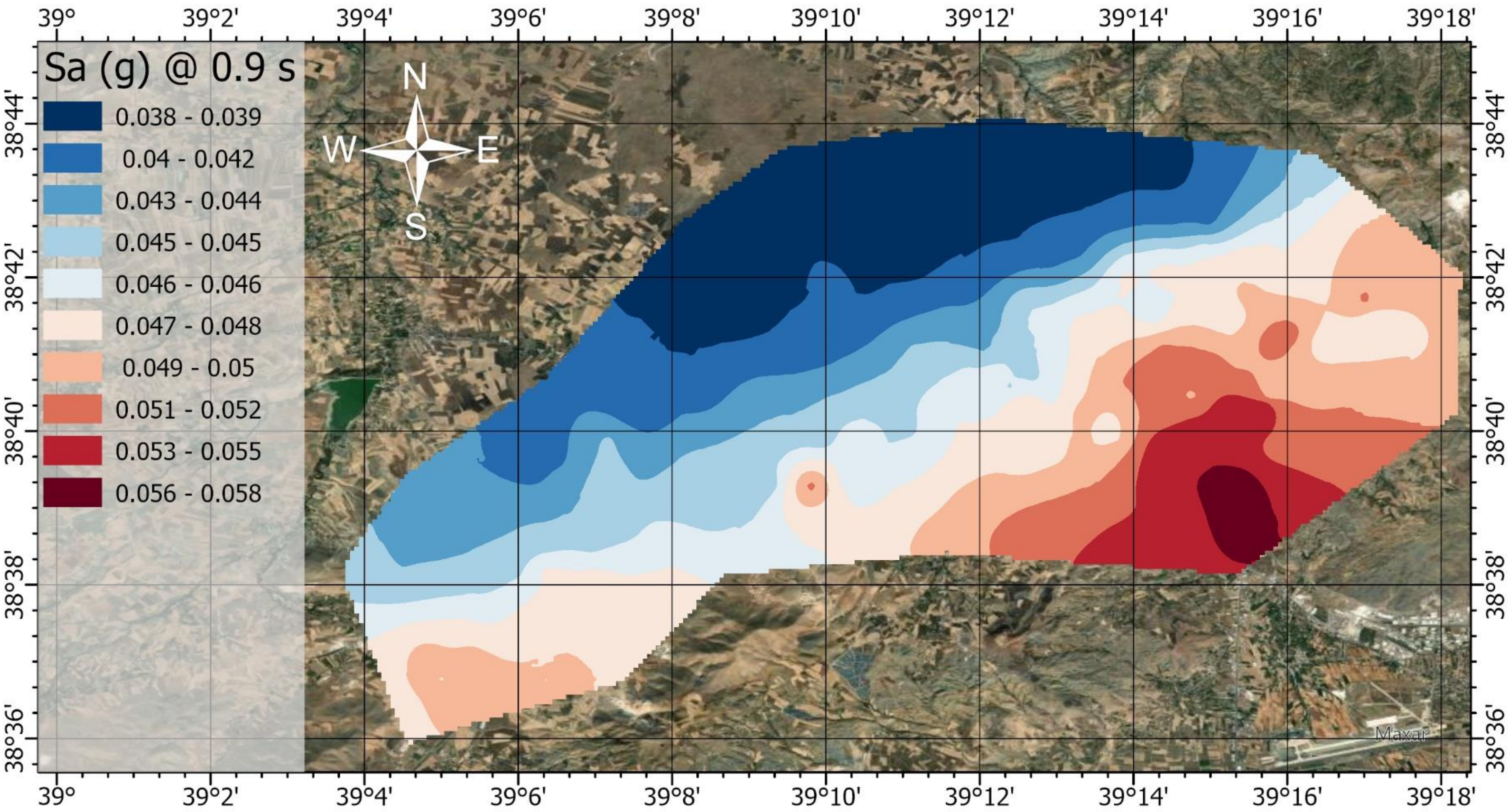

Figure 7.48 Spectral acceleration Sa (g) zonation map of Elazig-Center at Period T=0.9 s

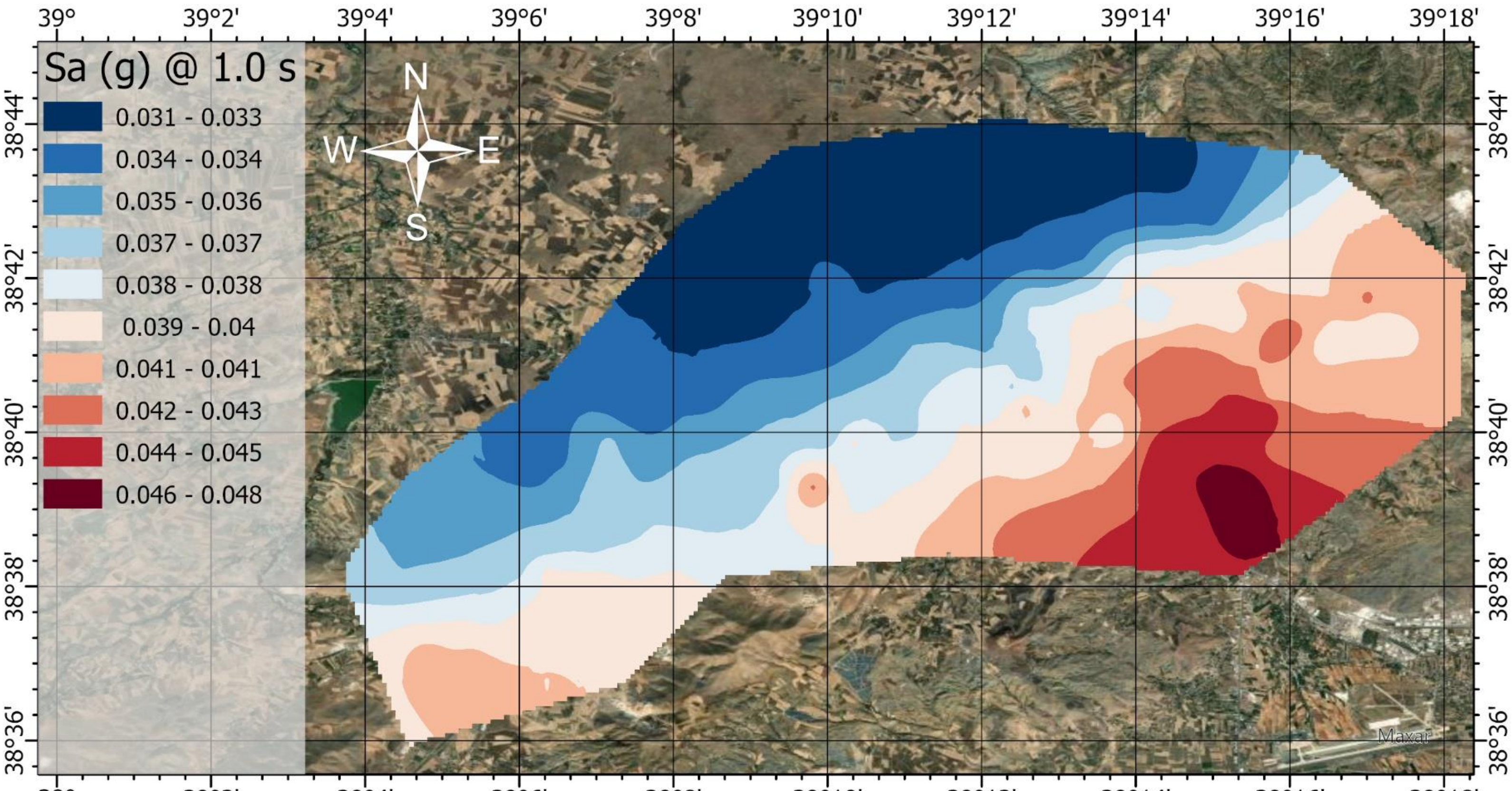

Figure 7.49 Spectral acceleration Sa (g) zonation map of Elazig-Center at Period T=1.0 s

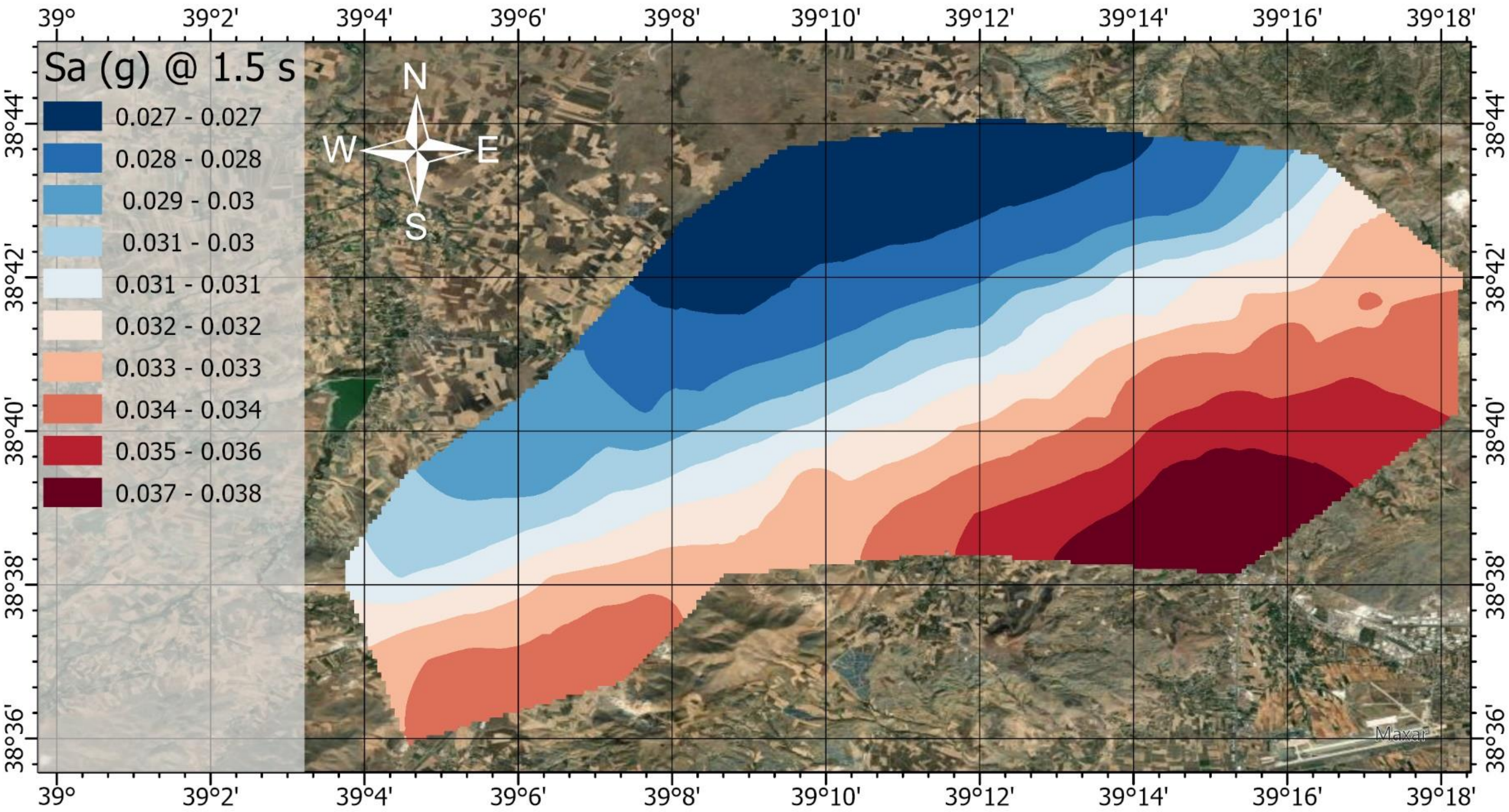

Figure 7.50 Spectral acceleration Sa (g) zonation map of Elazig-Center at Period T=1.5 s

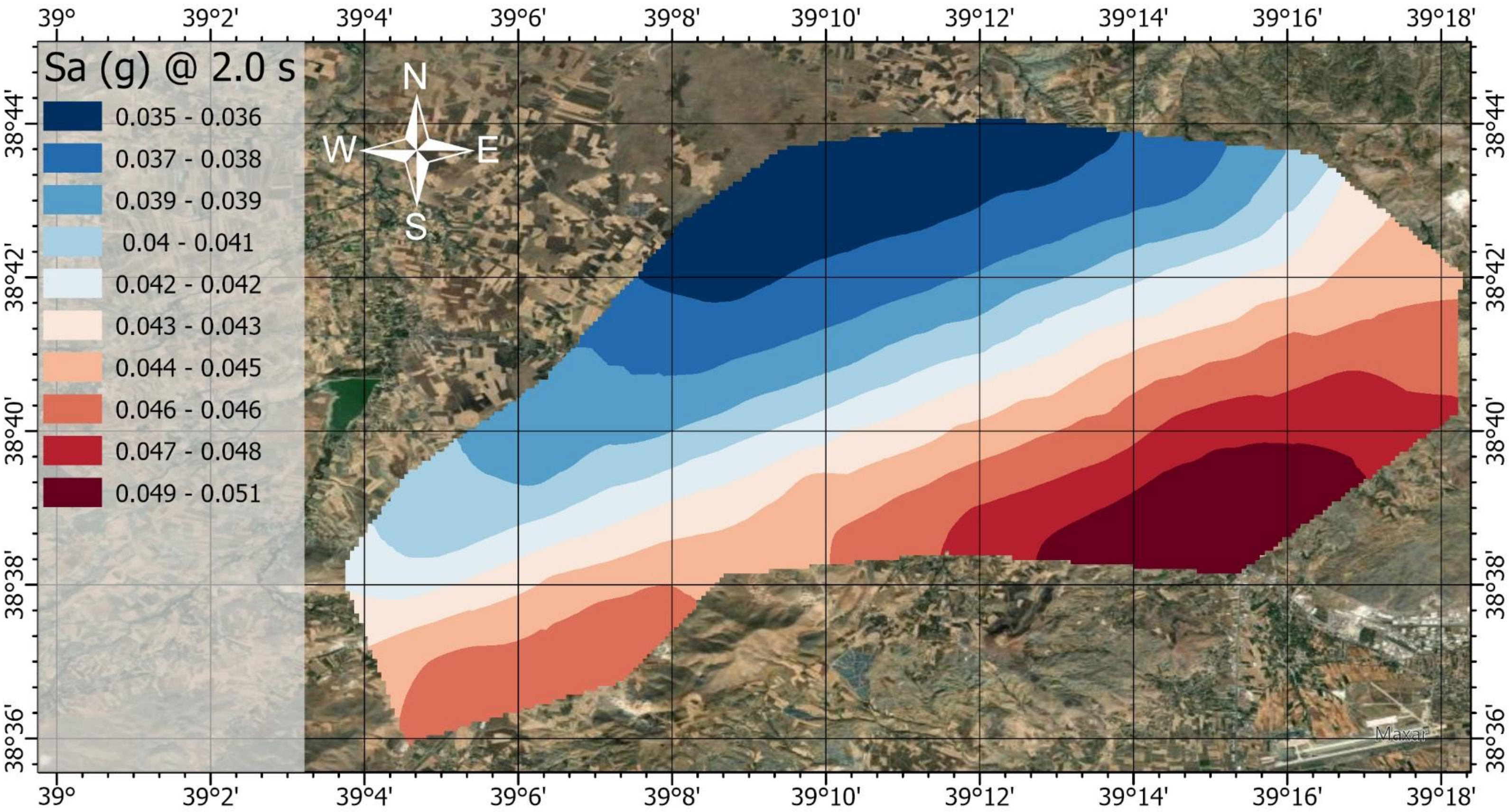

Figure 7.51 Spectral acceleration Sa (g) zonation map of Elazig-Center at Period T=2.0 s

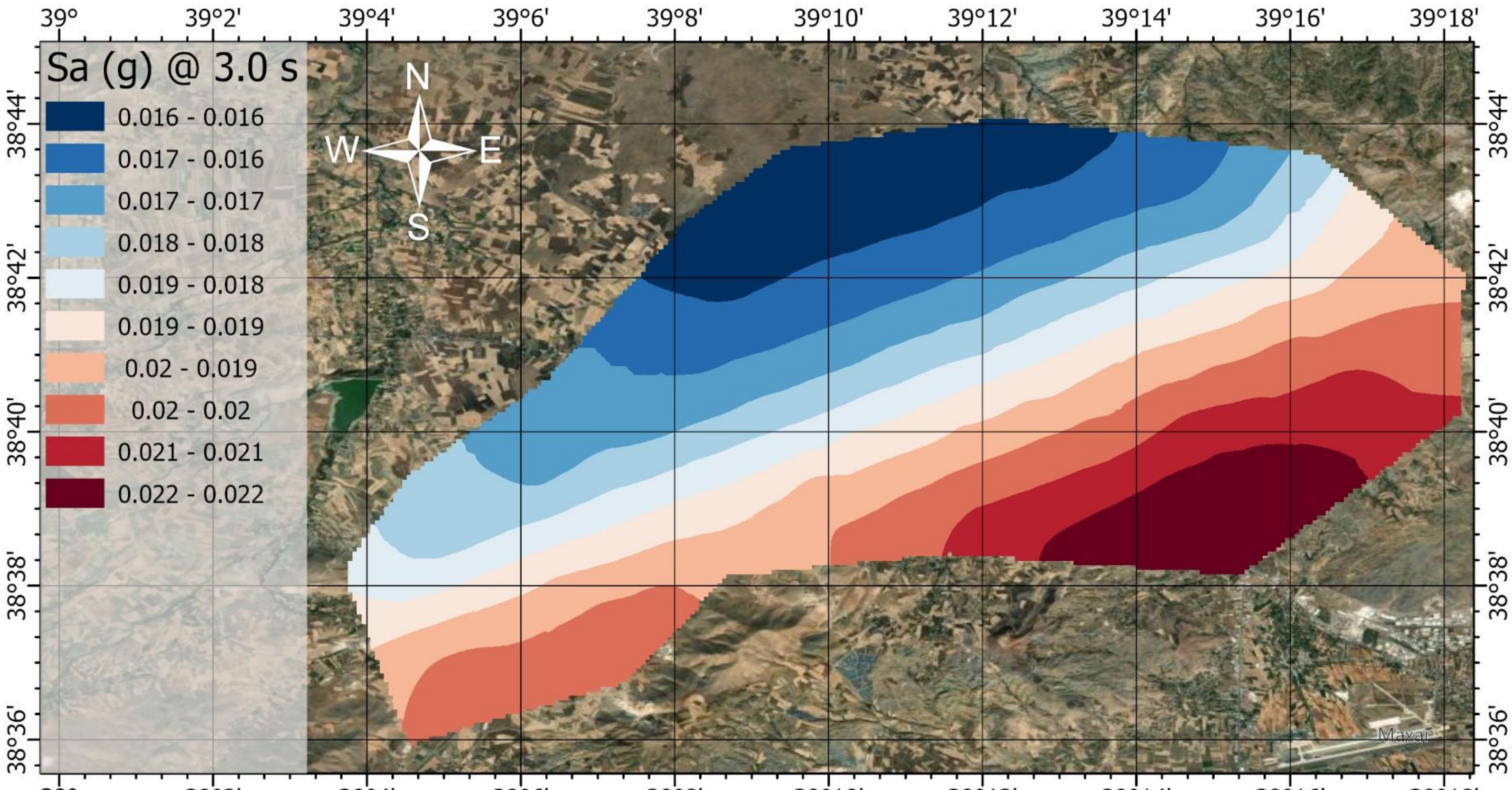

Figure 7.52 Spectral acceleration Sa (g) zonation map of Elazig-Center at Period T=3.0 s

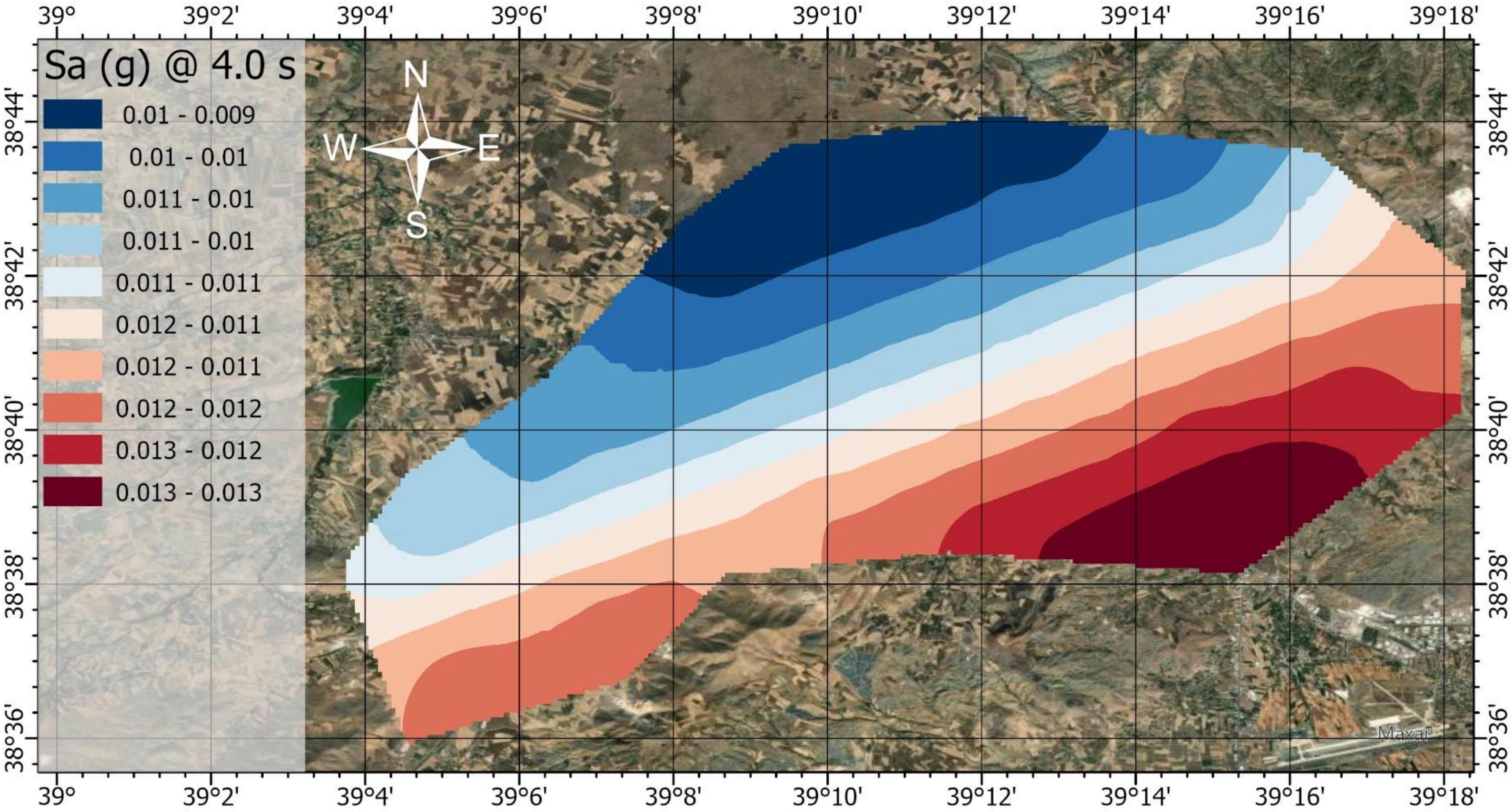

Figure 7.53 Spectral acceleration Sa (g) zonation map of Elazig-Center at Period T=4.0 s

CHAPTER 8

SUMMARY, AND CONCLUSION

8.1 Summary

This study aimed to examine the seismic site effects following the 2020 Elazig-Sivrice earthquake. Elazig, or more precisely, "Elazig-center," was the main focus of the research. This work began with a brief survey of the literature, attempting to cover key topics that were later employed throughout the study.

Following that, the city's geological, geographical, and seismological structure was discussed. It is geographically placed at the intersection of two main highways that connect Eastern and western Anatolia. Elazig comprises the Alluvium formation in the east, bounded on the north and east by Elazig Magmatites (gabbro-diorite). Continuing westward, the Kirkgecit formation is located in the heart of Elazig (limestone, claystone, and conglomerate). To the north and south of the Kirgecit formation are the Keban metamorphic formations (limestone). The Alibonca formation (limestone) is located in the north center, while a relatively minor section of the Seske formation (sandy mudstone–limestone) is located in the south. Elazig is considered a seismically active location, having a history of large earthquakes striking the region in the past. Additionally, the EAFZ, which extends from Karlova to Antakya, is an intracontinental strike-slip fault with NE-SW striking and left-lateral intracontinental. The Elazig fault runs east-west across the Elazig City Center settlement Area and north-south beyond the study area, as does the Palu Fault, which runs along the iro Stream from Hazar Lake to Sivrice–Doğanyol and north of Sincik.

Following a discussion of the region's geography, Chapter 4 conducted a subsurface study. The primary geotechnical source was the Elazig-Center Municipality geological-geotechnical survey report supplied by Akare Planlama (2015), which was quite informative. This work is entirely reliant on the occurrence of geotechnical data culled from the literature. A total of 210 boreholes were utilized in this investigation, dispersed around the city of Elazig-Cennter and covering all of the region's geological characteristics. When performing geotechnical studies, the unit weight (γ), the Plasticity Index (PI), the fines Contents (FC), the groundwater table level (GWT), and the shear wave velocity $(V_{s,30}, V_{s,12})$ are the primary characteristics that receive special attention. The work in this chapter was often either data collection from the literature or data generation for the missing parameters utilizing engineering sense and the geological structure by describing the assumptions upon which those estimations were based. Finally, an idealized soil profile for each borehole is produced and provided along with the boreholes' geographical locations.

After that comes Chapter 5, where the actual seismic analyses started to be conducted. This chapter started with a summary of the seismic features of the 2020 Elazig-Sivrice event. Following that, the observed "real" strong ground motion was examined using the region's available acceleration time history records acquired during the event and the NGA-WEST2 ground motion prediction equations. Following that, a time history record was utilized as a reference time history record and used as the main source throughout the research. An idealized shear wave velocity profile is then developed as a prologue to site response analysis by altering available shear wave velocity profiles in the literature and the velocity data for the boreholes. Then at the end, relatively deep and smooth profiles were introduced. Deepsoil software was used to perform a site response analysis; the analysis was performed in three stages: first, (i) the original outcrop acceleration time history recorded at the strong ground motion station is de-convolved into a within-motion at bedrock, and then (ii) this motion is scaled for each of the 210 boreholes. After that, (iii) an equivalent linear site response analysis is performed on 210 boreholes using convolution. This chapter presented in-situ outcrop time histories, spectral acceleration (S_a), and peak ground acceleration (PGA) values for each borehole. Finally, the spectral plots for all the boreholes were presented.

Next, Chapter 6 discussed liquefaction susceptibility and triggering analyses based on seismic data collected from the 2020 Elazig-Sivrice earthquake. The first section of this chapter identified all accessible boreholes for possibly liquefiable soils utilizing Seed et al. (2003) chart, the city; only seven boreholes were assumed to be prone to liquefaction out of 210 boreholes. The critical depth of these boreholes was located under the groundwater table level and had soils with a plasticity index PI$<$ 7, low SPT blow counts, and above the groundwater level. SK-138, SK-141, SK-142, SK-148, SK-171, and SK-172 are the boreholes. Following that, a liquefaction evaluation using the Cetin et al. (2000, 2004, and 2008) approach was conducted.

Finally, in Chapter 7, geological rock formations and GIS modeling techniques were used to provide a complete image of the geotechnical setting of the region, as well as a complete picture of earthquakes, their location, severity, and changes, as well as the potential danger they pose to people living on Earth's surface. Moreover, ArcGIS Pro 2.9.1 was used for GIS purposes. In general, the output data used in the construction of the zonation maps is divided into two categories: (i) geodata zonation maps (for the groundwater table (GWT), the SPT-N raw data, the pressuremeter test, and the shear wave velocity V_s), and (ii) seismic zonation maps (for the peak ground acceleration PGA, and the spectral acceleration S_a). In addition, three types of maps were presented depending on the need: the first type is a scatter discrete data map with real (actual) values scattered throughout the geological structure of Elazig-

Center; contour maps over the geological settings of the region; and color-fill zonation maps omitting the region's geological settings.

8.2 Discussion

This research aimed to study the seismic effects after the 2020 Sivrice-Elazig earthquake. First site response studies were performed to meet the study's goal, and peak ground acceleration PGA and spectral acceleration S_a values were acquired. Then, a liquefaction triggering assessment was carried out, and finally, zonation maps were generated.

A critical point to emphasize at this stage is that all analyses and outputs are contingent on the correctness of the data collected from the literature; if the geotechnical data acquired from the literature is inaccurate, the findings may be impacted. The author, however, assumed that the data was accurate and conducted the analyses accordingly.

8.2.1 The Geotechnical Data

The primary source for this thesis's geotechnical site parameters and features was the geological-geotechnical survey report supplied by Akare Planlama (2015), which contained a wealth of helpful information. This study covers 210 boreholes. Because they are spread out over the research area, the author believes that all of the region's essential features have been captured.

In general, the dominant soil type in certain regions is a rock with extremely high (or refusal) SPT-N values, while in other locations, the malleable character of cohesive soil layers dominated the Elazig alluvial geological setting. While conducting the geotechnical investigations, the main focus was on obtaining the following parameters; the unit weight (γ), the Plasticity Index (PI), the fines Contents (FC), the groundwater table level (GWT), and the shear wave velocity ($V_{s,30}, V_{s,12}$). For the Plasticity Index (PI) and the Fines Contents (FC), all data were taken directly from Akare Planlama (2015), with no alterations or assumptions made.

For the unit weight (γ), despite their importance, small changes in unit weight have a negligible effect on seismic analysis findings compared to other geotechnical parameters. The author, on the other hand, made a great effort to ensure that the weight of each unit was accurate, representative, and sensible. The process began with examining available data in the literature and then assigning their unit weights to comparable geological (or geotechnical) formations with missing unit weight data. Even if the actual situation differs from these assumptions, it will not have a significant influence on findings since the change (if any) is so small.

One of the parameters that have the most significant effect on the results is the groundwater table level. However, unfortunately, only five boreholes were reported to have a recorded groundwater table level. Due to the tremendous effect of this parameter, especially in liquefaction assessments, the author felt a need to investigate further and come up with a solution. Google Earth was used to estimate the groundwater table level in the remaining boreholes to ensure completeness. This was accomplished by comparing the elevation difference between boreholes with and without reported GWT levels and assigning the GWT level to boreholes lacking GWT data. It should be noted that while the groundwater table level seen on Google Earth is frequently too deep for most boreholes, this does not influence the computations. However, in certain boreholes, the GWT level was discovered to be near the ground surface, which undoubtedly influences the obtained output; as a last note on the GWT, what was mentioned is only an approach the author used for completeness. However, owing to precipitation, municipal works, or any other probable reason, the situation may change in the future, resulting in a change in the GWT level.

Another key parameter is the shear wave velocity, which may have the greatest influence on the outcomes of site response assessments. Although Akare Planlama (2015) reported seismic refraction tests, the complete shear wave velocity profile was required because the seismic refraction tests reported only average values: (i) average shear wave velocity at the upper layer (mostly the upper $5 - 8$ m), (ii) average shear wave velocity at the upper layer (assigned for the rock), and (iii) average shear wave velocity at the upper 30 meters. Additionally, the reported sites of seismic refraction tests do not correspond to the precise locations of the boreholes employed in this research. As a result, the closest average values obtained during the shear wave velocity measurement tests conducted to a borehole were allocated to it. To conduct high-quality site response analyses, deeper profiles were required; as a result, the profiles of the SGM stations were used, and because only three values were reported from the actual seismic refracture tests, a smooth, staircase-type, shear wave velocity profile was constructed using tailored SGM'velocity profiles.

The average shear wave velocity measured at the upper 30 meters ($V_{s,30}$) was projected using contour lines onto the geological map of Elazig-Center. The graphical maps demonstrates a correspondence between the shear wave velocity values and the city's geological structure. Elazig-Center, on average, has a relatively $V_{s,30}$, with the lowest $V_{s,30}$ measurements ranging between 605 and 734 m/s on the alluvium formation and the highest $V_{s,30}$ measurements ranging between 1019 and 1938 m/s in regions where Keban Metamorohites was the dominant geological structure.

8.2.2 The Seismic Site Response Analyses Results

Seismic evaluations of primarily two categories were conducted in this work. The equivalent linear technique was used to analyze the site response initially, and then liquefaction triggering evaluations were done as a second component of the seismic analysis. Finally, and following the completion of seismic assessments, zonation maps were created.

Elazig-Center’s seismic response varies significantly, as shown by the previous chapters' site response assessments and seismic maps. The discussion handles site response analyses first, beginning with the peak ground acceleration PGA.

The obtained PGA values from the analyses ranged from 0.0244 g "at SK-62" to 0.175 g "at SK-35." However, excluding outlier data, the region's most significant PGA values on average ranged between 0.136 g and 0.144 g in the east-south region of Elazig-center, or more precisely, between Sugözü and Çatal Çesme. When using Google Maps to view the region, it is clear that this location is not a residential neighborhood except for a small spot (Figure 8.1). However, there is another location with high PGA values (0.128 – 0.135 g) located south of Elazig-Center, or more precisely, south of the Sürsürü and Olgunlar areas and near the Elazig-Bingöl yolu (Figure 8.2).

With a deeper examination of the peak ground acceleration zonation maps, Elazig-Center can be subdivided into three distinct areas. The southeast (denoted as Zone 1 in Figure 8.1 and Figure 8.2). Zone 1 region reported the highest PGA values, to be precise, 0.30 – 0.35 g. The southwest area with intermediate PGA values is followed by the east (designated as Zone 2 in Figure 8.1 and Figure 8.2), and ultimately the north belt of Elazig-Center with the lowest PGA values is reached (denoted as Region 2 in Figure 8.1 and Figure 8.2).

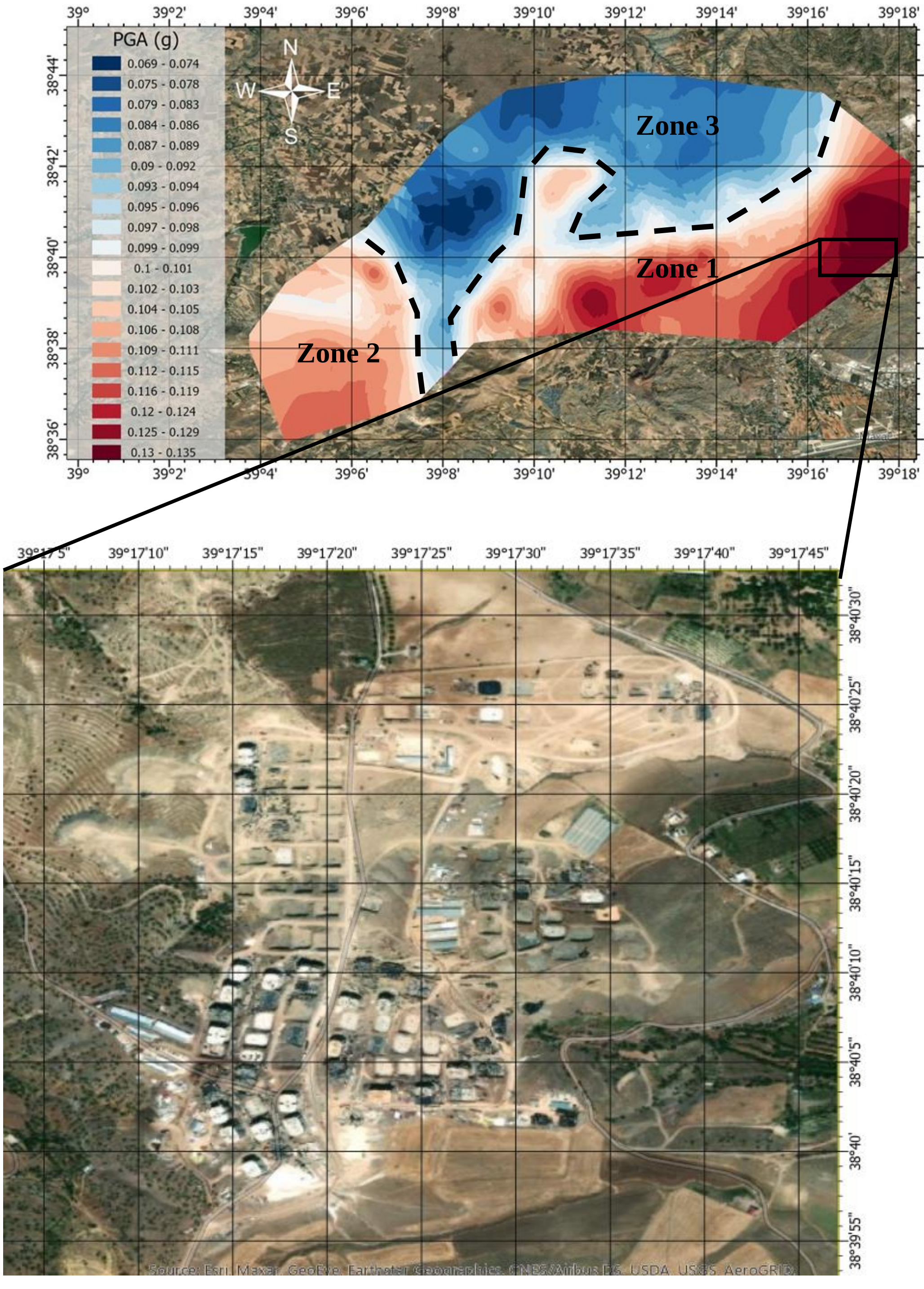

Figure 8.1. More detailed examination of the PGA zonation map-1.

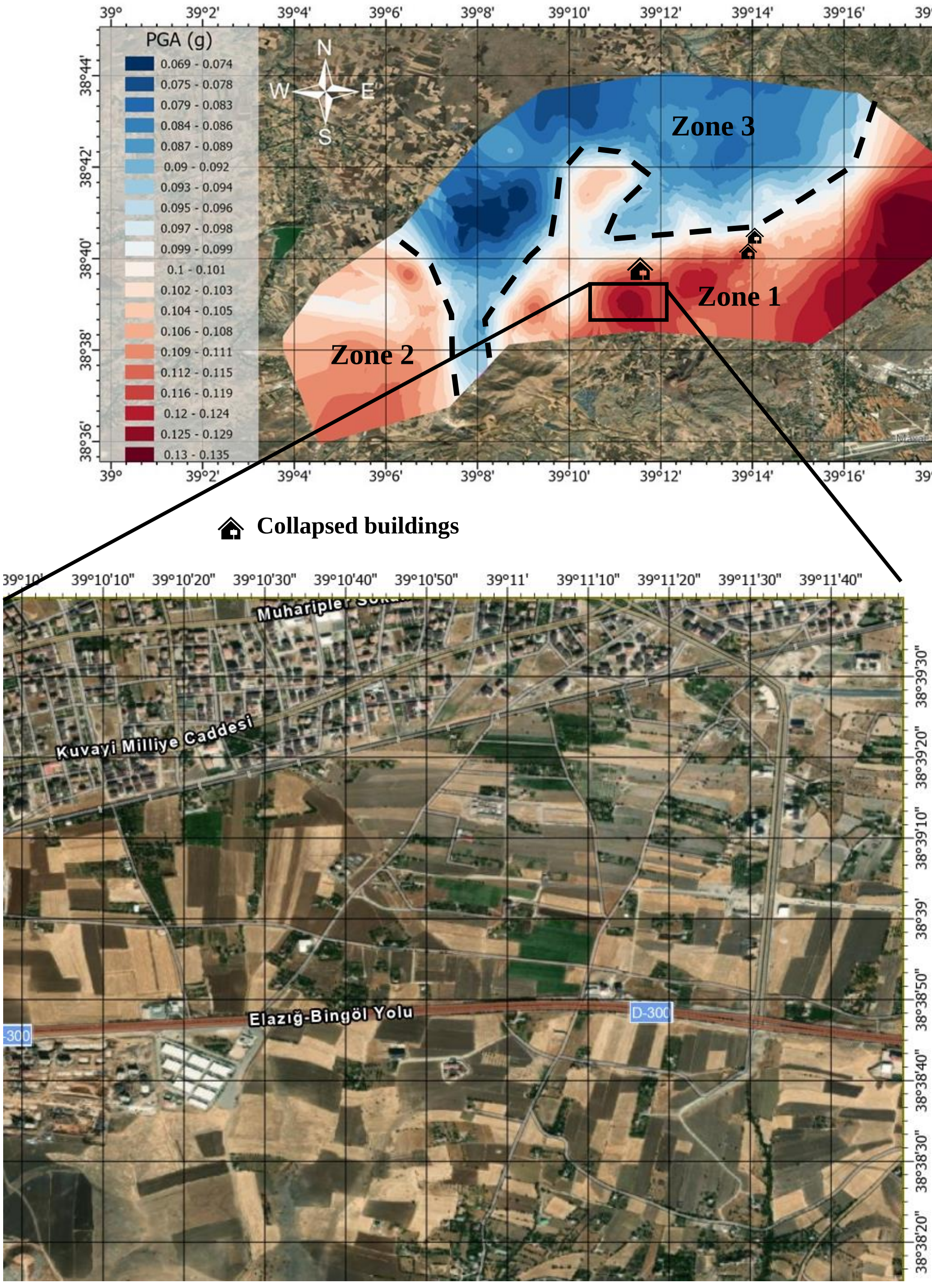

Figure 8.2. More detailed examination of the PGA zonation map.

The overall tendency indicates that the south section of Elazig-center (Zone 1, the zone nearest to the fault) has higher PGA values than the north belt (Further from the fault). However, It is evident that the near-fault effect is a reason for this distribution of the PGA variation over the study region, but it is not the only reason as there are some outliers, particularly in the middle north part of Elazig between $39^{o}10'$ - $39^{o}12'$N and $38^{o}40'$ - $38^{o}42'$ E. To determine the reason behind the existence of those outliers, one can examine the shear wave velocity maps V_{s30} for those coordinates from Figure 7.14, which show average shear wave velocity values near the ones measured in Zone 2 (804 m/s – 858 m/s).

Only three structures collapsed in Elazig-Center during the Elazig-Sivrice incident (METU-EERC, 2020); these structures were located in the Mustafa Pasa and Sursuru districts. As illustrated in Figure 8.2, all collapsed buildings are located within Zone-1, corroborating the study's findings.

To end the PGA discussion, the amplification factor should be mentioned. The results indicate that the soil column would amplify seismic waves in the majority of the region. PGA values in sediments can be up to 2.5 times those in bedrock (with only one outlier that amplifies the surface acceleration three times the bedrock acceleration SK-35, a rocky site with SPT >50). It is quite normal for borehole SK-35 to act as an outlier, as the closest shear wave velocity measurement to it reported with extremely high shear wave velocity values, with $V_{S.Lauer-1} = 311 m/s$, $V_{S30} = 1232\ m/s$, $V_{S.Lauer-2} = 11603\ m/s$. In general, the highest amplification was witnessed in boreholes that have shear wave velocity values that are relatively high; in order to help to envision how the shear wave velocity is impacting the results, V_{S30} values are given as an illustration; the highest amplifications were in SK-35, SK-135, SK-137, SK-20, SK-97, SK-114, and SK-17, and all of them are rock sites with V_{S30} value higher than 900 m/s.

If soil deposit stiffness increases with depth, the maximum ground acceleration will be increased (PGA). In such a situation, buildings would be more vulnerable to earthquake damage because of the greater surface PGA, especially when the natural frequency of an earthquake is similar to the natural frequency of a weaker and softer soil layer. It is more likely for seismic wave energy to travel through bedrock and foundations that are more solid, but the wave energy tends to amplify and absorb in more loose and less stable areas. The areas with looser and more unconsolidated materials tend to have more amplification, which leads to more ground movement and destruction.

Following the discussion of the initial output (PGA) acquired from the seismic site response analyses, the resulting spectral acceleration S_a is discussed next looking at the S_a plots presented in Chapter 5, Figure 5.27 through Figure 5.40.

To begin with, The distribution of spectral acceleration values across the city of Elazig-center is comparable to that of peak ground acceleration mentioned previously. The spectral acceleration S_a values obtained in the Elazig-Center are of extreme importance, as structures are more likely to achieve (partial) resonance when the natural frequency of the ground motion matches the structure's natural frequency. If resonance happens for a lengthy period of time, amplification of ground motion can inflict injury or catastrophe.

In nature, all structures tend to vibrate, but the problem is when Its fundamental period, or natural frequency, is achieved. High-rise structures (with a low natural frequency) behave entirely differently from lower structures (with a much higher natural frequency). For this reason, multiple spectral acceleration maps were provided, so say that an engineer is to build a one-story structure in Elazig center Zone-1 and that the location of this structure is within the extent of borehole SK-130, the engineer is supposed to check the S_a maps at period $T = 0.1$ s, in this specific example, the scatter data map shown in Figure 7.23 or the zonation map at

Figure 7.38. Matching the natural frequency period with the natural frequency of the ground motion should be avoided.

The spectral acceleration graphs depicted in Figure 5.27 – Figure 5.40 indicate that the largest S_a values occurred between periods $T = 0.05$ s and $T = 1$ s.

S_a levels steadily drop as the duration after $T = 1$ s increases. One can also notice a reduction in the irregularity of the zoning in the spectral acceleration zonation maps. A progressive rise is observed in the spectral acceleration (S_a) from north to south, showing that the distance to fault effect is the dominant component at lower T values, as illustrated in Figure 7.38 – Figure 7.51.

Following the completion of site response evaluations, liquefaction triggering assessments were carried out in accordance with Cetin et al. (2000, 2004, and 2018) methodology. Following the geotechnical analysis conducted in Chapter 4, and as previously stated, plastic-cohesive soil layers dominate the alluvial geological environment of Elazig-Center. As a result, the possible number of liquefiable sites and soil layers is restricted. In Chapter 6, liquefaction triggering investigations for potentially liquefiable soils was done, and the site was determined to be non-liquefiable (liquefaction triggering probabilities PL are lower than 1 percent). Cetin et al. results .'s and observations during their reconnaissance research are compatible.

The findings of the liquefaction evaluation in this study are dependent on various assumptions, beginning with SPT-N blow count adjustments where the SPT log data was not informative, and the author had to make assumptions to do the analysis. In addition to the assumptions related to the groundwater table level. The situation may alter in the future due to precipitation, municipal activities, or any other plausible reason, resulting in a change in the GWT level and, subsequently, a change in the liquefaction assessment findings.

To conclude the discussion, zonation maps were generated during this study, including the author's own findings and the collected geotechnical data. The reason behind creating the geodata zonation map is to serve as a tool in Elazig-center and help conduct more geotechnical and geological studies regarding this region. The seismic zonation maps, on the other hand, were presented in order to provide a reference that defines the seismic demand of the region. Moreover, those maps can be used to assess structural damage in the future.

8.3 Conclusion

This study aimed to determine the seismic impacts of the 2020 Sivrice-Elazig earthquake to mitigate future harm and loss in comparable disasters. After doing the study, it is possible to infer the following:

- The most significant PGA values on average ranged between 0.136 g and 0.144 g in the east-south region of Elazig-center, or more precisely, between Sugözü and Çatal Çesme.
- Elazig-Center may be split into three unique zones based on PGA findings: Zone 1 in the northeast of Elazig-Center, which has the most outstanding PGA values, Zone 2 in the west, which has intermediate PGA values, and Zone 3 in the north belt of Elazig, which has the lowest PGA values.
- While it is clear that the near-fault impact contributes to the distribution of PGA variation across the research region, other factors such as shear wave velocity values and the region's geological context also contribute.
- The peak ground acceleration (PGA) values in Elazig-Center can be amplified up to 2.5 times higher than those in bedrock.
- Multiple spectrum acceleration maps were created to account for the fundamental period or natural frequency of structures when a seismic design is to be conducted.

- The highest spectral acceleration (S_a) values in Elazig-Center occurred in periods between $T = 0.05$ s and $T = 1$ s.
- At lower period T values, the distance to fault effect dominates, and shorter periods reduce the irregularity of the spectral acceleration zonation maps.
- Plastic-cohesive soil layers dominate Elazig-Center alluvial geological settings.
- The number of liquefiable sites and soil layers is constrained Elazig-Center.
- For the current conditions, Elazig-Center is not prone to liquefaction, which is consistent with the reconnaissance findings by Cetin et al. (2020).
- This study's zoning maps included the author's seismic findings (PGA, S_a) and the geotechnical data from the literature (the groundwater table (GWT), the SPT-N raw data, the pressuremeter test, and the shear wave velocity V_s)
- The geodata zonation map was created to aid geotechnical and geological research in Elazig-Center.
- The seismic zonation maps were provided to offer a reference that identifies the region's seismic demand. Those maps can also be used to predict future structural problems.

8.4 Future recommendations

According to the findings of this study, adding other boreholes to the surrounding district, enlarging the study region, and performing further subsurface investigations to minimize ambiguities in the geotechnical data would enhance the study. In addition, performing nonlinear site response analysis and comparing the results with the current findings is recommended.

REFERENCES

A Hashash, Y. M. (2018). *Nonlinear and Equivalent Linear Seismic Site Response of One-Dimensional Soil Columns USER MANUAL*. www.illinois.edu/~deepsoil

Abrahamson, N., & Silva, W. (2008). Summary of the Abrahamson & Silva NGA ground-motion relations. *Earthquake Spectra*, *24*(1), 67–97.

Akgül, B. (1987). *KEBAN YÖRESİ METAMORFİK KAYAÇLARIN PETROGRAFIK INCELEMESİ*.

Akkar, S., Aldemir, A., Askan, A., Bakır, S., Canbay, E., Demirel, İ. O., Erberik, M. A., Gülerce, Z., Gülkan, P., & Kalkan, E. (2011). 8 March 2010 Elazıg-Kovancılar (Turkey) earthquake: observations on ground motions and building damage. *Seismological Research Letters*, *82*(1), 42–58.

Azak, S., Koçkaya, O., Çetin, K. Ö., Ilgaç, M., Can, G., Çakır, E., Söylemez, B., Gündoğan, A. A., Gülerce, Z., NAGHSHİNEH, S. K., ALTINDAL, A., Gör, M., Güceoğlu, F., Canbay, E., Binici, B., Budak, E., Ernerik, M. A., Çelik, A., Caner, A., … Yılmaz, D. (2020). *THE ELÂZIĞ-SİVRİCE EARTHQUAKE [24 JANUARY 2020 M W =6.8] FIELD OBSERVATIONS ON SEISMIC AND STRUCTURAL DAMAGE*.

Bardet, J. P., & Tobita, J. P. (2001). A Computer program for Nonlinear Earthquake site Response Analyses of Layered soil deposits. *J. Geotech. Geoenviron. Eng.* https://doi.org/10.1061/(ASCE)GT.1943-5606.0001496 , 04016042

Barka, A. (1996). Slip distribution along the North Anatolian fault associated with the large earthquakes of the period 1939 to 1967. *Bulletin of the Seismological Society of America*, *86*(5), 1238–1254.

Bingöl, A. F., & Beyarslan, M. (1996). *Elazığ Mağmatitlerinin jeokimyası ve petrolojisi*.

Boore, D. M., & Atkinson, G. M. (2008). Ground-motion prediction equations for the average horizontal component of PGA, PGV, and 5%-damped PSA at spectral periods between 0.01 s and 10.0 s. *Earthquake Spectra*, *24*(1), 99–138.

Boore, D. M., Stewart, J. P., Seyhan, E., and Atkinson, G. A., (2014). "NGA-West 2 equations for predicting PGA, PGV, and 5%-damped PSA for shallow crustal earthquakes", Earthquake Spectra 30, 1057–1087.

Bozkurt, E. (2001). Neotectonics of turkey–a synthesis. *Geodinamica Acta*, *14*(1–3), 3–30. https://doi.org/10.1080/09853111.2001.11432432

Campbell, G. S. (1985). *Soil physics with BASIC: transport models for soil-plant systems*. Elsevier.

Campbell, K. W., & Bozorgnia, Y. (2008). NGA ground motion model for the geometric mean horizontal component of PGA, PGV, PGD and 5% damped linear elastic response spectra for periods ranging from 0.01 to 10 s. *Earthquake Spectra*, *24*(1), 139–171.

Çetin, K. Ö. (2000). *Reliability-based assessment of seismic soil liquefaction initiation hazard* (Vol. 1). University of California, Berkeley.

Cetin, K. O., Cakir, E., Ilgac, M., Can, G., Soylemez, B., Elsaid, A., Cuceoglu, F., Gulerce, Z., Askan, A., Aydin, S., & Gor, M. (2021). Geotechnical aspects of reconnaissance findings after 2020 January 24th, M6.8 Sivrice–Elazig–Turkey earthquake. *Bulletin of Earthquake Engineering*, *19*(9), 3415–3459. https://doi.org/10.1007/s10518-021-01112-1

Cetin, K. O., Seed, R. B., der Kiureghian, A., Tokimatsu, K., Harder Jr, L. F., Kayen, R. E., & Moss, R. E. S. (2004). Standard penetration test-based probabilistic and deterministic assessment of seismic soil liquefaction potential. *Journal of Geotechnical and Geoenvironmental Engineering*, *130*(12), 1314–1340.

Chiou, B.-J., & Youngs, R. R. (2008). An NGA model for the average horizontal component of peak ground motion and response spectra. *Earthquake Spectra*, *24*(1), 173–215.

Chiou, B. S. J., and Youngs, R. R., (2014). “Update of the Chiou and Youngs NGA model for the average horizontal component of peak ground motion and response spectra”, Earthquake Spectra 30, 1117–1155.

Chopra, A. K. (2012). *Dynamics of structures: Theory and Applications to Earthquake Engineering* (4th ed., Vol. 4). Prentice-Hall, Englewood Cliffs, N.J.

Darendeli, M. B. (2001). *Development of a new family of normalized modulus reduction and material damping curves*. The university of Texas at Austin.

Darendeli, M. B., & Stokoe, K. H. (2001). II.(2001).“Development of a new family of normalized modulus reduction and material damping curves.” *Geotechnical Engineering Report GD01-1, University of Texas at Austin, Austin, TX*.

Duman, T. Y., & Emre, Ö. (2013). The East Anatolian Fault: geometry, segmentation and jog characteristics. *Geological Society, London, Special Publications*, *372*(1), 495–529.

Elazığ (Merkez) Belediyesi İmar Planına Esas Jeolojik-*Jeoteknik Etüt Raporu*. (2015).

Erdoğan, T. (1975). *Gölbaşı Yöresinin jeolojisi*.

Error, B. M. (2017). *Development of a Simplified Performance-Based Procedure for the Assessment of Liquefaction-Induced Settlements Using Liquefaction Loading Maps*. Brigham Young University.

Green, R. A., & Mitchell, J. K. (2004). Energy-based evaluation and remediation of liquefiable soils. In Geotechnical engineering for transportation projects (pp. 1961-1970).

Groholski, D., Hashash, D., Kim, Y., Musgrove, B., Harmon, M., & Stewart, J. (2016a). *Simplified Model for Small-Strain Nonlinearity and Strength in 1D Seismic Site Response Analysis*.

Groholski, D., Hashash, Y., Kim, B., Musgrove, M., Harmon, J., & Stewart, J. (2016b). Simplified Model for Small-Strain Nonlinearity and Strength in 1D Seismic Site Response Analysis. *J. Geotech. Geoenviron. Eng.* https://doi.org/10.1061/(ASCE)GT.1943-5606.0001496 , 04016042

Gülerce, Z., Tanvir Shah, S., Menekşe, A., Arda Özacar, A., Kaymakci, N., & Önder Çetin, K. (2017). Probabilistic seismic-hazard assessment for East Anatolian fault zone using planar fault source models. *Bulletin of the Seismological Society of America*, *107*(5), 2353–2366.

Hardin, B. O., & Drnevich, V. P. (1972). Shear modulus and damping in soils: design equations and curves. *Journal of the Soil Mechanics and Foundations Division*, *98*(7), 667–692.

Hashash, Y. M. A., Musgrove, M. I., Harmon, J. A., Groholski, D. R., Phillips, C. A., & Park, D. (2016). DEEPSOIL 6.1, user manual. Urbana, IL, Board of Trustees of University of Illinois at Urbana-Champaign

Hashash, Y. M., Phillips, C., Groholski, D. R., A, Y. M., & A Hashash Camilo Phillips, Y. M. (2010). *Mine Scholars' Mine International Conferences on Recent Advances in Geotechnical Earthquake Engineering and Soil Dynamics* (Vol. 8). https://scholarsmine.mst.edu/icrageesd/05icrageesd/session12/8

Hutabarat, D. (2016). *Evaluation of One-Dimensional Seismic Site Response Analyses at Small to Large Strain Levels*.

Iai, S., Matsunaga, Y., & Kameoka, T. (2011). Strain space plasticity model for cyclic mobility. *Report of Port and Harbour Research Institute*, *29*(4), 27–56.

Idriss, I. M. (2008). An NGA empirical model for estimating the horizontal spectral values generated by shallow crustal earthquakes. *Earthquake Spectra*, *24*(1), 217–242.

Ishihara, K. (1993). Liquefaction and flow failure during earthquakes. *Geotechnique*, *43*(3), 351–451.

Itasca. (2011). Cyclic characterization of liquefiable sands, Version 7.0. *Minneapolis, Minne Sota: Itasca Consulting Group, Inc.*

Iwan W, D. (1967). On a class of models for the yielding behavior of continuous and composite systems. *Journal of Applied Mechanics*, *34*(3), 612–617.

Jennings, P. C. (1985). Ground motion parameters that influence structural damage. *Strong Ground Motion Simulation and Engineering Applications, EERI Publication*, 82–85.

Joyner, W. B., & Boore, D. M. (1988). Measurement, characterization, and prediction of strong ground motion. *Earthquake Engineering and Soil*

Dynamics II, Proc. Am. Soc. Civil Eng. Geotech. Eng. Div. Specialty Conf, 27–30.

Kaklamanos, J., Baise, L. G., Thompson, E. M., & Dorfman, L. (2015). Comparison of 1D linear, equivalent-linear, and nonlinear site response models at six KiK-net validation sites. *Soil Dynamics and Earthquake Engineering*, *69*, 207–219.

Kaya, A. (2001). *Keban (Elazığ) civarındaki metamorfitlerin yapısal analizi ve tektonik evrimi*.

Kottke, A. R., & Rathje, E. M. (2009). *Technical Manual for Strata*. http://www.gnu.org/licenses/.

Kramer, S. L. (1996). *Geotechnical Earthquake Engineering (Kramer 1996)*. rentice Hall, Upper Saddle River.

Lasley, S. J., Green, R. A., & Rodriguez-Marek, A. (2014). Comparison of equivalent-linear site response analysis software. *NCEE 2014 - 10th U.S. National Conference on Earthquake Engineering: Frontiers of Earthquake Engineering*. https://doi.org/10.4231/D3P26Q42R

Matasovic, N., & Vucetic, M. (1993). Cyclic characterization of liquefiable sands. *J. Geotech. Engrg.*, *119*(11), 1805–1822.

Menq, F.-Y. (2003). *Dynamic properties of sandy and gravelly soils*. The University of Texas at Austin.

METU EERC. (2020). The Elâzığ-Sivrice Earthquake [24 January 2020 MW=6.8] Fıeld Observatıons On Seısmıc And Structural Damage. Ankara: Metu Eerc.

Michael Arndt, A. (2017). *Performance-Based Liquefaction Triggering Analyses with Two Liquefaction Models Using the Cone Penetration Test*. https://scholarsarchive.byu.edu/etd

Mroz, Z. (1967). On the description of anisotropic work hardening. *J. Mech. Phys. Solids, 15*, 163–175.

Naz, H. (1979). *Elazığ-Palu dolayının jeolojisi TPAO*.

Newmark, N. M. (1959). A Method of Computation for Structural Dynamics. *Journal of the Engineering Mechanics Division, ASCE, 85,* 67–94.

Özgül, N. (1976). Toroslar’m bazı temel jeoloji özellikleri. *Bulletin of the Geological Society of Turkey*, *19,* 65–78.

Palutoglu, M. (2014). *ELAZIĞ KENT MERKEZİNİN TEKTONİĞİ DEPREMSELLİĞİ VE MİKROBÖLGELEME*.

Palutoğlu, M., & Tanyolu, E. (2006). Elazığ İl Merkezi Yerleşim Alanının Depremselliği. *Fırat Üniv. Fen ve Müh. Bil. Dergisi*, *18*(4), 535–546.

Perinçek, D. (1979). The geology of Hazro - Korudağ - Çüngüş - Maden - Ergani - Hazar - Elazığ - Malatya area. *The Geologıcal Society of Turkey*.

Phillips, C., & Hashash, Y. M. A. (2009). Damping formulation for nonlinear 1D site response analyses". *Soil Dynamics and Earthquake Engineering*, *29*, 1143–1158.

Schnabel, P. B., Lysmer, J., & Bolton Seed, H. (1972). *A COMPUTER PROGRAM FOR EARTHQUAKE RESPONSE ANALYSIS OF HORIZONTALLY LAYERED SITES*.

Seed, H. B., & Idriss, I. M. (1971). Simplified procedure for evaluating soil liquefaction potential. *Journal of the Soil Mechanics and Foundations Division*, *97*(9), 1249–1273.

Stewart, J., Hashash, A., Matasovic, Y., Pyke, N., Wang, R., & Yang, Z. (2008). *Benchmarking of Nonlinear Geotechnical Ground Response Analysis Procedures*.

Tuna, E. ,. (1979). *Elazığ–Palu–Pertek bölgesinin jeolojisi*.

Türkmen, İ. (1988). *Palu-Çaybağı (Elazığ D'su) Yöresinin Sedimentolojik İncelenmesi*.

Türkmen, I., Inceöz, M., Aksoy, E., & Kaya, M. (2001). Elazığ yöresinin Eosen stratigrafisi ve paleocoğrafyası ile ilgili yeni bulgular. *Bulletin of Earth Sciences Application and Research Centre of Hacettepe University*, *24*, 81–95.

Utkucu, M., Nalbant, S. S., McCloskey, J., Steacy, S., & Alptekin, Ö. (2003). Slip distribution and stress changes associated with the 1999 November 12, Düzce (Turkey) earthquake (Mw= 7.1). *Geophysical Journal International*, *153*(1), 229–241.

Wood, H. O. (1912). *The elastic-rebound theory of Earthquakes: by HF Reid, University of California Publications, Bulletin of the Department of Geology, 6, 19, 1911*. The Seismological Society of America.

Yang. (2000). *Numerical modeling of earthquake site response including dilation and liquefaction*.

Yee, E., Stewart, J., & Tokimatsu, K. (2013). Elastic and Large-Strain Nonlinear Seismic Site Response from Analysis of Vertical Array Recordings. *J. Geotech. Geoenviron. Eng.*, *139*(10), 1789–1801.

Youd, T. L., & Idriss, I. M. (2001). Liquefaction resistance of soils: summary report from the 1996 NCEER and 1998 NCEER/NSF workshops on evaluation of liquefaction resistance of soils. *Journal of Geotechnical and Geoenvironmental Engineering*, *127*(4), 297–313.

APPENDICES

APPENDIX 1: THE INFORMATION OF THE BOREHOLES USED IN THE STUDY

1	Y	X	GWT		Depth (m)	Lithology
SK-1	513800	4282711	-	7.50	0.00-1.00	Fill
					1.00-7.50	Sandstone claystone alternation
SK-2	513185	4283595	-	7.50	0.00-7.50	Pebble
SK-3	512665	4284140	-	12.00	0.00-1.00	Organic Soil
					1.00-6.00	Weathered Sandstone
					6.00-12.00	Sandstone
SK-4	513472	4284161	-	9.00	000-9.00	Claystone Sandstone Intermediate
SK-5	514082	4284124	-	12.00	0.00-1.00	Fill
					1.00-4.00	Weathered Sandstone
					4.00-12.00	Sandstone
SK-6	515304	4283250	-	9.00	0.00-9.00	Diorite-Gabro
SK-7	515065	4285039	-	9.00	0.00-9.00	Diorite-Gabro
SK-8	512703	4285065	-	7.50	0.00-1.00	Organic Soil
					1.00-7.50	Sandstone
SK-9	514331	4284985	-	10.50	0.00-1.00	Fill
					1.00-10.50	Diorite-Gabro
SK-10	514354	4285398	-	9.00	10.00-9.00	Sandstone
SK-11	515810	4285013	-	10.50	0.00-10.50	Diorite-Gabro
SK-12	515215	4284303	-	7.50	0.00-0.50	Fill
					0.50-7.50	Pebble
SK-13	513539	4285087	-	7.50	0.00-7.50	Diorite-Gabro
SK-14	514379	4283775	-	9.00	0.00-1.00	Fill
					1.00-3.00	Residual Zone
					3.00-9.00	Pebble
SK-15	514385	4282453	-	9.00	0.00-3.00	Fill
					3.00-9.00	Diorite-Gabro
SK-16	512469	4283217	-	18.00	0.00-18.00	Sandstone
SK-17	515057	4282351	-	9.00	0.00-9.00	Diorite-Gabro
SK-18	512977	4282505	-	9.00	0.00-9.00	Diorite-Gabro
SK-19	515707	4282757	-	9.00	0.00-9.00	Diorite-Gabro
SK-20	516009	4283194	-	9.00	0.00-9.00	andesite
SK-21	518192	4282952	-	15.45	0.00-1.00	Fill
					1.00-15.45	Brown Graveled Sandy Silty Clay
SK-22	518130	4284235	-	7.50	0.00-7.50	Diorite-Gabro
SK-23	507263	4273869	9	15.45	0.00-9.00	Brown Fine Gravel Sandy Silty Clay
					9.00-15.45	Sandy Silty Clay

SK-24	507756	4273743	-	15.45	0.00-12.00	Brown Graveled Sandy Silty Clay
					12.00-15.45	Light Grayish Graveled Sandy Silty Clay
SK-25	507876	4274411	-	15.00	0.00-9.00	Brown Graveled Sandy Silty Clay
					9.00-15.00	Clay limestone-claystone alternation
SK-26	506944	4274423	-	15.00	0.00-1.00	Organic Soil
					1.00-15.00	Clay limestone-claystone alternation
SK-27	507123	4275124	-	15.00	0.00-1.00	Organic Soil
					1.00-15.00	Clay limestone-claystone alternation
SK-28	507688	4277213	-	15.00	0.00-1.00	Organic Soil
					1.00-5.00	Carbonated Solid Clay
					5.00-15.00	Clay limestone-claystone alternation
SK-29	507632	4277427	-	9.00	0.00-9.00	Clay limestone-claystone alternation
SK-30	508824	4277939	-	15.00	0.00-3.00	Altered Zone
					3.00-15.00	Crystallized Limestone
SK-31	508987	4278705	-	15.00	0.00-2.00	Altered Zone
					2.00-15.00	Crystallized Limestone
SK-32	509314	4277819	-	15.00	0.00-2.00	Altered Zone
					2.00-15.00	Crystallized Limestone
SK-33	509466	4278783	-	15.00	0.00-2.00	Altered Zone
					2.00-15.00	Crystallized Limestone
SK-34	510338	4278561	-	15.00	0.00-10.00	Clay Sandy Gravel (Weathered Zone)
					10.00-15.00	Crystallized Limestone
SK-35	509410	4279100	-	15.00	0.00-1.50	Altered Zone
					1.50-15.00	Crystallized Limestone
SK-36	510527	4279847	-	15.00	0.00-7.00	Brown Graveled Sandy Silty Clay
					7.00-10.00	Clay limestone-claystone alternation
					10.00-15.00	Crystallized Limestone
SK-37	509298	4277005	-	15.00	0.00-12.00	Clay Sand Gravel-Gravel Sand (Segregated Zone)
					12.00-15.00	Crystallized Limestone
SK-38	508916	4276172	-	15.00	0.00-6.50	Brown Graveled Sandy Silty Clay
					6.50-15.00	Clay limestone-claystone alternation
SK-39	509246	4275391	-	7.50	0.00-7.50	Crystallized Limestone
SK-40	508471	4275442	-	15.45	0.00-15.45	Brown Graveled Sandy Silty Clay
SK-41	508201	4274955	-	15.00	0.00-7.50	Brown Graveled Sandy Silty Clay

					7.50-15.00	Clay limestone-claystone alternation
SK-42	508539	4276986	-	15.00	0.00-6.50	Brown Graveled Sandy Silty Clay
					6.50-15.00	Clay limestone-claystone alternation
SK-43	511111	4280313	-	12.00	0.00-7.50	Clay Sand Gravel-Gravel Sand (Segregated Zone)
					7.50-12.00	Crystallized Limestone
SK-44	506477	4276242	-	15.00	0.00-7.00	Brown Graveled Sandy Silty Clay
					7.00-15.00	Clay limestone-claystone alternation
SK-45	511051	4278790	-	18.00	0.00-15.00	Brown Graveled Sandy Silty Clay
					15.00-18.00	Clay Limestone
SK-46	510399	4279590	-	15.00	0.00-6.00	Brown Graveled Sandy Silty Clay
					6.00-15.00	Clay limestone-claystone alternation
SK-47	511061	4279538	-	15.00	0.00-10.00	Brown Graveled Sandy Silty Clay
					10.00-15.00	Clay limestone-claystone alternation
SK-48	511266	4277492	-	7.50	0.00-7.50	Crystallized Limestone
SK-49	510359	4277660	-	15.00	0.00-0.50	Organic Soil
					0.50-9.00	Clay Sand Gravel
					9.00-15.00	Clay limestone-claystone alternation
SK-50	509199	4276425	-	20.00	0.00-16.00	Brown Graveled Sandy Silty Clay
					16.00-17.00	Sand Belt
					17.00-20.00	Clay Limestone
SK-51	510098	4276972	-	15.00	0.00-9.00	Brown Graveled Sandy Silty Clay
					9.00-15.00	Clay limestone-claystone alternation
SK-52	507578	4276121	-	15.50	0.00-15.50	Brown Graveled Sandy Silty Clay
SK-53	507181	4276789	-	15.50	0.00-15.50	Brown Graveled Sandy Silty Clay
SK-54	510206	4276150	-	10.50	0.00-3.00	Residual Zone
					3.00-6.00	Altere Limestone
					6.00-10.50	Crystallized Limestone
SK-55	511236	4276707	-	7.50	0.00-2.00	Altere Limestone
					2.00-7.50	Crystallized Limestone
SK-56	510817	4275920	-	15.00	0.00-5.50	Gravel Sand Clay Silt (Residual Zone)
					5.50-7.50	Altere Limestone
					7.50-15.00	Crystallized Limestone

SK-57	510265	4275330	-	10.50	0.00-4.00	Gravel Sand Clay Silt (Residual Zone)
					4.00-10.50	Crystallized Limestone
SK-58	511088	4275626	-	7.50	0.00-7.50	Crystallized Limestone
SK-59	514421	4279623	-	15.50	0.00-15.50	Brown Graveled Sandy Silty Clay
SK-60	511602	4276382	-	15.00	0.00-4.50	Gravel Sand Clay Silt (Residual Zone)
					4.50-15.00	Crystallized Limestone
SK-61	511576	4277163	-	10.50	0.00-3.00	Residual Zone
					3.00-4.50	Altere Limestone
					4.50-10.50	limestone
SK-62	514218	4278481	-	10.50	0.00-1.50	Fill
					1.50-10.50	Crystallized Limestone
SK-63	512635	4279185	-	9.00	0.00-9.00	Crystallized Limestone
SK-64	514467	4277680	-	10.50	0.00-10.50	Crystallized Limestone
SK-65	511555	4278019	-	10.50	0.00-2.00	Altere Limestone
					2.00-10.50	Fractured and Fragmented Limestone
SK-66	512367	4277783	-	10.50	0.00-10.50	Crystallized Limestone
SK-67	515003	4279559	-	20.00	0.00-20.00	Brown Graveled Sandy Silty Clay
SK-68	512097	4278612	-	9.00	0.00-9.00	Crystallized Limestone
SK-69	514917	4278694	-	13.50	0.00-4.00	Residual Zone
					4.00-7.50	Altere Limestone
					7.50-13.50	limestone
SK-70	514859	4277953	-	7.50	0.00-7.50	limestone
SK-71	515672	4279484	-	18.00	0.00-12.00	Brown Graveled Sandy Silty Clay
					12.00-18.00	Clay limestone-claystone alternation
SK-72	513440	4278995	-	10.50	0.00-2.00	Altere Limestone
					2.00-10.50	Fractured and Fragmented Limestone
SK-73	517414	4279282	-	20.00	0.00-20.00	Brown Graveled Sandy Silty Clay
SK-74	517372	4278337	-	15.50	0.00-15.50	Gravel Sandy Silty Clay
SK-75	512533	4278507	-	10.50	0.00-10.50	Crystallized Limestone
SK-76	513502	4278523	-	7.50	0.00-7.50	Crystallized Limestone
SK-77	513391	4277775	-	7.50	0.00-7.50	Crystallized Limestone
SK-78	517288	4277872	-	15.00	0.00-15.00	Abundantly Fractured and Cracked Diorite-Gabro
SK-79	516699	4277923	-	16.50	0.00-16.50	Abundantly Fractured and Cracked Diorite-Gabro
SK-80	516061	4277833	-	7.50	0.00-2.00	Altered Zone
					2.00-7.50	Diorite-Gabro
SK-81	515824	4278293	-	18.00	0.00-18.00	Abundantly Fractured and Cracked Diorite-Gabro
SK-82	516424	4278414	-	15.00	0.00-15.00	Abundantly Fractured and Cracked Diorite-Gabro

SK-83	516655	4279310	-	20.00	0.00-10.00	Weathered Limestone Interbedded Pebbly Sandy Silty Hard Clay
					10.00-20.00	Clay limestone-claystone alternation
SK-84	516130	4279809	-	20.00	0.00-12.00	Weathered Limestone Interbedded Pebbly Sandy Silty Hard Clay
					12.00-20.00	Clay limestone-claystone alternation
SK-85	514304	4280145	-	20.00	0.00-13.50	Weathered Limestone Interbedded Pebbly Sandy Silty Hard Clay
					13.50-20.00	Clay limestone-claystone alternation
SK-86	516796	4280337	-	20.00	0.00-15.00	Weathered Limestone Interbedded Pebbly Sandy Silty Hard Clay
					15.00-20.00	Clay limestone-claystone alternation
SK-87	514766	4280370	-	20.00	0.00-13.00	Weathered Limestone Interbedded Pebbly Sandy Silty Hard Clay
					13.00-20.00	Clay limestone-claystone alternation
SK-88	517605	4280241	-	15.00	0.00-12.00	Weathered Limestone Interbedded Pebbly Sandy Silty Hard Clay
					12.00-15.00	Clay limestone-claystone alternation
SK-89	517551	4281047	-	15.00	0.00-10.50	Weathered Limestone Interbedded Pebbly Sandy Silty Hard Clay
					10.50-15.00	Clay limestone-claystone alternation
SK-90	516937	4280628	-	15.00	0.00-12.00	Weathered Limestone Interbedded Pebbly Sandy Silty Hard Clay
					12.00-15.00	Clay limestone-claystone alternation
SK-91	516158	4280837	-	15.00	0.00-10.00	Weathered Limestone Interbedded Pebbly Sandy Silty Hard Clay
					10.00-15.00	Clay limestone-claystone alternation
SK-92	514509	4280732	-	15.00	0.00-12.00	Weathered Limestone Interbedded Pebbly Sandy Silty Hard Clay
					12.00-15.00	Clay limestone-claystone alternation

SK-93	515087	4280865	-	15.00	0.00-12.00	Weathered Limestone Interbedded Pebbly Sandy Silty Hard Clay
					12.00-15.00	Clay limestone-claystone alternation
SK-94	513528	4280263	-	15.00	0.00-10.50	Weathered Limestone Interbedded Pebbly Sandy Silty Hard Clay
					10.50-15.00	Clay limestone-claystone alternation
SK-95	512932	4279916	-	15.00	0.00-9.00	Weathered Limestone Interbedded Pebbly Sandy Silty Hard Clay
					9.00-15.00	Clay limestone-claystone alternation
SK-96	511938	4279365	-	15.00	0.00-9.00	Weathered Limestone Interbedded Pebbly Sandy Silty Hard Clay
					9.00-15.00	Clay limestone-claystone alternation
SK-97	511770	4280246	-	15.00	0.00-6.50	Sandy Clay Gravely Silt (Residual Zone)
					6.50-15.00	Crystallized Limestone
SK-98	512930	4280769	-	15.00	0.00-4.00	Weathered Limestone Interbedded Pebbly Sandy Silty Hard Clay
					4.00-15.00	limestone
SK-99	513245	4280978	-	15.00	0.00-4.50	Weathered Limestone Interbedded Pebbly Sandy Silty Hard Clay
					4.50-15.00	Crystallized Limestone
SK-100	513481	4281652	-	9.00	0.00-4.00	Sandy Clay Gravely Silt
					4.00-9.00	Crystallized Limestone
SK-101	514373	4281599	-	15.00	0.00-7.50	Brown Graveled Sandy Silty Clay
					7.50-15.00	Diorite-Gabro
SK-102	512175	4280714	-	15.00	0.00-5.00	Altere Limestone
					5.00-15.00	Crystallized Limestone
SK-103	516091	4281957	-	15.00	0.00-7.50	Brown Graveled Sandy Silty Clay
					7.50-15.00	Claystone-Clay Limestone Alternation
SK-104	516656	4281563	-	15.00	0.00-12.00	Brown Graveled Sandy Silty Clay
					12.00-15.00	Claystone-Clay Limestone Alternation
SK-105	517458	4281746	-	15.00	0.00-12.50	Brown Graveled Sandy Silty Clay
					12.50-15.00	Claystone-Clay Limestone Alternation

SK-106	518561	4281376	-	15.00	0.00-12.00	Brown Graveled Sandy Silty Clay
					12.00-15.00	Claystone-Clay Limestone Alternation
SK-107	516045	4285597	-	15.00	0.00-15.00	Sandstone
SK-108	516426	4285564	-	12.00	0.00-12.00	Sandstone
SK-109	517213	4284791	-	9.00	0.00-9.00	Diorite-Gabro
SK-110	516599	4285181	-	10.50	0.00-10.50	Diorite-Gabro
SK-111	515079	4285647	-	10.50	0.00-10.50	Sandstone
SK-112	517441	4284422	-	12.00	0.00-12.00	Diorite-Gabro
SK-113	519146	4282829	-	20.00	0.00-9.00	Gravel Sandy Silty Clay
					9.00-20.00	Brown Graveled Sandy Silty Clay
SK-114	516414	4283251	-	9.00	0.00-9.00	Diorite-Gabro
SK-115	517397	4283426	-	12.00	0.00-4.00	Weathered Zone
					4.00-12.00	Diorite-Gabro
SK-116	517556	4284017	-	10.50	0.00-10.50	Diorite-Gabro
SK-117	516753	4282590	-	10.50	0.00-10.50	Diorite-Gabro
SK-118	518747	4283631	-	20.00	0.00-15.00	Gravel Sandy Silty Clay- Clay Sand
					15.00-20.00	Gravel Clay Silty Sand
SK-119	519988	4283569	-	20.00	0.00-20.00	Gravel Sandy Silty Clay
SK-120	520173	4283901	-	20.00	0.00-12.00	Gravel Sandy Silty Clay- Clay Sand
					12.00-20.00	Gravel Clay Silty Sand
SK-121	520367	4283571	-	15.00	0.00-15.00	Gravel Sandy Silty Clay
SK-122	521584	4284274	-	15.00	0.00-15.00	Diorite-Gabro
SK-123	522289	4284128	-	15.00	0.00-6.00	Brown Graveled Sandy Silty Clay
					6.00-15.00	Diorite-Gabro
SK-124	522809	4284389	-	20.00	0.00-20.00	Gravel Sandy Silty Clay
SK-125	523084	4283517	-	15.00	0.00-7.00	Coarse Gravel Sandy Silty Clay
					7.00-15.00	Claystone-Clay Limestone Alternation
SK-126	523629	4282708	-	20.00	0.00-20.00	Gravel Sandy Silty Clay
SK-127	523882	4283199	-	15.00	0.00-15.00	Brown Graveled Sandy Silty Clay
SK-128	523301	4282232	-	20.00	0.00-4.00	Gravel Sandy Silty Clay
					4.00-9.00	Coarse Gravel Sandy Silty Clay
					9.00-20.00	Claystone
SK-129	522437	4283082	-	20.00	0.00-9.00	Gravel Sandy Silty Clay
					9.00-20.00	Claystone-Clay Limestone Alternation
SK-130	522187	4282624	-	15.00	0.00-8.00	Gravel Sandy Silty Clay
					8.00-12.00	Coarse Gravel Sandy Silty Clay
					12.00-15.00	Clay Limestone
SK-131	522195	4281864	-	12.00	0.00-12.00	Claystone-Clay Limestone Alternation
SK-132	522122	4281167	-	20.00	0.00-20.00	Gravel Sandy Silty Clay
SK-133	522881	4281894	-	20.00	0.00-20.00	Gravel Sandy Silty Clay

SK-134	523757	4281938	-	12.00	0.00-12.00	Diorite-Gabro
SK-135	524814	4282514	-	10.50	0.00-10.50	Diorite-Gabro
SK-136	522281	4279286	-	15.00	0.00-3.00	Gravel Sandy Silty Clay
					3.00-15.00	Diorite-Gabro
SK-137	524353	4281984	-	9.00	0.00-3.00	Ayrışmış Gabro
					3.00-9.00	Diorite-Gabro
SK-138	521461	4279321	10	20.00	0.00-20.00	Gravel Sandy Silty Clay
SK-139	521468	4279842	12	20.00	0.00-20.00	Gravel Sandy Silty Clay
SK-140	521410	4280654	14	20.00	0.00-20.00	Gravel Sandy Silty Clay
SK-141	520751	4281017	13	20.00	0.00-20.00	Gravel Sandy Silty Clay
SK-142	520384	4280946	12	20.00	0.00-20.00	Gravel Sandy Silty Clay
SK-143	519863	4279964	-	15.00	0.00-6.00	Gravel Clay Silty Sand (Residual Zone)
					6.00-15.00	Diorite-Gabro
SK-144	520082	4279580	-	15.00	0.00-15.00	Diorite-Gabro
SK-145	519845	4278801	-	15.00	0.00-15.00	Diorite-Gabro
SK-146	520780	4279363	-	20.00	0.00-9.00	Gravel Sandy Silty Clay
					9.00-20.00	Diorite-Gabro
SK-147	521617	4278395	-	15.00	0.00-9.00	Gravel Sandy Silty Clay
					9.00-15.00	Diorite-Gabro
SK-148	522225	4278425	-	15.00	0.00-10.00	Gravel Sandy Silty Clay
					10.00-15.00	Diorite-Gabro
SK-149	520151	4280987	-	20.00	0.00-20.00	Gravel Sandy Silty Clay
SK-150	519633	4281166	-	20.00	0.00-15.50	Gravel Sandy Silty Clay
					15.50-20.00	Brown Graveled Sandy Silty Clay
SK-151	519244	4280964	-	18.00	0.00-0.50	Gravel Sandy Silty Clay
					0.50-18.00	Brown Graveled Sandy Silty Clay
SK-152	518762	4280574	-	20.00	0.00-14.00	Gravel Sandy Silty Clay
					14.00-20.00	Brown Graveled Sandy Silty Clay
SK-153	518412	4281098	-	15.00	0.00-4.00	Brown Graveled Sandy Silty Clay
					4.00-15.00	Claystone - Clay Limestone Alternation
SK-154	517955	4280829	-	15.00	0.00-5.00	Brown Graveled Sandy Silty Clay
					5.00-15.00	Claystone - Clay Limestone Alternation
SK-155	518205	4280423	-	15.00	0.00-7.00	Brown Graveled Sandy Silty Clay
					7.00-15.00	Claystone - Clay Limestone Alternation

SK-156	518521	4279809	-	15.00	0.00-10.00	Brown Graveled Sandy Silty Clay
					10.00-15.00	Diorite-Gabro
SK-157	519570	4281400	-	15.00	0.00-7.50	Brown Graveled Sandy Silty Clay
					7.50-15.00	Claystone - Clay Limestone Alternation
SK-158	522096	4280408	-	20.00	0.00-20.00	Coarse Gravel Sandy Silty Clay
SK-159	520772	4278487	-	15.00	0.00-15.00	Fractured and Fractured Diorite-Gabro
SK-160	518858	4279211	-	15.00	0.00-4.00	Altered Diorite
					4.00-15.00	Diorite-Gabro
SK-161	519344	4280267	-	15.00	0.00-6.00	Brown Graveled Sandy Silty Clay
					6.00-15.00	Diorite-Gabro
SK-162	518322	4279031	-	15.00	0.00-15.00	Claystone - Clay Limestone Alternation
SK-163	518756	4278759	-	15.00	0.00-15.00	Diorite-Gabro
SK-164	518279	4278453	-	15.00	0.00-15.00	Claystone - Clay Limestone Alternation
SK-165	518388	4277679	-	12.00	0.00-12.00	Bazalt
SK-166	518794	4277934	-	12.00	0.00-12.00	Bazalt
SK-167	521205	4277867	-	15.00	0.00-5.00	Gravel Sandy Silty Clay
					5.00-15.00	Diorite-Gabro
SK-168	520690	4277842	-	15.00	0.00-15.00	Diorite-Gabro
SK-169	519993	4277918	-	15.00	0.00-15.00	Diorite-Gabro
SK-170	520462	4277142	-	15.00	0.00-15.00	Diorite-Gabro
SK-171	520074	4277170	-	15.00	0.00-2.50	Coarse Gravel Sandy Silty Clay
					2.50-15.00	Diorite-Gabro
SK-172	522853	4278660	-	15.00	0.00-8.00	Low Gravel Sandy Silty Clay
					8.00-15.00	Diorite-Gabro
SK-173	522937	4279375	-	15.00	0.00-5.00	Low Gravel Sandy Silty Clay
					5.00-15.00	Diorite-Gabro
SK-174	522853	4280683	-	15.00	0.00-2.00	Low Gravel Sandy Silty Clay
					2.00-15.00	Diorite-Gabro
SK-175	522778	4280412	-	15.00	0.00-10.50	Low Gravel Sandy Silty Clay
					10.50-15.00	Diorite-Gabro
SK-176	523633	4280664	-	12.00	0.00-1.00	Low Gravel Sandy Silty Clay
					1.00-12.00	Diorite-Gabro
SK-177	524382	4280870	-	12.00	0.00-1.00	Low Gravel Sandy Silty Clay
					1.00-12.00	Diorite-Gabro
SK-178	517333	4282180	-	15.00	0.00-10.00	Brown Graveled Sandy Silty Clay
					10.00-15.00	Claystone - Clay Limestone Alternation
SK-179	516363	4283785	-	12.00	0.00-12.00	Diorite-Gabro
SK-180	515682	4284354	-	12.00	0.00-12.00	Diorite-Gabro
SK-181	521739	4281385	-	30.00	0.00-10.50	Brown Graveled Sandy Silty Clay

					10.50-30.00	Sandy Silty Clay
SK-182	520686	4282568	-	30.00	1.00-15.00	Gravel Sand Silt
					15.00-30.00	Gravel Sandy Silty Clay
SK-183	520858	4281800	-	30.00	0.00-30.00	Gravel Sandy Silty Clay
SK-184	521707	4282532	-	30.00	0.00-30.00	Coarse Gravel Sandy Silty Clay
SK-185	521576	4282971	-	30.00	0.00-30.00	Gravel Sandy Silty Clay
SK-186	520959	4280393	-	30.00	0.00-20.00	Gravel Sandy Silty Clay
					20.00-30.00	Coarse Gravel Sandy Silty Clay
SK-187	524652	4282974	-	18.00	0.00-0.50	Organic Soil
					0.50-18.00	Diorite-Gabro
SK-188	518840	4286243	-	10.50	0.00-10.50	Diorite-Gabro
SK-189	518504	4286250	-	12.00	0.00-12.00	Diorite-Gabro
SK-190	520294	4286209	-	12.00	0.00-12.00	Diorite-Gabro
SK-191	519909	4286186	-	12.00	0.00-12.00	Diorite-Gabro
SK-192	521144	4286383	-	12.00	0.00-12.00	Diorite-Gabro
SK-193	518847	4285431	-	10.50	0.00-10.50	Diorite-Gabro
SK-194	518436	4285008	-	10.50	0.00-10.50	Diorite-Gabro
SK-195	519264	4284833	-	10.50	0.00-10.50	Diorite-Gabro
SK-196	520842	4284015	-	10.50	0.00-10.50	Diorite-Gabro
SK-197	517170	4285378	-	12.00	0.00-12.00	Sandstone
SK-198	519338	4283921	-	12.00	0.00-12.00	Diorite-Gabro
SK-199	518496	4285778	-	15.00	0.00-15.00	Diorite-Gabro
SK-200	520107	4284993	-	15.00	0.00-15.00	Diorite-Gabro
SK-201	520915	4284989	-	12.00	0.00-12.00	Diorite-Gabro
SK-202	517150	4281371	-	20.00	0.00-0.50	Organic Soil
					0.50-7.00	Brown Graveled Sandy Silty Clay
					7.00-20.00	Claystone - Clay Limestone Alternation
SK-203	520365	4285380	-	10.50	0.00-10.50	Diorite-Gabro
SK-204	520072	4285392	-	10.50	0.00-10.50	Diorite-Gabro
SK-205	521714	4284851	-	10.50	0.00-10.50	Diorite-Gabro
SK-206	517209	4281196	-	20.00	0.00-1.00	Organic Soil
					1.00-3.00	Brown Graveled Sandy Silty Clay
					3.00-20.00	Claystone - Clay Limestone Alternation
SK-207	517220	4281008	-	20.00	0.00-1.00	Fill
					1.00-3.00	Brown Graveled Sandy Silty Clay
					3.00-20.00	Claystone - Clay Limestone Alternation
SK-208	517553	4281229	-	20.00	0.00-1.00	Organic Soil
					1.00-4.50	Brown Graveled Sandy Silty Clay
					4.50-20.00	Claystone - Clay Limestone Alternation
SK-209	517764	4281188	-	20.00	0.00-1.00	Organic Soil
					1.00-5.00	Brown Graveled Sandy Silty Clay
					5.00-20.00	Claystone - Clay Limestone Alternation

SK-210	517556	4280757	-	20.00	0.00-1.00	Fill
					1.00-7.50	Brown Graveled Sandy Silty Clay
					7.50-20.00	

PUBLICATIONS

- Cetin, K. O., Papadimitriou, A. G., Altun, S., Pelekis, P., Unutmaz, B., Rovithis, E., ... & Mylonakis, G. (2021). The role of site effects on elevated seismic demands and corollary structural damage during the October 30, 2020, M7. 0 Samos Island (Aegean Sea) Earthquake. Bulletin of Earthquake Engineering, 1-30.
- Çetin et al. (2020). Seismological and Engineering Effects of the M 7.0 Samos Island (Aegean Sea) Earthquake.
- Cetin, K. O., Cakir, E., Ilgac, M., Can, G., Soylemez, B., Elsaid, A., ... & Gor, M. (2021). Geotechnical aspects of reconnaissance findings after 2020 January 24th, M6. 8 Sivrice–Elazig–Turkey earthquake. Bulletin of Earthquake Engineering, 1-45.
- Cetin, K. O., Altun, S., Askan, A., Akgün, M., Sezer, A., Kıncal, C., ... & Karaali, E. (2022). The site effects in Izmir Bay of October 30 2020, M7. 0 Samos Earthquake. Soil Dynamics and Earthquake Engineering, 152, 107051.